The QCD phase diagram at purely imaginary chemical potential from the lattice

Dissertation
zur Erlangung des Doktorgrades
der Naturwissenschaften

vorgelegt beim Fachbereich Physik
der Johann Wolfang Goethe-Universität
in Frankfurt am Main

von
Alessandro Sciarra
aus Genua, Italien

Frankfurt am Main 2016
D30

vom Fachbereich Physik der
Johann Wolfgang Goethe-Universität als Dissertation angenommen.

Dekan: Prof. Dr. R. Reifarth

Gutachter: Prof. Dr. O. Philipsen

Datum der Disputation:

We all know that light travels faster than sound.
That's why certain people appear bright until you hear them speak.

— **Albert Einstein** —

Table of Contents

Abstract

In this thesis, we study some features of the quantum chromodynamics (QCD) phase diagram at purely imaginary chemical potential using lattice techniques. This is one of the possible methodologies to get insights about the situation at finite density, where the sign problem prevents direct investigations from first principles.

We focus, in particular, on the Roberge-Weiss plane, where the phase structure with two degenerate flavours is studied both in the light and in the heavy quark mass limit. On the lattice, any result is affected by cut-off effects and so are the positions of the two tricritical points $m_{1,2}^{\text{tric}}$ separating the second-order intermediate mass region from the first-order triple light and heavy mass regions. Therefore, changing the lattice spacing a, the values of m_1^{tric} and m_2^{tric} will change. In order to find their position in the continuum limit – i.e. for $a \to 0$ – they have to be located on finer and finer lattices. Typically, in lattice QCD (LQCD) simulations, the temperature $T = (a\,N_t)^{-1}$ is tuned through the bare coupling β, on which a depends, while keeping N_t fixed. Hence, it is common to implicitly refer to how fine the lattice is just mentioning its temporal extent.

Using both Wilson and staggered fermions, we simulate $N_f = 2$ QCD on $N_t = 6$ lattices, varying the quark bare mass from the chiral ($m_{u,d} \to 0$) to the quenched ($m_{u,d} \to \infty$) limit. For each quark mass, a thorough finite scaling analysis is carried out, taking advantage of two different but consistent methods. In this way we identify the order of the phase transition locating, then, the position of the tricritical points. In order to convert our measurements to physical units we fix the scale measuring the lattice spacing as well as the pion mass corresponding to the quark bare mass used. This allows a comparison between different discretisation, getting a first idea of how serious are cut-off effects.

To be able to make a comparison between two different discretisations, we added an RHMC algorithm with staggered fermions to the CL^{2}QCD software, a GPU code based on OpenCL, which we released in 2014. A considerable part of our work has been invested in ameliorating and optimising CL^{2}QCD, as well as in developing new analysis tools regularly used next to it. Just to mention one, the multiple histogram method has been implemented in a completely general way and we took advantage of it in order to obtain more precise results. Finally, in order to efficiently handle and monitor the hundreds of simulations that are typically concurrently run in finite temperature LQCD, a completely new Bash library of tools has been developed. We plan to release it as a byproduct of CL^{2}QCD in the near future.

Deutsche Zusammenfassung

*«Und warum fallen wir, Sir? Damit wir
lernen können uns wieder aufzurappeln.»*

— **Alfred** —

Die Physik der fundamentalen Wechselwirkungen ist einer der spannendsten modernen Forschungsbereiche, von einer theoretischen und experimentellen Perspektive. Mit Ausnahme der Gravitation sind die drei anderen fundamentalen Kräfte – elektromagnetische, starke und schwache Kraft – im Standardmodell der Teilchenphysik enthalten, das mit seinem Erfolg im beschreiben einer Vielzahl von experimentellen Ergebnissen ein Fundament des heutigen Wissens bildet. Während die elektromagnetische und schwache Kräfte von S. Glashow, A. Salam und S. Weinberg in einer einheitlichen Beschreibung vereint wurden (Nobelpreis 1979), stellt die starke Wechselwirkung noch immer einen recht separaten Bereich des Standardmodells dar. Sie beschreibt die Interaktion zwischen Quarks und Gluonen, welche wiederum Hadronen formen. Insgesamt existieren sechs *Flavours* von Quarks (up, down, strange, charm bottom und top, vom Leichtesten zum Schwersten), von denen jeder in $N_c = 3$ verschiedenen Farben vorliegen kann. Die starke Kraft ist sensibel für Farbe, jedoch nicht für Flavour der Quarks. Aus diesem Grund spricht man bei dieser Theorie von Quanten-Chromodynamik (QCD), eine Eichtheorie basierend auf der nicht-abelschen $SU(N_c)$-Farbgruppe. Gluonen sind die Träger der starken Wechselwirkung zwischen den Quarks und jedes von ihnen trägt wiederum selbst eine Farbladung. Das erlaubt Quarks, unter Abgabe oder Absorption eines Gluons, die Farbe zu wechseln. Die Anzahl der verschiedenen Typen von Gluonen entspricht der Zahl der Generatoren der Farbgruppe: acht für $N_c = 3$. Die Existenz der Quarks und Gluonen sowie der drei verschiedenen Farben wurde indirekt in den späten Sechzigern bestätigt. Kein freies, stark wechselwirkendes Teilchen wurde jemals in der Natur beobachtet, was zu der Hypothese von *Confinement* führte, eine Eigenschaft der QCD die analytisch unerklärt bleibt. Unter normalen Bedingungen können zwei Quarks nicht voneinander

getrennt werden, da die Kraft zwischen ihnen nicht abnimmt wenn sie auseinander gezogen werden (ab einem gewissen Punkt ist die Kreation eines neuen Quark-Paares energetisch günstiger gegenüber weiterer Separation). Unter sehr hohen Energien und/oder Dichten wiederum verhalten sich Quarks und Gluonen annähernd frei. Diese Eigenschaft, üblicherweise bezeichnet als *asymptotische Freiheit*, wurde in den frühen Siebzigern von D. Politzer, F. Wilczek und D. Gross gefunden (Nobelpreis 2004).

Trotz der scheinbar einfachen Form ihres Lagrangians ist die QCD analytisch nicht lösbar. Darüber hinaus erlaubt die laufende Kopplungskonstante (eine Eigenschaft jeder renormierbaren Theorie) perturbative Ansätze nur bis zu bestimmten Energien und/oder Dichten, die viel größer sind als die QCD Skala Λ_{QCD}. Deren Wert hängt vom Renormierungsschema, der festen Energieskala, zu welcher sie ausgewertet wird, und der Anzahl der aktiven Flavours ab. Um ein Beispiel zu nennen: Auf einer Energieskala der Größenordnung der Masse des Z-Bosons existieren fünf aktive Flavours und im $\overline{\text{MS}}$ Schema findet man $\Lambda_{\text{QCD}} \approx 220\,\text{MeV}$. Die QCD Skala kann man als jene Skala sehen, zu welcher nicht-perturbative Effekte überhand nehmen. Daher ist die starke Wechselwirkung auf der Skala der typischen Hadronenformation intrinsisch nicht-perturbativ und dieser Aspekt erschwert jede Untersuchung. Abgesehen von effektiven Modellen, stellen Gitter Techniken heutzutage die einzige *a priori* Methode dar um auf jeder Energieskala Vorhersagen für die QCD zu machen. Die Formulierung der stark wechselwirkenden Theorie auf einer diskreten euklidischen Raumzeit trägt den Namen Gitter QCD und hat zwei klare Vorteilen. Erstens kann das Gitter als Regulierungsschema angesehen werden. Zu einem endlichen Gitterabstand a korrespondiert ein endlicher, ultravioletter cut-off π/a, wodurch keine Divergenzen auftauchen und die physikalischen renormierten Observablen bei $a \rightarrow 0$ endlich bleiben, dem sogenannten Kontinuumslimes. Zweitens ist jedes Pfadintegral der Feldtheorie auf dem Gitter wohl definiert und die üblichen numerischen Methoden können angewandt werden (z.B. Monte Carlo Methoden). Unter anderem lassen sich so Algorithmen aus der statistischen Mechanik verwenden um, zum Beispiel, Korrelationsfunktionen und Matrixelemente von Hadronoperatoren, mit Quark und Gluon Freiheitsgeraden, zu berechnen. Viele andere Probleme können auf dem Gitter untersucht werden und auch Vorhersagen zum Vergleich mit experimentellen Daten sind möglich (vorausgesetzt der Kontinuumslimes wurde berechnet).

Eine der anspruchsvollsten Herausforderungen der modernen Teilchenphysik liegt in der Kartierung des QCD Phasendiagrams als Funktion der Temperatur T und des chemischen Potenzials μ_B. Obwohl dies im Prinzip innerhalb des Gitter QCD Rahmens machbar ist, sind gewöhnliche numerische Methoden wegen des sogenannten *sign problem* nicht anwendbar für $\mu_B/T > 1$. Dennoch sind Untersuchungen bei abwesendem chemischen Potenzial möglich und es existieren eine Reihe verschiede-

ner Techniken um indirekt Einblicke auf das tatsächliche QCD Phasendiagramm zu bekommen. Eine davon, welche durchweg in dieser Arbeit verwendet wurde, besteht darin ein rein imaginäres chemisches Potenzial $\mu = \mu_B/3 = \imath\,\mu_I$ ($\mu_I \in \mathbb{R}$) einzuführen und zu untersuchen wie das Phasendiagram bei verschwindender Dichte beeinflusst wird. Die Phasenstruktur bei rein imaginärem Potenzial beschränkt die Situation bei reelem μ_B unter analytischer Fortsetzung. Um das Zusammenspiel zwischen Confinement und chiraler Symmetriebrechung, sowie deren Einfluss auf den thermalen Übergang zu verstehen ist es ebenso interessant das QCD Phasendiagramm unter variierenden Quarkmassen, zwischen dem chiralen ($M \to 0$) und dem quenched ($M \to \infty$) Limes, zu untersuchen. Im letzten Jahrzehnt haben die ersten Untersuchungen bei verschwindendem chemischen Potenzial qualitativ die Hauptmerkmale des sogenannten Columbia Plots bestimmt, nämlich wie sich die Ordnung des Phasenübergangs als Funktion der Massen der drei leichtesten Quarks ändert. Quantitativ, und selbst qualitativ, ist diese Untersuchung jedoch noch nicht abgeschlossen, und viele Aspekte bleiben unklar. Sowohl für zwei als auch drei degenerierte, leichte wie schwere, Quark Flavours gibt es Regionen, in welchen die chirale und deconfinement Übergänge erster Ordnung für grobe Gitter mit Standard Wirkungen sind. Dagegen zeigen mittlere Massenregionen inklusive des physikalischen Punktes ein crossover Verhalten. Für verbesserte Wirkungen ist die chirale Region erster Ordnung wesentlich schmaler, aber aktuell ist kein Kontinuumslimes für diese Eigenschaften verfügbar. Andere Szenarios sind noch im Rahmen des möglichen und es ist noch nicht ausgeschlossen, dass diese auf feineren Gittern umgesetzt werden können. Die QCD Phasenstruktur bei rein imaginären Werten des chemischen Potenzials ist greifbarer als für $\mu = 0$, aufgrund der so genannten Roberge-Weiss Symmetrie. Das impliziert, dass das System Phasenübergängen zwischen verschiedenen Zentrumssektoren für kritische Werte μ_I^{RW} des rein imaginären chemischen Potenzials unterliegt. Die Regionen erster Ordnung und des crossovers, die von Z_2 Linien im Columbia Plot separiert sind, werden zu Regionen mit erster Ordnung Tripelpunkten und mit zweiter Ordnung Punkten separiert durch trikritische Linien, jeweils bei $\mu_I = \mu_I^{\mathrm{RW}}$. Allerdings existiert noch keine quantitative Kontinuumsextrapolation der Lage dieser Regionen, hauptsächlich wegen der immensen Rechenkosten von Gitter QCD Simulationen bei endlicher Temperatur. Dennoch würde ein quantitatives Verständnis der Phasenstruktur bei rein imaginärem chemischen Potenzial viele Eigenschaften des Columbia Plots einschränken und aus diesem Grund werden viele numerische Ressourcen in diese Richtung investiert. In dieser Arbeit wurde das zwei-flavour QCD Phasendiagram bei kritischem μ_I^{RW} mit zwei verschiedenen Diskretisierungen (unverbesserte Wilson und staggered Fermionen) auf feineren Gittern als in früheren Arbeiten studiert. In beiden Fällen wurden Regionen mit ersten Ordnung tripelpunkten im chiralen und quenched Limit gefunden, mit

einer Region zweiter Ordnung für mittlere Massen. Außerdem wurde die Lage des tri-
kritischen Punktes ermittelt. Das ist ein vorbereitender erster Schritt für zukünftige
Kontinuumsextrapolationen der Werte der trikritischen Quarkmassen.

Gitter QCD ist, unter anderem, auch durch die gewaltigen Rechenkosten charakte-
risiert, die notwendig sind um Vorhersagen machen zu können. Deswegen war es seit
ihrer Geburtsstunde ein Bestreben schnellere und bessere Algorithmen zu entwickeln.
Zudem profitierte sie von der konstanten Zunahme der Rechenleistung. Seit Ende
des letzten Jahrhunderts wurde parallelisiertes Rechnen zu einer Standard Technik
für Rechnungen in Gitter QCD Anwendungen und auch die Evolution der Supercom-
puter, sowie die Software reflektiert diesen Aspekt. Kürzlich wurde erkannt, dass es
möglich ist Grafikkarten (engl. `GPUs`) für ganz allgemeine Zwecke zu nutzen – z.B.
numerische Kalkulationen – anstelle der Verarbeitung der Farbe jedes Pixels eines
Monitors. Dies war für die Gitter QCD ein Durchbruch, da es erstmals erlaubte Be-
rechnungen dermaßen zu beschleunigen, dass Probleme in Angriff genommen werden
konnten, die vorher als unnahbar galten. Der einzige Nachteil lag bei der existierenden
Software, die wesentlich umgeschrieben werden musste um auf `GPUs` zu laufen. Die
Mehrheit der `GPU` Programme basieren heutzutage auf `CUDA` und laufen ausschließlich
auf `nVIDIA` Hardware. Alternativ dazu kann der öffentliche Standard `OpenCL` genutzt
werden, welches unabhängig von der zugrunde liegenden Architektur funktioniert. Mit-
tels `OpenCL` ist es sogar möglich unterschiedliche Einrichtungen zu kombinieren (z.B.
`CPUs` und `GPUs`) und zeitgleich zu nutzen. Dies wird erfolgreich in `CL`^{2}`QCD` umgesetzt,
ein Gitter QCD `OpenCL` basierter Code, dessen Entwicklung schon vor einigen Jah-
ren begann und dadurch nicht auf `nVIDIA` Hardware limitiert ist. Im Umfang dieser
Arbeit wurde die staggered Diskretisierung zu `CL`^{2}`QCD` hinzugefügt und, neben vielen
Verfeinerungen, wurde die Software nach Bekanntgabe während des 32. Internationa-
lem Symposium für Gitter Feld Theorie 2014 öffentlich zugänglich gemacht. `CL`^{2}`QCD`
wurde in allen physikalischen Untersuchungen, die in dieser Thesis vorgestellt werden,
genutzt und lief sowohl auf dem `LOEWE-CSC` (in Frankfurt am Main) als auch auf dem
`L-CSC` (in Darmstadt) Cluster, welche beide mit `AMD` Hardware (4 `GPUs` pro Rechen-
noten) ausgestattet sind. Benchmark-Tests zeigen eine herausragende Leistung auf
jeder implementierten Fermion Diskretisierung.

Für Gitter QCD bei endlicher Temperatur ist es häufig notwendig hunderte Simu-
lationen gleichzeitig laufen zu lassen, welche Scans mit verschiedenen Parametern ent-
sprechen, um Phasenübergänge zu lokalisieren. Es ist klar, dass eine effektive Lösung
zum Umgang mit so vielen Simulationen auf einem, oder mehreren, Supercomputern
entscheidend ist. Diese Notwendigkeit führte zur Entwicklung eines mächtigen bash
Programms zum Überwachen und Verwalten von Simulationen (engl. `BaHaMAS`), wel-
ches voraussichtlich in der nahen Zukunft zu `CL`^{2}`QCD` freigegeben wird. Genauso wichtig

wie eine Methode zum automatischen überprüfen der laufenden Simulationen ist eine Software zum effektiven analysieren der produzierten Daten (selbst während der laufenden Produktion). Das erlaubt es schneller die relevante Breite von Parametern zu erkennen, zu der Simulationen durchzuführen sind, und spart dadurch Zeit und Ressourcen. Während dieser Arbeit wurde eine `C++` Bibliothek nützlicher Methoden kreiert und zur Analyse-Software der vorangegangenen Projekten hinzugefügt. Insbesondere wurde eine vollständig allgemeine Implementation der multi-Histogramm Methode für eine beliebige Anzahl von Parametern entwickelt, welche ausschlaggebend ist, um noch genauere physikalische Ergebnisse zu erzielen.

Der Großteil der Arbeit bestand darin eine solide Basis für zukünftige Untersuchungen zu schaffen und jene zu erleichtern. Beispielsweise wurde ein Modell entwickelt um eine spezielle Eigenschaft der Daten zu erläutern und ein teilweise neuer Ansatz in der Extraktion des kritischen Exponenten der chiralen/deconfinement Phasenübergänge wurde benutzt. Diese können zukünftige Studien des gleichen Themas inspirieren und, sind voraussichtlich – sowohl in Bezug auf Entwicklung numerischer Werkzeuge als auch darin bessere Methoden für physikalische Fragen zu finden – von großem Wert auf lange Sicht.

Introduction

If we had to explain in simple words how physics and more generally science work, we would probably immediately think of the modern scientific method. An interesting question, arising for example from a specific observation, leads to formulate a hypothesis about possible explanations. Assuming these, testable predictions should be developed and, using existing experiments or new ones, they have to be verified. At this stage, the hypothesis shall be adjusted, changed or even rejected in favour of others. New predictions and a new testing phase may begin. Successfully verified conjectures usually lead to theories that must not be in contradiction with other ones and have to be consistent with all available data. Meanwhile, new questions could arise and the scientific method should be thought as an ongoing process.

Few centuries ago, it was common for a physicist to deal with all the steps mentioned above. Nowadays, it is more and more unusual for a single person to work in so different areas. This does not mean at all that physicists are worse. Actually it does not even make sense to compare, just because the nature of the addressed phenomena is too different. In the seventeenth century Galileo Galilei made his astronomy discoveries alone with telescopes built by himself [1], while in recent years the combined effort of *thousands* of people has led to announce the discovery of the Higgs boson [2, 3] and the observation of gravitational waves [4]. The way to investigate the physics laws of nature has clearly changed. Today, theorists generally explore new mathematical models that, beyond agreeing with existing experiments, successfully predict future experimental results. Experimentalists, instead, project and perform experiments to test theoretical predictions and explore new phenomena. Due to the more and more specialistic knowledge that is required, the work of a theoretical and an experimental physicist has gradually become, in practice, less interconnected. A general understanding of experiments for a theorist – as well as of theories for an experimentalist – is important and encouraged, but a sector-based specialisation is at some point unavoidable. As consequence, it should not be hard to understand that the interplay of many people (often coming also from different fields) has an increasing importance these days and it is not a coincidence that the most extraordinary recent discoveries as those previously mentioned are the result of large collaborations.

Focusing on high energies physics only, there are many cases in which the synergy of physicists, engineers, computer and material scientists is crucial for the success of an experiment. All the accelerator facilities installed around the world are a clear example of that. On the theoretical side, instead, it could be argued that a single person alone can still contribute with some sensational idea to the common knowledge. In the end, ideas come from individuals, rarely from groups. This was, is and will always be true. The works of S. Weinberg [5] in 1967 and of J. M. Maldacena [6] in 1997 can be considered as two amazing examples. Nonetheless, when it comes to develop testable, maybe very precise predictions for experiments, it is uncommon to get an input from somebody alone. Already only for the fact that many results obtained from complicated calculations are carried out

using (super)computers implies that physics intuition and mathematical skills are still necessary but not sufficient anymore. Remaining on a more theoretical level, there are even areas of research where, already at the starting point, the hope of finding an analytic, exact solution of the problem has to be abandoned. In astrophysics, for instance, the Einstein's equations can be solved only under particular simplifying approximations. Whenever trying to describe a more realistic setup, numerical techniques are used. Another example comes from particle physics. Quantum chromodynamics (QCD) is believed to be the correct quantum field theory describing strong interactions, but its deceptively simple Lagrangian leads to equations of motion, for which an analytic solution is not known. Fortunately, though, this is not synonymous with loss of prediction. For many years, different powerful methods have been developed to study QCD in different energy ranges. In the Seventies, the discovery of asymptotic freedom [7–12] has justified the use of perturbative techniques in the high energy regime. At lower energies, the coupling constant of the theory is not much smaller than one anymore and alternative approaches are needed. Many effective models developed in last decades – such as the PNJL model, the instanton liquid model, the (extended) linear sigma model, matrix and quark models – capture many essential features of QCD and are able to reproduce experimental features where perturbative results are not reliable, but their range of applicability is often very limited and some known measurement has to be used as input. This approach could sound unsatisfactory, since we would like to interpret a significant discrepancy between our prediction and an experimental result as evidence of new physics and this is hardly possible whenever we rely on experimental data in our calculation. Driven by this idea, F. Wegner in 1971 and, independently, K. Wilson in 1974 proposed [13, 14] a completely revolutionary way of studying non-perturbative phenomena, which took later the name of lattice QCD (LQCD). Inspired by numerical methods used in statistical mechanics, their idea was a real breakthrough in a historical moment where predictions were limited to the perturbative regime or to models of QCD and an ab initio study of strong interaction using directly the Lagrangian of the theory was missing. In the following years, LQCD started to be ameliorated and many unresolved problems began to be addressed. Somehow, if today we believe that QCD is the theory of strong interactions, it is also because of the achievements of LQCD.

The fact that the predictive aspect of a theory – in astrophysics as in QCD and in any other field – is subject to the use of numerical methods has transformed the way of making predictions. A different background knowledge is more and more required and the interplay between physicists and computer scientists can be amazingly productive. LQCD is one of the clearest examples. Calculations are carried out on huge supercomputers and, in order to do so, appropriate software has to be developed. Obviously, it must be fast and low-level optimisations are needed. Not only speed is important, since problems can also arise from the amount of required storage memory. Moreover, considering that often the codes are highly parallelised, communications among different nodes of the supercomputers have to be efficient. Ultimately, these are not responsibilities of a physicist, which, nevertheless, has to be able to use (and sometimes modify) advanced software, produce data, elaborate them and, especially, use his knowledge to interpret and draw conclusions from them. This thesis has been written with this idea in mind and, therefore, it also contains technical numerical aspects that, however, have been bounded to a single chapter.

Our field of research is particle physics and this work is, after all, related to the QCD phase diagram. A complete understanding of the behaviour of strong interacting matter as a function of temperature T and density would have many implications – for instance, it would give access to information regarding the evolution of the universe as well as about many astrophysical systems. Hence, it is worth spending some words about the experimental efforts devoted to this subject. The probably most famous particle physics experiments are being done at CERN (Switzerland, France), where the biggest accelerator facility has been recently built. Using a series of bigger and bigger rings, the last of which is called LHC and is 27 km long, protons and heavy ions are accelerated at very high energies (the highest ever reached so far) and collide almost at the speed of light (about $3.1\,\mathrm{m\,s^{-1}}$ less than c). This technique, completely general and used in all accelerators, allows to
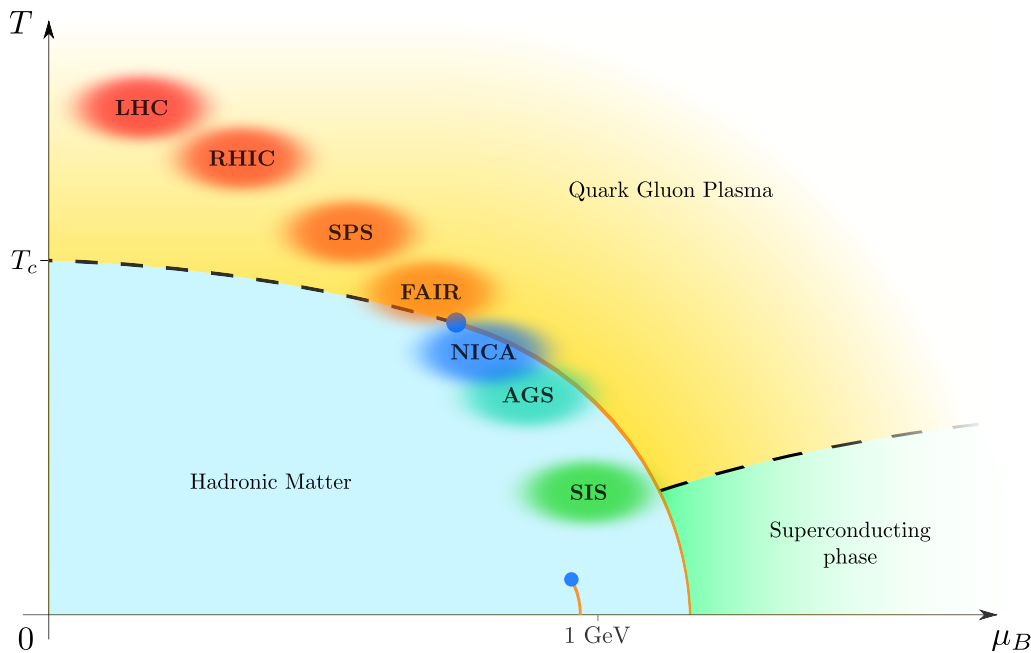
Figure 1: *Conjectured phase diagram of strongly interacting matter. The orange solid (black dashed) lines depict first-order (crossover) phase transitions, while the blue dots are second-order critical endpoints. This is only a qualitative representation and only the main features are drawn. The axes scales are linear and T_c has been estimated in LQCD [15] to be between $150\,\mathrm{MeV}$ and $170\,\mathrm{MeV}$. Some of the main experimental facilities to probe different regions of the phase diagram have been included. Consider that their range of investigation could be wider than drawn and this is the reason why the borders are shaded.*

gather insights about how particles interact and, therefore, to study the fundamental laws of nature. Clearly, this is possible using very sophisticated detectors, which are able to observe and register the result of the collisions. Though it would be interesting, we will not discuss here all the experiments and the topics studied at CERN. It is enough to say that some of them regard our universe and the early stages of its life, while some others investigate not well understood aspects of particle physics – a more detailed, quite qualitative description of both experiments and physics topics can be found at `https://home.cern/about`. As it can be seen in Figure 1, in LHC experiments (e.g. ALICE, CMS, ATLAS), matter at very high temperatures but quite small densities is probed. Many other ongoing experiments investigate what happens at higher densities. Just to cite some accelerators, ordered for decreasing temperature and increasing density of the studied phenomena, we have RHIC at Brookhaven National Laboratory in Upton (New York, United States), SPS at CERN, FAIR in Darmstadt (Germany), NICA in Dubna (Russia), AGS in Upton and SIS in Darmstadt. The ranges of investigations of these experiments have been qualitatively depicted in Figure 1. It is worth remarking that one of the main goals is to understand whether there is a critical endpoint in the QCD phase diagram and, if yes, at which temperature and density.

From the theoretical point of view, unfortunately, no ab initio method is available at non-zero (and not asymptotically large) baryonic density[1]. Any LQCD investigation is prevented by the sign problem, which means, roughly speaking, that we do not know an efficient algorithm to make numerical predictions [16]. This is the reason why most of the effective non-perturbative models are developed to study finite temperature and density features of the QCD phase diagram. Nevertheless,

---

[1]Here, again, we are implicitly referring to the range of parameters where the perturbative approach is not possible anymore. In general, at large chemical potential and temperature, perturbation theory works well.

at zero baryonic chemical potential, $\mu_B = 0$, standard numeric techniques can be used and, indeed, on the lattice, it is possible to gain insights of what happens for small density, more precisely for $\mu_B/T \lesssim 1$. Moreover, studying QCD properties for unphysical quark masses or a reduced number of flavours could lead to important consequences about the structure of the phase diagram. Hence, in the last decade, many efforts and computational resources have been devoted to finite temperature QCD studies on the lattice. The order of the phase transition, which a strong interacting system undergoes at zero chemical potential, depends, among others, both on the number of flavours and on their mass. A complete understanding of this dependence is still missing and it would be a solid starting point for further investigations of the QCD phase diagram. Despite that simulations at $\mu_B = 0$ are not affected by the sign problem and studies from first principles can be carried out, chiral and continuum extrapolations are still very costly and any cheaper alternative is welcome. As it will be extensively discussed, the use of a purely imaginary chemical potential can be very advantageous and it played a central role in this work. Even though any LQCD result can be conclusive and used as a basis for comparison with experiments only if the continuum limit has been taken, often this is not possible in a few years time. Therefore, it is important to proceed to meticulous studies on finite lattices, so that different people can combine their resources using as input the output of previous works. Keeping this in mind, we proceeded in our survey as accurately as possible and our outcomes will be used in future for further investigations.

This thesis has been written mainly for a person who wishes to work on the same or on similar topics. We rarely assumed the Reader to be an expert of the subject and whenever we had to skip some details we provided information about where to find them. Sometimes we intentionally preferred to keep the discussion on a qualitative level, in order to give a broader, less technical overview, possibly complementary to more detailed reviews present in the literature. Occasionally, instead, we thought it would have been difficult for the Reader to gather all the information using external references and we preferred to make a self-consistent, as complete as possible discussion. Despite the fact that many topics can be found on standard LQCD textbooks, we always tried to work out calculations which are generally omitted and we are confident that also the more experienced Reader will find interesting inspirations.

The content of this thesis has been organised as follows. Chapter 1 is a pedagogical introduction to some aspects of LQCD. Here, we clearly had to make a selection of topics and only the essential concepts for the following chapters have been discussed. The Reader well acquainted with the basic notions of LQCD can skip it entirely. In chapter 2, the state of the art of the knowledge about the QCD phase diagram is analysed. Avoiding to draw conclusions based on effective models or on preliminary lattice studies not yet extrapolated in the continuum, most of the logically possible scenarios are considered and discussed. Particular attention is devoted to the $\mu_B = 0$ case and to describe the phase structure of QCD at purely imaginary chemical potential. Once established the theoretical framework, we will temporarily move slightly away from physics in chapter 3, where the main numerical ingredients needed in our projects are explained. In this chapter, technical computations and qualitative descriptions will be alternated in order to introduce all the needed techniques which have been used in the physical investigations. On one hand we tried to confine here all the computational details to make the rest of the thesis less technical, but at the same time, doing so, the Reader can use the information provided as documentation of completely general numerical methods. The studies and the obtained results are presented and discussed in chapter 4. The main goal has been to locate the two tricritical points present in two-flavour QCD at the Roberge-Weiss critical value of the purely imaginary critical potential with unimproved both Wilson and staggered fermions on $N_t = 6$ lattices. Many problems and unexpected features appeared during our research, but everything was scrupulously studied and understood. New strategies to analyse the data were formulated, successfully used and, hence, here presented. A critical discussion of the results together with a comparison of the measurements done in the past on coarser lattices has also been included.

Notation

For the sake of completeness, we decided to recapitulate here some of the conventions we will use throughout the thesis. Few assumptions are understood when recalling quantum field theory and statistical mechanics notions. First of all, we use natural units, setting $\hbar = c = k_{\mathrm{B}} = 1$. Moreover, we call propagator of a theory the vacuum expectation value of the time-ordered product of fields, *without any prefactor* (as it is sometimes found). Our metric tensor reads

$$g_{\mu\nu} = g^{\mu\nu} = \mathrm{diag}(1, -1, -1, -1) \ .$$

Our choice of the indices is quite standard: Greek (Roman) indices in the middle and in the beginning of the alphabet are used for Lorentz (spatial) and Dirac (colour) indices, respectively. However, this is not a strict rule and from the context should help to avoid any confusion. If not differently specified, repeated indices are summed. Nevertheless, we prefer sometimes to explicitly indicate the sum, like for example when it helps for a later definition.

Often, the domain of integration is omitted. In this case it coincide with the largest possible one, coherently with the meaning of the integration variable. This is a standard choice and the Reader should be used to it. Instead, it is not universal to consider $0 \in \mathbb{N}$ and therefore it is important to clarify this point. To use an unquestionable notation, we define

$$\mathbb{N}_{\geqslant 0} \equiv \{0, 1, 2, \ldots\}$$
$$\mathbb{N}_{> 0} \equiv \{1, 2, 3, \ldots\} \ .$$

Finally, in many formulae, we decided to use colours to help the Reader to follow calculations. Their meaning should be self-explanatory; the idea behind is to colour in the same way connected quantities in subsequent steps. A trivial example could be,

$$\left\langle \left(x - \langle x\rangle\right)^3 \right\rangle = \left\langle x^3 + 3\,x\,\langle x\rangle^2 - 3\,x^2\,\langle x\rangle - \langle x\rangle^3 \right\rangle =$$
$$= \langle x^3\rangle + 3\,\langle x\rangle\,\langle x\rangle^2 - 3\,\langle x^2\rangle\,\langle x\rangle - \langle x\rangle^3 = \langle x^3\rangle - 3\,\langle x^2\rangle\,\langle x\rangle + 2\,\langle x\rangle^3$$

and, even if this could seem unnecessary, sometimes it turns out to be really useful to follow the details of a formula (e.g. compare with calculation at page 22).

LQCD: An introduction **1**

«Any fool can know. The point is to understand.»

— **Albert Einstein** —

This chapter is thought as a pedagogical introduction for the Reader new to LQCD. Despite the fact it could be argued that the topics discussed here can be found on many different textbooks, we decided to include them for the sake of completeness and to introduce names and notations used in the following chapters. Actually, the constant effort in not omitting any calculation detail, which is usually given as understood, makes this introduction to LQCD complementary to others present in the literature. Obviously, it is not possible to be as general as possible and we had to make a selection of topics. This was done choosing those arguments somehow relevant for this thesis. For instance, we will not discuss at all the regularisation on the lattice of a bosonic field and only the fermionic discretisations actually used in the numeric studies will be presented. The Reader can refer to [17–20], as well as to other books on the subject, for further aspects not discussed here.

In the same spirit, a QCD introduction in the continuum could have been here included. Nevertheless, this would have brought us too far from the core of this thesis and to consider continuum quantum field theory as prerequisite is a common practice in lattice gauge theories. Moreover, we would have disliked to report an unavoidably dense series of notions without too many justifications, probably neither useful for a Reader new to the subject nor for an expert. Therefore, we preferred to recall continuum quantum field theory notions whenever required in our discussion.

§ 1.1 The free Dirac theory on the lattice

As starting point[1], let us consider the action of a spin $1/2$ particle of mass M_0

$$\mathcal{S}_F\big[\psi,\bar\psi\big] = \int \mathrm{d}^4x \ \bar\psi(x) \left(\imath\gamma^\mu\partial_\mu - M_0\right)\psi(x) \ = \sum_{\alpha,\beta}\int \mathrm{d}^4x \, \mathrm{d}^4y \ \bar\psi_\alpha(x)K_{\alpha\beta}(x,y)\psi_\beta(y) \ ,$$

where

$$K_{\alpha\beta}(x,y) = \left(\imath\gamma^\mu\partial_\mu - M_0\right)_{\alpha\beta} \delta^{(4)}(x-y) \ .$$

Varying $\mathcal{S}_F$ with respect to the fields ψ and $\bar\psi$ independently, the Dirac equation for ψ

$$\left(\imath\gamma^\mu\partial_\mu - M_0\right)\psi(x) = 0 \tag{1.1}$$

---

[1]Here, the standard quantum field theory notation [21] is used: ψ is a 4-component field whose components are identified by Greek indices, γ^μ are the Dirac matrices such that $\{\gamma^\mu,\gamma^\nu\} = 2\,g^{\mu\nu}$, while $\bar\psi(x) \equiv \psi^\dagger(x)\gamma^0$.

is obtained. Proceeding with the standard quantisation of the fields ψ and $\bar{\psi}$, the two-point correlation function – the *fermion propagator* – is given by

$$\langle\Omega\,|\,\mathbf{T}\big(\Psi_\alpha(x)\bar{\Psi}_\beta(y)\big)\,|\,\Omega\rangle = \imath K_{\alpha\beta}^{-1}(x,y) \;, \tag{1.2}$$

where $\mathbf{T}$ denotes the time-ordering operation, while the operators Ψ and $\bar{\Psi}$ are elements of a Grassmann algebra satisfying to the equal-time commutation relation

$$\big\{\,\Psi_\alpha(\vec{x},t),\,\Psi_\beta(\vec{y},t)\,\big\} = \delta_{\alpha\beta}\,\delta^{(3)}(\vec{x}-\vec{y}) \;.$$

Eq. (1.2) can be understood considering the fact that the fermion propagator is the Green's function of the Dirac operator appearing in Eq. (1.1). Using differentiation and integration properties of Grassmann variables leads to a Path Integral representation of the two-point correlation function

$$\langle\Omega\,|\,\mathbf{T}\big(\Psi_\alpha(x)\bar{\Psi}_\beta(y)\big)\,|\,\Omega\rangle = \imath K_{\alpha\beta}^{-1}(x,y) = \frac{\int \mathcal{D}\bar{\psi}\,\mathcal{D}\psi\;\psi_\alpha(x)\,\bar{\psi}_\beta(y)\,e^{\,\imath\,\mathcal{S}_F[\psi,\bar{\psi}]}}{\int \mathcal{D}\bar{\psi}\,\mathcal{D}\psi\,e^{\,\imath\,\mathcal{S}_F[\psi,\bar{\psi}]}} \;, \tag{1.3a}$$

where

$$\mathcal{D}\bar{\psi}\,\mathcal{D}\psi \;=\; \prod_{\alpha,x}\mathrm{d}\bar{\psi}_\alpha(x)\prod_{\beta,y}\mathrm{d}\psi_\beta(y) \;. \tag{1.3b}$$

Since the number of degrees of freedom is infinite, the measure above is only formally defined. This is a common fact in field theory for Path Integral expressions for Green's functions. A way to give them a precise meaning is to discretise continuous degrees of freedom, namely to introduce a space-time lattice. At some point, such a lattice will have to be removed taking the so-called continuum limit. Since this is not at all a trivial procedure, we will discuss in detail how to do in §1.2 and §1.6. The introduction of a space-time lattice allows, at least in principle, to tackle any problem numerically. Indeed, in order to really be able to do so, we also need to continue the real time to imaginary values[2]. Let us then perform the Wick rotation

$$x^0 = -\imath x_4, \quad y^0 = -\imath y_4, \quad \text{etc.}$$

From $\mathcal{S}_F$, the euclidean action can be obtained. Considering that the Lorentz group in the Minkowski space is replaced by the rotations group in the euclidean space, we can introduce a new set of matrices $\{\gamma_1^E,\gamma_2^E,\gamma_3^E,\gamma_4^E\}$ such that

$$\begin{aligned}\gamma_4^E &= \gamma_0 \\ \gamma_k^E &= -\imath\gamma^k = \imath\gamma_k\end{aligned} \qquad \text{and satisfying the algebra} \qquad \{\gamma_\mu^E,\gamma_\nu^E\} = 2\,\delta_{\mu\nu} \;.$$

Therefore

$$\begin{aligned}\imath\,\mathcal{S}_F\big[\psi,\bar{\psi}\big] &= \imath\int \mathrm{d}x^0\,\mathrm{d}\vec{x}\;\bar{\psi}(x)\big(\imath\gamma_0\partial_0 - \imath\gamma_k\partial_k - M_0\big)\psi(x) \;= \\[4pt] &= \imath\int \mathrm{d}\vec{x}\,(-\imath\,\mathrm{d}x_4\,)\;\bar{\psi}(x)\big(-\gamma_0^E\partial_0 - \imath\gamma_k^E\partial_k - M_0\big)\psi(x) \;= \\[4pt] &= -\int \mathrm{d}^4x\;\bar{\psi}(x)\big(\gamma_\mu^E\partial_\mu + M_0\big)\psi(x) \;\equiv\; -\mathcal{S}_F^{(\text{eucl.})} \;. \tag{1.4}\end{aligned}$$

From now on we will deal almost only with quantities in the euclidean space and then any label remembering this fact will be dropped. For those few continuum expressions that will be recalled an explicit remark will be done. The *fourth* component of any 4-vector will be the *temporal* one.

---

[2]Even though this statement could sound quite cryptic now, its meaning will be definitely clear further in the thesis (cf. chapter 3). For the curious Reader, it is enough to say that the exponential factor in the Path Integrals is numerically interpreted as probability distribution and this implies it to be real (and positive).

Let us then introduce a space-time lattice. Since there is no reason to treat any direction differently, the lattice spacing a will be the same in each direction. The coordinates on our lattice will be specified using collective indices – e.g. $n \equiv (n_1, n_2, n_3, n_4)$ – that are the analogue of the 4-vectors in the continuum. The measure in Eq. (1.3b) becomes

$$\mathcal{D}\bar{\psi}\,\mathcal{D}\psi \;=\; \prod_{\alpha,n} \mathrm{d}\bar{\psi}_\alpha(na) \prod_{\beta,m} \mathrm{d}\psi_\beta(ma)$$

and is now mathematically well defined. The following step to get the lattice formulation of the free Dirac theory is to rewrite the action in terms of dimensionless quantities, which will be denoted using a *hat* on them (e.g. $\hat{\psi}$, $\hat{M}_0$, etc.). The replacements we need are the following:

$$M_0 = a^{-1}\,\hat{M}_0 \tag{1.5a}$$

$$\psi_\alpha(x) = a^{-3/2}\,\hat{\psi}_\alpha(n) \tag{1.5b}$$

$$\bar{\psi}_\alpha(x) = a^{-3/2}\,\bar{\hat{\psi}}_\alpha(n) \tag{1.5c}$$

$$\partial_\mu\,\psi_\alpha(x) = a^{-5/2}\,\hat{\partial}^S_\mu\,\hat{\psi}_\alpha(n)\ , \tag{1.5d}$$

where

$$\hat{\partial}^S_\mu\,\hat{\psi}_\alpha(n) \equiv \frac{1}{2}\Big[\hat{\psi}_\alpha(n+\hat{\mu}) \,-\, \hat{\psi}_\alpha(n-\hat{\mu})\Big] \tag{1.5e}$$

and

$$\int \mathrm{d}^4 x \;\to\; \sum_n a^4\ . \tag{1.5f}$$

Here $n \pm \hat{\mu}$ denotes the next neighbour forward or backward in the direction μ, while the label S on $\hat{\partial}_\mu$ gives emphasis to the *symmetric* the discretisation we made. Despite the fact that naïvely Eq. (1.5e) could sound the most natural choice, there are deeper reasons while one side derivatives should be avoided. We will comment further on this point at the end of §1.2 after having discussed the doubling problem. For the moment let us simply plug Eqs. (1.5) in Eq. (1.4). The lattice action $\mathcal{S}_F$ then reads

$$\mathcal{S}_F = \sum_n \left\{ \sum_{\mu=1}^4 \left[\bar{\hat{\psi}}(n)\ \gamma_\mu\ \frac{1}{2}\Big(\hat{\psi}(n+\hat{\mu}) \,-\, \hat{\psi}(n-\hat{\mu})\Big) \right] + \bar{\hat{\psi}}(n)\,\hat{M}_0\,\hat{\psi}(n) \right\} =$$

$$= \sum_{n,m} \sum_{\alpha,\beta} \bar{\hat{\psi}}_\alpha(n)\,K_{\alpha\beta}(n,m)\,\hat{\psi}_\beta(m)\ , \tag{1.6a}$$

with

$$K_{\alpha\beta}(n,m) \equiv \sum_{\mu=1}^4 \frac{1}{2}\big(\gamma_\mu\big)_{\alpha\beta}\Big[\delta_{m,n+\hat{\mu}} - \delta_{m,n-\hat{\mu}}\Big] + \hat{M}\delta_{m,n}\delta_{\alpha,\beta}\ . \tag{1.6b}$$

It is also straightforward to write down the lattice version of Eq. (1.3a),

$$\big\langle\,\hat{\Psi}_\alpha(n)\ \bar{\hat{\Psi}}_\beta(m)\,\big\rangle = \frac{\int \mathcal{D}\bar{\hat{\psi}}\,\mathcal{D}\hat{\psi}\ \hat{\psi}_\alpha(n)\ \bar{\hat{\psi}}_\beta(m)\,e^{-\mathcal{S}_F}}{\int \mathcal{D}\bar{\hat{\psi}}\,\mathcal{D}\hat{\psi}\ e^{-\mathcal{S}_F}} = K^{-1}_{\alpha\beta}(n,m)\ , \tag{1.7a}$$

where

$$\mathcal{D}\bar{\hat{\psi}}\,\mathcal{D}\hat{\psi} = \prod_{n,\alpha} \mathrm{d}\bar{\hat{\psi}}_\alpha(n) \prod_{m,\beta} \mathrm{d}\hat{\psi}_\beta(m)\ . \tag{1.7b}$$

In Eq. (1.7a) the vacuum $|\Omega\rangle$ as well as the time-ordering operation have been intentionally omitted, since we are referring to the lattice correlation function. In order to make the Reader become more acquainted with the lattice formalism, but also to introduce some notation for future use, let us

calculate explicitly the lattice fermion propagator. An easy way to proceed is to find the Fourier transform $\tilde{K}_{\lambda\beta}(\hat{k})$ and then write directly down $K_{\alpha\beta}(n,m)$. In general, the Fourier transform of a function $f(n_1,\ldots,n_l)$ defined on integers is a function $\tilde{f}(\hat{k}_1,\ldots,\hat{k}_l)$ defined on reals which is periodic with period 2π in each direction and whose variables then range in the so-called (first) Brillouin zone, i.e. $\hat{k}_i \in [-\pi,\pi)$. It can be shown that, whenever the function f depends on two variables n_i and n_j through the difference $n_i - n_j$ only, then the function $\tilde{f}$ depends trivially on one of its variables and it can be rewritten in a way such that it depends only on $l-1$ variables[3]. This is the reason why the fermion propagator in momentum space depends only on $\hat{k}$. By definition we have

$$K_{\lambda\beta}(l,m) = \int_{-\pi}^{\pi} \frac{\mathrm{d}^4\hat{k}}{(2\pi)^4} \, \tilde{K}_{\lambda\beta}(\hat{k}) \, e^{\imath\,\hat{k}\cdot(l-m)} \tag{1.8a}$$

$$K_{\alpha\lambda}^{-1}(n,l) = \int_{-\pi}^{\pi} \frac{\mathrm{d}^4\hat{k}}{(2\pi)^4} \, \tilde{G}_{\alpha\lambda}(\hat{k}) \, e^{\imath\,\hat{k}\cdot(n-l)} \tag{1.8b}$$

$$\delta_P(\hat{k}) = \frac{1}{(2\pi)^4} \sum_n e^{-\imath\,\hat{k}\cdot n} \tag{1.8c}$$

and it is not difficult to show that

$$\delta_{n,m} = \int_{-\pi}^{\pi} \frac{\mathrm{d}^4\hat{k}}{(2\pi)^4} \, e^{\imath\,\hat{k}\cdot(n-m)} \;. \tag{1.8d}$$

Starting from the fact that

$$\sum_{\lambda,l} K_{\alpha\lambda}^{-1}(n,l) \, K_{\lambda\beta}(l,m) = \delta_{\alpha,\beta}\, \delta_{n,m}$$

and making use of Eqs. (1.8), we get

$$\sum_{\lambda} \int_{-\pi}^{\pi} \frac{\mathrm{d}^4\hat{k}\,\mathrm{d}^4\hat{q}}{(2\pi)^4\,(2\pi)^4} \, \tilde{G}_{\alpha\lambda}(\hat{k})\, \tilde{K}_{\lambda\beta}(\hat{q})\, e^{\imath\,\hat{k}\cdot n - \imath\,\hat{q}\cdot m} \sum_l e^{\imath\,(\hat{q}-\hat{k})\cdot l} = \int_{-\pi}^{\pi} \frac{\mathrm{d}^4\hat{k}}{(2\pi)^4}\, \delta_{\alpha,\beta}\, e^{\imath\,\hat{k}\cdot(n-m)}$$

$$\sum_{\lambda} \int_{-\pi}^{\pi} \frac{\mathrm{d}^4\hat{k}\,\mathrm{d}^4\hat{q}}{(2\pi)^4} \, \tilde{G}_{\alpha\lambda}(\hat{k})\, \tilde{K}_{\lambda\beta}(\hat{q})\, \delta_P(\hat{k}-\hat{q})\, e^{\imath\,\hat{k}\cdot n - \imath\,\hat{q}\cdot m} = \int_{-\pi}^{\pi} \frac{\mathrm{d}^4\hat{k}}{(2\pi)^4}\, \delta_{\alpha,\beta}\, e^{\imath\,\hat{k}\cdot(n-m)}$$

$$\sum_{\lambda} \int_{-\pi}^{\pi} \frac{\mathrm{d}^4\hat{k}}{(2\pi)^4} \, \tilde{G}_{\alpha\lambda}(\hat{k})\, \tilde{K}_{\lambda\beta}(\hat{k})\, e^{\imath\,\hat{k}\cdot(n-m)} = \int_{-\pi}^{\pi} \frac{\mathrm{d}^4\hat{k}}{(2\pi)^4}\, \delta_{\alpha,\beta}\, e^{\imath\,\hat{k}\cdot(n-m)}$$

$$\sum_{\lambda} \tilde{G}_{\alpha\lambda}(\hat{k})\, \tilde{K}_{\lambda\beta}(\hat{k}) = \delta_{\alpha,\beta} \;.$$

It remains then to find the matrix $\tilde{K}_{\lambda\beta}(\hat{k})$ and invert it. This is nothing more than an algebraic exercise,

$$\tilde{K}_{\lambda\beta}(\hat{k}) \equiv \sum_{n-m} K_{\lambda\beta}(n,m)\, e^{-\imath\,\hat{k}\cdot(n-m)} =$$

$$= \sum_{n-m} \left\{ \sum_{\mu=1}^{4} \frac{1}{2}(\gamma_\mu)_{\lambda\beta}\left[\delta_{m,n+\hat{\mu}} - \delta_{m,n-\hat{\mu}}\right] + \hat{M}_0\delta_{m,n}\delta_{\lambda,\beta} \right\} e^{-\imath\,\hat{k}\cdot(n-m)} =$$

$$= \sum_{\mu=1}^{4} \frac{1}{2}(\gamma_\mu)_{\lambda\beta}\left[e^{\imath\,\hat{k}_\mu} - e^{-\imath\,\hat{k}_\mu}\right] + \hat{M}_0\,\delta_{\lambda,\beta} =$$

---

[3]We summarised in §C.1 how the Fourier transform of a function $f : \mathbb{Z} \to \mathbb{R}$ is defined.

$$= \imath \sum_{\mu=1}^{4} (\gamma_\mu)_{\lambda\beta} \ \sin \hat{k}_\mu + \hat{M}_0 \ \delta_{\lambda,\beta} \ .$$

Observing that

$$\sum_\lambda \left\{ \left[\hat{M}_0 \ \delta_{\alpha,\lambda} - \imath \sum_{\mu=1}^{4} (\gamma_\mu)_{\alpha\lambda} \ \sin \hat{k}_\mu \right] \cdot \left[\hat{M}_0 \ \delta_{\lambda,\beta} + \imath \sum_{\nu=1}^{4} (\gamma_\nu)_{\lambda\beta} \ \sin \hat{k}_\nu \right] \right\} =$$

$$= \hat{M}_0{}^2 \ \delta_{\alpha,\beta} + \imath \ \hat{M}_0 \sum_{\nu=1}^{4} \cancel{(\gamma_\nu)_{\alpha\beta}} \ \sin \hat{k}_\nu - \imath \ \hat{M}_0 \sum_{\mu=1}^{4} \cancel{(\gamma_\mu)_{\alpha\beta}} \ \sin \hat{k}_\mu + \sum_{\mu=1}^{4} \sum_{\nu=1}^{4} (\gamma_\mu \gamma_\nu)_{\alpha\beta} \ \sin \hat{k}_\mu \sin \hat{k}_\nu =$$

$$= \hat{M}_0{}^2 \ \delta_{\alpha,\beta} + \sum_{\mu=1}^{4} \sum_{\nu=1}^{4} \left(\frac{1}{2} \left[\gamma_\mu, \gamma_\nu \right] + \frac{1}{2} \left\{ \gamma_\mu, \gamma_\nu \right\} \right)_{\alpha\beta} \ \sin \hat{k}_\mu \sin \hat{k}_\nu = \left(\hat{M}_0{}^2 + \sum_{\mu=1}^{4} \sin^2(\hat{k}_\mu) \right) \cdot \delta_{\alpha,\beta} \ ,$$

where in the last step the fact that $\sum_{\mu,\nu} [\gamma_\mu, \gamma_\nu] = 0$ was used, we finally get the fermion propagator in momentum space,

$$\tilde{G}_{\alpha\lambda}(\hat{k}) = \frac{\hat{M}_0 \ \delta_{\alpha,\lambda} - \imath \sum_{\mu=1}^{4} (\gamma_\mu)_{\alpha\lambda} \ \sin \hat{k}_\mu}{\hat{M}_0{}^2 + \sum_{\mu=1}^{4} \sin^2(\hat{k}_\mu)} \ .$$

Inserting $\tilde{G}$ in Eq. (1.8b) leads to the two-point correlation function on the lattice.

What we did so far can be summarised in few words. Starting from the action of the theory in Minkowski space-time and performing the Wick rotation, we obtained the euclidean version of it. We then discretised the space-time introducing an isotropic lattice, we got rid of any dimensionful quantity rescaling them using the lattice spacing and we calculated the fermion propagator. And we did everything in the easiest possible way. Even if not shown here, the same procedure in the free scalar field theory turns out to work perfectly. And a priori there is no reason why such a procedure should fail in the free Dirac theory. Nevertheless it fails. With this being completely unexpected, it is worth discussing the reasons behind such a failure quite in detail in next section.

$$\mathcal{S}_F^{(\text{cont.})} = \int \mathrm{d}^4 x \ \bar{\psi}(x) \left(\gamma_\mu \partial_\mu + M_0 \right) \psi(x)$$

$$\langle \Omega \, | \, \mathbf{T} \big(\Psi_\alpha(x) \bar{\Psi}_\beta(y) \big) \, | \, \Omega \rangle = \int_{-\infty}^{+\infty} \frac{\mathrm{d}^4 p}{(2\pi)^4} \cdot \frac{M_0 - \imath \not{p}}{M_0^2 + p^2} \cdot e^{-\imath \, p \cdot (x-y)}$$

$$\mathcal{S}_F^{(\text{latt.})} = \sum_n \left\{ \sum_{\mu=1}^{4} \left[\ \bar{\hat{\psi}}(n) \ \gamma_\mu \ \frac{1}{2} \Big(\ \hat{\psi}(n+\hat{\mu}) \ - \ \hat{\psi}(n-\hat{\mu}) \ \Big) \right] + \ \bar{\hat{\psi}}(n) \ \hat{M}_0 \ \hat{\psi}(n) \right\}$$

$$\langle \ \hat{\Psi}_\alpha(n) \ \bar{\hat{\Psi}}_\beta(m) \ \rangle = \int_{-\pi}^{\pi} \frac{\mathrm{d}^4 \hat{k}}{(2\pi)^4} \cdot \frac{\hat{M}_0 \ \delta_{\alpha,\beta} - \imath \sum_{\mu=1}^{4} (\gamma_\mu)_{\alpha\beta} \ \sin \hat{k}_\mu}{\hat{M}_0{}^2 + \sum_{\mu=1}^{4} \sin^2(\hat{k}_\mu)} \cdot e^{\imath \, \hat{k} \cdot (n-m)}$$

§ 1.2   The naïve continuum limit

If we were asked, as exercise, to consider the expression summarised at the end of the previous section and to obtain the continuum equations starting from the lattice ones, probably we would feel bored for such an easy request. But trying to tackle this problem would turn quickly more difficult than expected. Let us see, then, what happens. The way to proceed is clear (and is usually referred as *naïve continuum limit*). Using Eqs. (1.5a) to (1.5c) and (1.5f), the physical dimensions
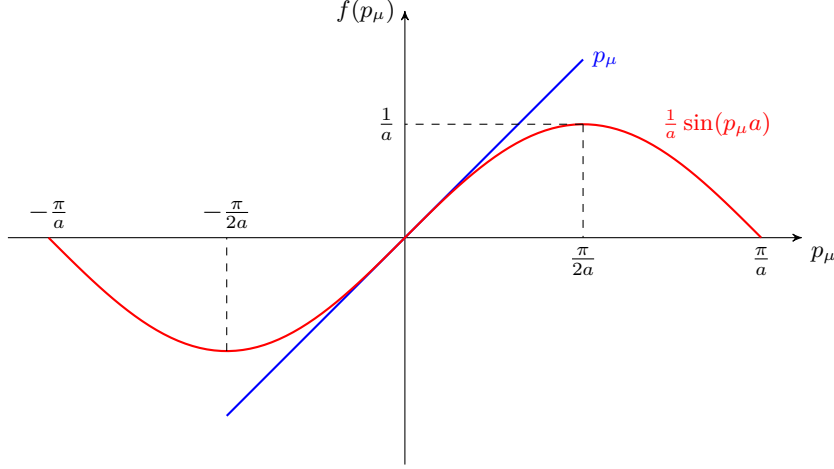
Figure 1.1: *Plot of $\sin(p_\mu a)/a$ as function of p_μ. It is clear that it cannot be replaced by p_μ in the whole Brillouin zone. Both momenta close to $p_\mu = 0$ and to $p_\mu = \pm\pi/a$ contribute to the limit in Eq.* (1.9).

can be introduced again, while, to deal with the fields in next neighbour lattice sites, the Taylor expansion

$$\hat{\psi}_\alpha(n \pm \hat{\mu}) \,=\, a^{3/2}\, \psi_\alpha(na \pm a\hat{\mu}) \,=\, a^{3/2} \left[\, \psi_\alpha(na) \,\pm\, a\, \partial_\mu\, \psi_\alpha(na) \,+\, \mathcal{O}(a^2)\, \right]$$

can be used. Afterwards, the limit of a going to 0 has to be evaluated. It is quite immediate to show that $\mathcal{S}_F^{(\text{cont.})} \to \mathcal{S}_F^{(\text{latt.})}$. In fact,

$$\mathcal{S}_F^{(\text{latt.})} = \sum_n a^4 \sum_{\alpha,\beta} \left\{ \left[\, \bar{\psi}_\alpha(na)\, \left(\gamma_\mu\right)_{\alpha\beta}\, \partial_\mu\, \psi_\beta(na) \,+\, \bar{\psi}_\alpha(na)\, M_0\, \delta_{\alpha,\beta}\, \psi_\beta(na)\, \right] + \mathcal{O}(a) \right\} \,,$$

from which[4]

$$\lim_{a\to 0} \mathcal{S}_F^{(\text{latt.})} = \int \mathrm{d}^4x \sum_{\alpha,\beta} \bar{\psi}_\alpha(x) \left[\left(\gamma_\mu\right)_{\alpha\beta} \partial_\mu + M_0\, \delta_{\alpha,\beta} \right] \psi_\beta(x) \,=\, \mathcal{S}_F^{(\text{cont.})} \,.$$

Performing the same steps starting from the lattice fermion propagator[5] leads to

$$\langle\, \psi_\alpha(x)\, \bar{\psi}_\beta(y)\, \rangle = \lim_{a\to 0} \int_{-\frac{\pi}{a}}^{\frac{\pi}{a}} \frac{\mathrm{d}^4p}{(2\pi)^4} \cdot \frac{M_0\, \delta_{\alpha,\beta} - \imath \sum_{\mu=1}^4 \left(\gamma_\mu\right)_{\alpha\beta} \frac{1}{a} \sin(p_\mu a)}{M_0^2 + \sum_{\mu=1}^4 \frac{1}{a^2} \sin^2(p_\mu a)} \cdot e^{\,\imath\, p\cdot(x-y)} \,, \tag{1.9}$$

but this time the limit operation is not trivial at all[6]. A typical argument to show that there is something suspicious in Eq. (1.9) is the following. If we could replace $\sin(p_\mu a)/a$ with p_μ, then we would obtain the well known fermion propagator. Unfortunately, this replacement is not allowed because the sine-function bends away from p_μ at the corners of the Brillouin zone as it can be seen in Figure 1.1. Furthermore, considering for simplicity the massless case, there are sixteen regions in the Brillouin zone where the integrand is singular (sixteen different poles). The fact that there are only sixteen contributions to the integral in Eq. (1.9) can be deduced admitting, for

---

[4]Strictly speaking, this limit has to be performed taking also, simultaneously, the limit $n \to \infty$ with $na \to x$.

[5]The fact that $\hat{k} = a\, p$ and $a\,(n - m) = x - y$ has to be considered together with Eqs. (1.5).

[6]In Eq. (1.9) the vacuum state $|\Omega\rangle$ and the time-ordering operation have not been reintroduced in the left hand side to signal that this is not identical to the continuum propagator (as discussed from here on).

a moment, to interchange the limit and the integral operations. Doing so, then the limit of the integrand has to be carried out keeping $p_\mu a$ fixed[7]. Now, if $p_\mu a$ is such that $\sin(p_\mu a) \neq 0$, then, for $a \to 0$, the numerator diverges as a^{-1} while the denominator goes to infinity as a^{-2} does. Hence the integrand vanishes (the phase factor does not really play a role[8]). On the other hand, all values of $p_\mu a$ such that $\sin(p_\mu a) = 0$ will give a contribution to the right hand side of Eq. (1.9). This reasoning, although not rigorous, is quite valid and it explains that Eq. (1.9) does not reproduce the correct propagator of a theory describing one non interacting Dirac particle. A more rigorous Reader could not be satisfied with this argument and still wonder what happens for $a \to 0$. So far we have not shown that. It is not so difficult, but it leads to extremely long expressions. The best strategy is to take the limit for a going to 0 explicitly in two dimensions. Then, just by sight, we can write down the generalisation to four dimensions.

Let us start rewriting Eq. (1.9) in two dimensions,

$$\langle\, \psi_\alpha(x)\, \bar{\psi}_\beta(y)\, \rangle = \lim_{a\to 0} \int_{-\frac{\pi}{a}}^{\frac{\pi}{a}} \frac{\mathrm{d}p_1\, \mathrm{d}p_2}{(2\pi)^2} \cdot \frac{M_0\, \delta_{\alpha,\beta} - \imath \sum_{\mu=1}^{2} \left(\gamma_\mu\right)_{\alpha\beta} \frac{1}{a} \sin(p_\mu a)}{M_0^2 + \sum_{\mu=1}^{2} \frac{1}{a^2} \sin^2(p_\mu a)} \cdot e^{\,\imath\, p\cdot(x-y)}$$

$$\equiv \lim_{a\to 0} \int_{-\frac{\pi}{a}}^{\frac{\pi}{a}} \frac{\mathrm{d}p_1\, \mathrm{d}p_2}{(2\pi)^2} \cdot I(p_1,\, p_2) \equiv \lim_{a\to 0} \mathcal{I}(a) \,,$$

and let us focus for the moment only on the double integral $\mathcal{I}(a)$. The first step is to split each momentum integration into two regions,

$$|p_\mu| < \frac{\pi}{2a} \qquad \text{and} \qquad \frac{\pi}{2a} < |p_\mu| < \frac{\pi}{a} \,.$$

Doing so, the Brillouin zone is split in four different parts, as drawn in Figure 1.2 and the integral $\mathcal{I}(a)$ can be decomposed as well as

$$\mathcal{I}(a) = \mathcal{I}_A(a) + \mathcal{I}_B(a) + \mathcal{I}_C(a) + \mathcal{I}_D(a) \,,$$

where, symbolically,

$$\mathcal{I}_A(a) = \int_{-\frac{\pi}{2a}}^{\frac{\pi}{2a}} \int_{-\frac{\pi}{2a}}^{\frac{\pi}{2a}} \frac{\mathrm{d}^2 p}{(2\pi)^2} \cdot I(p_1,\, p_2) \,, \tag{1.10a}$$

$$\mathcal{I}_B(a) = \left[\int_{-\frac{\pi}{a}}^{-\frac{\pi}{2a}} \int_{-\frac{\pi}{2a}}^{\frac{\pi}{2a}} + \int_{\frac{\pi}{2a}}^{\frac{\pi}{a}} \int_{-\frac{\pi}{2a}}^{\frac{\pi}{2a}} \right] \frac{\mathrm{d}^2 p}{(2\pi)^2} \cdot I(p_1,\, p_2) \,, \tag{1.10b}$$

$$\mathcal{I}_C(a) = \left[\int_{-\frac{\pi}{2a}}^{\frac{\pi}{2a}} \int_{-\frac{\pi}{a}}^{-\frac{\pi}{2a}} + \int_{-\frac{\pi}{2a}}^{\frac{\pi}{2a}} \int_{\frac{\pi}{2a}}^{\frac{\pi}{a}} \right] \frac{\mathrm{d}^2 p}{(2\pi)^2} \cdot I(p_1,\, p_2) \,, \tag{1.10c}$$

$$\mathcal{I}_D(a) = \left[\int_{-\frac{\pi}{a}}^{-\frac{\pi}{2a}} \int_{-\frac{\pi}{a}}^{-\frac{\pi}{2a}} + \int_{-\frac{\pi}{a}}^{-\frac{\pi}{2a}} \int_{\frac{\pi}{2a}}^{\frac{\pi}{a}} + \int_{\frac{\pi}{2a}}^{\frac{\pi}{a}} \int_{-\frac{\pi}{a}}^{-\frac{\pi}{2a}} + \int_{\frac{\pi}{2a}}^{\frac{\pi}{a}} \int_{\frac{\pi}{2a}}^{\frac{\pi}{a}} \right] \frac{\mathrm{d}^2 p}{(2\pi)^2} \cdot I(p_1,\, p_2) \,. \tag{1.10d}$$

The next step is to make a change of variables on each of the eight integrals in Eqs. (1.10b) to (1.10d). The idea is to collect some integrals together and, then, to end up with only integrals over the part

---

[7]Roughly speaking, this is due to the fact that the integration region expands as a decreases. Taking the limit inside the integral fixing only p_μ would be like replacing $\sin(p_\mu a)/a$ with p_μ in all the Brillouin zone. And this is clearly wrong.

[8]Keeping $p_\mu a$ fixed, then the phase factor $\exp\left(\imath\, p\cdot(x-y)\right)$ could seem to be a problem, since it does not admit a limit. Indeed it is a bounding factor and the squeeze theorem can be used to perform the limit of the integrand.
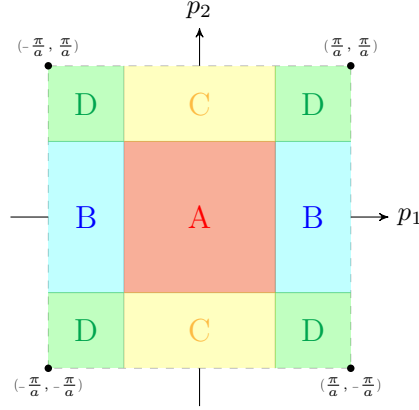
Figure 1.2: *Sketch of how the Brillouin zone has been divided for our calculation. There are only four different parts due to periodic boundary conditions: A, B, C and D.*

A of the Brillouin zone. The right choice is

$$\int_{\pm \frac{\pi}{a}}^{\pm \frac{\pi}{2a}} \mathrm{d}p_\mu \qquad \longleftrightarrow \qquad p_\mu = \pm \frac{\pi}{a} + q_\mu \; ;$$

of course, we are making a change of variables in a two dimensional integral and the determinant $\det J$ of the Jacobian of every transformation has to be evaluated. All the transformations we need can be easily listed using a symbolic notation:

$$\mathcal{I}_B(a) \;\rightarrow\; \begin{cases} p_1 = -\frac{\pi}{a} + q_1 \\ p_2 = q_2 \end{cases} + \begin{cases} p_1 = \frac{\pi}{a} + q_1 \\ p_2 = q_2 \end{cases} \quad,$$

$$\mathcal{I}_C(a) \;\rightarrow\; \begin{cases} p_1 = q_1 \\ p_2 = -\frac{\pi}{a} + q_2 \end{cases} + \begin{cases} p_1 = q_1 \\ p_2 = \frac{\pi}{a} + q_2 \end{cases} \quad,$$

$$\mathcal{I}_D(a) \;\rightarrow\; \begin{cases} p_1 = -\frac{\pi}{a} + q_1 \\ p_2 = -\frac{\pi}{a} + q_2 \end{cases} + \begin{cases} p_1 = -\frac{\pi}{a} + q_1 \\ p_2 = \frac{\pi}{a} + q_2 \end{cases} + \begin{cases} p_1 = \frac{\pi}{a} + q_1 \\ p_2 = -\frac{\pi}{a} + q_2 \end{cases} + \begin{cases} p_1 = \frac{\pi}{a} + q_1 \\ p_2 = \frac{\pi}{a} + q_2 \end{cases} \quad.$$

It is straightforward to show that $\det J = 1$ for any of them. Continuing in detail the calculation in Eq. (1.10b) and leaving to the Reader analogous steps in Eqs. (1.10c) and (1.10d), we have

$$\int_{-\frac{\pi}{a}}^{-\frac{\pi}{2a}} \int_{-\frac{\pi}{2a}}^{\frac{\pi}{2a}} \frac{\mathrm{d}p_1 \, \mathrm{d}p_2}{(2\pi)^2} \cdot \frac{M_0 \, \delta_{\alpha,\beta} - \imath (\gamma_1)_{\alpha\beta} \frac{1}{a} \sin(p_1 a) - \imath (\gamma_2)_{\alpha\beta} \frac{1}{a} \sin(p_2 a)}{M_0^2 + \frac{1}{a^2} \sin^2(p_1 a) + \frac{1}{a^2} \sin^2(p_2 a)} \cdot e^{\imath p_1 (x_1 - y_1)} \, e^{\imath p_2 (x_2 - y_2)} \quad +$$

$$+ \int_{\frac{\pi}{2a}}^{\frac{\pi}{a}} \int_{-\frac{\pi}{2a}}^{\frac{\pi}{2a}} \frac{\mathrm{d}p_1 \, \mathrm{d}p_2}{(2\pi)^2} \cdot \frac{M_0 \, \delta_{\alpha,\beta} - \imath (\gamma_1)_{\alpha\beta} \frac{1}{a} \sin(p_1 a) - \imath (\gamma_2)_{\alpha\beta} \frac{1}{a} \sin(p_2 a)}{M_0^2 + \frac{1}{a^2} \sin^2(p_1 a) + \frac{1}{a^2} \sin^2(p_2 a)} \cdot e^{\imath p_1 (x_1 - y_1)} \, e^{\imath p_2 (x_2 - y_2)} \quad =$$

$$= \int_{0}^{\frac{\pi}{2a}} \int_{-\frac{\pi}{2a}}^{\frac{\pi}{2a}} \frac{\mathrm{d}q_1 \, \mathrm{d}q_2}{(2\pi)^2} \cdot \frac{M_0 \, \delta_{\alpha,\beta} + \imath (\gamma_1)_{\alpha\beta} \frac{1}{a} \sin(q_1 a) - \imath (\gamma_2)_{\alpha\beta} \frac{1}{a} \sin(q_2 a)}{M_0^2 + \frac{1}{a^2} \sin^2(q_1 a) + \frac{1}{a^2} \sin^2(q_2 a)} \cdot e^{\imath q_1 (x_1 - y_1)} \, e^{\imath q_2 (x_2 - y_2)} e^{-\imath \frac{\pi}{a} (x_1 - y_1)} \quad +$$

$$+ \int_{-\frac{\pi}{2a}}^{0} \int_{-\frac{\pi}{2a}}^{\frac{\pi}{2a}} \frac{\mathrm{d}q_1 \, \mathrm{d}q_2}{(2\pi)^2} \cdot \frac{M_0 \, \delta_{\alpha,\beta} + \imath (\gamma_1)_{\alpha\beta} \frac{1}{a} \sin(q_1 a) - \imath (\gamma_2)_{\alpha\beta} \frac{1}{a} \sin(q_2 a)}{M_0^2 + \frac{1}{a^2} \sin^2(q_1 a) + \frac{1}{a^2} \sin^2(q_2 a)} \cdot e^{\imath q_1 (x_1 - y_1)} \, e^{\imath q_2 (x_2 - y_2)} e^{+\imath \frac{\pi}{a} (x_1 - y_1)} \quad =$$

$$= e^{i\pi(n_1-m_1)} \int_{-\frac{\pi}{2a}}^{\frac{\pi}{2a}} \int_{-\frac{\pi}{2a}}^{\frac{\pi}{2a}} \frac{dq_1 \, dq_2}{(2\pi)^2} \cdot \frac{M_0 \, \delta_{\alpha,\beta} + i(\gamma_1)_{\alpha\beta} \frac{1}{a} \sin(q_1 a) - i(\gamma_2)_{\alpha\beta} \frac{1}{a} \sin(q_2 a)}{M_0^2 + \frac{1}{a^2} \sin^2(q_1 a) + \frac{1}{a^2} \sin^2(q_2 a)} \cdot e^{i q_1 (x_1-y_1)} e^{i q_2 (x_2-y_2)} \quad =$$

$$= e^{i \bar{p}^B \cdot (n-m)} \int_{-\frac{\pi}{2a}}^{\frac{\pi}{2a}} \int_{-\frac{\pi}{2a}}^{\frac{\pi}{2a}} \frac{dp_1 \, dp_2}{(2\pi)^2} \cdot \frac{M_0 \, \delta_{\alpha,\beta} - i \sum_{\mu=1}^2 e^{i\bar{p}_\mu^B} (\gamma_\mu)_{\alpha\beta} \frac{1}{a} \sin(p_\mu a)}{M_0^2 + \sum_{\mu=1}^2 \frac{1}{a^2} \sin^2(p_\mu a)} \cdot e^{i p \cdot (x-y)} = \mathcal{I}_B(a) \, ,$$

where

- in the second step the fact that $(n_1 - m_1) \in \mathbb{Z}$ was used;

- in the last step the vector $\bar{p}^B = (\pi, 0)$ was introduced and q_i was renamed to p_i.

Introducing three new two-dimensional vectors $\bar{p}^A = (0,0)$, $\bar{p}^C = (0,\pi)$, $\bar{p}^D = (\pi,\pi)$ we can write down analogous expressions for the other three integrals,

$$\mathcal{I}_A(a) = e^{i \bar{p}^A \cdot (n-m)} \int_{-\frac{\pi}{2a}}^{\frac{\pi}{2a}} \int_{-\frac{\pi}{2a}}^{\frac{\pi}{2a}} \frac{dp_1 \, dp_2}{(2\pi)^2} \cdot \frac{M_0 \, \delta_{\alpha,\beta} - i \sum_{\mu=1}^2 e^{i \bar{p}_\mu^A} (\gamma_\mu)_{\alpha\beta} \frac{1}{a} \sin(p_\mu a)}{M_0^2 + \sum_{\mu=1}^2 \frac{1}{a^2} \sin^2(p_\mu a)} \cdot e^{i p \cdot (x-y)}$$

$$\mathcal{I}_C(a) = e^{i \bar{p}^C \cdot (n-m)} \int_{-\frac{\pi}{2a}}^{\frac{\pi}{2a}} \int_{-\frac{\pi}{2a}}^{\frac{\pi}{2a}} \frac{dp_1 \, dp_2}{(2\pi)^2} \cdot \frac{M_0 \, \delta_{\alpha,\beta} - i \sum_{\mu=1}^2 e^{i \bar{p}_\mu^C} (\gamma_\mu)_{\alpha\beta} \frac{1}{a} \sin(p_\mu a)}{M_0^2 + \sum_{\mu=1}^2 \frac{1}{a^2} \sin^2(p_\mu a)} \cdot e^{i p \cdot (x-y)}$$

$$\mathcal{I}_D(a) = e^{i \bar{p}^D \cdot (n-m)} \int_{-\frac{\pi}{2a}}^{\frac{\pi}{2a}} \int_{-\frac{\pi}{2a}}^{\frac{\pi}{2a}} \frac{dp_1 \, dp_2}{(2\pi)^2} \cdot \frac{M_0 \, \delta_{\alpha,\beta} - i \sum_{\mu=1}^2 e^{i \bar{p}_\mu^D} (\gamma_\mu)_{\alpha\beta} \frac{1}{a} \sin(p_\mu a)}{M_0^2 + \sum_{\mu=1}^2 \frac{1}{a^2} \sin^2(p_\mu a)} \cdot e^{i p \cdot (x-y)} \, ,$$

which, put in $\mathcal{I}(a)$, gives

$$\mathcal{I}(a) = \sum_{\bar{p}} e^{i \bar{p} \cdot (n-m)} \int_{-\frac{\pi}{2a}}^{\frac{\pi}{2a}} \frac{d^2 p}{(2\pi)^2} \cdot \frac{M_0 \, \delta_{\alpha,\beta} - i \sum_{\mu=1}^2 e^{i \bar{p}_\mu} (\gamma_\mu)_{\alpha\beta} \frac{1}{a} \sin(p_\mu a)}{M_0^2 + \sum_{\mu=1}^2 \frac{1}{a^2} \sin^2(p_\mu a)} \cdot e^{i p \cdot (x-y)} \, ,$$

where $\bar{p} \in \{(0,0), \, (\pi,0), \, (0,\pi), \, (\pi,\pi)\}$. Eventually, we have our physical propagator in two dimensions,

$$\langle \, \psi_\alpha(x) \, \bar{\psi}_\beta(y) \, \rangle = \lim_{a \to 0} \sum_{\bar{p}} e^{i \bar{p} \cdot \frac{(x-y)}{a}} \int_{-\frac{\pi}{2a}}^{\frac{\pi}{2a}} \frac{d^2 p}{(2\pi)^2} \cdot \frac{M_0 \, \delta_{\alpha,\beta} - i \sum_{\mu=1}^2 e^{i\bar{p}_\mu} (\gamma_\mu)_{\alpha\beta} \frac{1}{a} \sin(p_\mu a)}{M_0^2 + \sum_{\mu=1}^2 \frac{1}{a^2} \sin^2(p_\mu a)} \cdot e^{i p \cdot (x-y)} \, .$$

It is clear how easy is to generalise this result to four dimensions: There will be 16 different vectors $\bar{p}$, each corresponding to one of the 16 parts in which the Brillouin zone is divided. Proceeding as done above leads to

$$\langle \, \psi_\alpha(x) \, \bar{\psi}_\beta(y) \, \rangle =$$
$$\lim_{a \to 0} \sum_{\bar{p}} e^{i \bar{p} \cdot \frac{(x-y)}{a}} \int_{-\frac{\pi}{2a}}^{\frac{\pi}{2a}} \frac{d^4 p}{(2\pi)^4} \cdot \frac{M_0 \, \delta_{\alpha,\beta} - i \sum_{\mu=1}^4 e^{i\bar{p}_\mu} (\gamma_\mu)_{\alpha\beta} \frac{1}{a} \sin(p_\mu a)}{M_0^2 + \sum_{\mu=1}^4 \frac{1}{a^2} \sin^2(p_\mu a)} \cdot e^{i p \cdot (x-y)} \quad (1.12)$$

The extremely important fact is that now all the integrations in Eq. (1.12) are extended to a reduced Brillouin zone and this means that $\sin(p_\mu a)/a$ can be replaced with p_μ in the continuum limit. Nevertheless due to the blue factors, the *mathematical* limit for a going to zero exists only if $\bar{p} = (0,0,0,0)$. It is now evident that there are 15 doublers without any continuum analogue. In other words, we started from a continuum theory whose propagator is made up of only one term, we regularised it introducing a space-time lattice, we naïvely removed the lattice and we ended up having such a term plus other fifteen. Let us have a closer look to these new contributions. Each term with $\bar{p} \neq (0,0,0,0)$ has a structure similar to that for $\bar{p} = (0,0,0,0)$, except that the sign of

the γ-matrix is reversed if $\bar{p}_\mu = \pi$. This means nothing but that we have the Dirac propagator in a different representation of the γ-matrices. In fact, it can be proven that there exists a similarity transformation such that

$$\mathcal{T}_{\bar{p}}\,\gamma_\sigma\,\mathcal{T}_{\bar{p}}^{-1} = e^{\imath\,\bar{p}_\sigma}\,\gamma_\sigma$$

for each $\bar{p} \neq (0,0,0,0)$. In particular, writing as subscript the component of $\bar{p}$ that is equal to π, we have the following transformations[9] (all can be checked to be unitary):

$$\mathcal{T}_\mu = \gamma_\mu\gamma_5 \quad , \quad \mathcal{T}_{\mu\nu} = \gamma_\mu\gamma_\nu \quad , \quad \mathcal{T}_{\mu\nu\lambda} = \gamma_\mu\gamma_\nu\gamma_\lambda \quad , \quad \mathcal{T}_{\mu\nu\lambda\rho} = \gamma_5 \equiv \gamma_1\gamma_2\gamma_3\gamma_4 \quad .$$

Close enough to the continuum limit (i.e. for $a \ll 1$), $\sin(p_\mu a)/a$ can be replaced with p_μ in Eq. (1.12):

$$\langle\,\psi_\alpha(x)\,\bar{\psi}_\beta(y)\,\rangle \approx \sum_{\bar{p}} e^{\imath\,\bar{p}\cdot\frac{(x-y)}{a}}\,\mathcal{T}_{\bar{p}}\left[\int_{-\infty}^{\infty}\frac{\mathrm{d}^4p}{(2\pi)^4}\cdot\frac{M_0\cdot\mathbb{1} - \imath\sum_{\mu=1}^{4}\gamma_\mu\,p_\mu}{M_0^2 + \sum_{\mu=1}^{4}p_\mu^2}\cdot e^{\imath\,p\cdot(x-y)}\right]\mathcal{T}_{\bar{p}}^{-1} =$$

$$= \sum_{\bar{p}} V_{\bar{p}}\,(x)\,S_F^{(0)}(x-y)\,V_{\bar{p}}^{-1}(y)\,, \tag{1.13}$$

where

$$V_{\bar{p}}\,(z) \equiv e^{\imath\,\bar{p}\frac{z}{a}}\,\mathcal{T}_{\bar{p}}$$

and

$$S_F^{(0)}(x-y) \equiv \int_{-\infty}^{\infty}\frac{\mathrm{d}^4p}{(2\pi)^4}\cdot\frac{M_0\cdot\mathbb{1} - \imath\sum_{\mu=1}^{4}\gamma_\mu\,p_\mu}{M_0^2 + \sum_{\mu=1}^{4}p_\mu^2}\cdot e^{\imath\,p\cdot(x-y)}\,.$$

is the continuum Dirac propagator. Here the $\bar{p} = (0,0,0,0)$ case has been included setting $\mathcal{T}_0 = \mathbb{1}$. Eq. (1.13) should not be misleading. Despite the fact that it includes the continuum two-point correlation function, the limit $a \to 0$ has not been really evaluated. Here the lattice spacing a appears in $V_{\bar{p}}\,(z)$, which has no analogue in the continuum. Quite surprisingly, the above structure just reflects a symmetry of the lattice action. Since

$$V_{\bar{p}}\,(z)\gamma_\mu V_{\bar{p}}^{-1}(z \pm \hat{\mu}a) = e^{\imath\,\bar{p}\frac{z}{a}}\,\mathcal{T}_{\bar{p}}\,\gamma_\mu\,\mathcal{T}_{\bar{p}}^{-1}\,e^{-\imath\,\bar{p}\frac{z\pm\hat{\mu}a}{a}} =$$

$$= e^{\imath\,\bar{p}\frac{z}{a}}\,e^{-\imath\,\bar{p}\frac{z}{a}}\,e^{\imath\,\bar{p}_\mu}\gamma_\mu\,e^{\mp\imath\,\bar{p}\cdot\hat{\mu}} = e^{\imath\,(\bar{p}_\mu \mp \bar{p}_\mu)}\,\gamma_\mu = \gamma_\mu$$

the lattice action

$$\mathcal{S}_F^{(\mathrm{latt.})} = \sum_x a^4\left\{\sum_{\mu=1}^{4}\left[\,\bar{\psi}(x)\,\gamma_\mu\,\frac{1}{2}\Big(\,\psi(x+\hat{\mu}a)\,-\,\psi(x-\hat{\mu}a)\,\Big)\right] + \bar{\psi}(x)\,M_0\,\psi(x)\right\}$$

is invariant[10] under the transformation

$$\begin{cases} \psi(x) \to \psi'(x) = V_{\bar{p}}\,(x)\,\psi(x) \\ \bar{\psi}(x) \to \bar{\psi}'(x) = \bar{\psi}(x)\,V_{\bar{p}}^{-1}(x) \end{cases}\,, \tag{1.14}$$

as it can be easily checked. There are 16 symmetry transformations, namely as many as the number of possible $\bar{p}$. The fermion doubling phenomenon is a consequence of the existence of these symmetry transformations.

Although they spoil the naïve lattice approach to the free Dirac theory, doublers are somehow necessary in order to explain an apparent contradiction. The massless QED action is invariant under the global transformation

$$\begin{cases} \psi(x) \to \psi'(x) = e^{\imath\,\theta\gamma_5}\,\psi(x) \\ \bar{\psi}(x) \to \bar{\psi}'(x) = \bar{\psi}(x)\,e^{\imath\,\theta\gamma_5} \end{cases}\,, \tag{1.15}$$

---

[9] Obviously all indices are distinct.

[10] Observe that $V_{\bar{p}}\,(z)\gamma_\mu V_{\bar{p}}^{-1}(z \pm \hat{\mu}a) = \gamma_\mu$ implies $\gamma_\mu = V_{\bar{p}}^{-1}(z)\gamma_\mu V_{\bar{p}}\,(z \pm \hat{\mu}a)$ and vice versa.

since the matrix γ_5 anticommutes with any γ_μ. For the Noether's theorem this would imply a conserved axial vector current. Nevertheless, it was shown by Adler [22], Bell and Jackiw [23] in 1969 that this is not the case due to quantum fluctuations. This is the so-called *ABJ-anomaly*, known also simply as axial anomaly. On the other hand, in our naïve lattice theory, such axial vector current is exactly conserved for any lattice spacing[11]. And this is precisely due to doublers that cancel the anomaly of the continuum theory. Therefore, if the Reader could have thought to use this naïve discretisation of the theory in order to describe a system composed by 16 non interacting Dirac particles, actually this is not the case. Besides the continuum action and the continuum propagator, any candidate for a lattice field theory should also reproduce the axial anomaly in the continuum.

To conclude this section, let us come back for a moment to when the lattice has been introduced. At that point, the operator $\hat{\partial}_\mu^S$ was chosen as discretisation of the continuum operator ∂_μ. Since this leads to the doubling problem, the Reader probably will wonder whether a one-side *forward* or *backward* derivative

$$\hat{\partial}_\mu^F \, \hat{\psi}_\alpha(n) \;\equiv\; \hat{\psi}_\alpha(n+\hat{\mu}) \;-\; \hat{\psi}_\alpha(n)$$

$$\hat{\partial}_\mu^B \, \hat{\psi}_\alpha(n) \;\equiv\; \hat{\psi}_\alpha(n) \;-\; \hat{\psi}_\alpha(n-\hat{\mu})$$

could help. Unfortunately, Rothe and Sadooghi [24] showed that a lattice action, discretised with a fixed choice of one–sided lattice differences does not define a renormalisable field theory. This is the reason why the symmetric derivative has to be used and trickier solutions to the doubling problem have to be found.

§ 1.3 Wilson fermions

From the quite detailed discussion of §1.2 it should be clear that, to avoid the doubling problem, the lattice action should not be invariant under the transformation (1.14). The Reader could also have the feeling that doublers are somehow related to the chiral symmetry. Indeed, in 1981, Nielsen and Ninomiya [25] proved the so-called *no-go theorem*: Any lattice action cannot be, at the same time, local, translationally invariant, symmetric under chiral transformations and free from doublers.

K Wilson proposed in 1975 one of the first ways to avoid the doubling problem. His idea is related to a simple observation: There is an infinite number of lattice actions that tend to $\mathcal{S}_F^{(\text{cont.})}$ for $a \to 0$. Without loss of generality, in fact, any lattice action can be written as

$$\mathcal{S}_F^{(\text{latt.})} = \mathcal{S}_0 + a^4 \sum_n \sum_{k=1}^{K} c_k(n) a^k \;,$$

where K is an integer bigger than one, $c_k(n)$ are functions on the lattice not depending on a and $\mathcal{S}_0$ is the naïve action of Eq. (1.6a). Clearly, taking the limit of a going to 0, we have $\mathcal{S}_F^{(\text{latt.})} \to \mathcal{S}_F^{(\text{cont.})}$ because all the terms with a power of a higher than four are *irrelevant* and we already showed that $\mathcal{S}_0$ tends to the continuum action. Let us consider the action

$$\mathcal{S}_F^W = \mathcal{S}_0 - \frac{r}{2} \sum_n \bar{\hat{\psi}}(n) \, \hat{\Box} \, \hat{\psi}(n) \;, \tag{1.16}$$

---

[11]With what has been explained so far, it is not so straightforward to understand this statement. But, after all, the axial current non-conservation arises from a non-invariance either of the fermionic integration measure or of the fermionic action under the chiral transformation (1.15). And, in the naïve regularisation, none of these two aspects is present.

where $r \in \mathbb{R}$, $r \neq 0$ is the so-called Wilson parameter, while $\hat{\Box}$ is the lattice version of the d'Alambert operator,

$$\hat{\Box}\,\hat{\psi}(n) \;=\; \sum_{\mu=1}^{4} \Big[\, \hat{\psi}(n+\hat{\mu}) \;+\; \hat{\psi}(n-\hat{\mu}) \;-\; 2\,\hat{\psi}(n) \,\Big]\,. \tag{1.17}$$

The extra label on $\mathcal{S}_F$ is in memory of Wilson; in general it is common to refer to this regularisation as *Wilson fermionic action* or more simply as *Wilson fermions*. Since

$$\hat{\psi} = a^{3/2}\,\psi \qquad \text{and} \qquad \hat{\Box} = a^2\,\Box\,,$$

the new term in Eq. (1.16) – also referred as *Wilson term* – is clearly irrelevant for $a \to 0$. Inserting Eq. (1.17) into Eq. (1.16) leads, after some algebra, to

$$\mathcal{S}_F^W = \mathcal{S}_0 - \frac{r}{2} \sum_n \sum_{\mu=1}^{4} \Big[\, \bar{\hat{\psi}}(n)\,\hat{\psi}(n+\hat{\mu}) \;+\; \bar{\hat{\psi}}(n)\,\hat{\psi}(n-\hat{\mu}) \;-\; 2\,\bar{\hat{\psi}}(n)\,\hat{\psi}(n) \,\Big] =$$

$$= \sum_n \left\{ \frac{1}{2} \sum_{\mu=1}^{4} \Big[\big(r-\gamma_\mu\big)\,\bar{\hat{\psi}}(n)\,\hat{\psi}(n+\hat{\mu}) + \big(r+\gamma_\mu\big)\,\bar{\hat{\psi}}(n)\,\hat{\psi}(n-\hat{\mu}) \Big] + \big(\hat{M}_0 + 4r\big)\,\bar{\hat{\psi}}(n)\,\hat{\psi}(n) \right\},$$

namely

$$\mathcal{S}_F^W = \sum_{n,m} \sum_{\alpha,\beta} \bar{\hat{\psi}}_\alpha(n)\; K_{\alpha\beta}^W(n,m)\; \hat{\psi}_\beta(m)\;, \tag{1.18a}$$

with

$$K_{\alpha\beta}^W(n,m) \equiv \big(\hat{M}_0 + 4r\big)\,\delta_{m,n}\,\delta_{\alpha,\beta} - \frac{1}{2}\sum_{\mu=1}^{4}\Big[\big(r-\gamma_\mu\big)_{\alpha\beta}\,\delta_{m,n+\hat{\mu}} + \big(r+\gamma_\mu\big)_{\alpha\beta}\,\delta_{m,n-\hat{\mu}}\Big]. \tag{1.18b}$$

The easiest way to see that the Wilson term removes the doublers is to prove that the action $\mathcal{S}_F^W$ is not invariant under the transformation (1.14). In order to do so, it is convenient to reintroduce the explicit dependence on the lattice spacing,

$$\mathcal{S}_F^W = \mathcal{S}_0 - a\,\frac{r}{2}\sum_n a^4 \sum_{\mu=1}^{4} \Big[\, \bar{\psi}(x)\,\psi(x+\hat{\mu}a) \;+\; \bar{\psi}(x)\,\psi(x-\hat{\mu}a) \;-\; 2\,\bar{\psi}(x)\,\psi(x) \,\Big]\,,$$

and we have that

$$\bar{\psi}'(x)\,\psi'(x \pm \hat{\mu}a) \;\to\; \bar{\psi}(x)\,V_{\bar{p}}^{-1}(x)V_{\bar{p}}\,(x \pm \hat{\mu}a)\,\psi(x \pm \hat{\mu}a) \;\neq\; \bar{\psi}(x)\,\psi(x \pm \hat{\mu}a)\;,$$

which proves that the Wilson action is not invariant under the transformation (1.14). This already ensures the absence of doublers, but it is interesting to see this fact also from the expression of the fermion propagator. Inverting the matrix $K_{\alpha\beta}^W(n,m)$ in a similar way as done in §1.1 leads to

$$\langle\,\psi_\alpha(x)\;\bar{\psi}_\beta(y)\,\rangle = \lim_{a\to 0}\int_{-\frac{\pi}{a}}^{\frac{\pi}{a}} \frac{\mathrm{d}^4 p}{(2\pi)^4} \cdot \frac{M_0(p)\,\delta_{\alpha,\beta} - \imath\sum_{\mu=1}^{4}\big(\gamma_\mu\big)_{\alpha\beta}\,\frac{1}{a}\sin(p_\mu a)}{[M_0(p)]^2 + \sum_{\mu=1}^{4}\frac{1}{a^2}\sin^2(p_\mu a)} \cdot e^{\,\imath\,p\cdot(x-y)} \tag{1.19a}$$

where

$$M_0(p) = M_0 + \frac{2r}{a}\sum_{\mu=1}^{4}\sin^2\!\Big(\frac{p_\mu a}{2}\Big)\,. \tag{1.19b}$$

Let us repeat now the argument presented after Eq. (1.9). Bringing the limit operation inside the integral and thinking to $p_\mu a$ as fixed, again the integrand vanishes if $\sin(p_\mu a) \neq 0$. But this time, fifteen of the sixteen contributions for $\sin(p_\mu a) = 0$ are trivial. In fact, if $p_\mu a = \pi$ for at least one

value of μ, then $M(p)$ diverges for $a \to 0$ and the integrand vanishes again. It can be shown that such a contribution leads exactly to the continuum fermion propagator[12].

Adding the Wilson term to the naïve lattice action removes doublers and at the same time does not violate hermiticity, locality or translational invariance. This means that, because of the Nielsen and Ninomiya no-go theorem, the action $\mathcal{S}_F^W$ cannot be symmetric under the chiral transformation (1.15). It is known from standard quantum field theory that the mass term in the Dirac action breaks explicitly the chiral symmetry. In the massless case, such a term vanishes and the action is then chirally invariant. As explicit in Eq. (1.18b), the Wilson term introduces in the action a new mass-like term that does not vanish for $M_0 \to 0$. This means that the chiral symmetry is explicitly broken even in the massless case. Differently said, whenever the Wilson term is present, the fermion mass renormalises not only multiplicatively but also additively ($M_0 = \mathscr{A} \, M_{\text{phys.}} + \mathscr{B}$) and this requires a *fine-tuning* to understand to which value the bare mass M_0 should tend to take the chiral limit[13]. This is probably the main limitation, which makes such a regularisation more technical and theoretically involved when studying phenomena connected, for example, to the spontaneous chiral symmetry breaking in QCD. There are though many advantages in using Wilson fermions, like not having any limitation on the number of non-degenerate quarks to be studied (as, instead, in other formulations). Furthermore, the numerical cost of simulations which use this discretisation is nowadays more and more affordable and this makes Wilson fermions one of the most used fermion formulations in the LQCD community.

§ 1.4 Staggered fermions

The problems encountered taking the naïve continuum limit of the two-point correlation function arise mainly at the edges of the Brillouin zone. Therefore, at least in theory, it should be useful to reduce its extent or, in other words, to increase the lattice spacing. This is exactly the basic idea of the staggered[14] formulation, proposed by Kogut and Susskind [26] in 1975 and refined some time later by Susskind [27] and Banks et al. [28]. Nevertheless, even if it can sound easy, there are a lot of technical difficulties and also some drawbacks. We decided to propose in this section a sketch of the main aspects of this formulation and to dedicate appendix A to work out in extreme detail each result presented here. It is worth doing so in order to make the Reader get first the main points and then, in case, understand the intimate details. Moreover, to prove certain statements takes really long time and presenting everything together would probably make the thread of the discussion difficult to be followed.

In simple terms, it is possible to make a change of variables in the naïve fermion action and reduce the number of degrees of freedom per site from four to one[15]. Then, considering a proper linear combination of the sixteen degrees of freedom at the vertices of each unit lattice hypercube, four fermionic fields are obtained. They now live on a lattice with double lattice spacing than before and it can be shown that there are not non-physical contributions to the fermionic propagator (to get an idea on how the degree of freedom are grouped, see Figure 1.3). More quantitatively, if $T(n)$ are unitary 4×4 matrices, such that

$$T^\dagger(n) \, \gamma_\mu \, T(n \pm \hat{\mu}) = \eta_\mu(n) \, \mathbb{1} \, , \tag{1.20}$$

---

[12]Referring to Eq. (1.13) and keeping only the $\bar{p} = (0,0,0,0)$ term, it is obvious that $\langle \psi_\alpha(x) \, \bar{\psi}_\beta(y) \rangle \to S_F^{(0)}(x-y)$ for $a \to 0$.

[13]The *chiral limit* is the limit for $M_{\text{phys.}} \to 0$. For $r = 0$ – and in general whenever the renormalisation of the mass parameter is only multiplicative – the chiral limit is equivalent to zero bare mass limit. In this case, the constant $\mathscr{A}$ would not be relevant and no fine-tuning would be needed.

[14]Even if the idea is for sure *amazing*, here the term `staggered` refers to the verb *to stagger* with the meaning of *arranging in any of various zigzags, alternations, or overlaps of position*.

[15]If not explicitly said, we will ignore the colour degree of freedom, because it does not enter the staggering procedure. This is why we start only with *four* degrees of freedom per site (instead of *twelve*).
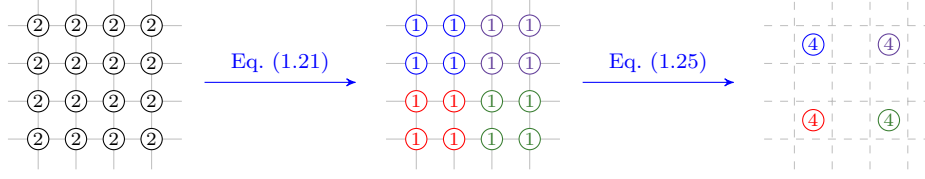
Figure 1.3: *Sketch of the staggering procedure in 2 dimensions (the number inside each circle indicates how many degrees of freedom belong to each lattice site). At the beginning we have 2 degrees of freedom per site, since the Dirac field has $2^{d/2}$ components in d-dimensions (for even space-time dimensions). Thanks to the change of variables of Eq.* (1.21) *this number is reduced to 1. Then one can combine the fields at the vertices of each lattice unitary square (hypercube in d-dimensions) in order to build 2 physical fields, each with 2 components. Notice that after having applied the transformation in Eq.* (1.25) *the lattice spacing is doubled.*

then the transformation

$$\begin{cases} \hat{\psi}(n) = T(n)\ \chi(n) \\ \bar{\hat{\psi}}(n) = \bar{\chi}(n)\ T^\dagger(n) \end{cases} \tag{1.21}$$

makes the action

$$\mathcal{S}_F = \frac{1}{2}\sum_{n,\mu}\Big[\ \bar{\hat{\psi}}(n)\,\gamma_\mu\,\hat{\psi}(n+\hat{\mu})\ -\ \bar{\hat{\psi}}(n)\,\gamma_\mu\,\hat{\psi}(n-\hat{\mu})\ \Big] + \hat{M}_0\sum_n \bar{\hat{\psi}}(n)\ \hat{\psi}(n)$$

diagonal in the Dirac space. Note that the *hat* on the χ-fields has been removed for the sake of simplicity. It is understood that also χ and $\bar{\chi}$ are dimensionless. The complex numbers η_μ are the so called *staggered phases*. The standard choice of $T(n)$ is

$$T(n) = \gamma_1^{n_1}\ \gamma_2^{n_2}\ \gamma_3^{n_3}\ \gamma_4^{n_4}$$

that implies

$$\begin{cases} \eta_1(n) = 1 \\ \eta_\mu(n) = (-1)^{\sum_{\nu<\mu} n_\nu} & \text{if } \mu \neq 1\ . \end{cases} \tag{1.22}$$

To show that Eq. (1.21) makes the action $\mathcal{S}_F$ diagonal in Dirac space is straightforward. Using Eq. (1.20) leads to

$$\mathcal{S}_F = \frac{1}{2}\sum_{n,\mu}\Big[\ \bar{\chi}(n)\,T^\dagger(n)\gamma_\mu T(n+\hat{\mu})\,\chi(n+\hat{\mu})\ -\ \bar{\chi}(n)\,T^\dagger(n)\gamma_\mu T(n-\hat{\mu})\,\chi(n-\hat{\mu})\ \Big]+$$

$$+\ \hat{M}_0\sum_n \bar{\chi}(n)\,T^\dagger(n)T(n)\,\chi(n)\ =$$

$$=\ \sum_{n,\mu,\alpha,\beta}\delta_{\alpha,\beta}\,\eta_\mu(n)\,\bar{\chi}_\alpha(n)\,\hat{\partial}^S_\mu\,\chi_\beta(n)\ +\ \hat{M}_0\sum_{n,\alpha,\beta}\delta_{\alpha,\beta}\,\bar{\chi}_\alpha(n)\,\chi_\beta(n)\ . \tag{1.23}$$

So far Eq. (1.23) is nothing more than a rewriting of the naïve action. Nevertheless, the γ-matrices have been replaced by the two $\delta_{\alpha,\beta}$. Hence, even if in principle we could make the α and β indices run from 1 to k, the simplest choice is to fix $k=1$, namely to omit the Dirac index from now on[16]. Doing this, we end up with an action wherein each field has only one component per site,

$$\mathcal{S}_F^{(\text{stagg.})} = \frac{1}{2}\sum_{n,\mu}\eta_\mu(n)\Big[\ \bar{\chi}(n)\,\chi(n+\hat{\mu})\ -\ \bar{\chi}(n)\,\chi(n-\hat{\mu})\ \Big] + \hat{M}_0\sum_n \bar{\chi}(n)\,\chi(n)\ , \tag{1.24}$$

---

[16]With this choice, the *bar* over the χ field looses its original meaning, in the sense that it is simply $\bar{\chi} = \chi^\dagger$. Nevertheless we will continue to use $\bar{\chi}$ instead of $\chi^\dagger$, only because it seems to be the most common notation in the literature.

and the only trace of the Dirac index lies in the (local) staggered phases η_μ. We have then reduced the number of degrees of freedom per site by a factor four. Let us see now what happens in the naïve continuum limit. It is possible to prove that the staggered action can be rewritten in a way such that it converges to the action of a system describing four non-interacting, degenerate Dirac particles for $a \to 0$. Explicitly,

$$\lim_{a \to 0} \mathcal{S}_F^{(\text{stagg.})} = \int \mathrm{d}^4 x \sum_{f=1}^{4} \sum_{\alpha,\beta} \bar{\psi}_\alpha^f(x) \, (\gamma_\mu \partial_\mu + M_0)_{\alpha\beta} \, \psi_\beta^f(x) \ ,$$

where the fields ψ_α^f are a linear combination of the staggered fields χ. To show the limit above, a slight change of notation is needed. Considering a hypercube on the lattice of edge length a having a vertex at position $n = 2N$ (with both n and N multi-indices), the coordinates of its 16 vertices will be $r = 2N + \rho$, with ρ a vector with only 0 or 1 components. It is then possible to gather all the values of the field $\chi(r)$ in one spinor as

$$\chi_\rho(N) \equiv \chi(2N + \rho) \ ,$$

were ρ is now a multi-index such that $\rho \in \{(0,0,0,0), \dots, (1,1,1,1)\}$. The label N indicates a position on a lattice whose lattice spacing is $b \equiv 2a$. The fields $\chi_\rho(N)$ can be linearly combined to build four Dirac fields. After some complicated algebra, it turns out that the transformation

$$\hat{\psi}_\alpha^f(N) = \frac{1}{\sqrt{2}} \sum_\rho (T_\rho)_{\alpha f} \, \chi_\rho(N) \quad \text{with} \quad T_\rho = \gamma_1^{\rho_1} \gamma_2^{\rho_2} \gamma_3^{\rho_3} \gamma_4^{\rho_4} \tag{1.25}$$

allows to rewrite Eq. (1.24) as

$$\mathcal{S}_F^{(\text{stag.})} = \sum_{f=1}^{4} \sum_N \bar{\hat{\psi}}^f(N) \, (\gamma_\mu \hat{\partial}_\mu^S + 2\hat{M}_0) \, \hat{\psi}^f(N) \ + \mathfrak{R} \ ,$$

where $\hat{\partial}_\mu^S$ is the symmetric derivative on the coarser lattice and $\mathfrak{R}$ contains an irrelevant term which disappears in the naïve continuum limit[17]. It is then trivial to reintroduce the physical units (using this time the lattice spacing b) and to show that $\mathcal{S}_F^{(\text{stag.})}$ tends to the action of four non-interacting, degenerate Dirac particles for $b \to 0$.

Starting from Eq. (1.24), the two-point correlation function can be calculated and it can be shown that there is no unphysical contribution to the fermion propagator. Because of the Nielsen and Ninomiya no-go theorem, the chiral symmetry should then be broken. Indeed, the term in $\mathfrak{R}$ is not so different from the Wilson term and it breaks chiral symmetry explicitly. Nevertheless, a non trivial part of it survives in the massless case. For $\hat{M}_0 = 0$, in fact, the staggered action preserves a continuous $U(1) \times U(1)$ symmetry. This remnant of the original symmetry group guarantees that the mass renormalises only multiplicatively ($M_0 = \mathscr{A} \, M_{\text{phys}}$) and that the *fine-tuning* necessary with Wilson fermions is not needed anymore. Therefore, taking the limit for the bare mass going to zero coincides with the chiral limit and this is one of the most attractive feature of this formulation[18]. Obviously, there are also drawbacks. The most important one is that we are obliged to deal with *four* degenerate Dirac particles. So far, we pretended not to see the fact that we discretised the continuous action describing *one* fermion and we ended up with a lattice theory describing *four* fermions. It is common to refer to this residual doubler degree of freedom as *taste*. More precisely, we will say that a single staggered fermion corresponds to four tastes of continuum fermions. It is

---

[17]The Reader could wonder about the factor 2 in front of the lattice mass. It is basically due to the fact that now the lattice spacing has doubled. Reintroducing the physical units using the lattice spacing b would mean to set $\hat{M}_0 = \frac{b}{2} M_0$.

[18]Actually, there are other formulations that preserve the chiral symmetry in a better way, for which we refer to the literature. Unfortunately, they are usually very much costly to be used in numerical simulations, whereäs the numerical cost of an equivalent simulation making use of staggered fermions is affordable.

important to stress that, strictly speaking, the *taste* degree of freedom does not coincide with the physical *flavour*. It would be interesting to explain this statement further, especially since it has a series of consequences, but it would be extremely premature. On one hand, this chapter is meant to be an introduction to LQCD and this technical discussion would be difficult to be followed. On the other hand, important topics needed to address this problem, like for example the gauge invariance of the theory, have not been covered so far. Hence, it is better to postpone any further analysis. At the end of appendix A, we will come back to this aspect of the staggered formulation making use of what has been and will be discussed in this chapter. For those Readers not new to LQCD, a quite complete discussion (though not detailed) can be found in §6.3 of [18].

§ 1.5   The gauge invariance on the lattice

So far we dealt with the *free* Dirac theory and we discovered two ways of regularise it on a space-time lattice. We decided on purpose to neglect any bosonic degree of freedom not to introduce too much new information at once and in order to focus mainly on the doubling problem. It is now time to consider the *full* QCD action for one single flavour,

$$\mathcal{S}_{QCD} = \int \mathrm{d}^4 x \left\{ \bar{\psi}_i(x) \left[\left(\imath \, \slashed{\partial} - M_0 \right) \delta_{i,j} - g_0 \, t_{ij}^A \, \slashed{A}^A(x) \right] \psi_j(x) - \frac{1}{4} \, F_A^{\mu\nu}(x) \, F_{\mu\nu}^A(x) \right\} \qquad (1.26a)$$

where

$$F_{\mu\nu}^A(x) = \partial_\mu \, A_\nu^A(x) - \partial_\nu \, A_\mu^A(x) - g_0 \, f^{ABC} \, A_\mu^B(x) \, A_\nu^C(x) \ , \qquad (1.26b)$$

and to see how it looks like on the lattice[19]. We know that the regularisation is carried out in euclidean context and, then, we will need at some point to continue the real time to imaginary values. Let us do it immediately as first step. The Wick rotation to be performed reads

$$\begin{cases} x^0 \ \to \ -\imath \, x_4 \\ A^{A\,0} \ \to \ +\imath \, A_4^A \end{cases} \ , \qquad (1.27)$$

where the transformation of the field A_μ can be justified thinking to the pure gauge case – i.e. when $A_\mu(x) = \partial_\mu \Lambda(x)$ – and remembering that $\partial_0 \to +\imath \, \partial_4$. With some trivial algebra it is easy to show that

$$\imath \, \mathcal{S}_{QCD} = - \int \mathrm{d}^4 x \ \bar{\psi}(x) \left[\gamma_\mu^E \left(\partial_\mu + \imath \, g_0 \, t^A A_\mu^A(x) \right) + M_0 \right] \psi(x) - \int \mathrm{d}^4 x \, \frac{1}{4} \, F_A^{\mu\nu}(x) \, F_{\mu\nu}^A(x) \equiv -\mathcal{S}_{QCD}^{(\text{eucl.})} \ ,$$

where we did not write the colour index explicitly for the quark fields. As done in §1.1, any label about the euclidean metric will be considered as understood and hence from now on dropped. It could be possible to consider $\mathcal{S}_{QCD}$ and try to introduce a space-time lattice as done in the free Dirac theory. Nevertheless, it is better to use one of the found discretisations for the fermion part and to make it gauge invariant. This will let the term $\bar{\psi} \, \slashed{A} \, \psi$ appear in a much more natural way. We will find later a discretised version of the pure gauge term of the QCD action.

Let us start considering the lattice action of N_c degenerate fields ψ^A of mass M_0,

$$\mathcal{S}_F = (M_0 + 4r) \sum_n \sum_{A=1}^{N_c} \psi^A(n) \, \psi^A(n) +$$

---

[19]Again, standard quantum field theory notation is used: $\psi_i(x)$, $A_\mu^A(x)$ and $F_A^{\mu\nu}(x)$ are the quark field in the fundamental representation of the $SU(3)$ gauge group, the gluon fields in the adjoint representation of the $SU(3)$ gauge group and the gauge invariant gluon field strength tensor, respectively. The parameter g_0 is the bare strong interaction coupling constant, the matrices t_{ij}^A are the gauge group generators and the real numbers f^{ABC} are the gauge algebra structure constants. A *slashed* symbol means that its Dirac index is contracted with that of a γ-matrices set.

$$- \frac{1}{2} \sum_{n,\mu} \sum_{A=1}^{N_c} \left[\bar{\psi}^A(n) \, (r - \gamma_\mu) \, \psi^A(n + \hat{\mu}) \, + \, \bar{\psi}^A(n + \hat{\mu}) \, (r + \gamma_\mu) \, \psi^A(n) \right] .$$

Here any hat to denote dimensionless quantities has been removed for the sake of simplicity. If not differently said, we will deal with lattice quantities only. Throughout this section we will use a tilde under those quantities having colours degrees of freedom, as a sort of vectorial notation. For example,

$$\underset{\sim}{\bar{\psi}} = \left(\bar{\psi}^1, \ldots, \bar{\psi}^{N_c} \right) \qquad \text{and} \qquad \underset{\sim}{\psi} = \begin{pmatrix} \psi^1 \\ \vdots \\ \psi^{N_c} \end{pmatrix} .$$

The choice of using here the Wilson discretisation is to some extent arbitrary. We could have used staggered fermions as well. In the end, here, we are interested in those terms that involve next neighbour sites and both formulations contain some.

The action $\mathcal{S}_F$ is invariant under *global* $SU(N_c)$ transformations,

$$\begin{cases} \underset{\sim}{\psi}(n) \; \to \; \underset{\sim}{\psi}'(n) \; = \underset{\sim}{G} \cdot \underset{\sim}{\psi}(n) \\ \underset{\sim}{\bar{\psi}}(n) \; \to \; \underset{\sim}{\bar{\psi}}'(n) \; = \; \underset{\sim}{\bar{\psi}}(n) \cdot \underset{\sim}{G}^{-1} \end{cases} ,$$

with $\underset{\sim}{G} \in SU(N_c)$. Our aim is to make it invariant under *local* transformations, namely when $\underset{\sim}{G}$ depends on the position n on the lattice[20], $\underset{\sim}{G} = \underset{\sim}{G}(n)$. Due to the derivative discretisation, there are terms in the action involving different lattice sites. Since $\underset{\sim}{G}(n)$ does not act on the Dirac indices, it is enough to focus on a bilinear term like $\underset{\sim}{\bar{\psi}}(n) \; \underset{\sim}{\psi}(n + \hat{\mu})$. In the continuum, such a term is not invariant under gauge transformations,

$$\underset{\sim}{\bar{\psi}}(x) \; \underset{\sim}{\psi}(y) \; \to \; \underset{\sim}{\bar{\psi}}(x) \; \underset{\sim}{G}^{-1}(x) \; \underset{\sim}{G}(y) \; \underset{\sim}{\psi}(y) \; ,$$

and it is clear that a new non gauge invariant quantity should be introduced between $\underset{\sim}{\bar{\psi}}(x)$ and $\underset{\sim}{\psi}(y)$. Such a factor, also known as *Schwinger line integral* or more simply as *parallel transport*, is

$$\underset{\sim}{U}(x,y) = \mathbf{P}\left(e^{\imath \, g_0 \int_{\mathcal{C}} \, \mathrm{d}x'_\mu \, \underset{\sim}{A}_\mu(x')} \right) , \qquad (1.28)$$

where $\mathcal{C}$ is a path connecting x and y, the index μ is summed, $\underset{\sim}{A}_\mu(x)$ is the gauge field with g_0 the bare strong coupling constant, while $\mathbf{P}$ is the so-called *path-ordering* operator, needed due to the non-abelian nature of the gauge group[21]. Here, and in general in this section, when the colour index on the field $\underset{\sim}{A}_\mu(x)$ is omitted, we also consider the implicit presence of the matrices t^A, namely

$$\underset{\sim}{A}_\mu(x) \equiv \sum_A \underset{\sim}{A}_\mu^A(x) \, t^A .$$

It can be shown[22] that

$$\underset{\sim}{U}(x,y) \; \to \; \underset{\sim}{G}(x) \; \underset{\sim}{U}(x,y) \; \underset{\sim}{G}^{-1}(y)$$

---

[20] We will refer to such a kind of transformation with the name of *gauge transformation*.

[21] The operator $\mathbf{P}$ orders the fields $\underset{\sim}{A}_\mu(x)$ according to their position along the path $\mathcal{C}$.

[22] It is everything but trivial to show it. Only to make it plausible, let us sketch the proof in the $U(1)$ *abelian* case, where it is straightforward. There, the path-ordering operator is not needed and we have

$$A_\mu(x) \; \to \; A_\mu(x) - \frac{1}{e} \, \partial_\mu \Lambda(x) \qquad \text{where} \qquad G(x) = e^{\imath \, \Lambda(x)}$$

that implies

$$U(x,y) \; \to \; \left(e^{\imath \, e \int_{\mathcal{C}} \, \mathrm{d}x'_\mu \, A_\mu(x')} \right)\left(e^{-\imath(\Lambda(y) - \Lambda(x))} \right) \; = \; G(x) \; U(x,y) \; G^{-1}(y) \; .$$

under gauge transformation and this implies that

$$\bar{\psi}(x)\ U(x,y)\ \psi(y)$$

is gauge invariant. To find the counterpart on the lattice, it is sufficient to consider $y = x + \varepsilon$, with ε infinitesimal. It is then easy to show that $\bar{\psi}(x)\,\psi(x+\varepsilon)$ and $\bar{\psi}(x+\varepsilon)\,\psi(x)$ can be made gauge invariant if substituted by

$$\bar{\psi}(x)\ U(x,x+\varepsilon)\ \psi(x+\varepsilon)$$
$$\bar{\psi}(x+\varepsilon)\ U^{\dagger}(x,x+\varepsilon)\ \psi(x)\ ,$$

where

$$U(x,x+\varepsilon)\ =\ e^{\,\imath\, g_0 \varepsilon\cdot A(x)}\ \equiv U_{x,x+\varepsilon} \qquad \text{with} \qquad \varepsilon\cdot A(x)\ =\ \sum_{\mu}\varepsilon_{\mu}A_{\mu}(x)\ .$$

Thus, the action $\mathcal{S}_F$ will become invariant under gauge transformations with the following substitutions:

$$\bar{\psi}(n)\,(r-\gamma_{\mu})\,\psi(n+\hat{\mu}) \quad \rightarrow \quad \bar{\psi}(n)\,(r-\gamma_{\mu})\,U_{n,n+\hat{\mu}}\,\psi(n+\hat{\mu})$$
$$\bar{\psi}(n+\hat{\mu})\,(r+\gamma_{\mu})\,\psi(n) \quad \rightarrow \quad \bar{\psi}(n+\hat{\mu})\,(r+\gamma_{\mu})\,U_{n+\hat{\mu},n}\,\psi(n)\ ,$$

where

$$U_{n+\hat{\mu},n} = U_{n,n+\hat{\mu}}^{\dagger} \qquad \text{with} \qquad U_{n,n+\hat{\mu}} \in SU(N_c)\ .$$

Belonging to $SU(N_c)$, the parallel transports can be rewritten as

$$U_{n,n+\hat{\mu}} = e^{\,\imath\,\phi_{\mu}(n)}\ , \tag{1.29}$$

with $\phi_{\mu}(n)$ a traceless hermitian matrix of the algebra $su(N_c)$. To adapt our notation to the most common one in literature, let us define

$$U_{\mu}(n)\ \equiv U_{n,n+\hat{\mu}} \quad \text{and} \quad U_{\mu}^{\dagger}(n)\ \equiv U_{n+\hat{\mu},n} \quad \text{which implies} \quad U_{-\mu}(n)\ =\ U_{\mu}^{\dagger}(n-\hat{\mu})\ .$$

It is worth remarking that $U_{\mu}(n)$ connects two next neighbour sites on the lattice. This is the reason why often they are referred as *link variables* or more simply as *links*. It is clear that they are oriented quantities and it is possible to use a graphic notation

to represent them (the hermitian conjugation inverts the orientation of the link). We can now write the action in a gauge invariant form. It reads

$$\mathcal{S}_F = (\hat{M}_0 + 4r)\sum_{n}\ \bar{\psi}(n)\,\psi(n)\ +$$
$$-\frac{1}{2}\sum_{n,\mu}\Big[\ \bar{\psi}(n)\,(r-\gamma_{\mu})\,U_{\mu}(n)\,\psi(n+\hat{\mu})\ +\ \bar{\psi}(n+\hat{\mu})\,(r+\gamma_{\mu})\,U^{\dagger}(n)\,\psi(n)\ \Big]\ , \tag{1.30}$$

that, summarising, is invariant under the *local* transformations

$$\begin{cases} \psi(n)\ \rightarrow\ G(n)\cdot\psi(n) \\ \bar{\psi}(n)\ \rightarrow\ \bar{\psi}(n)\cdot G^{-1}(n) \end{cases} \quad \text{and} \quad \begin{cases} U_{\mu}(n)\ \rightarrow\ \quad G(n)\cdot U_{\mu}(n)\cdot G^{-1}(n+\hat{\mu}) \\ U_{\mu}^{\dagger}(n)\ \rightarrow\ G(n+\hat{\mu})\cdot U_{\mu}^{\dagger}(n)\cdot G^{-1}(n) \end{cases} \quad .$$

Here $\underset{\sim}{G}(n)$ is an $SU(N_c)$ element and therefore it can be written as $\underset{\sim}{G}(n) = e^{\imath \underset{\sim}{\Lambda}_\mu(n)}$ with $\underset{\sim}{\Lambda}_\mu(n) \in su(N_c)$. The Reader familiar with how the gauge invariance is introduced in the Dirac theory in the continuum could wonder why we did not simply promoted the derivative ∂_μ to the covariant one $D_\mu \equiv \partial_\mu + \imath\, g_0\, A_\mu(x)$. It can be shown that this choice, though in principal completely legitimate, would lead to violations of the gauge invariance in higher orders of the lattice spacing[23]. This is the reason why, in the lattice formulation of QCD, the gauge fields belong to the group $SU(N_c)$ and not to the algebra $su(N_c)$ as in the continuum.

We could be satisfied with Eq. (1.30) and accept it as it is. Nevertheless, in order to introduce some relations that will be used later, let us perform the naïve continuum limit and show, as expected, that

$$\lim_{a \to 0} \mathcal{S}_F = \int \mathrm{d}^4 x\ \bar{\psi}(x) \left[\gamma_\mu \big(\partial_\mu + \imath\, g_0\, t^A \underset{\sim}{A}^A_\mu(x) \big) + M_0 \right] \underset{\sim}{\psi}(x)\ . \tag{1.32}$$

At the beginning of the Seventies, Gell-Mann and Fritzsch introduced for the first time the *colour* degree of freedom, according to which quarks and antiquarks should appear in *three* different coloured versions (ψ^A, $A = 1, 2, 3$), while observed strongly interacting particles are colour singlets. Let us then specialise the following discussion to the real case, $N_c = 3$. Any element Θ of the algebra $su(3)$ can be written as

$$\underset{\sim}{\Theta} = \sum_{A=1}^{8} \Theta^A\, t^A = \sum_{A=1}^{8} \Theta^A\, \frac{\lambda^A}{2}\ ,$$

where the algebra generators t^A have been chosen in the last step to be proportional to the eight 3×3 Gell-Mann matrices λ^A (and this is by far the most common choice), which satisfy the commutation relation

$$\left[\lambda^A, \lambda^B \right] = 2\, \imath \sum_{C=1}^{8} f^{ABC}\, \lambda^C$$

as well as the orthogonal property (a c label will denote that the trace is taken in the colour space)

$$\mathrm{Tr}_c\big(\lambda^A \lambda^B \big) = 2\, \delta_{A,B}\ .$$

We now need a relation between the link variables $\underset{\sim}{U}_\mu(n)$ and the vector potential $\underset{\sim}{A}_\mu(x)$. Because of Eq. (1.28) in its infinitesimal form and considering the fact that the field $\phi_\mu(n)$ in Eq. (1.29) is, per lattice site, an $su(3)$ matrix carrying a Lorentz index as well as $\underset{\sim}{A}_\mu(x)$, it will be natural to write

$$\underset{\sim}{\phi}_\mu(na)\ = \kappa\, a\, \underset{\sim}{A}_\mu(na)\ , \tag{1.33}$$

where physical dimensions have been reintroduced and κ is a proportionality constant to be determined. Let us take the naïve continuum limit of $\mathcal{S}_F$. Using Eq. (1.33) in Eq. (1.29) and expanding for small value of a leads to

$$\underset{\sim}{U}_\mu(n)\ = \mathbb{1} + \imath\, \kappa\, a\, \underset{\sim}{A}_\mu(na)\ + \mathcal{O}(a^2)\ , \tag{1.34}$$

which introduced into Eq. (1.30) gives

- $\displaystyle \sum_n \bar{\psi}(n)\, \hat{M}_0\, \underset{\sim}{\psi}(n)\ = \sum_n a^4\, \bar{\psi}(na)\, M_0\, \underset{\sim}{\psi}(na)\ $;

---

[23]More explicitly, this means that non gauge invariant terms would appear expanding all quantities in series of a. An idea of which kind of expansions we are referring to here can be found later in this section.

- $$\sum_{n,\mu} \bar{\psi}(n)\, \gamma_\mu\, U_\mu(n)\, \psi(n+\hat{\mu}) = \sum_{n,\mu} a^3\, \bar{\psi}(na)\, \gamma_\mu e^{\imath\, \kappa\, a\, A_\mu(na)}\, \psi(na+\hat{\mu}a) =$$

$$= \sum_{n,\mu} a^3\, \bar{\psi}(na)\, \gamma_\mu \big(\mathbb{1} + \imath\, \kappa\, a\, A_\mu(na) + \mathcal{O}(a^2)\big)\, \big(\psi(na) + a\, \partial_\mu\, \psi(na) + \mathcal{O}(a^2)\big) =$$

$$= \sum_{n,\mu} a^3\, \bar{\psi}(na)\, \gamma_\mu \Big[\mathbb{1} + a\, \partial_\mu + \imath\, \kappa\, a\, A_\mu(na) + \mathcal{O}(a^2)\Big]\, \psi(na) =$$

$$= \sum_{n,\mu} a^3\, \bar{\psi}(n)\, \gamma_\mu\, \psi(n) + \Xi\,[\kappa, \gamma_\mu] + \mathcal{O}(a^5)\ ;$$

- $$\sum_{n,\mu} \bar{\psi}(n+\hat{\mu})\, \gamma_\mu\, U_\mu^\dagger(n)\, \psi(n) = \sum_{n,\mu} \bar{\psi}(n)\, \gamma_\mu\, U_\mu^\dagger(n-\hat{\mu})\, \psi(n-\hat{\mu}) =$$

$$= \sum_{n,\mu} a^3\, \bar{\psi}(na)\, \gamma_\mu \Big[\mathbb{1} - a\, \partial_\mu - \imath\, \kappa\, a\, A_\mu(na) + \mathcal{O}(a^2)\Big]\, \psi(na) =$$

$$= \sum_{n,\mu} a^3\, \bar{\psi}(n)\, \gamma_\mu\, \psi(n) - \Xi\,[\kappa, \gamma_\mu] + \mathcal{O}(a^5)\ ;$$

where we defined

$$\Xi\,[\kappa, \gamma_\mu] \equiv \sum_{n,\mu} a^4\, \bar{\psi}(na)\, \gamma_\mu \Big[\partial_\mu + \imath\, \kappa\, A_\mu(na)\Big]\, \psi(na)\ .$$

Putting everything together, we get

$$\mathcal{S}_F = \hat{M}_0 \sum_n a^4\, \bar{\psi}(n)\, \psi(n) + 4r \sum_n a^3\, \bar{\psi}(n)\, \psi(n) +$$

$$-\frac{1}{2}\Bigg[\sum_{n,\mu} a^3\, r\, \bar{\psi}(n)\, \psi(n) + \Xi\,[\kappa, r] + \sum_{n,\mu} a^3\, r\, \bar{\psi}(n)\, \psi(n) - \Xi\,[\kappa, r] +$$

$$- \Xi\,[\kappa, \gamma_\mu] - \sum_{n,\mu} a^3\, \bar{\psi}(n)\, \gamma_\mu\, \psi(n) - \Xi\,[\kappa, \gamma_\mu] + \sum_{n,\mu} a^3\, \bar{\psi}(n)\, \gamma_\mu\, \psi(n)\Bigg] =$$

$$= \hat{M}_0 \sum_n a^4\, \bar{\psi}(n)\, \psi(n) + \sum_{n,\mu} a^4\, \bar{\psi}(na)\, \gamma_\mu \Big[\partial_\mu + \imath\, \kappa\, A_\mu(na)\Big]\, \psi(na)\ , \tag{1.36}$$

which implies Eq. (1.32) once set $\kappa = g_0$.

Let us go on finding a discretisation for the pure gauge term of the QCD action. The best way to proceed is to understand which kind of terms can appear in the lattice action and then find out their continuum counterpart. Of course, any new valid term has to be gauge invariant and, if we are looking for a pure gauge term, it has to depend on link variables only. The only meaningful operation between links is the multiplication (in the sense of the group they belong to). It is easy to realise that a connected[24] product of links on the lattice from the point n_1 to the point n_2 will be mapped, under a gauge transformation, into the same product times $G(n_1)$ from the left, times $G^{-1}(n_2)$ from the right. Therefore the trace of any closed loop of links ($n_1 = n_2$) is gauge invariant. Since the QCD action is local, it makes sense to consider the smallest closed loop, the so-called *plaquette*,

$$\Pi_{\mu\nu}(n) \equiv U_\mu(n)\, U_\nu(n+\hat{\mu})\, U_\mu^\dagger(n+\hat{\nu})\, U_\nu^\dagger(n)\ . \tag{1.37}$$

It can be also graphically represented as

---

[24]The adjective *connected* refers to the path drawn on the lattice: each link has to start from the site to which the previous arrived, building in this way a *connected path*.
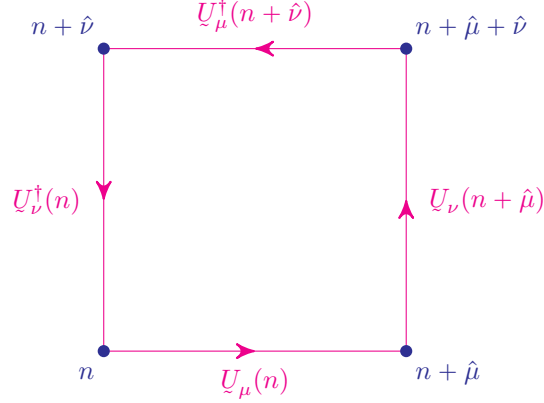
and it is interesting to see how it behaves for small values of the lattice spacing. In order to do that, the Baker–Campbell–Hausdorff relation is needed,

$$\exp(A)\,\exp(B) = \exp\left\{A+B+\frac{[A,B]}{2}+\frac{[A,[A,B]]+[B,[B,A]]}{12}-\frac{[B,[A,[A,B]]]}{24}+\Sigma\right\}\,, \quad (1.38)$$

where A and B are general operators and Σ contains in general an infinite series of terms that will not play a role in our calculation. We want now to insert Eq. (1.29) in Eq. (1.37) and find a result in the limit of small a. In order to keep the expressions simpler[25], let us omit the lattice spacing in the argument of the A_μ field. The calculation is quite long and it is better to split it in two parts:

$$\Pi_{\mu\nu}(n) \;=\; \underbrace{e^{\,\imath\,g_0\,a\,A_\mu(n)}\,e^{\,\imath\,g_0\,a\,A_\nu(n+\hat\mu)}}_{P_I}\,\underbrace{e^{\,-\imath\,g_0\,a\,A_\mu(n+\hat\nu)}\,e^{\,-\imath\,g_0\,a\,A_\nu(n)}}_{P_{II}}\,.$$

We have now to make use of Eq. (1.38) in P_I and P_{II}. Taking the logarithm of both sides just to avoid to have an exponential function at the right hand side, we have

$$\log(P_I) = \imath\,g_0\,a\,A_\mu(n) + \imath\,g_0\,a\,A_\nu(n+\hat\mu) + \frac{(\imath\,g_0\,a)^2}{2}\Big[A_\mu(n),A_\nu(n+\hat\mu)\Big]+$$

$$+ \frac{(\imath\,g_0\,a)^3}{12}\left\{\Big[A_\mu(n),\Big[A_\mu(n),A_\nu(n+\hat\mu)\Big]\Big]+\Big[A_\nu(n+\hat\mu),\Big[A_\nu(n+\hat\mu),A_\mu(n)\Big]\Big]\right\}+$$

$$- \frac{(\imath\,g_0\,a)^4}{24}\Big[A_\nu(n+\hat\mu),\Big[A_\mu(n),\Big[A_\mu(n),A_\nu(n+\hat\mu)\Big]\Big]\Big] + \mathcal{O}(a^5)$$

$$\log(P_{II}) = -\imath\,g_0\,a\,A_\mu(n+\hat\nu) - \imath\,g_0\,a\,A_\nu(n) + \frac{(-\imath\,g_0\,a)^2}{2}\Big[A_\mu(n+\hat\nu),A_\nu(n)\Big]+$$

$$+ \frac{(-\imath\,g_0\,a)^3}{12}\left\{\Big[A_\mu(n+\hat\nu),\Big[A_\mu(n+\hat\nu),A_\nu(n)\Big]\Big]+\Big[A_\nu(n),\Big[A_\nu(n),A_\mu(n+\hat\nu)\Big]\Big]\right\}+$$

$$- \frac{(-\imath\,g_0\,a)^4}{24}\Big[A_\nu(n),\Big[A_\mu(n+\hat\nu),\Big[A_\mu(n+\hat\nu),A_\nu(n)\Big]\Big]\Big] + \mathcal{O}(a^5)\,.$$

Using again Eq. (1.38) in the product $P_I \cdot P_{II}$ and defining

$$\mathcal{A}_I \equiv \Big[A_\mu(n),\Big[A_\mu(n),A_\nu(n+\hat\mu)\Big]\Big]+\Big[A_\nu(n+\hat\mu),\Big[A_\nu(n+\hat\mu),A_\mu(n)\Big]\Big]$$

$$\mathcal{B}_I \equiv \Big[A_\nu(n+\hat\mu),\Big[A_\mu(n),\Big[A_\mu(n),A_\nu(n+\hat\mu)\Big]\Big]\Big]$$

$$\mathcal{A}_{II} \equiv \Big[A_\mu(n+\hat\nu),\Big[A_\mu(n+\hat\nu),A_\nu(n)\Big]\Big]+\Big[A_\nu(n),\Big[A_\nu(n),A_\mu(n+\hat\nu)\Big]\Big]$$

---

[25]This means that $A_\mu(na)$ will be written as $A_\mu(n)$ and $A_\nu(na+\hat\mu a)$ as $A_\nu(n+\hat\mu)$ Wherever the a appears in front of A_μ, it means that the field is dimensional and so is its argument.

$$\mathcal{B}_{II} \equiv \left[A_\nu(n), \left[A_\mu(n+\hat{\nu}), \left[A_\mu(n+\hat{\nu}), A_\nu(n) \right] \right] \right]$$

leads to

$$\log(P_I\,P_{II}) = P_I + P_{II} + \frac{[P_I, P_{II}]}{2} + \frac{[P_I,[P_I,P_{II}]]}{12} +$$

$$+ \frac{[P_{II},[P_{II},P_I]]}{12} - \frac{[P_{II},[P_I,[P_I,P_{II}]]]}{24} + \Sigma =$$

$$= \imath\, g_0\, a\, A_\mu(n) + \imath\, g_0\, a\, A_\nu(n+\hat{\mu}) + \frac{(\imath\, g_0\, a)^2}{2} \left[A_\mu(n), A_\nu(n+\hat{\mu}) \right] +$$

$$- \imath\, g_0\, a\, A_\mu(n+\hat{\nu}) - \imath\, g_0\, a\, A_\nu(n) + \frac{(\imath\, g_0\, a)^2}{2} \left[A_\mu(n+\hat{\nu}), A_\nu(n) \right] +$$

$$+ \frac{(\imath\, g_0\, a)^3}{12} (\mathcal{A}_I - \mathcal{A}_{II}) - \frac{(\imath\, g_0\, a)^4}{24} (\mathcal{B}_I + \mathcal{B}_{II}) +$$

$$- \frac{(\imath\, g_0\, a)^2}{2} \left[A_\mu(n) + A_\nu(n+\hat{\mu}), A_\mu(n+\hat{\nu}) + A_\nu(n) \right] +$$

$$+ \frac{(\imath\, g_0\, a)^3}{4} \left[A_\mu(n) + A_\nu(n+\hat{\mu}), \left[A_\mu(n+\hat{\nu}), A_\nu(n) \right] \right] +$$

$$- \frac{(\imath\, g_0\, a)^4}{24} \left[A_\mu(n) + A_\nu(n+\hat{\mu}), \mathcal{A}_{II} \right] +$$

$$- \frac{(\imath\, g_0\, a)^3}{4} \left[\left[A_\mu(n), A_\nu(n+\hat{\mu}) \right], A_\mu(n+\hat{\nu}) + A_\nu(n) \right] +$$

$$+ \frac{(\imath\, g_0\, a)^4}{8} \left[\left[A_\mu(n), A_\nu(n+\hat{\mu}) \right], \left[A_\mu(n+\hat{\nu}), A_\nu(n) \right] \right] +$$

$$- \frac{(\imath\, g_0\, a)^4}{24} \left[\mathcal{A}_I, A_\mu(n+\hat{\nu}) + A_\nu(n) \right] +$$

$$- \frac{(\imath\, g_0\, a)^3}{12} \left[A_\mu(n) + A_\nu(n+\hat{\mu}), \left[A_\mu(n) + A_\nu(n+\hat{\mu}), A_\mu(n+\hat{\nu}) + A_\nu(n) \right] \right] +$$

$$+ \frac{(\imath\, g_0\, a)^4}{24} \left[A_\mu(n) + A_\nu(n+\hat{\mu}), \left[A_\mu(n) + A_\nu(n+\hat{\mu}), \left[A_\mu(n+\hat{\nu}), A_\nu(n) \right] \right] \right] +$$

$$- \frac{(\imath\, g_0\, a)^4}{24} \left[A_\mu(n) + A_\nu(n+\hat{\mu}), \left[\left[A_\mu(n), A_\nu(n+\hat{\mu}) \right], A_\mu(n+\hat{\nu}) + A_\nu(n) \right] \right] +$$

$$- \frac{(\imath\, g_0\, a)^4}{24} \left[\left[A_\mu(n), A_\nu(n+\hat{\mu}) \right], \left[A_\mu(n) + A_\nu(n+\hat{\mu}), A_\mu(n+\hat{\nu}) + A_\nu(n) \right] \right] +$$

$$+ \frac{(\imath\, g_0\, a)^3}{12} \left[A_\mu(n+\hat{\nu}) + A_\nu(n), \left[A_\mu(n+\hat{\nu}) + A_\nu(n), A_\mu(n) + A_\nu(n+\hat{\mu}) \right] \right] +$$

$$- \frac{(\imath\, g_0\, a)^4}{24} \left[A_\mu(n+\hat{\nu}) + A_\nu(n), \left[\left[A_\mu(n+\hat{\nu}), A_\nu(n) \right], A_\mu(n) + A_\nu(n+\hat{\mu}) \right] \right] +$$

$$+ \frac{(\imath\, g_0\, a)^4}{24} \left[A_\mu(n+\hat{\nu}) + A_\nu(n), \left[A_\mu(n+\hat{\nu}) + A_\nu(n), \left[A_\mu(n), A_\nu(n+\hat{\mu}) \right] \right] \right] +$$

$$- \frac{(\imath\, g_0\, a)^4}{24} \left[\left[A_\mu(n+\hat{\nu}), A_\nu(n) \right], \left[A_\mu(n+\hat{\nu}) + A_\nu(n), A_\mu(n) + A_\nu(n+\hat{\mu}) \right] \right] +$$

$$+ \frac{(\imath\, g_0\, a)^4}{24} \left[A_\mu(n+\hat{\nu}) + A_\nu(n), \left[A_\mu(n) + A_\nu(n+\hat{\mu}), \right. \right.$$

$$\left. \left. \left[A_\mu(n) + A_\nu(n+\hat{\mu}), A_\mu(n+\hat{\nu}) + A_\nu(n) \right] \right] \right] + \mathcal{O}(a^5) ,$$

where all terms of order fifth or higher in a were included into $\mathcal{O}(a^5)$. The arrows connect terms that are mapped one to another up to a sign by exchange of the indices μ and ν. We will come back in a moment to this point. Before let us rewrite in a slightly more explicit way the last term.

Making use of the expansions

$$A_\nu(n+\hat\mu) \;=\; A_\nu(n) \;+\; a\,\partial_\mu\,A_\nu(n) \;+\; a^2\,\partial_\mu^2\,A_\nu(n) \;+\; a^3\,\partial_\mu^3\,A_\nu(n) \;+\; \mathcal{O}(a^4) \tag{1.40a}$$

$$A_\mu(n+\hat\nu) \;=\; A_\mu(n) \;+\; a\,\partial_\nu\,A_\mu(n) \;+\; a^2\,\partial_\nu^2\,A_\mu(n) \;+\; a^3\,\partial_\nu^3\,A_\mu(n) \;+\; \mathcal{O}(a^4) \tag{1.40b}$$

it is easy to show that

$$\Big[A_\mu(n), A_\mu(n+\hat\nu)\Big] = \mathcal{O}(a) \qquad \text{as well as} \qquad \Big[A_\nu(n+\hat\mu), A_\nu(n)\Big] = \mathcal{O}(a)$$

and then the cyan term becomes

$$\frac{(\imath g_0\,a)^4}{24}\Big[A_\mu(n+\hat\nu),\Big[A_\mu(n),\Big[A_\mu(n),A_\nu(n)\Big]\Big]\Big] +$$

$$+\frac{(\imath g_0\,a)^4}{24}\Big[A_\mu(n+\hat\nu),\Big[A_\mu(n),\Big[A_\nu(n+\hat\mu),A_\mu(n+\hat\nu)\Big]\Big]\Big] +$$

$$+\frac{(\imath g_0\,a)^4}{24}\Big[A_\mu(n+\hat\nu),\Big[A_\nu(n+\hat\mu),\Big[A_\mu(n),A_\nu(n)\Big]\Big]\Big] +$$

$$+\frac{(\imath g_0\,a)^4}{24}\Big[A_\mu(n+\hat\nu),\Big[A_\nu(n+\hat\mu),\Big[A_\nu(n+\hat\mu),A_\mu(n+\hat\nu)\Big]\Big]\Big] +$$

$$+\frac{(\imath g_0\,a)^4}{24}\Big[A_\nu(n),\Big[A_\mu(n),\Big[A_\mu(n),A_\nu(n)\Big]\Big]\Big] +$$

$$+\frac{(\imath g_0\,a)^4}{24}\Big[A_\nu(n),\Big[A_\mu(n),\Big[A_\nu(n+\hat\mu),A_\mu(n+\hat\nu)\Big]\Big]\Big] +$$

$$+\frac{(\imath g_0\,a)^4}{24}\Big[A_\nu(n),\Big[A_\nu(n+\hat\mu),\Big[A_\mu(n),A_\nu(n)\Big]\Big]\Big] +$$

$$+\frac{(\imath g_0\,a)^4}{24}\Big[A_\nu(n),\Big[A_\nu(n+\hat\mu),\Big[A_\nu(n+\hat\mu),A_\mu(n+\hat\nu)\Big]\Big]\Big] ,$$

with some higher order terms in a as usually to be included in $\mathcal{O}(a^5)$. It is possible to make use of Eqs. (1.40) to further simplify $\log(P_I\,P_{II})$. Let us start from the terms of order one and two in $\imath\,g_0\,a$. Considering that any operator commutes with itself, we have

- $\imath\,g_0\,a$

$$A_\mu(n) + A_\nu(n) + a\,\partial_\mu A_\nu(n) \boxed{+\, a^2\,\partial_\mu^2 A_\nu(n) + a^3\,\partial_\mu^3 A_\nu(n)} +$$
$$-\,A_\mu(n) - a\,\partial_\nu A_\mu(n) \boxed{-\, a^2\,\partial_\nu^2 A_\mu(n) - a^3\,\partial_\nu^3 A_\mu(n)} -\,A_\nu(n)$$

- $\frac{1}{2}(\imath\,g_0\,a)^2$

$$\big[A_\mu(n),\,A_\nu(n)\big]\boxed{+\,\big[A_\mu(n),\,a\,\partial_\mu A_\nu(n)\big] + \big[A_\mu(n),\,a^2\,\partial_\mu^2 A_\nu(n)\big]}$$
$$+\big[A_\mu(n),\,A_\nu(n)\big]\boxed{+\,\big[a\,\partial_\nu A_\mu(n),\,A_\nu(n)\big] + \big[a^2\,\partial_\nu^2 A_\mu(n),\,A_\nu(n)\big]}$$
$$-\big[A_\mu(n),\,A_\nu(n)\big] - \big[A_\nu(n),\,A_\mu(n)\big]\boxed{-\,\big[A_\nu(n),\,a\,\partial_\nu A_\mu(n)\big] - \big[A_\nu(n),\,a^2\,\partial_\nu^2 A_\mu(n)\big]}$$
$$\boxed{-\,\big[a\,\partial_\mu A_\nu(n),\,a\,\partial_\nu A_\mu(n)\big] - \big[a\,\partial_\mu A_\nu(n),\,A_\mu(n)\big] - \big[a^2\,\partial_\mu^2 A_\nu(n),\,A_\mu(n)\big]}$$

where, again, we neglected $\mathcal{O}(a^5)$ and we highlighted the terms of order higher than two that are antisymmetric by exchange of the indices μ and ν (it will be clear soon why). Let us go on considering those terms not connected by arrows and not already considered. It can be shown that they do not contribute to the order four in a. In order to do so, we need to use the following commutator property,

$$[A,[B,[C,D]]] + [D,[A,[B,C]]] + [C,[D,[A,B]]] + [B,[C,[D,A]]] = [[A,C],[B,D]] ,$$

which leads to the following identities in case some of the operators are the same:

$$A = B = C \quad \Leftrightarrow \quad \big[A, \big[A, \big[A, D\big]\big]\big] + \big[A, \big[A, \big[D, A\big]\big]\big] = 0 \tag{1.41a}$$

$$A = C \wedge B = D \quad \Leftrightarrow \quad \big[A, \big[B, \big[A, B\big]\big]\big] + \big[B, \big[A, \big[B, A\big]\big]\big] = 0 \tag{1.41b}$$

$$A = D \wedge B = C \quad \Leftrightarrow \quad \big[A, \big[B, \big[B, A\big]\big]\big] + \big[B, \big[A, \big[A, B\big]\big]\big] = 0 \tag{1.41c}$$

$$A = B = D \quad \Leftrightarrow \quad \big[A, \big[A, \big[C, A\big]\big]\big] + \big[A, \big[A, \big[A, C\big]\big]\big] = 0 \;. \tag{1.41d}$$

Using Eqs. (1.40) once again (here only the leading order is considered since we are already dealing with terms of fourth order in a), we then have that

$$\mathcal{B}_I + \mathcal{B}_{II} = \big[A_\nu(n), \big[A_\mu(n), \big[A_\mu(n), A_\nu(n)\big]\big]\big] + \big[A_\nu(n), \big[A_\mu(n), \big[A_\mu(n), A_\nu(n)\big]\big]\big] = 0$$

because of Eq. (1.41c) and the cyan term becomes

$$\frac{(\imath\, g_0\, a)^4}{24}\big[A_\mu(n), \big[A_\mu(n), \big[A_\mu(n), A_\nu(n)\big]\big]\big] + \quad\longleftarrow$$
$$+ \frac{(\imath\, g_0\, a)^4}{24}\big[A_\mu(n), \big[A_\mu(n), \big[A_\nu(n), A_\mu(n)\big]\big]\big] + \quad\longleftarrow \quad \text{Eq. (1.41a)}$$
$$+ \frac{(\imath\, g_0\, a)^4}{24}\big[A_\mu(n), \big[A_\nu(n), \big[A_\mu(n), A_\nu(n)\big]\big]\big] +$$
$$\text{Eq. (1.41b)} \quad + \frac{(\imath\, g_0\, a)^4}{24}\big[A_\mu(n), \big[A_\nu(n), \big[A_\nu(n), A_\mu(n)\big]\big]\big] + \quad\longleftarrow$$
$$+ \frac{(\imath\, g_0\, a)^4}{24}\big[A_\nu(n), \big[A_\mu(n), \big[A_\mu(n), A_\nu(n)\big]\big]\big] + \quad\longleftarrow \quad \text{Eq. (1.41c)}$$
$$+ \frac{(\imath\, g_0\, a)^4}{24}\big[A_\nu(n), \big[A_\mu(n), \big[A_\nu(n), A_\mu(n)\big]\big]\big] +$$
$$\text{Eq. (1.41d)} \quad + \frac{(\imath\, g_0\, a)^4}{24}\big[A_\nu(n), \big[A_\nu(n), \big[A_\mu(n), A_\nu(n)\big]\big]\big] +$$
$$+ \frac{(\imath\, g_0\, a)^4}{24}\big[A_\nu(n), \big[A_\nu(n), \big[A_\nu(n), A_\mu(n)\big]\big]\big] = 0 \;.$$

Putting what found so far all together leads to

$$\log(P_I\, P_{II}) = \imath\, g_0\, a^2 \Big(\partial_\mu A_\nu(n) - \partial_\nu A_\mu(n) + \imath\, g_0 \big[A_\mu(n), A_\nu(n)\big]\Big) + E^3_{\mu\nu}(n)\, a^3 + E^4_{\mu\nu}(n)\, a^4 + \mathcal{O}(a^5) \;,$$

where in $E^3_{\mu\nu}(n) = -E^3_{\nu\mu}(n)$ and $E^4_{\mu\nu}(n) = -E^4_{\nu\mu}(n)$ we included all the terms previously highlighted as antisymmetric in μ and ν (here 3 and 4 are clearly labels and not powers). We can now finally deal with all these terms. Since all this long calculation could have made us loose a bit the thread, let us remind that we are looking for a lattice version of the pure gauge part of the QCD action. And we already know that it should contain a term proportional to the trace of the plaquette. Let us see what happens if such a term consists of the real part of the trace of the plaquette. One way to take the real part of a complex number is to add it to its complex conjugate and divide by two. For small lattice spacing, the plaquette can be written as a series in a and the trace operation as well as the real part one can be carried out on each single term. Moreover,

$$\mathrm{Tr}_c\big[\, \Pi_{\mu\nu}(n)\, \big]^\star = \mathrm{Tr}_c\big[\, \Pi^\dagger_{\mu\nu}(n)\, \big] = \mathrm{Tr}_c\big[\, \Pi_{\nu\mu}(n)\, \big] \;,$$

which means that, if a generic term is antisymmetric in μ and ν, it will vanish taking the real part of its trace,

$$E_{\mu\nu} = -E_{\nu\mu} \quad \Leftrightarrow \quad \Re[\mathrm{Tr}_c(E_{\mu\nu})] = \frac{\mathrm{Tr}_c(E_{\mu\nu}) + \mathrm{Tr}_c(E_{\mu\nu})^\star}{2} = \frac{\mathrm{Tr}_c(E_{\mu\nu}) + \mathrm{Tr}_c(E_{\nu\mu})}{2} = 0 \;.$$

On the contrary, if a term is symmetric, it has to be real. But then we finally find that, for small a, $\Re\{\mathrm{Tr}_c[\,\Pi_{\mu\nu}(n)\,]\}$ can be approximated as

$$\Re\left\{\mathrm{Tr}_c\left[e^{\,\imath\, g_0\, a^2\,(\partial_\mu A_\nu(n)-\partial_\nu A_\mu(n)+\imath\, g_0\,[A_\mu(n),\, A_\nu(n)])+\, E^3_{\mu\nu}(n)\,a^3+\, E^4_{\mu\nu}(n)\,a^4+\mathcal{O}(a^5)}\right]\right\} =$$

$$= \Re\left\{\mathrm{Tr}_c\left[\mathbb{1} + \imath\, g_0\, a^2\, F_{\mu\nu}(n) + E^3_{\mu\nu}(n)\,a^3 + E^4_{\mu\nu}(n)\,a^4 - \frac{1}{2}\, g_0^2\, a^4\, F_{\mu\nu}(n)\, F_{\mu\nu}(n) + \mathcal{O}(a^5)\right]\right\} =$$

$$\approx N_c - \frac{1}{2}\, g_0^2\, a^4\, \mathrm{Tr}_c\Big[\, F_{\mu\nu}(n)\, F_{\mu\nu}(n)\,\Big].$$

that clearly suggests that, to have

$$\lim_{a\to 0} \mathcal{S}_G^{(\text{latt.})} = \frac{1}{4}\int \mathrm{d}^4x\, F^A_{\mu\nu}(x)\, F^A_{\mu\nu}(x) = \mathcal{S}_G^{(\text{cont.})}\ ,$$

we have to choose

$$\mathcal{S}_G^{(\text{latt.})} = \beta \sum_n \sum_{\mu<\nu}\left[1 - \frac{1}{N_c}\Re\big(\mathrm{Tr}_c\,\Pi_{\mu\nu}(n)\big)\right] \qquad \text{with} \qquad \beta \equiv \frac{2N_c}{g_0^2}\ . \tag{1.42}$$

It is worth remarking where the factor $1/4$ that appears in the continuum action comes from. In Eq. (1.42) we summed over $\mu < \nu$ while in $\mathcal{S}_G^{(\text{cont.})}$ all possible values of the indices μ and ν are considered. But we already observed that the real part of the trace of the plaquette is not affected by swapping μ and ν. Furthermore, there is no contribution to $\mathcal{S}_G^{(\text{latt.})}$ for $\mu = \nu$. This explains a factor $1/2$. The other comes from the trace operation. In fact,

$$\mathrm{Tr}_c\big(\, F_{\mu\nu}(x)\, F_{\mu\nu}(x)\,\big) = \mathrm{Tr}_c\big(F^A_{\mu\nu}(x)\, t^A\, F^B_{\mu\nu}(x)\, t^B\big) = \mathrm{Tr}_c\left(F^A_{\mu\nu}(x)\, \frac{\lambda^A}{2}\, F^B_{\mu\nu}(x)\, \frac{\lambda^B}{2}\right) =$$

$$= \frac{1}{4}\, F^A_{\mu\nu}(x)\, F^B_{\mu\nu}(x)\, \mathrm{Tr}_c\big(\lambda^A\lambda^B\big) = \frac{1}{4}\, F^A_{\mu\nu}(x)\, F^B_{\mu\nu}(x)\, 2\delta_{A,B} =$$

$$= \frac{1}{2}\, F^A_{\mu\nu}(x)\, F^A_{\mu\nu}(x)\ .$$

To conclude this section, we still need to discuss an important aspect of gauge invariance that is in general easy to forget. The QCD action is used in the path integral formalism to get correlation functions and expectation values of observables. Any such an integral will involve an integration on the links, namely an integration over a special unitary group. Now, after having made the action gauge invariant, it would be really a shame if quantum fluctuations destroyed this invariance. In general, the link integration measure – the so-called *Haar measure*, usually denoted by $\mathcal{D}U$ – depends on the $N_c^2 - 1$ parameters that identify an element of $SU(N_c)$ and the integral has to be done on the differential manifold to which the group is diffeomorphic. Denoting by α_k^A the parameters on which the kth link depends, then the Haar measure will be of the form

$$\mathcal{D}U = \prod_k \mathcal{J}\big(\alpha_k^1,\ldots,\alpha_k^{N_c^2-1}\big)\,\mathrm{d}\alpha_k\ ,$$

where

$$\mathrm{d}\alpha_k \equiv \prod_{A=1}^{N^2-1}\mathrm{d}\alpha_k^A\ .$$

The Jacobian $\mathcal{J}$ has often a complicated structure that has to be derived imposing gauge - invariance. A particular, easier example is when $N_c = 2$. Let us briefly consider it. It is interesting to write down the Haar measure in this case especially because, numerically, it can be used [29] to approach

problems with $N_c > 2$. It is known that any element $U \in SU(2)$ can be written as $U = u_0 + \imath \vec{u} \cdot \vec{\sigma}$ with $u_\alpha \in \mathbb{R}$ and $2\sigma_i$ the Pauli matrices. Since $UU^\dagger = \mathbb{1}$ as well as $\det(U) = 1$, then $u_0^2 + |\vec{u}|^2 = 1$ and it is clear that the manifold to consider is the 3-sphere. Using spherical coordinates,

$$\begin{cases} u_0 = \cos\chi \\ u_1 = \sin\chi \, \cos\theta \\ u_2 = \sin\chi \, \sin\theta \, \cos\varphi \\ u_3 = \sin\chi \, \sin\theta \, \sin\varphi \end{cases}$$

with

$$\begin{cases} 0 \leqslant \varphi < 2\pi \\ 0 \leqslant \theta \leqslant \pi \\ 0 \leqslant \chi \leqslant \pi \end{cases} \quad ,$$

it follows immediately that the Haar measure is

$$\mathcal{D}U = \prod_k \sin^2(\chi_k) \, \sin(\theta_k) \, \mathrm{d}\chi_k \, \mathrm{d}\theta_k \, \mathrm{d}\varphi_k \ ,$$

where χ_k, θ_k and φ_k are the three parameters that identify the kth link. The general rules to perform invariant integration over $SU(N)$ have been discussed by Creutz [30] in 1978 and we refer to the literature for any further information.

$$\mathcal{S}_{QCD}^{(\mathrm{W.})} = \mathcal{S}_G[U] + \mathcal{S}_F^{(\mathrm{W.})}[U, \psi, \bar{\psi}] \quad \longleftrightarrow \quad \mathcal{S}_{QCD}^{(\mathrm{stagg.})} = \mathcal{S}_G[U] + \mathcal{S}_F^{(\mathrm{stagg.})}[U, \chi, \bar{\chi}]$$

$$\mathcal{S}_G = \frac{6}{g_0^2} \sum_n \sum_{\mu < \nu} \left[1 - \frac{1}{3} \Re\Big(Tr_C \big(\underset{\sim}{U}_\mu(n) \, \underset{\sim}{U}_\nu(n+\hat\mu) \, \underset{\sim}{U}_\mu^\dagger(n+\hat\nu) \, \underset{\sim}{U}_\nu^\dagger(n) \big) \Big) \right]$$

$$\mathcal{S}_F^{(\mathrm{W.})} = (\hat{M}_0 + 4r) \sum_n \underset{\sim}{\bar\psi}(n) \, \underset{\sim}{\psi}(n) +$$

$$- \frac{1}{2} \sum_{n,\mu} \Big[\underset{\sim}{\bar\psi}(n) \, (r - \gamma_\mu) \, \underset{\sim}{U}_\mu(n) \, \underset{\sim}{\psi}(n+\hat\mu) \ + \ \underset{\sim}{\bar\psi}(n+\hat\mu) \, (r + \gamma_\mu) \, \underset{\sim}{U}_\mu^\dagger(n) \, \underset{\sim}{\psi}(n) \Big]$$

$$\mathcal{S}_F^{(\mathrm{stagg.})} = \frac{1}{2} \sum_{n,\mu} \underset{\sim}{\bar\chi}(n) \, \eta_\mu(n) \Big[\underset{\sim}{U}_\mu(n) \, \underset{\sim}{\chi}(n+\hat\mu) \ - \ \underset{\sim}{U}_\mu^\dagger(n-\hat\mu) \, \underset{\sim}{\chi}(n-\hat\mu) \Big] + \hat{M}_0 \sum_n \underset{\sim}{\bar\chi}(n) \, \underset{\sim}{\chi}(n)$$

In the rest of this thesis, we will drop the tilde under any field; it will be clear from the context whether the field has or has not a colour degree of freedom.

§ 1.6   The continuum limit

In the previous sections of this chapter we regularised the QCD action introducing a space-time isotropic lattice and most of the time was spent to show that our regularisation is correct in the naïve continuum limit. Probably, the Reader has been wondering about the adjective *naïve* for a while. It is now time to address this point. Let us start observing that continuum physics is extracted when the lattice is removed, i.e. when $a \to 0$. The naïve continuum limit is simply an analytic procedure that consists in reintroducing the physical dimension in the lattice formulation and to let the lattice spacing go to zero. Nevertheless a does not appear explicitly anywhere in the lattice action and then it is not a parameter that can be tuned. How to proceed, then, in a numerical simulation to extract physical information? Clearly, it is not trivial.

As already remarked at the beginning of §1.3, there are infinitely many lattice regularisations that possess the correct naïve continuum limit and we merely chose the simplest one. Indeed there is a wide set of so-called *improved actions* that take advantage of this fact to reduce lattice artefacts and extract continuum physics for larger lattice spacings[26]. Nevertheless, to have the correct naïve continuum limit does not guarantee that the considered theory coincides with QCD. For this to be the case, it has to exist in the lattice theory a region in the parameter space where the correlation lengths diverge or, said in an other way, the continuum theory can be realised only at a second order critical point. To further clarify this statement, let us consider a lattice gauge theory and let us suppose that it admits a continuum limit. We can then extract the mass spectrum of the corresponding field theory, studying correlation functions for large euclidean time. Since the physical masses M_i are finite, it means that the correspondent ones in lattice units, $\hat{M}_0[i] = a \cdot M_i$, have to go to zero in the continuum limit. Therefore, the correlation lengths $\hat{\xi}_i$ which will have to be calculated have to diverge for $a \to 0$ and this shows exactly what was previously said. Intuitively, this is the only way for the system to loose memory of the underlying lattice structure. We conclude then that *if a regularised theory does not have any critical point for some value of its parameters, it cannot describe any continuum field theory.* In QCD, focusing for simplicity on the pure gauge case, the only parameter that can be tuned to study the system near criticality is the coupling constant g_0 and this is also the only parameter on which a physical quantity can depend. To require that there exists a second order critical point means that there exists a critical point $g_0^\star$ such that

$$\lim_{g_0 \to g_0^\star} \hat{\xi}(g_0) = +\infty \ .$$

It is worth remarking that this property follows from the request that any observable is finite in the continuum limit. This also implies that the bare parameter g_0 depends on the lattice spacing[27]. In fact, considering a quantity Θ with dimension d_Θ in mass and denoting with $\hat{\Theta}$ the corresponding lattice quantity that depends in general on g_0, it must be

$$\Theta(g_0, a) = \left(\frac{1}{a}\right)^{d_\Theta} \hat{\Theta}(g_0) \ . \tag{1.45}$$

If we want the left hand side of Eq. (1.45) to be finite for $a \to 0$, it must be $g_0 = g_0(a)$ and

$$\lim_{a \to 0} \Theta\big(g_0(a), a\big) = \Theta_{\text{phys}} \ .$$

Now, if the dependence of $\hat{\Theta}$ on g_0 was known for sufficiently small values of a, we could deduce the function $g_0(a)$ approximating the left hand side of Eq. (1.45) with Θ_{phys}. And in principle $\hat{\Theta}$ could be numerically measured for different values of g_0. But what does it mean *sufficiently small*? And, especially, in which range should we measure $\hat{\Theta}$ if we do not know how g_0 depends on a? We clearly need to deduce $g_0(a)$ in an other way. Before doing that, it is better to comment a bit further on Eq. (1.45). It could seem that the dependence $g_0(a)$ can vary changing the considered observable. Actually, this is the case for coarse lattices. Nevertheless, for smaller and smaller a, it must exist a universal function $g_0(a)$, which ensures each observable to stay finite. Differently said, given two different observables

$$\begin{cases} \hat{O}_1(g_0) = a^{d_1} \, O_1 \\ \hat{O}_2(g_0) = a^{d_2} \, O_2 \end{cases} \ ,$$

it must be

$$\frac{\big(\hat{O}_1(g_0)\big)^{1/d_1}}{\big(\hat{O}_2(g_0)\big)^{1/d_2}} = \text{const.} \quad \text{for} \quad g_0 \approx g_0^\star \ . \tag{1.46}$$

---

[26] Just to mention some, the Symanzik improvement [31] was proposed in 1983, the Naik improvement [32] appeared in 1989 and the twisted mass Wilson fermions formulation was outlined in [33–36] around 2000.

[27] This is true in general for any bare parameter and it should not surprise. In fact, varying a, the number of links and lattice sites within a given physical volume changes as well and the theory parameters have to be adjusted if we want the physics to be the same.

The region of values of g_0 such that Eq. (1.46) is fulfilled is called *scaling region* or, which is the same, we say that there is scaling whenever such a relation is valid.

Coming back to the dependence $g_0(a)$, let us consider Eq. (1.45) once again. For small values of a, g_0 has to vary in a way such that Θ becomes independent from the lattice spacing. Therefore, $\Theta(g_0, a)$ has to fulfil the renormalisation group equation

$$\left[a \frac{\partial}{\partial a} - \beta(g_0) \frac{\partial}{\partial g_0} \right] \Theta(g_0, a) = 0 , \qquad (1.47a)$$

where

$$\beta(g_0) = -a \frac{\partial g_0}{\partial a} \qquad (1.47b)$$

is the so-called Callan-Symanzik β-function [37, 38], which cannot be calculated exactly to all orders in perturbation theory. Nevertheless, Eq. (1.47a) must hold order by order and perturbatively, for $SU(N_c)$ and N_f massless fermions, we have

$$\beta(g_0) = -\beta_0 \, g_0^3 - \beta_1 \, g_0^5 + \mathcal{O}(g_0^7) , \qquad (1.48)$$

where

$$\beta_0 = \frac{1}{(4\pi)^2} \left(\frac{11}{3} N_c - \frac{2}{3} N_f \right)$$

$$\beta_1 = \frac{1}{(4\pi)^4} \left(\frac{34}{3} N_c^2 - \frac{10}{3} N_c N_f - \frac{N_c^2 - 1}{N_c} N_f \right)$$

are universal coefficients not depending on the chosen renormalisation scheme. In our case, $N_c = 3$ and $N_f = 0$ that implies

$$\beta_0 = \frac{11}{16 \, \pi^2} \qquad \text{and} \qquad \beta_1 = \frac{102}{256 \, \pi^4} .$$

Inserting Eq. (1.48) into Eq. (1.47b) leads to

$$-a \frac{\partial g_0}{\partial a} = -\beta_0 g_0^3 - \beta_1 g_0^5$$

from which, using the separation of variables technique, we get

$$\int \frac{\mathrm{d}a}{a} = \int \frac{\mathrm{d}g_0}{\beta_0 g_0^3 + \beta_1 g_0^5} \quad \Rightarrow \quad \int \frac{\mathrm{d}a}{a} = -\frac{\beta_0}{\beta_1^2} \int \frac{\mathrm{d}g_0}{g_0} - \frac{1}{\beta_0} \int \frac{\mathrm{d}g_0}{g_0^3} + \frac{\beta_1}{2\beta_0^2} \int \frac{2\beta_1 g_0 \, \mathrm{d}g_0}{\beta_0 + \beta_1 g_0^2}$$

$$\log(a) = -\frac{\beta_1}{\beta_0^2} \log(g_0) - \frac{1}{2\beta_0 g_0^2} + \frac{\beta_1}{2\beta_0^2} \log\left(\beta_0 + \beta_1 g_0^2 \right) + \text{const.}$$

$$a(g_0) = \frac{1}{\Lambda_L} \left(\beta_0 + \beta_1 g_0^2 \right)^{\beta_1/(2\beta_0^2)} \cdot \left(g_0^2 \right)^{\beta_1/2\beta_0^2} \cdot \exp\left(-\frac{1}{2\beta_0 g_0^2} \right)$$

$$= \frac{1}{\Lambda_L} \left(\beta_0 g_0^2 + \beta_1 g_0^4 \right)^{\beta_1/(2\beta_0^2)} \cdot \exp\left(-\frac{1}{2\beta_0 g_0^2} \right)$$

$$= \frac{1}{\Lambda_L} \left(\beta_0 g_0^2 \right)^{\beta_1/(2\beta_0^2)} \cdot \exp\left(-\frac{1}{2\beta_0 g_0^2} \right) \cdot \left(1 + \mathcal{O}(g_0^2) \right) \equiv \frac{1}{\Lambda_L} R(g_0) + \mathcal{O}\!\left(R g_0^2 \right) .$$

Usually,

$$a_{2\text{loops}} \equiv \frac{1}{\Lambda_L} R(g_0) , \qquad (1.49)$$

where Λ_L is the integration constant and it is a mass scale in term of which any quantity can be measured. We will come back soon to this point. Let us first determine the value $g_0^\star$. The fact that

the coefficient β_0 is positive together with Eqs. (1.47b) and (1.48) implies that g_0 has to decrease, if a is decreased. From Eq. (1.49) it is trivial to take the limit $a \to 0$ and we find $g_0^\star = 0$. We are now ready to answer the main question of this section: How can we be sure in a numerical simulation to be extracting continuum physics? The answer is hidden in Eq. (1.49). Inserting it into Eq. (1.45) and remembering that Θ has to be finite in the continuum limit, we have

$$\lim_{g_0 \to 0} \hat{\Theta}(g_0) = \hat{C}_\Theta \cdot \left(R(g_0) \right)^{d_\Theta} ,$$

or, equivalently,

$$\frac{\hat{\Theta}(g_0)}{(R(g_0))^{d_\Theta}} = \text{const.} \quad \text{for} \quad g_0 \approx g_0^\star , \tag{1.50}$$

where $\hat{C}_\Theta$ is a dimensionless constant. We will say that there is *asymptotic scaling* in the region of values of g_0 which fulfil Eq. (1.50). Since the ratio in Eq. (1.50) can be directly measured, we can guarantee that *we are simulating in the continuum limit whenever such a ratio stays constant for different values of the lattice coupling.* A graphical overview of what happens reducing g_0 should look like
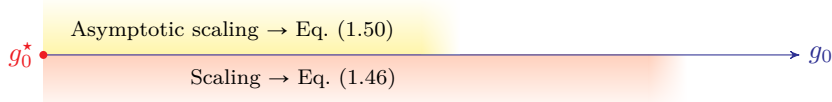
where the shaded background remark the fact that the separation of these regions cannot be a priori predicted.

To conclude this section, let us comment a bit further on the constant Λ_L. The asymptotic scaling condition tells us also that

$$\Theta_{phy} = \hat{C}_\Theta \cdot (\Lambda_L)^{d_\Theta} ,$$

which highlights another important fact of lattice QCD: Any observable can be numerically determined only in terms of an unknown scale and, thus, *numerical simulations can only determine ratios of homogenous observables*, as, for instance, particles masses. It is worth remarking that the appearance of Λ_L in a theory that is, in principle, free from any scale is not peculiar of the lattice approach. In perturbative QCD as well, the need of the theory to be renormalised brings to the introduction of the Λ_{QCD} scale. The Reader could wonder whether these two scales coincide. Indeed they do not. A nice explanation of the connection between them can be found in §15.5 of [17].

§ 1.7   Finite Temperature LQCD and discretisation errors

In this section, we want to understand how temperature can be introduced on the lattice and, in general, how it can be varied. This is the starting point when the structure of the phase diagram of a theory has to be investigated. We will remain on a rather qualitative level, trying to sketch the main ideas. This is due to the fact that there exists a big variety of textbooks about quantum field theory at finite temperature – e.g. [39] – in which the Reader can find any desired detail. Moreover, many books about lattice theories have one or more sections about finite temperature investigations [17–19].

So far, we kept silent about the meaning of the lattice spatial and temporal extents and about any condition they should fulfil. Since there is no reason to treat any spatial direction differently, we will always assume that our lattice has the same number of sites along x, y and z. We denote this number with $N_s = N_x = N_y = N_z$. In principle, instead, the temporal direction could have

a different extent N_t (we will see in a moment that N_t is related to the temperature) and we will refer to the lattice dimensions using the $N_t \times N_s^3$ notation. It can be shown that there is a structural equivalence between our field theory and statistical mechanics. In particular, the Euclidean canonical partition function of QCD reads[28]

$$\mathcal{Z}\big(T, V; M_f, g\big) = \mathrm{Tr}\big(e^{-\mathcal{H}/T}\big) = \int \mathcal{D}A \, \mathcal{D}\bar{\psi} \, \mathcal{D}\psi \, e^{-\mathcal{S}_{QCD}} \, , \tag{1.51}$$

where T and V denote the temperature and the volume of the system, respectively, $\mathcal{H}$ is the Hamiltonian operator and $\mathcal{S}_{QCD}$ is here the euclidean QCD action generalised to N_f non degenerate quarks and modified to a generic value of the temperature,

$$\mathcal{S}_{QCD} = \mathcal{S}_g + \mathcal{S}_f$$

with

$$\mathcal{S}_g = \int_0^{\frac{1}{T}} \mathrm{d}x_4 \int_V \mathrm{d}^3x \, \frac{1}{4} \, F_A^{\mu\nu}(x) \, F_{\mu\nu}^A(x) \tag{1.52a}$$

and

$$\mathcal{S}_f = \int_0^{\frac{1}{T}} \mathrm{d}x_4 \int_V \mathrm{d}^3x \left\{ \sum_{f=1}^{N_f} \bar{\psi}^f(x) \left[\gamma_\mu \big(\partial_\mu + \imath \, g_0 \, t^A A_\mu^A(x) \,\big) + M_0 \right] \psi^f(x) \right\} . \tag{1.52b}$$

The integration over the space has been limited to a box of volume V just because in this way the connection to the lattice is immediate. At some point, the thermodynamic limit will have to be taken, sending $V \to \infty$. In statistical mechanics, the symbol β is reserved to indicate the inverse temperature of the system. Even though the context should be sufficient to avoid any confusion, we will use in general β only for the inverse gauge coupling and write explicitly $1/T$ where needed. In §1.5, whenever continuum expressions were recalled, we always had infinite extensions in all directions. Indeed, we were considering the vacuum case and no thermal effect was relevant for the discussion. Nevertheless, this is somehow a particular situation and in general QCD lives on a torus whose radius is connected to the temperature. Moreover, the trace in Eq. (1.51) implies that bosonic (fermionic) fields are periodic (anti-periodic) in time, ensuring the Bose-Einstein statistics (the Pauli principle). Taking the $T \to 0$ limit, the infinite four-volume case is recovered. This fact already leads to a first important remark when the theory is discretised: Since the temporal lattice extent cannot be infinitely long, any numerical simulation will be carried out at finite (maybe small) temperature. Supposing to have chosen N_s big enough to make physics insensitive to the finite spatial volume, then, from the space-time symmetry of the euclidean path integral formulation (at $T = 0$) it will follow that physics will be also insensitive to the boundaries in the time direction if $N_t > N_s$. This is what people consider understood speaking about *zero temperature* simulations[29].

If, instead, we desire to study QCD at finite temperature, we will set $N_t < N_s$. Once on the lattice, the temporal extension in physical units is connected to the temperature of the system via

$$a \, N_t = \frac{1}{T} \, . \tag{1.53}$$

Therefore, the temperature can be changed either in a discontinuous way varying N_t or in a continuous way changing the lattice spacing a through the gauge coupling g_0. The latter approach is usually preferable when trying to locate any phase transition, because the minimum variation of N_t is in practice too rough to properly resolve an often rapid change in the thermodynamic quantities. It is worth remarking that varying the lattice spacing to tune the temperature implies

---

[28] For the derivation of the path integral representation refer, for example, to [39].

[29] Of course, whether N_s is big enough to make finite size effects negligible can be understood only a posteriori and the fact that $N_t > N_s$ does not guarantee anything in this regard. Nevertheless, working with $N_t > N_s$ will ensure a "zero temperature" once the spatial volume will be big enough.

that different simulation points have different cut-off effects[30]. Hence, in LQCD, the coupling β is used as synonym of temperature and, for example, the position of a phase transition is given giving β_c (together with the other parameters). If we are, then, interested in translating β_c to the critical temperature in physical units, we could be tempted to use Eq. (1.49). Actually, this is not a good idea, since perturbation theory, with which Eq. (1.49) has been found, is not valid at accessible lattice spacings. If simulating at physical quark masses, one could determine the critical temperature in physical units measuring the mass of a hadron in lattice units. In fact,

$$\frac{T_c}{M_H} = \frac{1}{M_H \, a_c \, N_t} = \frac{1}{\hat{M}_H \, N_t} \qquad \Rightarrow \qquad T_c = \frac{1}{\hat{M}_H \, N_t} M_H \; ,$$

where the mass of the hadron in lattice units must be measured at zero temperature and at the critical value of the coupling, $\hat{M}_H(\beta_c)$. If the quark masses in the simulation are not the physical ones – and this is often the case when addressing still open theoretical questions – the previous approach would lead to wrong values of T_c. The scale should then be set using different observables that are not so sensible to the quark mass values, like for example the Sommer scale [40].

To conclude this section, let us spend some words about those constraints that should be fulfilled in a simulation in order to make the result meaningful. For $T < T_c$, the inverse of the lightest hadron mass (M_H^{-1}) coincides with the correlation length ξ of the statistical system. In order to be able to resolve the hadron as well as to keep finite size effect small, it should be

$$a \ll \xi \ll a \, N_s \quad \Leftrightarrow \quad \hat{M}_H \ll 1 \ll \hat{M}_H \, N_s \; . \tag{1.54}$$

This relation is in general very difficult to be fulfilled. On one hand the lattice spacing should be small, but the smaller it is the bigger N_s has to be. If on top of that we consider that the symbol $\ll$ should be synonym of *at least one order of magnitude*, then it is clear that nowadays computing power is not enough to guarantee Eq. (1.54). Practitioners are usually satisfied when this inequality holds in its weak version, i.e. when the much smaller symbol is substituted by just a less then sign.

In the deconfined phase, at $T > T_c$, we cannot speak of hadrons anymore and the mass scale to be considered is the screening mass[31], that scales proportionally to the temperature. Therefore,

$$a \ll \frac{1}{T} \ll a \, N_s \quad \Leftrightarrow \quad \frac{1}{N_t} \ll 1 \ll a \, N_s \, T \quad \Leftrightarrow \quad 1 \ll N_t \ll N_s \; . \tag{1.55}$$

Often, the second part of Eq. (1.55) is referred saying that the so-called aspect ratio of the lattice – i.e. N_s/N_t – has to be as large as possible. Again, in practice, only a weaker version of Eq. (1.55) can be fulfilled, due to limited computing power. Until some years ago, most simulations have been carried out on lattices with $N_t < 6$ and with aspect ratios up to 4. More recently, we are getting closer to fulfil the requirement of having N_t of the order of 10 and bigger and bigger spatial volumes can be simulated.

Despite the fact that Eqs. (1.54) and (1.55) are completely general, the meaning of the $\ll$ symbol can vary from problem to problem. Therefore, a careful study of finite size effects as well as cut-off effects should be done in each situation since it could lead to different conclusions and/or simplifications.

§ 1.8   Finite Density on the Lattice

The partition function in Eq. (1.51) describes a system with complete balance between quarks and anti-quarks. In fact, in absence of any chemical potential, it can be shown that the QCD action

---

[30]As it is easy to imagine since the lattice acts as a ultraviolet regulator, cut-off effects are all those effects due to the fact that the lattice spacing is finite. They are reduced on finer lattices and in the end removed in the continuum limit.

[31]In a quark-gluon plasma, the chromo-electric fields exhibit a characteristic screening length similarly to what the electromagnetic fields do in an electromagnetic plasma. Its inverse is the so-called (Debye) *screening mass*.

is invariant under charge conjugation and this can be understood, for example, using the Noether's theorem and the axial $U(1)$ symmetry. This leads to the conserved current

$$J_\mu(x) \equiv \bar{\psi}(x)\,\gamma_\mu\,\psi(x)\ ,$$

from which we get the conserved charge

$$Q = \int \mathrm{d}^3x\ \psi^\dagger(x)\,\psi(x)\ .$$

The expectation value of operator Q in a state gives the difference N between the number N_p of particles and the number N_a of anti-particles in such a state. Therefore, recalling that the charge conjugation operation changes the charge of the quarks and then flips the sign of the quantity $N_p - N_a$, it easy to conclude that N is zero on average in the vacuum state if this is invariant under charge conjugation, like in QCD.

In statistical mechanics, switching from the canonical ensemble to the grand-canonical one allows to study the case $N \neq 0$. Using the equivalence between statistical mechanics and our field theory, we can consider the grand-canonical partition function Ξ – that, indeed, we will continue to call $\mathcal{Z}$ – in which a chemical potential μ_f for each quark species coupled to the operator Q_f is introduced,

$$\mathcal{Z}\big(T,V,\mu_f;M_f,g\big) = \mathrm{Tr}\big(e^{-(\mathcal{H}-\mu_f\,Q_f)/T}\big) = \int \mathcal{D}A\,\mathcal{D}\bar{\psi}\,\mathcal{D}\psi\,e^{-\mathcal{S}_{QCD}}\ . \tag{1.56}$$

Here the QCD action is the sum of $\mathcal{S}_g$ and $\mathcal{S}_f$ as in Eqs. (1.52) plus the term

$$\mathcal{S}_\mu = -\int_0^{\frac{1}{T}}\mathrm{d}x_4 \int_V \mathrm{d}^3x \sum_{f=1}^{N_f} \bar{\psi}^f(x)\,\mu_f\gamma_4\,\psi^f(x)\ = -\sum_{f=1}^{N_f}\mu_f\int_0^{\frac{1}{T}}\mathrm{d}x_4\,Q_f\ , \tag{1.57}$$

where $\mu_f \in \mathbb{R}$. The fact that the operator Q_f changes sign under charge conjugation leads to an important symmetry of the partition function. We already recalled that the gauge and fermionic parts of the action are invariant under charge conjugation. Thus,

$$\mathcal{Z}^C\big(\mu_1,\ldots,\mu_{N_f}\big) = \int \mathcal{D}A^C\,\mathcal{D}\bar{\psi}^C\,\mathcal{D}\psi^C\,e^{-\mathcal{S}_g^C-\mathcal{S}_f^C-\mathcal{S}_\mu^C}$$

$$= \int \mathcal{D}A\,\mathcal{D}\bar{\psi}\,\mathcal{D}\psi\,e^{-\mathcal{S}_g-\mathcal{S}_f+\mathcal{S}_\mu} = \mathcal{Z}\big(-\mu_1,\ldots,-\mu_{N_f}\big)\ , \tag{1.58}$$

since the integration measure is also invariant under charge conjugation.

Let us focus now on how to discretise on the lattice the new part of the action reported in Eq. (1.57), that for simplicity we will consider in the case of one only quark species. Naïvely, we could argue that the new term has the same structure as a mass term and we could be tempted to set

$$\mathcal{S}_\mu = \hat{\mu}\sum_n \bar{\hat{\psi}}(n)\,\gamma_4\,\hat{\psi}(x)\ , \tag{1.59}$$

where $\hat{\mu} = a\,\mu$ is the chemical potential made dimensionless using the lattice spacing in the standard way. Unfortunately, this approach leads to wrong results when taking the continuum limit. In particular, this can be shown calculating the energy density $\varepsilon(\mu)$ in the free case and taking the continuum limit. We will not present here the detail of the calculation – they can be found on standard textbooks like, for example §12.2.1 of [19] – but we will discuss the result. Some quite straightforward steps lead to

$$\varepsilon(\mu) - \varepsilon(0) \propto \left(\frac{\mu}{a}\right)^2 \qquad \text{for} \qquad a \ll 1\ ,$$

where the vacuum subtraction is needed for renormalisation reasons. It is clear that the discretisation proposed in Eq. (1.59), leading to a divergence in the $a \to 0$ limit, spoils the renormalisability of the theory and cannot be used[32]. The right way to proceed was explained at the beginning of the Eighties by Hasenfratz and Karsch [41]. Introducing the chemical potential, we added to the Lagrangian the term

$$\mu \, \bar{\psi}(x) \, \gamma_4 \, \psi(x)$$

and this is not so different from the interaction term between the gauge and the fermion fields,

$$\imath \, g_0 \, \bar{\psi}(x) \, \gamma_\nu \, A_\nu(x) \, \psi(x) \ .$$

It is possible then to rewrite the new term in the Lagrangian as

$$\imath \, g_0 \, \bar{\psi}(x) \, \gamma_\nu \, A_\nu^{\text{ext.}}(x) \, \psi(x) \, \delta_{\nu,4} \qquad \text{with} \qquad A_\nu^{\text{ext.}}(x) \, = -\imath \, \frac{\mu}{g_0}$$

and proceed to its discretisation exactly as we did in §1.5 for the gauge field. This time the gauge field will be abelian and the group invariance which will have to be considered is $U(1)$. Once such global symmetry is required to be local in time only, new parallel transports will be needed, since terms like

$$\bar{\psi}(n) \, \psi(n + \hat{4}) \qquad \text{and} \qquad \bar{\psi}(n + \hat{4}) \, \psi(n) \ ,$$

which are present in the discretisation of the derivative ∂_μ, will not be invariant anymore. The new links must be introduced only in the time direction and, since the external field $A_4^{\text{ext.}}(x)$ has a constant imaginary value, we will have U and U^{-1} forward and backward in time direction, rather than U and $U^\dagger$,

$$U_4^{\text{ext.}}(n) \, = e^{\imath \, g_0 \, A_4^{\text{ext.}}(x)} \, = e^{\hat{\mu}} \qquad \text{and} \qquad U_{-4}^{\text{ext.}}(n) \, = e^{-\imath \, g_0 \, A_4^{\text{ext.}}(x)} \, = e^{-\hat{\mu}} \ .$$

The naïve approach to discretise Eq. (1.57) fails in the same way it would fail the introduction of a naïvely discretised covariant derivative – remember the discussion done at page 18 after Eq. (1.30). Said in a different way, introducing on the lattice the quark number term as part of the covariant derivative leaves the lattice action invariant under a $U(1)$ gauge symmetry, which protects the theory against new divergences[33]. Of course, there is no connection with the doubling problem and the chemical potential can be introduced in the same way in the Wilson action

$$\mathcal{S}_F^{(\text{W.})} = (\hat{M}_0 + 4r) \sum_n \bar{\psi}(n) \, \psi(n) +$$

$$- \frac{1}{2} \sum_n \left\{ e^{\hat{\mu}} \, \bar{\psi}(n) \, (r - \gamma_4) \, U_4(n) \, \psi(n + \hat{4}) \, + e^{-\hat{\mu}} \, \bar{\psi}(n + \hat{4}) \, (r + \gamma_4) \, U_4^\dagger(n) \, \psi(n) + \right.$$

$$\left. + \sum_{j=1}^3 \Big[\, \bar{\psi}(n) \, (r - \gamma_j) \, U_j(n) \, \psi(n + \hat{j}) \, + \, \bar{\psi}(n + \hat{j}) \, (r + \gamma_j) \, U_j^\dagger(n) \, \psi(n) \, \Big] \right\} \quad (1.60)$$

in the staggered action,

$$\mathcal{S}_F^{(\text{stagg.})} = \hat{M}_0 \sum_n \bar{\chi}(n) \, \chi(n)$$

$$+ \frac{1}{2} \sum_n \left\{ \bar{\chi}(n) \, \eta_4(n) \Big[e^{\hat{\mu}} \, U_4(n) \, \chi(n + \hat{4}) \, - e^{-\hat{\mu}} \, U_4^\dagger(n - \hat{4}) \, \chi(n - \hat{4}) \, \Big] + \right.$$

$$\left. + \sum_{j=1}^3 \bar{\chi}(n) \, \eta_j(n) \Big[\, U_j(n) \, \chi(n + \hat{j}) \, - \, U_j^\dagger(n - \hat{j}) \, \chi(n - \hat{j}) \, \Big] \right\} , \quad (1.61)$$

---

[32]Just to clarify further any possible doubt, the divergence arising from Eq. (1.59) is not related to the doubling problem. With or without the Wilson term, the energy density will not stay finite for $a \to 0$.

[33]A term on the lattice like that in Eq. (1.59) is invariant under $U(1)$ symmetry, but does not balance those terms that are, instead, at all order in a compensated from the new links. It is possible to check this directly expanding all fields in series of a as done in §1.5.

or in any other formulation. It can be also shown [41] that calculating the energy density with the correct chemical potential discretisation leads to no additional divergences, as long as the theory has been properly regularised for zero temperature and density.

It is possible to show that the symmetry in Eq. (1.58) is still valid on the lattice, but it implies some algebraic work. The starting point is the fact that under charge conjugation on the lattice we have

$$\phi(n) \rightarrow \phi^C(n) = C^{-1} \bar{\phi}^T(n)$$
$$\bar{\phi}(n) \rightarrow \bar{\phi}^C(n) = -\phi^T(n) C \qquad \text{and} \qquad U_\mu(n) \rightarrow U_\mu^C(n) = \left[U_\mu^\dagger(n) \right]^T ,$$

where ϕ is the the fermionic field (i.e. ψ in the Wilson formulation and χ in the staggered case) and the charge conjugation matrix acts only on the Dirac indices fulfilling the relation

$$C \gamma_\mu C^{-1} = -\gamma_\mu^T .$$

In the Wilson case, the calculation is straightforward and can be found in §5.4.1 of [19]. With staggered fermions, instead, there is more to do because of the staggering procedure. The fact that the action is symmetric under charge conjugation in absence of a chemical potential has to be shown in the *spin* ⊗ *taste* space and can be found in [42]. Using similar techniques, it can be also proven that Eq. (1.58) still holds.

To conclude this section, let us have a look to how the determinant of the Dirac operator changes when we introduce a chemical potential μ. In order not to rely on any lattice formulation, we will stay in the continuum. The best way to proceed is to write explicitly the spin structure of the Dirac euclidean operator, i.e. to write it as a 2×2 block matrix[34]. Without loss of generality we can choose a representations of the γ matrices, since it is known that, in an even number of dimensions, all representation of a given Clifford algebra are equivalent. We will use the so-called chiral representation, in which

$$\gamma_i = \begin{pmatrix} 0 & +\imath \sigma_i \\ -\imath \sigma_i & 0 \end{pmatrix} \qquad \text{and} \qquad \gamma_4 = \begin{pmatrix} 0 & \mathbb{1}_{2\times 2} \\ \mathbb{1}_{2\times 2} & 0 \end{pmatrix} ,$$

where σ_i are the three Pauli matrices. Eqs. (1.52b) and (1.57) can be rewritten together in the case of one quark species as

$$\mathcal{S}_f + \mathcal{S}_\mu = \int_0^{\frac{1}{T}} \mathrm{d}x_4 \int_V \mathrm{d}^3 x \; \bar{\psi}(x) \underbrace{\left(\gamma_\nu D_\nu + M_0 - \mu \gamma_4 \right)}_{\mathfrak{D}(\mu)} \psi(x) .$$

Writing the operator X using the explicit form of the γ matrices leads to

$$\mathfrak{D}(\mu) = \begin{pmatrix} M_0 \mathbb{1} & +\imath \sigma_i D_i + D_4 - \mu \\ -\imath \sigma_i D_i + D_4 - \mu & M_0 \mathbb{1} \end{pmatrix} \equiv \begin{pmatrix} M_0 & -\mu \\ -\mu & M_0 \end{pmatrix} + \begin{pmatrix} \mathbb{0} & \imath X \\ \imath X^\dagger & \mathbb{0} \end{pmatrix} ,$$

where $X \equiv \sigma_i D_i - \imath D_4$. Clearly, the operator $\mathfrak{D}$ is the sum of two terms, one hermitian and one anti-hermitian. Therefore, in general, its eigenvalues are complex and its determinant is complex as well. The Reader not completely new to the topic could be at this point a bit confused, because, in the $\mu = 0$ case, the operator $\mathfrak{D}$ is known to have a real determinant, despite the fact that it is still the sum of a hermitian term and an anti-hermitian one. Indeed, there is no contradiction here. In absence of a chemical potential, the operator $\mathfrak{D}$ is γ_5-hermitian,

$$\gamma_5 \, \mathfrak{D} \, \gamma_5 = \mathfrak{D}^\dagger ,$$

---

[34]Clearly, the γ matrices are 4×4 matrices, but in the most used representations they can be written in a block form using the Pauli matrices and the identity matrix.

and this implies that its eigenvalues are either real or come in pairs of complex conjugated numbers[35]. Consequently, γ_5-hermiticity implies the reality of the determinant and this is what happens in the $\mu = 0$ case. It is worth remarking that in general, if an operator is not γ_5-hermitian, it could still have a real determinant.

To be more specific, it should be also considered that the operator $\mathfrak{D}$ depends on the gauge field and that different values of it give different results for the determinant. What said so far proves, on one hand, that such a determinant is in general complex. On the other hand, we can say something more coming back to the partition function of Eq. (1.56). Integrating out the fermionic fields leads to

$$\mathcal{Z} = \mathrm{Tr}\big(e^{-(\mathcal{H}-\mu Q)/T}\big) = \int \mathcal{D}A \, \det \mathfrak{D} \, e^{-\mathcal{S}_g} \ .$$

The right hand side of this equation can be thought as an ensemble average of $\det \mathfrak{D}$, where each weight is given once the gauge field is fixed. Since the partition function is real, such an average must be real as well. Therefore, any complex part of the determinant must cancel in the average procedure. Going back to the starting point of the path integral formulation of the theory, we have that the $\mathcal{Z}$ can also be written as

$$\mathcal{Z} = \sum_{\{u_i\}} \langle u_1 | \, e^{-\delta\,(\mathcal{H}-\mu Q)} \, | u_2 \rangle \ldots \langle u_{n-1} | \, e^{-\delta\,(\mathcal{H}-\mu Q)} \, | u_1 \rangle \equiv \sum_{\{u_i\}} \mathcal{P}(u) \ , \qquad (1.62)$$

where $\{|u_i\rangle\}$ is a complete basis and $\delta = (n\,T)^{-1}$. What said before about $\det \mathfrak{D}$ translates here to the statement that $\mathcal{P}(u)$ is in general complex, but the sum over u is in the end real. Writing $\mathcal{Z}$ as in Eq. (1.62), it should be clear that whether $\mathcal{P}(u)$ is real or complex depends on the choice of the basis $\{|u_i\rangle\}$. If we were able to choose a basis of eigenstates of the operator $\mathcal{H} - \mu Q$, $\mathcal{P}(u)$ would be real, but we would also have solved any problem exactly.

Beyond what said so far, we should emphasise that in presence of non-zero chemical potential, a finite imaginary part of the $\det \mathfrak{D}$ is actually needed for physical reasons. In fact, it can be shown [43] that the free energy of a quark q or of an anti-quark $\bar{q}$ in a plasma is given by

$$e^{-(F_q - F_0)/T} = \left| \left\langle \Re(\mathrm{Tr}\,L)\,\Re(\det \mathfrak{D}) - \Im(\mathrm{Tr}\,L)\,\Im(\det \mathfrak{D}) \right\rangle_g \right|$$
$$e^{-(F_{\bar{q}} - F_0)/T} = \left| \left\langle \Re(\mathrm{Tr}\,L)\,\Re(\det \mathfrak{D}) + \Im(\mathrm{Tr}\,L)\,\Im(\det \mathfrak{D}) \right\rangle_g \right|$$
$$\text{where} \quad \langle \mathcal{O} \rangle_g = \frac{1}{\mathcal{Z}} \int \mathcal{D}A \, \mathcal{O} \, e^{-\mathcal{S}_g} \ .$$

Here, L denotes the Polyakov loop, which will be defined in §1.9 and whose meaning is not important for the moment. If $\Im(\det \mathfrak{D})$ was zero for any value of the gauge field in presence of a chemical potential, namely in presence of a net baryon number, it would cost the same amount of energy to add to the plasma a quark or an anti-quark and this is in contradiction with the $\mu \neq 0$ condition.

To summarise, in absence of a chemical potential, the determinant of the Dirac operator in the fermionic part of the action is real, while it becomes complex if $\mu \neq 0$. Even though this could seem a harmless property, it is indeed a true disaster since it prevents a big class of numeric techniques from being applied. People refer to this fact as "sign problem", even though it is nothing that can be avoided[36]. We will come back later in the thesis to this aspect of QCD and it will be clear why a complex determinant of the Dirac operator is a big disadvantage. For the moment, then, it is better to postpone any further comment (the impatient Reader can find a sort of continuation of this discussion in §2.3 and then in chapter 3).

---

[35] In order to prove this, it is sufficient to calculate the characteristic polynomial of the operator,

$$P(\lambda) = \det\big[\mathfrak{D} - \lambda \mathbb{1}\big] = \det\big[\gamma_5^2(\mathfrak{D} - \lambda \mathbb{1})\big] = \det\big[\gamma_5(\mathfrak{D} - \lambda \mathbb{1})\gamma_5\big] = \det\big[\mathfrak{D}^\dagger - \lambda \mathbb{1}\big] = \det\big[\mathfrak{D} - \lambda^\star \mathbb{1}\big]^\star = P(\lambda^\star)^\star \ ,$$

and remember that zeros of it are eigenvalues of $\mathfrak{D}$.

[36] Generally, people call solution of the sign problem a numeric technique that allows to calculate observables as it is done via standard techniques in the $\mu = 0$ case.

§ 1.9   The centre symmetry

To conclude this chapter, let us explore another symmetry of the partition function of QCD that we did not mention so far and that will play a key role in the rest of this thesis. Such a symmetry – known as *centre symmetry* or as *Z_N-symmetry* – is present only when fermions are not considered (or, that is the same, when they are infinitely heavy) and whenever the temporal direction is compact[37]. We know that the latter condition is always fulfilled on the lattice. Let then suppose for the moment that $M_f \to \infty$; we will release this hypothesis in the end of the section. As discussed in §1.7, the gauge fields are periodic in the time direction,

$$U_\mu(\vec{n}, n_t + N_t) \;=\; U_\mu(\vec{n}, n_t) \;. \tag{1.63}$$

From §1.5, instead, we have that the action is invariant under $SU(N)$ gauge transformation if the links transform properly, in formulae

$$\mathcal{S}'_g = \mathcal{S}_g \quad \Leftrightarrow \quad U_\mu(n) \;\to\; U'_\mu(n) \;=\; G(n) \cdot U_\mu(n) \cdot G^{-1}(n + \hat{\mu}) \;, \tag{1.64}$$

with $G(n) \in SU(N)$. Remember that, whenever not differently stated, a multi-index notation is used to locate a point on the lattice, $n \equiv (n_x, n_y, n_z, n_t) = (\vec{n}, n_t)$. Supposing that

$$G(\vec{n}, n_t + N_t) \;=\; G(\vec{n}, n_t) \tag{1.65}$$

and making use of Eqs. (1.63) and (1.64), it is possible to show that the periodicity requirement also holds on the transformed gauge fields,

$$U'_\mu(\vec{n}, n_t + N_t) \;=\; G(\vec{n}, n_t + N_t) \cdot U_\mu(\vec{n}, n_t + N_t) \cdot G^{-1}\big((\vec{n}, n_t + N_t) + \hat{\mu}\big) \;=$$
$$=\; G(\vec{n}, n_t) \cdot U_\mu(n) \cdot G^{-1}\big((\vec{n}, n_t) + \hat{\mu}\big) \;=\; U'_\mu(\vec{n}, n_t) \;,$$

as it should be. Nevertheless, that in Eq. (1.65) is not the most general choice. In principle, wrapping around the lattice, the $SU(N)$ element $G(n)$ could pick up a factor and be mapped into another group element,

$$G(\vec{n}, n_t + N_t) = H \cdot G(\vec{n}, n_t) \qquad \text{with} \qquad H \in SU(N) \;. \tag{1.66}$$

Of course, the periodicity requirement on the gauge field ensures the Bose-Einstein statistics and cannot be spoiled by a gauge transformation. This means that H cannot be a general element of $SU(N)$. It is easy to show that it has to belong to the centre of the gauge group[38]. In fact,

$$U'_\mu(\vec{n}, n_t + N_t) \;=\; G(\vec{n}, n_t + N_t) \cdot U_\mu(\vec{n}, n_t + N_t) \cdot G^{-1}\big((\vec{n}, n_t + N_t) + \hat{\mu}\big) \;=$$
$$=\; H \cdot G(\vec{n}, n_t) \cdot U_\mu(n) \cdot G^{-1}\big((\vec{n}, n_t) + \hat{\mu}\big) \cdot H^{-1} \;=$$
$$=\; H \cdot U'_\mu(\vec{n}, n_t) \cdot H^{-1} \stackrel{!}{=} U'_\mu(\vec{n}, n_t) \;,$$

and the last equality is fulfilled if and only if $U(n)$ and H commute – i.e. $H \in Z\big(SU(N)\big)$. The centre of $SU(N)$ can be shown to be isomorphic to the cyclic group Z_N, whose elements are

$$H = h\mathbb{1} \qquad \text{with} \qquad h = e^{i\frac{2\pi k}{N}} \qquad \text{where} \qquad k \in \{0, 1, \dots, N-1\} \;. \tag{1.67}$$

For $k = 0$, Eq. (1.66) reduces to Eq. (1.65). We will call such a transformation *topologically trivial*. Values of k different from zero will define *topologically non-trivial* gauge transformations. At finite temperature, the pure gauge theory action is symmetric under this latter class of transformations.

---

[37]It is frequent to refer to this situation as *finite temperature pure gauge theory* or as *finite temperature Yang-Mills theory*.

[38]The centre of a group G is denoted by $Z(G)$ and is defined as $Z(G) = \{h \in G \mid \forall g \in G, h \cdot g = g \cdot h\}$.

Sometimes people use a different nomenclature. They consider as gauge transformation only the topologically trivial ones and call *centre transformation* the map of a link configuration into another that is identical to the initial one except for a given time slice $n_t = \bar{n}_t$ where the links in time direction are multiplied by the same element of the centre group Z_N. Indeed, a centre transformation defined in this way is nothing but a gauge transformation with

$$G(\vec{n}, \bar{n}_t) = H \qquad \text{and} \qquad G(\vec{n}, n_t) = \mathbb{1} \qquad \text{if} \qquad n_t \neq \bar{n}_t \; .$$

Therefore, what we called topologically non-trivial gauge transformation is the composition of a topologically trivial transformation with a centre transformation. We will use indistinctly all the above terms; just consider the gauge transformation to be trivial if not differently said.

To find out why the centre symmetry is an important symmetry of the theory, let us try to find an observable directly connected to it. In §1.5 we learnt that gauge invariant observables, in absence of fermions, are built of traced loops of links on the lattice. Intuitively, we have to consider a loop that winds at least once around the temporal boundary in order to be sensitive to it. The simplest is the so-called *Polyakov loop* as well as *thermal Wilson line*, which is defined as the product of all the links in the temporal direction at a given spatial site,

$$L(\vec{n}) \equiv \frac{1}{N_c} \prod_{n_t=1}^{N_t} U_4(\vec{n}, n_t) \; . \tag{1.68}$$

Let us see how its (colour) trace transforms under topologically trivial and non-trivial transformations. Keeping a general centre element H, we have

$$\text{Tr}\, L'(\vec{n}) = \frac{1}{N_c} \text{Tr}\left[\prod_{n_t=1}^{N_t} U'_4(\vec{n}, n_t) \right] =$$
$$= \frac{1}{N_c} \text{Tr}\Big[G(\vec{n}, 1) \cdot U_4(\vec{n}, 1) \cdot G^{-1}(\vec{n}, 2) \cdot$$
$$\cdot\, G(\vec{n}, 2) \cdot U_4(\vec{n}, 2) \cdot G^{-1}(\vec{n}, 3) \,\cdot \ldots \cdot$$
$$\cdot\, G(\vec{n}, N_t) \cdot U_4(\vec{n}, N_t) \cdot G^{-1}(\vec{n}, N_t + 1) \Big] =$$
$$= \frac{1}{N_c} \text{Tr}\Big[G(\vec{n}, 1) \cdot L(\vec{n}) \cdot G^{-1}(\vec{n}, 1) \cdot H^{-1} \Big] = h^\star \, \text{Tr}\, L(\vec{n}) \; ,$$

where in the last step the cyclic property of the trace has been used together with Eq. (1.67). Therefore, we obtain an invariance either if the gauge transformation is topologically trivial or if the traced Polyakov loop is zero.

In §1.8 we already met the traced Polyakov loop[39] and we anticipated that it gives the free energy difference between a Yang-Mills plasma with or without a static quark sitting at $\vec{n}$. To avoid any confusion, it is worth remarking that, even if we are considering a pure gauge theory, it is possible to introduce the creation and the annihilation operators $\hat{\psi}_A^\dagger(\vec{n}, n_t)$ and $\hat{\psi}_A(\vec{n}, n_t)$ of static (i.e. infinitely heavy) quarks with colour A at position $\vec{n}$. At the beginning of the Eighties, McLerran and Svetitsky [43] studied this theory, showing that the Polyakov loop corresponds to the propagator of a static quark and that

$$\left| \langle \text{Tr}\, L \rangle \right| = \frac{1}{\mathcal{Z}} \int \mathcal{D}U \; \text{Tr}\, L \, e^{-\mathcal{S}_g} = e^{-(F_q - F_0)/T} \; . \tag{1.69}$$

This relation, together to how the coupling is connected with the temperature, allows to show that QCD in the pure gauge limit has a non-analytic deconfinement phase transition. To prove this, it

---

[39] Often, people refer to the traced Polyakov loop simply as Polyakov loop. Sometimes the spatial average of the traced Polyakov loop is just called Polyakov loop. Even though the context should help to clarify which quantity is being considered, we will try to be as explicit as possible.

is enough to see what happens in the zero and infinite temperature limits. For $T \to 0$ we have a confining theory and an infinite amount of energy is needed to remove a quark from the plasma, $F_q = \infty$. Hence, $|\langle \text{Tr} \, L \rangle| = 0$. On the other hand, for $T \to \infty$, we know that the QCD exhibits asymptotic freedom. Said in an other way, the $T \to \infty$ and $\beta \to \infty$ limits are equivalent and the latter implies that the gauge coupling goes to zero. Therefore, in this limit, all the links become the identity and Eq. (1.68) implies that $|\langle \text{Tr} \, L \rangle| = 1$. Now, we found an observable that, in the confined phase of the theory, has a zero expectation value and that is invariant under centre transformations, while, in the deconfined phase, it takes non-zero values and is not any more symmetric. This is the typical behaviour of an order parameter that signals a spontaneous breaking of a symmetry. We conclude, then, what previously revealed.

To terminate this section, it is interesting to see what happens when we introduce dynamical quarks, namely when we release the infinite quark mass assumption. Again, from §1.7 we know that fermionic fields must fulfil antiperiodic boundary conditions in the temporal direction to guarantee the Pauli principle,

$$\hat{\psi}(\vec{n}, n_t + N_t) = -\hat{\psi}(\vec{n}, n_t) \ . \tag{1.70}$$

Plugging Eq. (1.66) in Eq. (1.70) leads to

$$\hat{\psi}'(\vec{n}, n_t + N_t) = G(\vec{n}, n_t + N_t) \cdot \hat{\psi}(\vec{n}, n_t + N_t) = -H \cdot G(\vec{n}, n_t) \cdot \hat{\psi}(\vec{n}, n_t) = -H \cdot \hat{\psi}'(\vec{n}, n_t) \ ,$$

which shows that the gauge-transformed fermionic field fulfils the correct boundary conditions if and only if $H = \mathbb{1}$. This means that the theory has no Z_N-symmetry if $\hat{M}_f < \infty$, because a centre transformation (with a non trivial centre element) would break the correct temporal boundary conditions for fermionic fields and, consequently, the Pauli principle would be lost. From the physical point of view, the presence of dynamical quarks and the phenomenon of string breaking maintains F_q finite and then $|\langle \text{Tr} \, L \rangle| \neq 0$ also in the confined phase. Strictly speaking, the Polyakov loop is not anymore a true order parameter to distinguish between the confined and the deconfined phases, which, in principle, could also be connected by a smooth crossover.

QCD phase diagram from the lattice **2**

«The greatest enemy of knowledge is not ignorance, it is the illusion of knowledge.»

— **Daniel J. Boorstin** —

Even though it has been one of the most active research topic in the last decades, QCD phase diagram studies are still at the beginning and many issues remain unsettled. Due to the presence of the sign problem at finite baryon density, LQCD does not provide, by now, an exact method to investigate in this region and most of conjectured results are based on effective models. Therefore, statements seem often stronger that they actually are and, strictly speaking, we are far from being able to draw conclusions.

In this chapter, after a general introduction and overview of the topic in §2.1, we will exclusively focus on the inputs that can come from LQCD. This implicitly means that we will never consider a system at real non-zero baryonic chemical potential. Already at $\mu_B = 0$, there are many long-standing problems difficult to be tackled, mainly because of their high numeric cost. In §2.2 the QCD phase structure in the $(m_{u,d}, m_s)$ plane will be discussed. §2.3 will be devoted to illustrate recent developments of LQCD at purely imaginary chemical potential, one of the possibilities to circumvent the sign problem, but also an indirect way to investigate $\mu = 0$ features. In particular, we will concentrate on which phase transitions a system at $\mu \equiv \mu_B/3 = \imath\,\mu_I$ undergoes and how their order depends on different parameters. As a natural conclusion, notions acquired in §2.2 and §2.3 will be combined in §2.4 to settle the background of this thesis project.

In all the chapter, we will try to consider and discuss many logically possible phase-diagram scenarios, that have not been ruled out by a priori arguments. Too fancy and unnatural possibilities will not be included, but we decided to partially ignore all those effective models that claim the existence of a particular type of phase transition. Clearly, this does not mean that we consider them wrong, we just do not include their outcomes in our overview. Also LQCD results not obtained in the continuum limit will be considered just as a hint in some direction, but they will not be used to rule out any scenario. The main advantage of this approach is that a broader overview of the subject can be given. Undoubtedly, in some cases, our discussion shall lack details and the Reader will feel like deepening more into the topic. In this regard, references to textbooks, reviews and articles will be provided all along the chapter.

§ 2.1 The conjectured QCD phase diagram

A nice and useful way to describe matter behaviour is using phase diagrams. In principle, considering a system at equilibrium, it is possible to investigate its properties varying some internal or external parameters. A phase diagram is a chart used to summarise the result of such a study,

Notation	Type	Description
	1st order	A first-order phase transition is characterised by the presence of a two-phases coexistence. They involve a latent heat that is connected to the jump of the order parameter, which is discontinuous at the transition. Typical examples are the phase transitions of water between the liquid and solid phase or between the liquid and vapour phase.
	2nd order Z_2 $O(4)$	In a second-order phase transition – also known as *continuous phase transition* – the order parameter does not show any discontinuity, but its first derivative does. They are characterised by a divergent susceptibility and an infinite correlation length. The ferromagnetic transition is an example.
	Triple point	A triple point refers to the special condition in which three phases of a system coexist. It is not hard to understand that this is possible only if three first-order lines meet in the same point. Many substances in nature show this behavior, like water at $273.16\,\text{K}$ and at $611.657\,\text{Pa}$.
	Quadruple point	A coexistence of four phases is referred to as quadruple point. In a system with only one component, it is not possible to have one.
	Tricritical point	By definition, a tricritical point is a point of a phase diagram at which a three-phase coexistence terminates. Since a first-order line always stops in a second-order point, it is easy to show that at a tricritical point a first order line meets a second order one. There are not trivial systems that have such a feature, but we will see that QCD has some.
(---)	Crossover	A crossover transition is not properly a phase transition. There is no not-analytic point in the partition function connected to it and the phases it separates are continuously connected. This is the reason why crossover lines are usually not drawn in phase diagrams. We will often stick to this rule. In those cases where, for the sake of clarity, a line is worth being drawn, a dashed notation will be used. The solid to liquid state phase transition of butter is a crossover.

Table 2.1: *Type of phase boundaries relevant for the QCD phase diagram. For second-order transitions we distinguished between two different universality classes.*

showing in which conditions thermodynamically distinct phases occur or coexist. It is, then, particularly useful to illustrate whether the system undergoes phase transitions and, in case, of which type they are. In general, there can be several parameters on which the system behaviour depends and, therefore, it could happen that more phase diagrams are needed to give a complete pictorial overview. Different regions usually correspond to different phases and they are separated by the so-called *phase boundaries* along which phase transitions occur. Phase boundaries can intersect or end in special points where the system shows particular features. It is common to choose a line or region style to identify a particular type of phase transition, but, unfortunately, there is no standard way to do so. Therefore, we decided to fix one and be coherent with it. For example, we will use different coloured solid lines to distinguish between different types of phase transition. In Table 2.1, the Reader can find our notation together with a recall of the meaning of each term.

In the spirit of the above discussion, since many decades by now, people have studied, both theoretically and experimentally, the hadronic matter from zero to very high temperature and baryon density with the common goal of understanding how the QCD phase diagram looks like. Unfortunately, the lack of an exact solution of the theory as well as the missing understanding of many phenomena related to strong interacting matter have brought only to few recognised features. Nowadays, the community agrees on the existence of three different regimes: the confined hadron matter at low temperature and low density, a colour super-conducting state at high density and low temperature and a quark gluon plasma at high temperature and high density. It is as well believed that, at the beginning of our universe life, matter underwent the transition from a quark gluon plasma state to the confined matter as known today.

QCD is a theory with many parameters and it is the typical example of a situation in which many phase diagrams can be drawn and are needed to give a complete overview. Just focusing on the three lightest quarks, we have 5 parameters that can be varied (the quark masses, the temperature and the density of the system). Of course, in nature, the masses of the quarks take precise values, but theoretically they can be changed and often, doing so, leads to good insight about the real situation. Nevertheless, any reasonable approximation is welcome to simplify the problem and, therefore, up and down quark are always considered degenerate, reducing then to 4 the number of parameters ($m_{u,d}$, m_s, T and the baryon chemical potential μ_B for the density). Often – and the same will be done in this section – the temperature and the baryon chemical potential are used as axes of a 2D phase diagram and many plots are drawn for different masses. Moreover, it is natural to start from the simplest cases, when $m_{u,d} = 0$ and $m_s = \infty$ or when $m_{u,d} = 0$ and $0 < m_s < \infty$ or when $m_{u,d} = 0$ and $m_s = 0$. To suppose in a first moment the up and down quark masses to be zero is reasonable since they are very light; of course, later this approximation should be released.

Given the existence of the three regimes described above, it is natural to ask ourselves whether there is a phase transition between different states and, in case, of which type. Unfortunately, LQCD has no access to the (T, μ_B) plane because of the sign problem and, then, any prediction has to rely on alternative approaches like, for example, effective models. It should never be forgotten though that, even if an effective model has the same symmetries of QCD and it can be argued that it belongs to the same universality class, its prediction will be valid only near critical points. The only a priori features of the QCD phase diagram that we can deduce are usually based on symmetry arguments.

Considering the complexity of the subject and the lack of exact methods, it is not hard to understand that the situation is not yet well established and that many questions remain open. Many conjectures have been done and, even if some features still have to be confirmed (or contradicted), it is worth reporting here the most common ones. In the following, we will briefly describe the main aspects without many details. This choice is due to the fact that there are nice reviews on the subject in the literature. We suggest [44–46] as general overviews; the last two focus more (but not only) on the high density part of the phase diagrams. The references therein should be more than enough to deepen into any aspect we will illustrate from here till the end of the section.
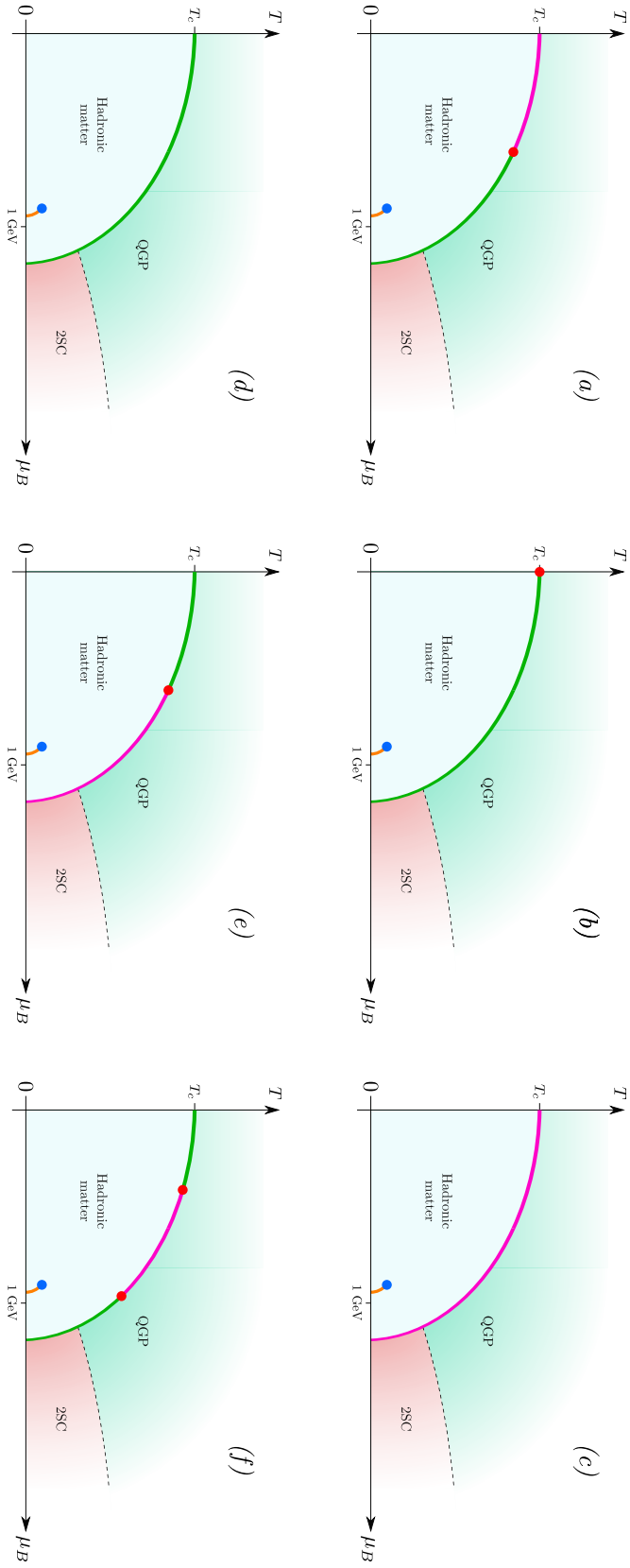
Figure 2.1: *Possible scenarios for the phase diagram of two-massless flavour QCD. Scenario (a) is the most common since in agreement with predictions of many effective models. Scenarios (b) to (f) are alternatives that have not been ruled out so far. Note that even fancier scenarios (e.g. with more tricritical points) could be drawn and they were not considered here. Refer to Table 2.1 for the colour conventions.*
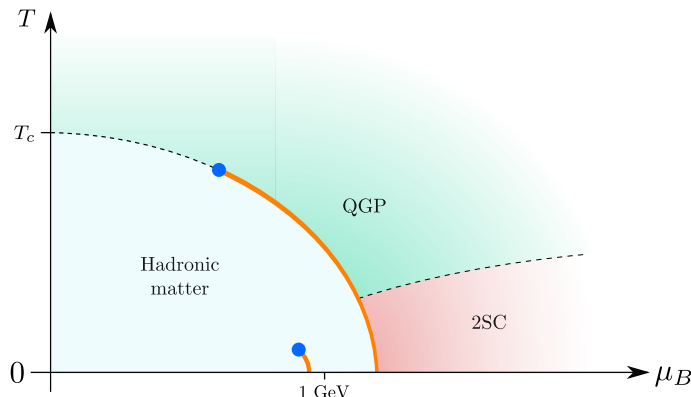
Figure 2.2: *Plausible scenario for the phase diagram of two flavour QCD with $m_{u,d} = m_{u,d}^{phys.}$. Refer to Table 2.1 for the colour conventions.*

When the mass of the strange quark is set to infinity, the QCD phase diagram for two degenerate massless flavours could look like in Figure 2.1(a). Even though at $\mu_B = 0$ the transition was marked to be second order, its type could be also first order triple[1]. Indeed, the only certain statement that can be done regards the existence of a phase transition. If the quarks are massless, the action is invariant under chiral transformations, but this symmetry is broken spontaneously at low temperatures. On the other hand, at high temperature, chiral symmetry is restored and, therefore, there must be a phase boundary, as always between thermodynamic states with different global symmetries. Alternative scenarios are possible and the situation remains unclear. We will discuss further this aspect for $\mu_B = 0$ in §2.2. At higher densities and zero temperature, hadronic matter enters the two-flavour colour superconducting phase (2SC) undergoing a phase transition that is believed to be first order[2] (triple). Since there cannot exist an isolated first-order triple point, this implies that a first-order triple line departs from the horizontal axis. Without considering too fancy hypotheses, this first-order triple line can meet the second-order line emerging from the vertical axis in a tricritical point or could extend towards the vertical axis ending on it. We decided to collect in Figures 2.1(b) to 2.1(f) some alternatives that do not take into account any effective model result and that, in principle, are still plausible. Varying the temperature at high values of the chemical potential brings the system from the 2SC phase to the quark gluon plasma phase or vice versa. A symmetry argument given in [45] at the end of §2 explains that there is no need for a true phase transition between these two phases. In Figures 2.1(a) to 2.1(f) there is another short phase boundary departing from the horizontal axis slightly before $\mu_B = 1\,\text{GeV}$. It is the so called *liquid-gas nuclear matter transition*. At small temperatures of order of few MeV, if the density is not high enough, nucleons do not bind and form a *gas*. Increasing μ_B leads to the formation of nuclei that can be considered as a *liquid*. At $T = 0$, Lorentz-boost symmetry is unbroken on the left (where no baryon is present and there is no preferred frame) and breaks going past the critical value of μ_B; thus, there must be a phase transition. At $T \neq 0$, such a symmetry is broken in both phases and then there is no need for a true phase transition and that is why this line terminates (at a temperature comparable with the binding energy of nucleons in nuclei).

When the massless approximation for the up and down quarks is released and their mass is set to the real value, the QCD phase diagram is not qualitatively too much different. The main aspect that changes is the phase boundary that separates the hadronic matter from the quark gluon plasma. In fact, since a mass term in the action breaks explicitly the chiral symmetry, the confined

---

[1]If there is a phase coexistence, it has to be a coexistence of three and not only two phases. In fact, the order parameter associated to the restoration of the chiral symmetry is the chiral condensate, which, at the critical temperature and/or density can be positive, negative or zero identifying then three different phases [47].

[2]Again, this statement is based on many effective models, but, strictly speaking, it could be still not true.

(a) $m_{u,d} = 0$ *and physical strange mass*

(b) *Physical quark masses*
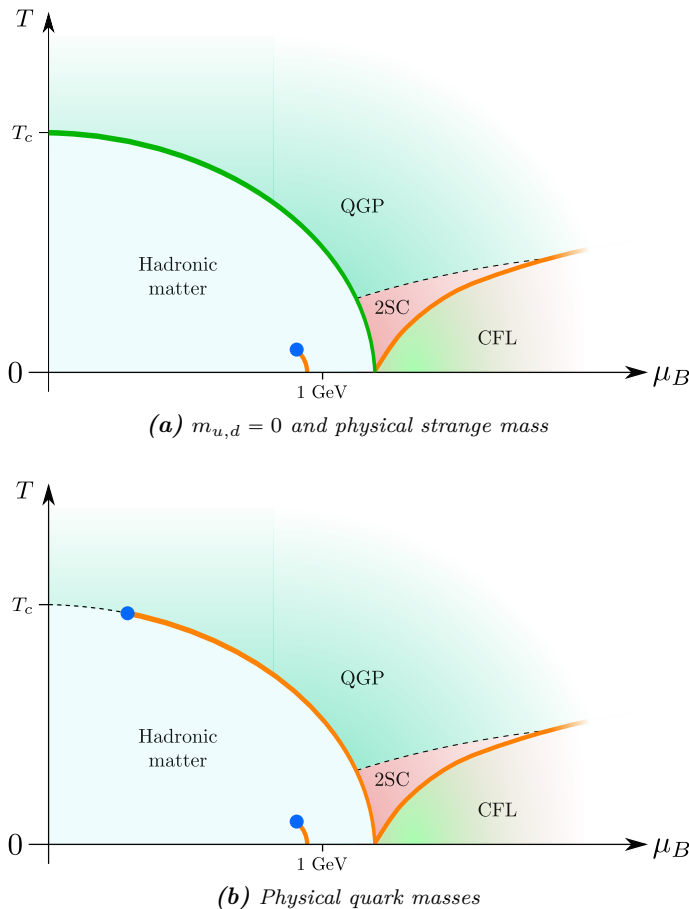
Figure 2.3: *Conjectured phase diagram for three-flavour QCD. Refer to Table 2.1 for the colour conventions.*

phase must be smoothly connected to the quark gluon plasma phase (i.e. there will be a crossover transition for some combination of the theory parameters). This is the case at small densities and for $\mu_B = 0$ it has been directly checked in the LQCD framework, where the value of T_c can be estimated and the type of transition identified. Indeed, there has been a long debate – also known as T_c *crisis* – between different collaborations, about the value of the critical temperature. Eventually it was settled [15] to be between 170 MeV and 150 MeV depending on the observable[3]. In Figure 2.2 we reported the most common scenario for the two-flavour QCD phase diagram. Again, this is only one possibility, for which much evidence exists.

The mass of the up and down quarks could be increased above the physical value – and this is usually done in LQCD simulations – but we will not discuss this case here. In §2.2, we will see how the type of the transition between hadronic matter and quark gluon plasma changes at zero density varying $m_{u,d}$.

To conclude this section, let us briefly say something about what happens introducing a non-infinitely heavy strange quark, keeping $m_{u,d} = 0$. Indeed, Alford addressed this problem exhaustively in 2001 and we refer to his work [45] for any detail. What it is worth saying here is

---

[3]In the crossover case, there is not a single value for the critical temperature, but rather an interval. Different observables can lead to different values for T_c. This, of course, was not the origin of the debate, where, instead, the complete temperature dependence of the same observable was not the same between different collaborations. For the curious Reader, the reason of the discrepancy turned out in the end to be due to lattice artefacts.

that the strange flavour makes a new phase appear in the phase diagram, known as *colour-flavour locked* (CFL) phase. It is always a colour superconducting phase, but the QCD flavour and colour symmetries are broken down to a global vector symmetry which transforms in the same way colour, left-handed and right-handed flavours. This is also the origin of the name: The colour degree of freedom has to be locked to the flavour one in order to have a symmetry of the theory. This phase is for sure entered at very high densities and, since it has different global symmetries than both the 2SC and the quark gluon plasma phases, there must be a true phase transition when leaving it. Strictly speaking, if the mass of the strange quark is bigger than the physical one, there could be also a $2SC + s$ phase, where the chiral symmetry is unbroken but the $U(1)_s$ rotation group of the strange quark breaks down. For $m_s = m_s^{\text{phys.}}$, though, it is believed not to be present and the conjectured phase diagram looks like that in Figure 2.3(a). Again, releasing the massless hypothesis for the up and down quarks brings to the same qualitative effect as in the two-flavour case. The only difference is that the presence of the strange quark makes the second-order endpoint move closer to the $\mu_B = 0$ axis, as it can be seen comparing Figure 2.3(b) to Figure 2.2.

§ 2.2 Lattice QCD at zero density: the Columbia plot

Finite temperature QCD at zero density is, nowadays, one of the main areas of lattice simulations, since the absence of the sign problem allows to use standard numeric approaches, some of which will be discussed in chapter 3. Leaving aside for the moment the techniques used to obtain any result, let us focus on the outcome of the recent LQCD investigations at $\mu_B = 0$. The phase structure is quite rich and, as we already explained in the previous section, it depends mainly on the masses of the quarks. A nice overview can be given using the so-called *Columbia plot* [48], which looks like in Figure 2.4. In it, the up and down quarks are considered to be degenerate and their mass together with the strange one are put on the axis, ranging from 0 to ∞. Different cases are possible (remember that an infinitely heavy quark decouples from the system):

- on the right axis, $m_{u,d} = \infty$, we have only one flavour ($N_f = 1$);

- on the upper axis, $m_s = \infty$, we have only two degenerate flavours ($N_f = 2$);

- on the bottom-left, upper-right diagonal we have three degenerate flavours ($N_f = 3$);

- any other point has different masses for the light and the strange quarks ($N_f = 2 + 1$).

The Columbia plot, strictly speaking, is not a phase diagram, since different regions in it do not refer to different phases of matter. For each point, using different notations, the type of the transition which the system undergoes increasing the temperature is represented. The deconfinement and the chiral transitions are then here combined, even though they should not be confused. In fact, it is known that the Polyakov loop and the chiral condensate are true order parameters for the deconfinement and for the chiral transitions *only* if quarks are infinitely heavy or massless, respectively. A finite quark mass will break both the centre symmetry and the chiral symmetry explicitly, weakening any phase transition present in the limiting case[4]. This is the reason why, for example, moving along the $N_f = 3$ line, the first-order regions in the corners are separated by a crossover interval. Keeping this in mind, in the Columbia plot, we will call *chiral region* the (lower) left part and *deconfinement region* the (upper) right part. In principle, it would be possible to add a third axis for the temperature, having hadronic matter and quark gluon plasma below and above the critical temperature, respectively. Usually, this is not done because the information that would be added can be understood without ambiguity. Moreover, the third axis can be then reserved for another parameter, as will be done in §2.4.

---

[4]Remember that an explicit symmetry breaking weakens any phase transition present in the symmetric case. Since, usually, the symmetry is broken by a continuous parameter that can be arbitrarily small (as the quark mass in our case), a first-order transition remains if the symmetry is not too much explicitly broken, while a second-order one immediately disappears. Clearly, varying the breaking parameter also a first-order phase transition will eventually go away.
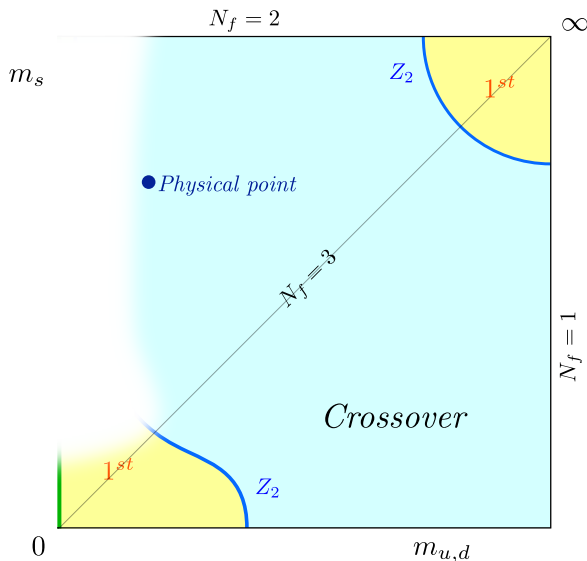
Figure 2.4: *The Columbia plot. Only features that were **directly** measured on (coarse) lattices have been drawn. The order of the phase transition in the two-flavour massless limit is still under debate and, therefore, the structure on the left part of the plot remains unclear. Even though from indirect measurements on coarse lattices it has been found to be first order, cut-off effects are still too big to draw any conclusion.*

Already more than ten years ago the picture reported in Figure 2.4 had been outlined. The Reader who would like to have more detailed information can rely on many reviews available in the literature; we suggest [49] and the references therein. Many efforts have been done to give to the Columbia plot a quantitative structure. For example, the existence of first-order transitions in the deconfined and in the chiral regions have been numerically verified and the Z_2 critical masses on the $N_f = 3$ line have been found. Unfortunately, due to the extremely high numeric cost of any investigation, all studies have been carried out for many years on coarse lattices, typically with $N_t = 4$. Only more recently, results closer to the continuum have been obtained, but it is still early for any conclusion. Moreover, in §1.7 we learnt that the lattice extents should be such that $1 \ll N_t \ll N_s$, but this is never the case in practice. Therefore, it should be clear that systematic errors (e.g. cut-off effects) are still not negligible and it could happen that future investigations lead to some changes. For example, the position of the Z_2 lines is expected to change approaching the continuum limit, i.e. locating them on finer and finer lattices will give different outcomes, reaching some unique value for $a \approx 0$. This is due to cut-off effects that are different if a varies. To motivate this statement further, but indeed only to give an idea without pretending to make a quantitative discussion, the following argument can be given. In the Columbia plot, the masses considered as parameters are the bare ones of the light and the strange quarks, but, theoretically, in order to mark the boundaries of the first order regions, it would be possible to use renormalised ones (of the quarks or of a particle which can be extracted from lattice simulations). Now, let us consider a Z_2 point; it will separate a first-order region from a crossover one. In the continuum limit, its position is unique, say at $m_c^{\text{cont.}}$. When the critical mass is measured on the lattice, cut-off effects will affect its value and we will have, in general,

$$m_c^{\text{latt.}}(a) = m_c^{\text{cont.}} + \sum_{k=1}^{\infty} c_k \, a^k \, ,$$

where the coefficients c_k are unknown. The smaller a is, the more terms in the series can be

neglected. When the lattice spacing is small enough to keep only the linear term,

$$m_c^{\text{latt.}}(a) = m_c^{\text{cont.}} + c_1\, a \; , \tag{2.1}$$

we can have two scenarios, depending on the sign of c_1 $(a_1 < a_2 < a_3)$,
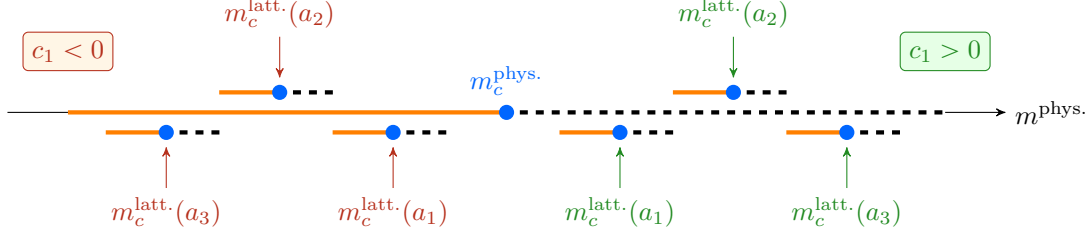
and this means that the first-order region can expand or shrink going from coarser to finer lattices. Obviously, if the lattice spacing is not small enough to neglect corrections higher than linear to the continuum result, then the critical values found on the lattice may not converge monotonically to the physical one and, even if they do, it will be too early for any extrapolation. The sign of c_1 is hard to be predicted a priori in general and it could change considering different observables. To get a hint – and nothing more, since there are many caveats to the following argument – we could calculate the dispersion relation as pole of the propagator in the free theory on the lattice. Of course this calculation is, then, formulation dependent. For example, using the Wilson fermion propagator of Eq. (1.19a) at page 12, we can look for the zeros of the denominator, expanding for small a. Calling the bare mass simply m_q, we have

$$\left[m_q + \frac{2r}{a} \sum_{\mu=1}^{4} \sin^2\!\left(\frac{p_\mu a}{2}\right) \right]^2 + \sum_{\mu=1}^{4} \frac{1}{a^2} \sin^2(p_\mu a) =$$

$$= \left[m_q + \frac{2r}{a} \sum_{\mu=1}^{4} \left(\frac{p_\mu a}{2} + \mathcal{O}(a^3)\right)^2 \right]^2 + \sum_{\mu=1}^{4} \frac{1}{a^2} \left(p_\mu a + \mathcal{O}(a^3)\right)^2 = m_q^2 + r\, m_q\, a\, p^2 + p^2 + \mathcal{O}(a^2) \overset{!}{=} 0 \; ,$$

where we have defined $p^2 \equiv \sum_{\mu=1}^{4} p_\mu^2$. Solving with respect to p leads to the dispersion relation, which gives the physical mass of the particle[5],

$$m_q^{\text{cont.}} = m_q - \frac{1}{2}\, r\, m_q^2\, a + \mathcal{O}(a^2) \; ,$$

that has to be compared to Eq. (2.1). Paying attention to the fact that now $m^{\text{cont.}}$ is at the left hand side, we can say that c_1 could be positive and the scenario in which we reach the continuum Z_2 point from the right could be the real one. This would imply that on finer lattices the deconfinement first-order region enlarges, while the chiral one shrinks[6]. Indeed, this behaviour has already been detected at both Z_2 boundaries in the Columbia plot (see e.g. [50–52]).

The attentive Reader could wonder why the left edge of Figure 2.4 has been drawn as triple line. Thinking of the chiral symmetry, it should be easy to be explained. Since the light quarks are massless, there are three coexisting phases at the critical temperature: one in which the chiral symmetry is restored, $\langle \bar{\psi}\psi \rangle = 0$, and two where it is broken, distinguished by the positive or negative value of the chiral condensate [47]. Obviously, in the bottom edge, the chiral region does not end in a triple line and there is no tricritical point because only the strange quark is

---

[5]Here, the adjective *physical* is used only for comparison with the previous expressions. No renormalisation has been done and the free case has been considered. As already stressed, we want to get only an idea.

[6]There is no reason why c_1 should have different sign in the chiral region with respect to the deconfinement one. Therefore, both Z_2 boundaries will move towards either smaller or higher masses.

(a) Classic first-order scenario

(b) Standard second-order scenario

(c) *Fancier first-order scenario*

(d) *Alternative second-order scenario*
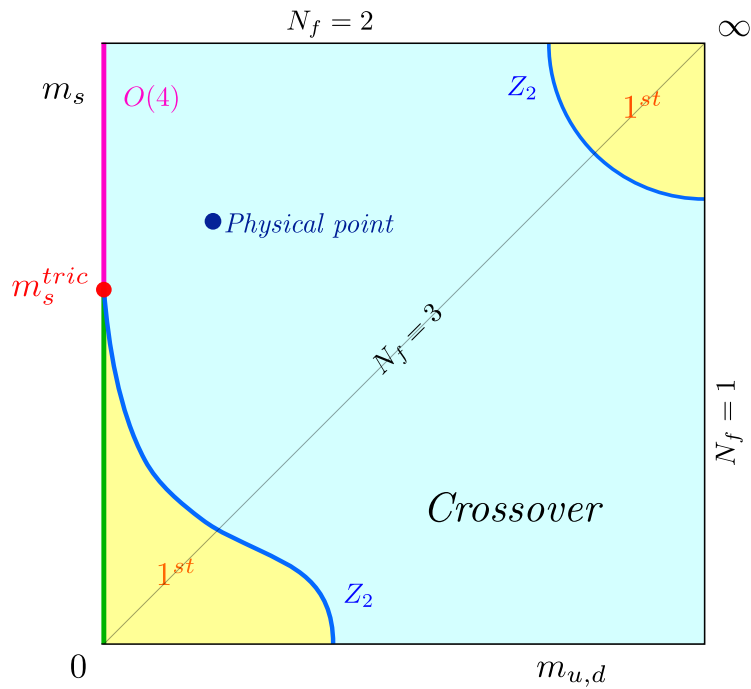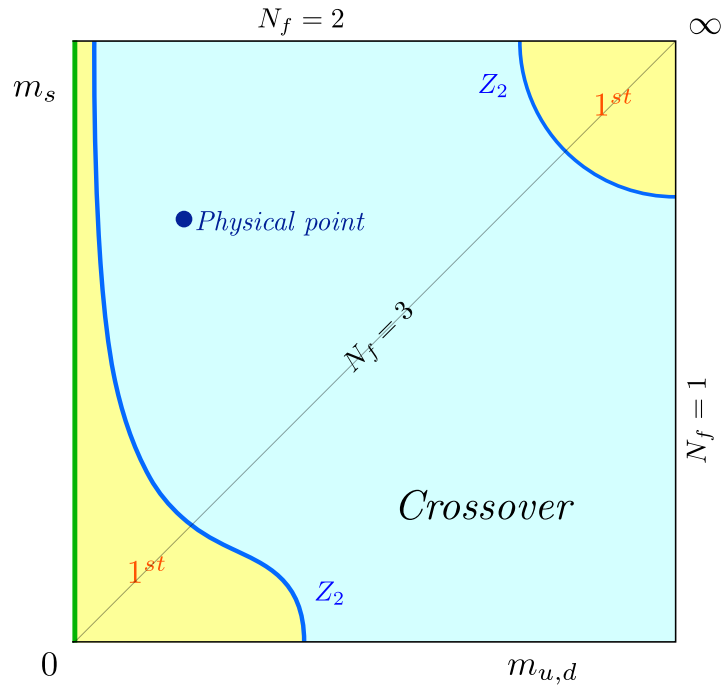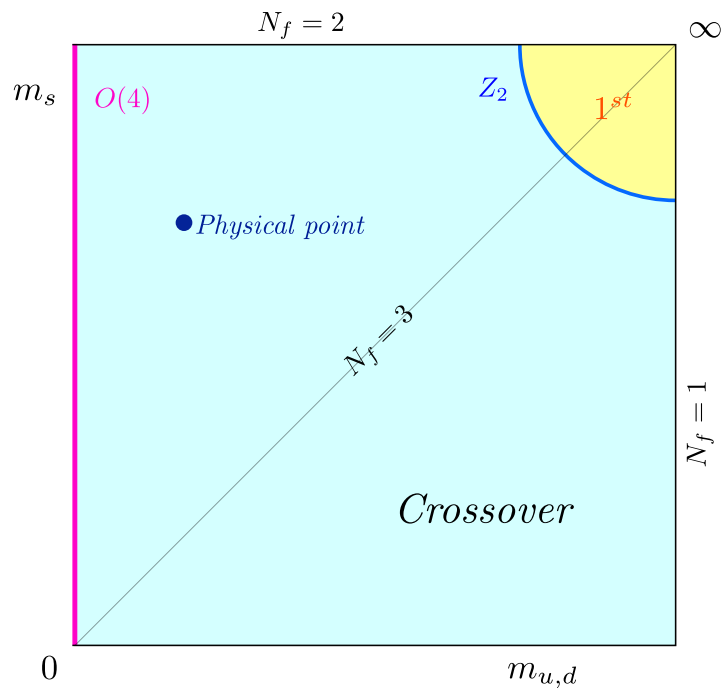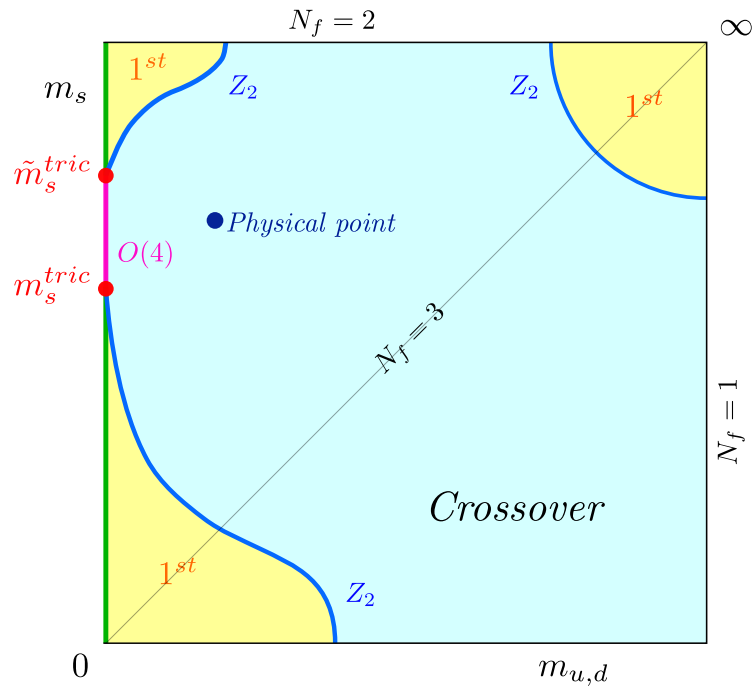
Figure 2.5: *The order of the chiral transition in $N_f = 2$ and $N_f = 3$ QCD is still under debate and many scenarios are still possible. Moreover, it remains unclear how the first-order regions change (if they do not disappear at all) as the $a \rightarrow 0$ limit is taken. Here the main alternatives for the continuum Columbia plot are sketched.*

massless and there is no chiral symmetry with only one flavour (this is also the reason why there is not a first-order region in the lower-right corner of the Columbia plot). Regarding, instead, the white cloud covering the upper-left part of the plot, it is meant to stress that, there, the situation remains unclear. Indeed, the order of the chiral transition in the $N_f = 2$ massless limit is a very long-standing issue that has been debated for more than thirty years by now. There are mainly two scenarios: either the $U_A(1)$ axial symmetry is still broken at the critical temperature and, then, the only symmetry that is restored is

$$SU_L(2) \times SU_R(2) \simeq O(4) \,,$$

or the axial symmetry is restored (or only weakly broken) and the restored symmetry is

$$U_L(2) \times U_R(2) \simeq U_{R+L}(4) \,.$$

In the first case, we would have an $O(4)$ second order point in the upper-left corner of the Columbia plot (with a $O(4)$ line on the left edge) and the first-order chiral region should terminate somewhere in a tricritical point, $m_s^{\mathrm{tric.}}$, as drawn in Figure 2.5(b). In the second case, instead, the chiral Z_2 line would extend until touching the upper edge of the plot at a non-zero value of the light quark mass, as drawn in Figure 2.5(a). These possibilities are related to the various scenarios for the phase diagram of two-massless flavour QCD presented in Figure 2.1. Basically, Figures 2.1(a) and 2.1(c) are connected to Figure 2.5(b), while Figures 2.1(d) to 2.1(f) reflects Figure 2.5(a). Figure 2.1(b), instead, is by far more exotic[7] and it would imply the chiral Z_2 line ending exactly in the upper-left corner with $m_s^{\mathrm{tric.}} = \infty$. The position of this tricritical point, if present, is especially important with respect to the physical point, since knowing it would help in taking the chiral limit at physical quark mass values (refer to [54] for more details). Actually, taking the chiral limit for the light quarks at the physical strange quark mass and looking at scaling properties of some observables has been exactly the strategy of some recent work of the Bielefeld-BNL-CCNU collaboration [55]. Their outcome is that there is no evidence for a Z_2 point moving horizontally in the Columbia plot from the physical point towards the left edge. On the contrary, they claim that, for small quark masses, $O(4)$ scaling is seen. Strictly speaking, this result has to be taken with a pinch of salt. The continuum limit should be taken before taking the chiral limit and to reverse this order could lead to wrong conclusions[8]. Moreover, this study has been done with staggered fermions only and, therefore, it would be good to have a cross-check using a different formulation. Nevertheless, if confirmed, it would rule out the scenario reported in Figure 2.5(a), since the point on the left edge of the Columbia plot at the physical strange quark mass should be a $O(4)$ point. Strictly speaking, ruling out the existence of a unique first-order region in the chiral limit, extending from the lower-left corner to the upper-left, does not exclude the possibility that the phase transition is first order in the $N_f = 2$ and $N_f = 3$ massless limits. In fact, as depicted in Figure 2.5(c), there could be two disconnected first-order regions separated by a $O(4)$ line. This bizarre situation – which would also imply the existence of *two* tricritical points on the left edge of the Columbia plot – is exactly what is observed on coarse lattices, if we put together the outcome of the scaling investigation at the physical strange quark mass and the fact that Z_2 points have been found in the $N_f = 2$ and $N_f = 3$ chiral regions[9]. The ultimate question which remains without an answer regards the continuum limit. Which is the correct scenario on finer lattices? Do any of the first-order chiral regions disappear? If both do, then a further scenario is possible: The left edge of the Columbia plot could be simply an $O(4)$ line and, in this case, no tricritical point would be present. Clearly, the problem is still open and only future investigations can settle this issue.

---

[7]Depending on the strength of the anomaly, even different scenarios are allowed [53].

[8]Decreasing the quark bare mass at finite lattice spacing, unphysical phases (e.g. the Aoki phase with Wilson fermions) could be entered and a later continuum extrapolation would result in erroneous conclusions. With rooted staggered fermions, the continuum limit should be taken in first place, since the correctness of the rooting trick fully relies on it, as discussed in appendix B.

[9]In the two flavour case, a Z_2 point in the massless limit has not been directly observed, but only indirectly found [56]. We will discuss the strategy of such a measurement in §2.4.

It is also important to observe that, despite how it has been drawn in Figures 2.4 and 2.5, the shape of the chiral Z_2 line for small values of the strange quark mass is not known. Said in other words, numerically, it has never been verified that there is a change of concavity in this line (it has been partially mapped out on coarse lattices [57, 58], but not far below the $N_f = 3$ diagonal).

To conclude this section, let us spend some more words about the connection between the Columbia plot and the QCD phase diagram in the (T, μ_B) plane at the physical point. In Figure 2.3(b) the most common scenario of the latter has been drawn. In it, at zero density, the transition at $T = T_c$ is a crossover and this is connected to the position in the Columbia plot of the physical point, that seems to be in the crossover region [52]. Now, if we consider Figure 2.4 and we add a third axis on which we put the baryonic chemical potential, it is possible to sit at the physical point and move vertically increasing the density. This would mean to move along the crossover line in Figure 2.3(b) from left to right. If the conjectured scenario in the (T, μ_B) plane is correct, a first-order region should be entered through a Z_2 point – the so-called QCD *critical endpoint*. Adding a third axis to the Columbia plot, the Z_2 lines would become critical surfaces and, naïvely, it could be guessed that the chiral one bends toward the physical point and it is exactly what is met moving up from the $\mu = 0$ plane. Even though this argument sounds reasonable, it does not seem to be the case [59]. Since in the literature there are many articles and reviews on this topic – e.g. [60] – we will not discuss it further here.

§ 2.3 The QCD phase diagram at purely imaginary chemical potential

From the overview given in §2.1, it should be clear that the knowledge of the QCD phase diagram is still incomplete, despite the fact that people have been studying it for many decades. This is mainly due to the lack of an a priori method to tackle the problem. In fact, the standard lattice approach cannot be applied when $\mu_B \neq 0$ and this limits substantially our possibilities. In chapter 3 we will illustrate in detail how the main standard numerical techniques work and it will be clear that a real chemical potential breaks them down. However, it is possible to give now the basic idea. On one hand, according to the analysis made in §1.8, we know that the introduction of μ_B on the lattice makes the determinant of the Dirac operator complex. On the other hand, with the path integral notation, it is possible to write the expectation value of any observable as

$$\langle \mathcal{O} \rangle = \frac{\int \mathcal{D}U \, \mathcal{D}\bar{\psi} \, \mathcal{D}\psi \, \mathcal{O}[U] \, e^{-\mathcal{S}}}{\int \mathcal{D}U \, \mathcal{D}\bar{\psi} \, \mathcal{D}\psi \, e^{-\mathcal{S}}} = \frac{\int \mathcal{D}U \, \mathcal{O}[U] \, \det \mathfrak{D} \, e^{-\mathcal{S}_g}}{\int \mathcal{D}U \, \det \mathfrak{D} \, e^{-\mathcal{S}_g}} \equiv \frac{1}{\mathcal{Z}} \int \mathcal{D}U \, \mathcal{O}[U] \, \det \mathfrak{D} \, e^{-\mathcal{S}_g} \, ,$$

where, in the second step, the integration over the Grassmann variables ψ and $\bar{\psi}$ has been carried out (this is possible only if the observable does not depend on the fermionic fields, as usually the case). As long as $\mathcal{P}(U) \equiv \mathcal{Z}^{-1} \det \mathfrak{D} \exp(-\mathcal{S}_G)$ is real and not negative, it can be interpreted as probability distribution and it is possible, using some dedicated algorithm, to extract configurations according to it, evaluating in the end $\langle \mathcal{O} \rangle$ as an arithmetic average. Obviously, this is not possible if $\det \mathfrak{D} \in \mathbb{C}$ and in this case the theory is said to suffer from the so-called *sign problem*. Since the end of the Eighties, many alternative methods to circumvent it have been developed. Even if it would be interesting to go through each of them discussing advantages and limitations, we will focus here only on the imaginary chemical potential technique, which has been applied in this thesis. This choice is reasonable because many standard books on the topic – as well as general LQCD reviews – discuss all these techniques. As starting point, the interested Reader could refer to §12.3 of [19] and to the references therein.

We know from §1.8 that, if the Dirac operator $\mathfrak{D}$ is γ_5-hermitian,

$$\gamma_5 \, \mathfrak{D} \, \gamma_5 = \mathfrak{D}^\dagger$$

then its determinant is real. This is the case in most lattice fermionic formulations, if $\mu = 0$. Using this property in presence of a chemical potential (thought as a general complex number) leads to

$$\gamma_5 \left(\mathfrak{D} - \gamma_4\,\mu \right) \gamma_5 = \mathfrak{D}^\dagger - \gamma_5\,\gamma_4\,\mu\,\gamma_5 = \left(\mathfrak{D} + \gamma_4\,\mu^\star \right)^\dagger ,$$

where in the last step we used the fact that γ_4 is hermitian and anti-commutes with γ_5. For the determinant this equation becomes

$$\det(\mathfrak{D} - \gamma_4\,\mu) = \det{}^\star(\mathfrak{D} + \gamma_4\,\mu^\star) .$$

Immediately, we can infer that

$$\det(\mathfrak{D} - \gamma_4\,\mu) \in \mathbb{R} \qquad \Leftrightarrow \qquad \mu = \imath\,\mu_I . \tag{2.2}$$

This means that QCD at purely imaginary chemical potential is free from the sign problem and standard numeric techniques can be applied. But what do we gain in this way? How is it, then, possible to extract information about the physical QCD phase diagram? Clearly, the chemical potential is a physical quantity and it is real. To make it complex is just a technical, convenient trick and there is no deeper meaning behind it[10]. However, this allows us to study the functional dependence of any observable on μ_I and, writing down its Taylor expansion

$$\langle \mathcal{O} \rangle(\mu_I) = \sum_{k=1}^{\infty} c_k \left(\frac{\mu_I}{T} \right)^k , \tag{2.3}$$

we can understand up to which order the series has to be considered to well represent the observable at the left hand side. It is worth remarking that $\langle \mathcal{O} \rangle(\mu_I)$ is the outcome of LQCD simulations and can, in principle, be evaluated with high accuracy. Performing the analytic continuation $\mu_I \to -\imath\,\mu_I$ in the truncated series will give the behaviour of the observable at real chemical potential. Of course, it should be kept in mind that the analytic continuation is valid as far as the function is analytic. Said in other words, it will be possible to explore the $(T,\,\mu)$ plane until a phase transition is encountered. Indeed, it is of utmost importance to study exhaustively the phase diagram of the theory at imaginary chemical potential, since non-analytic points in the complex, accessible region would limit as well the validity of the analytic continuation.

Let us now have a closer look to what happens when a purely imaginary chemical potential is introduced on the lattice. The discussion made in §1.8 after Eq. (1.59) at page 32 is still valid. The only difference is that this time the external $U(1)$ field will be real valued. The analogue of Eqs. (1.60) and (1.61) will be

$$\mathcal{S}_F^{(\mathrm{W.})} = (\hat{M}_0 + 4r) \sum_n \bar{\psi}(n)\,\psi(n) +$$

$$- \frac{1}{2} \sum_n \left\{ e^{\imath\,\hat{\mu}_I}\,\bar{\psi}(n)\,(r - \gamma_4)\,U_4(n)\,\psi(n + \hat{4}) + e^{-\imath\,\hat{\mu}_I}\,\bar{\psi}(n + \hat{4})\,(r + \gamma_4)\,U_4^\dagger(n)\,\psi(n) + \right.$$

$$\left. + \sum_{j=1}^{3} \left[\bar{\psi}(n)\,(r - \gamma_j)\,U_j(n)\,\psi(n + \hat{j}) + \bar{\psi}(n + \hat{j})\,(r + \gamma_j)\,U_j^\dagger(n)\,\psi(n) \right] \right\} \tag{2.4}$$

and

$$\mathcal{S}_F^{(\mathrm{stagg.})} = \hat{M}_0 \sum_n \bar{\chi}(n)\,\chi(n)$$

$$+ \frac{1}{2} \sum_n \left\{ \bar{\chi}(n)\,\eta_4(n) \left[e^{\imath\,\hat{\mu}_I}\,U_4(n)\,\chi(n + \hat{4}) - e^{-\imath\,\hat{\mu}_I}\,U_4^\dagger(n - \hat{4})\,\chi(n - \hat{4}) \right] + \right.$$

$$\left. + \sum_{j=1}^{3} \bar{\chi}(n)\,\eta_j(n) \left[U_j(n)\,\chi(n + \hat{j}) - U_j^\dagger(n - \hat{j})\,\chi(n - \hat{j}) \right] \right\} . \tag{2.5}$$

---

[10] Actually, to some extent, the complexification of real quantities is often used in physics (e.g. in classical electrodynamics).

It can be proven that a constant phase factor appearing next to each link in one direction as in Eqs. (2.4) and (2.5) can be reabsorbed in a modified boundary condition in such a direction for the fermionic field (the validity of this statement should be evident from §C.2, setting there $\theta_t = \hat{\mu}_I N_t$ and $\theta_x = \theta_y = \theta_z = 0$). More explicitly, the partition function of the system can be written as

$$\mathcal{Z}\left(\frac{\mu_I}{T}\right) = \int \mathcal{D}U\,\mathcal{D}\bar{\phi}\,\mathcal{D}\phi\,e^{-\mathcal{S}} \quad \text{with} \quad \phi(\vec{n}, n_t + N_t) = -e^{\imath\,\hat{\mu}_I\,N_t}\,\phi(\vec{n}, n_t) = -e^{\imath\frac{\mu_I}{T}}\,\phi(\vec{n}, n_t)\ ,\ (2.6)$$

where ϕ is a generic fermionic field (this discussion is discretisation independent) and, in the last equality, Eq. (1.53) has been used. If now we change the value of the imaginary chemical potential by an amount $\delta\mu_I$, we will in general alter the partition function. Nevertheless, if

$$\mu_I \to \mu_I + \frac{2\pi k}{N_c}\,T \qquad \text{with} \qquad k \in \{0, 1, \ldots, N_c - 1\}\ ,$$

Eq. (2.6) becomes

$$\mathcal{Z}\left(\frac{\mu_I}{T} + \frac{2\pi k}{N_c}\right) = \int \mathcal{D}U\,\mathcal{D}\bar{\phi}\,\mathcal{D}\phi\,e^{-\mathcal{S}} \quad \text{with} \quad \phi(\vec{n}, n_t + N_t) = -e^{\imath\frac{\mu_I}{T}}e^{\frac{2\pi k}{N_c}}\,\phi(\vec{n}, n_t)\ , \qquad (2.7)$$

which is mapped back into Eq. (2.6) under the inverse of the topologically non-trivial gauge transformation

$$G(\vec{n}, n_t + N_t) = H \cdot G(\vec{n}, n_t) \qquad \text{with} \qquad H = e^{\frac{2\pi k}{N_c}}\ .$$

Therefore, the partition functions in Eqs. (2.6) and (2.7) describe the same physics,

$$\mathcal{Z}\left(\frac{\mu_I}{T}\right) = \mathcal{Z}'\left(\frac{\mu_I}{T} + \frac{2\pi k}{N_c}\right)\ , \qquad (2.8)$$

and we can conclude that, in presence of a purely imaginary chemical potential,

- the QCD partition function is periodic with period $2\pi/N_c$;

- the Z_{N_c} symmetry is a good symmetry also in presence of fermions in the sense that a centre transformation does not change the physics.

On top of these property, it is worth mentioning also that, under charge conjugation, the partition function is symmetric on condition that the chemical potential is reversed,

$$\mathcal{Z}\left(\mu\right) = \mathcal{Z}^C\left(-\mu\right)\ . \qquad (2.9)$$

The phase structure at imaginary chemical potential was predicted in 1986 by Roberge and Weiss [61] and has been numerically confirmed in the recent past [62–65], focusing exclusively on the physical case, $N_c = 3$. Varying the imaginary chemical potential at fixed T, different Z_3 sectors are traversed at critical values of μ_I,

$$\mu_I^c = (2k + 1)\frac{\pi\,T}{3} \qquad \text{with} \qquad k \in \mathbb{Z}\ .$$

From Eqs. (2.8) and (2.9) it follows that the partition function has a reflection symmetry about μ_I^c,

$$\mathcal{Z}\left(\mu_I^c + \delta\mu_I\right) = \mathcal{Z}^C\left(-\mu_I^c - \delta\mu_I\right) = \mathcal{Z}^{C'}\left(-\mu_I^c - \delta\mu_I + \frac{2\pi k}{3}\right) = \mathcal{Z}^{C''}\left(\mu_I^c - \delta\mu_I\right)\ , \qquad (2.10)$$

since $\exists\,k\mid -\mu_I^c + \frac{2\pi k}{3} = \mu_I^c$. It has been shown [62, 63] that there are first order phase transitions at high temperatures, while different Z_3 sectors are connected by smooth crossovers at low temperatures. These sectors can be distinguished by the phase φ of the Polyakov loop,

$$L(\vec{n}) \equiv \frac{1}{N_c} \prod_{n_t=1}^{N_t} U_4(\vec{n}, n_t) = |L(\vec{n})|e^{\imath\varphi}\ , \qquad (2.11)$$

(a) *Phase of the Polyakov loop*

(b) *Modified phase of the Polyakov loop*
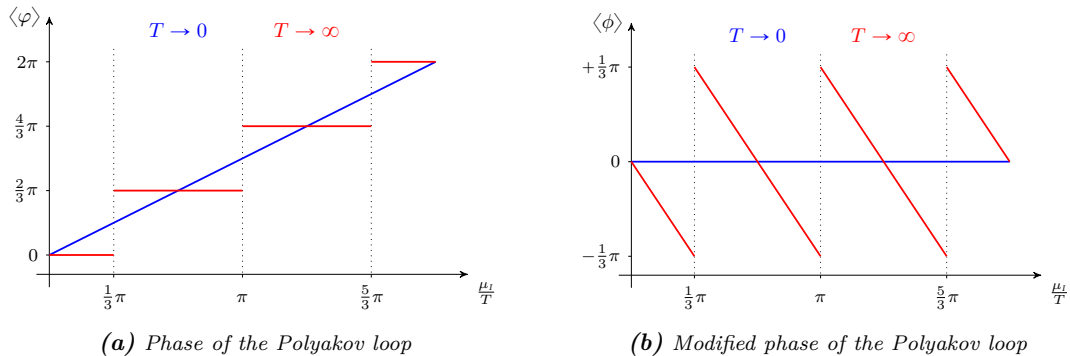
Figure 2.6: *Functional behaviour of the phases of the Polyakov loop. From the plot (a) it is clear that $\langle\varphi\rangle$ does not show the typical property of an order parameter of being zero either at high or at low temperature. Note that $\langle\phi\rangle$ has the same periodicity as the partition function. For $T > T_c$ both phases are discontinuous at $\mu_I = \mu_I^c$, signalling a first-order phase transition.*

that takes the different values $\langle\varphi\rangle = 2\pi n/3$, $n \in \{0, 1, 2\}$. As shown in Figure 2.6(a), φ is not ideal to describe the transition between two adjacent sectors, since it has not the Roberge-Weiss periodicity of the partition function. It is possible to build a suitable order parameter shifting φ conveniently, $\phi \equiv \varphi - \mu_I/T$. People usually refer to ϕ as *modified Polyakov loop phase*. At low temperature, the ground state is symmetric and we have $\langle\phi\rangle = 0$ at any value of μ_I. At high temperature, instead, ϕ becomes discontinuous at the boundaries between Z_3 sectors as shown in Figure 2.6(b). At $\mu_I = \mu_I^c$ there is a two-phases coexistence: one with $\langle\phi\rangle = -\pi/3$ and one with $\langle\phi\rangle = \pi/3$. In the thermodynamic limit, the system will prefer one of the two phases and the symmetry in Eq. (2.10) is spontaneously broken.

Changing, instead, the temperature at fixed chemical potential[11], the system undergoes the chiral/deconfinement phase transition at $T = T_c(m_{u,d}, m_s)$, which depends on the quark masses. The critical temperatures at different μ_I will draw a line in the (T, μ_I) plane starting from T_c at $\mu_I = 0$. It is present consensus that this line joins the endpoints of the first-order vertical lines separating different Z_3 sectors – also known as *Roberge-Weiss endpoints*. Thus, the phase diagram in the (T, μ_I) plane looks like drawn in Figure 2.7(a). From the discussion in §2.1 and §2.2, we know that the nature of the chiral/deconfinement transition depends on both the number of flavours and on the quark masses. Hence, these two parameters play a role when drawing any QCD phase diagram. In Figure 2.7(a), this is reflected in the dash-dotted line, which can be of various types. Moreover, one should consider that the situation is still unclear in the upper-left corner of the Columbia plot – i.e. in the $N_f = 2$ chiral limit. Exactly because of this reason, in order to describe the QCD phase diagram at imaginary chemical potential, we decided to set here $N_f = 3$. Actually, if the first-order scenario is the correct one – as it seems to be at least on very coarse lattices [56] – then the $N_f = 3$ discussion will be qualitatively the same in the $N_f = 2$ case. We will denote the mass of the degenerate quarks simply with m_q. The nature of the Roberge-Weiss endpoints as function of the quark mass has been studied in the last decades and can be summarised as in Figure 2.7(b). Both at small and large masses, they are triple points since the chiral/deconfinement transition is first order at any value of μ_I: The confined phase coexists with the two deconfined phases (one in each of the adjacent Z_3 sectors). For intermediate values of the quark mass, instead, the chiral/deconfinement transition is a crossover everywhere and the nature of the Roberge-Weiss endpoints changes to second order. Therefore, there must be two particular values of the quark

---

[11]To avoid any confusion, it is worth recalling that here we give as understood that the temperature is varied on the lattice changing the gauge coupling β. This means that the ratio μ_I/T is fixed once the temporal lattice extent has been fixed and it is equal to $\hat{\mu}_I N_t$. Therefore, to say that the temperature is varied at fixed chemical potential is equivalent to move vertically in the (T, μ_I) plane.

(a) The (T, μ_I) plane

(b) The $(T, m_{u,d})$ plane at $\mu_I = \mu_I^c$
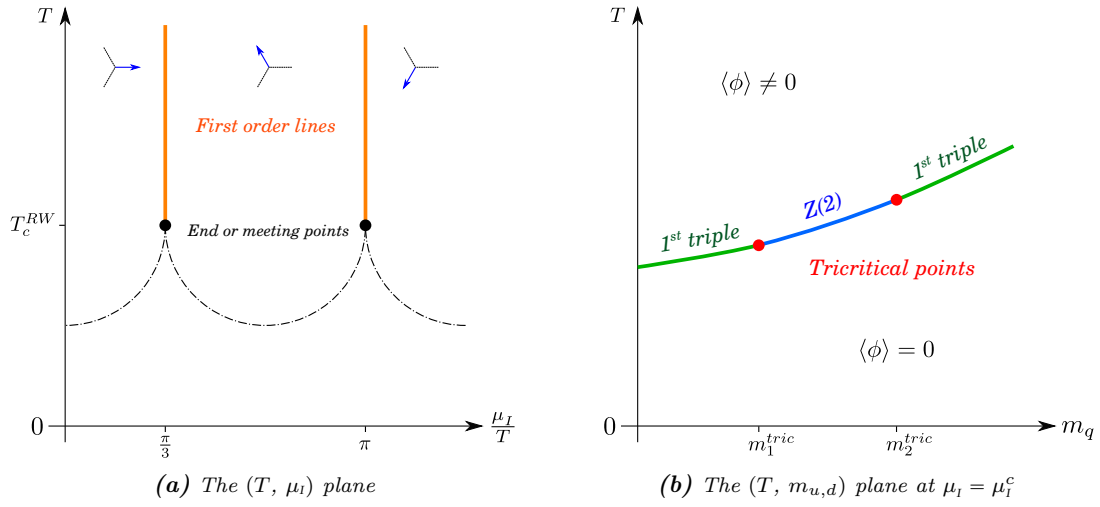
Figure 2.7: *Two different views of the QCD phase diagram at imaginary chemical potential. The dash-dotted line in (a) depicts the chiral/deconfinement transition whose nature depends on the quark masses. The three blue arrows refers to the average values of the Polyakov loop in the different Z_3 sectors. The orange lines represent the Roberge-Weiss transitions. The black dots, where the first-order lines terminate, can be first-order triple points, tricritical points or second-order endpoints as shown in the plot (b). Note that the critical temperature grows as the quark mass is increased.*
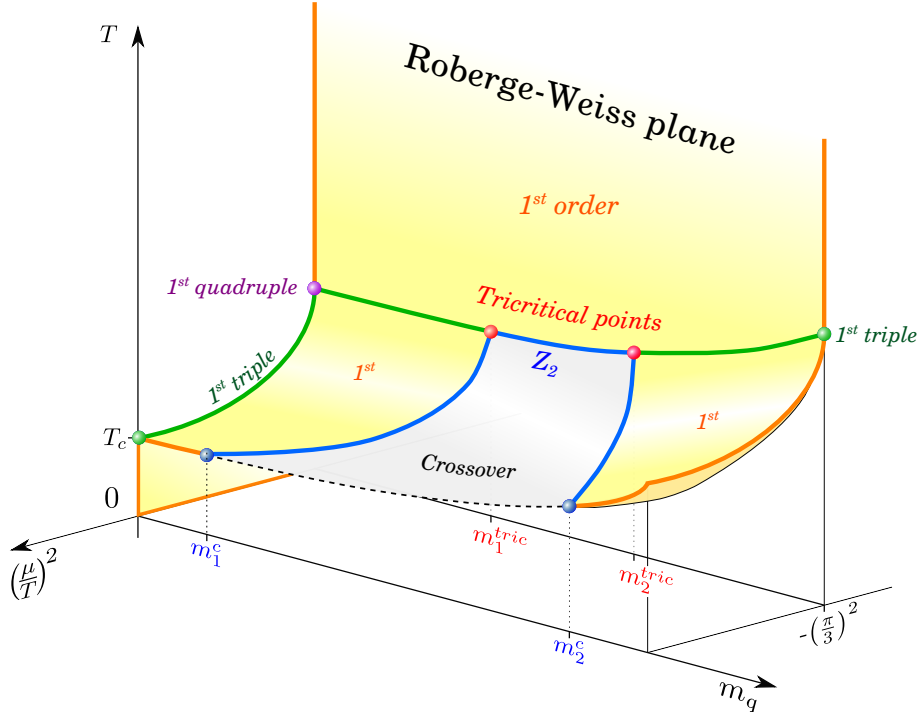
Figure 2.8: *$N_f = 3$ QCD phase diagram at present state of knowledge (i.e. from studies on rather coarse lattices) in the $T - \mu - m_q$ space.*

(a) $m_q = 0$

(b) $0 < m_q < m_1^c$

(c) $m_1^c < m_q < m_1^{tric}$

(d) $m_q = m_1^{tric}$

(e) $m_1^{tric} < m_q < m_2^{tric}$

(f) $m_q = m_2^{tric}$

(g) $m_2^{tric} < m_q < m_2^c$ *(h)* $m_q > m_2^c$
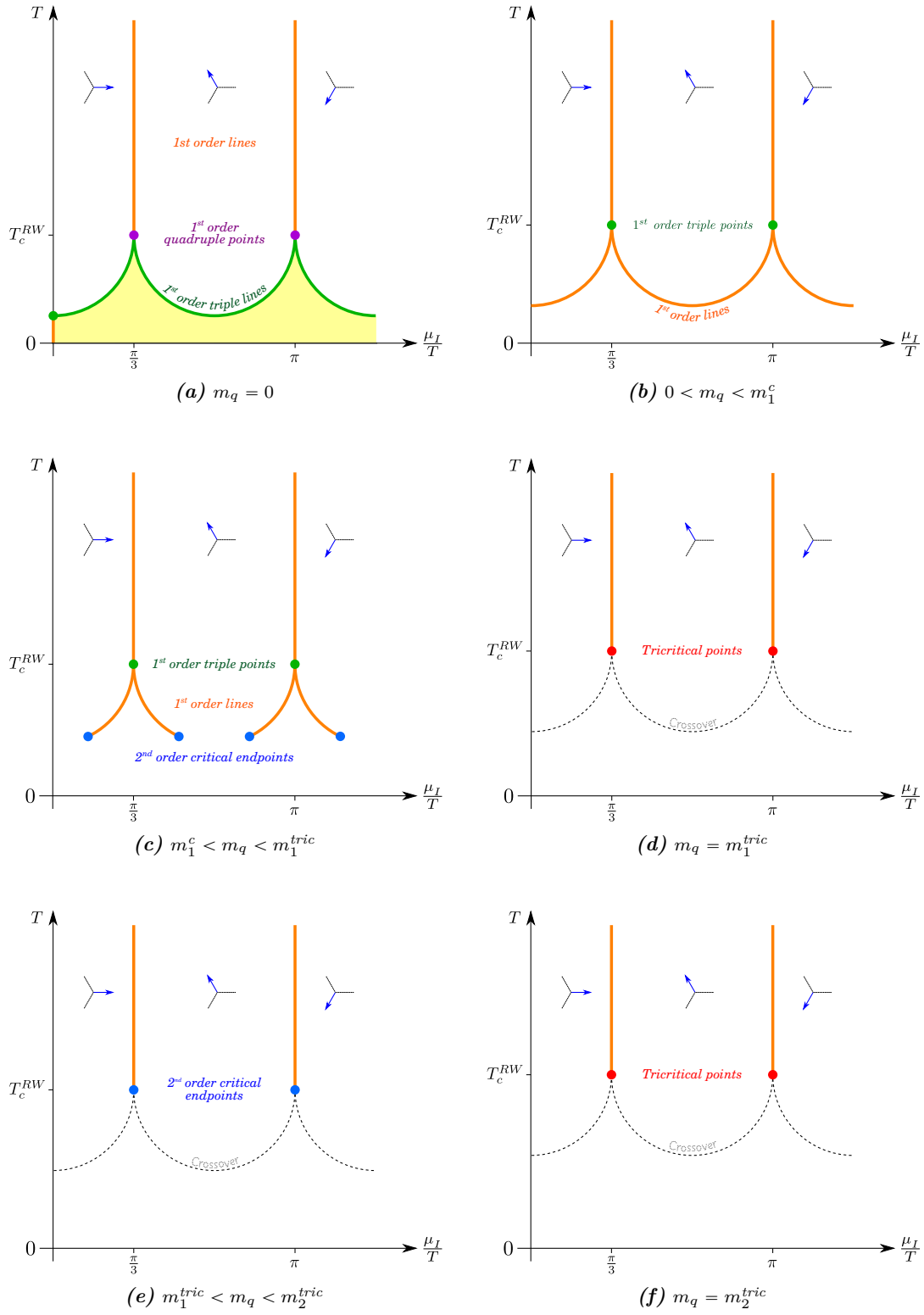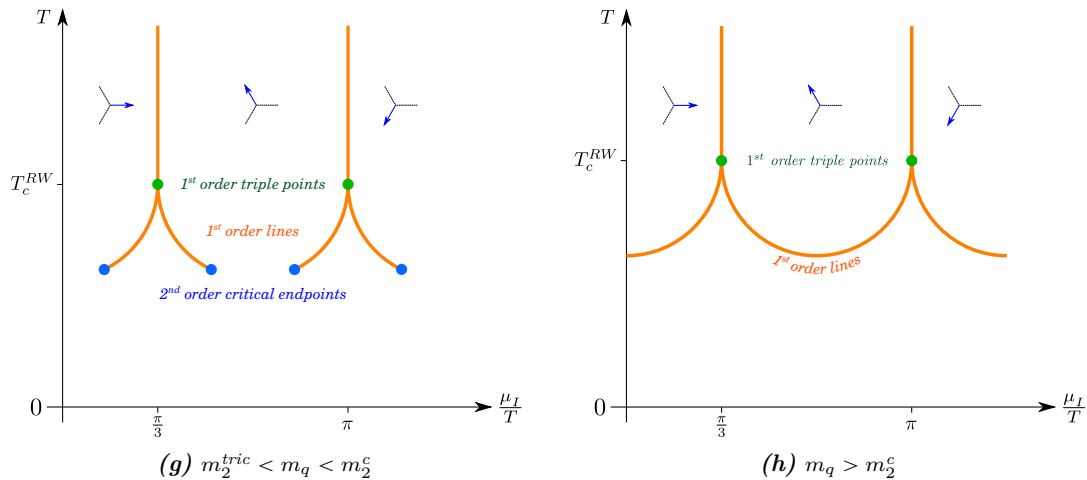
Figure 2.9: *Different sections of Figure 2.8 at increasing quark mass. Note how the Roberge-Weiss critical temperature moves towards larger values as the quark mass is increased.*

mass, $m_q = m_1^{\mathrm{tric}}$ and $m_q = m_2^{\mathrm{tric}}$, at which the Roberge-Weiss endpoints are tricritical. Obviously, the position of the tricritical points is affected by cut-off effects and in Figure 2.7(b) it has been reported the outcome of studies on quite coarse lattices[12] – [66] for example. The value of the deconfinement temperature grows from small to large mass values (as in the $\mu = 0$ case). This fact may be understood thinking that, in the $m_q = \infty$ case, the only bound states that can be excited are rather heavy glueballs.

Knowing how both the nature of the Roberge-Weiss endpoints and the type of the chiral/deconfinement phase transition at zero chemical potential change varying m_q, we can deduce how the dash-dotted line has to be drawn for different values of the quark mass. Indeed, considering degenerate quark masses, we are left with only three parameters that can be varied: T, μ_I and m_q. Therefore, it is possible to produce a 3D phase diagram that will give a complete overview of the phase structure of QCD at purely imaginary chemical potential. Excluding any exotic scenario[13] – that after all has never been found in LQCD simulations – we obtain Figure 2.8. Here, we restricted the imaginary chemical potential to the first Z_3 sector. The symmetry properties of the partition function reported in Eqs. (2.8) and (2.9) allow to extend the plot to different values of μ_I. It is interesting to observe how the Z_2 points at $\mu = 0$ move to closer values towards the first Roberge-Weiss plane (i.e. the plane at $\mu_I^c = \pi T/3$). This means that $m_1^c < m_1^{\mathrm{tric}}$ and $m_2^c > m_2^{\mathrm{tric}}$. Since any numerical simulation is more costly at smaller masses, it is easier to study the chiral region using a non-zero purely imaginary chemical potential. Sectioning Figure 2.8 at constant m_q gives the evolution of the (T, μ_I) plane phase diagram from massless to very heavy quarks. We reported eight of these transversal sections in Figure 2.9. Let us comment further on what is expected to happen in the $m_q = 0$ plane. Starting at $\mu_I = 0$, for $T < T_c$, the chiral symmetry is spontaneously broken and a first-order transition takes place. This is connected to the discontinuous sign change of the chiral condensate that acts as order parameter. At the critical temperature, there will be a three-phases coexistence: one in which the chiral symmetry is restored and two in which it is broken, with positive and negative $\langle \bar{\psi}\psi \rangle$. Moving along the $T = T_c$ line towards the Roberge-Weiss plane, the situation does not change as far as $\mu_I < \mu_I^c$. At the boundary between the first and the second Z_3 sectors, $\mu_I = \mu_I^c$, there will be a two phases coexistence both below and above the critical temperature due to the spontaneous breaking of the chiral and centre symmetry,

---

[12]Most of the plot in this section combine findings on coarse lattices and speculations, in the sense that the actual shape of lines and surfaces has not been determined in real simulations.

[13]In general, a first order line could stop in a Z_2 point and start again with another Z_2 point (and this pattern could happen several times). Nevertheless, it should be possible to find a reason for such a behaviour.
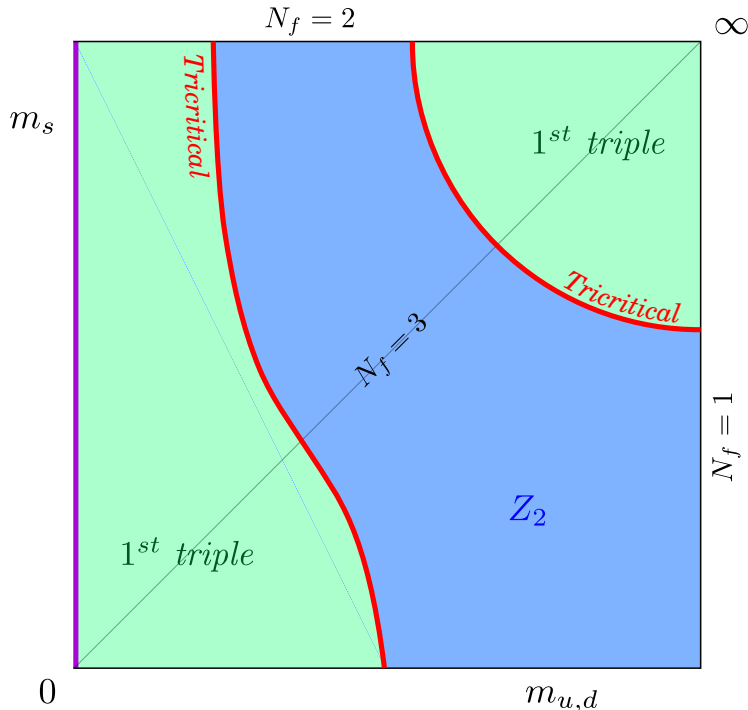
Figure 2.10: *The Roberge-Weiss Columbia plot. Despite the quite coarse lattices used, numeric investigations are so far consistent with each other and lead to this scenario.*

respectively. This very particular scenario results in a quadruple point at $T = T_c$, where the four phases coexist.

To conclude this section, let us briefly discuss how the Columbia plot looks like at $\mu_I^c = \pi\,T/3$. We will refer to it as the *Roberge-Weiss Columbia plot* as well as *Columbia plot in the Roberge-Weiss plane*. Due to the transition between two Z_3 sectors, the phase structure is more complicated than at $\mu = 0$, even if it looks qualitatively the same, as shown in Figure 2.10. In particular, each first-order (crossover) region is now a region of triple (Z_2) points, while the Z_2 boundaries are tricritical lines. Observe that the triple line at $\mu = 0$ becomes here a line of quadruple points. Comparing the Columbia plot in Figure 2.4 with the Roberge-Weiss one in Figure 2.10, it is clear that the triple regions in the latter are wider than the first-order ones in the former. This is expected from the already remarked fact that $m_1^c < m_1^{\mathrm{tric}}$ and $m_2^c > m_2^{\mathrm{tric}}$ in Figure 2.8 (looking at it from above at $\mu/T = 0$ and at $\mu/T = \imath\,\pi/3$, the $N_f = 3$ diagonals of Figures 2.4 and 2.10 are obtained, respectively). Regarding, instead, the upper-left corner, in the Roberge-Weiss Columbia plot the situation seems to be clear. Lattice investigations in the Roberge-Weiss plane with two flavours have always found a tricritical mass value m_1^{tric} in the chiral region, while often simulations at $\mu = 0$ have just put an upper-bound for the hypothetical critical mass m_1^c. Once again, it is better to recall that, so far, only rather coarse lattices have been used and no continuum extrapolation is at the moment available. When the lattice spacing is reduced, the (tri)critical lines will in general move, as already discussed in §2.2.

Figures 2.8 and 2.9 refer to the $N_f = 3$ case and we already observed that the situation would not be qualitatively different with only two flavours, if the first-order scenario for the Columbia plot was the correct one. For the sake of completeness, we decided to redraw in Figure 2.11 some of the previously presented plots, modifying them according to the standard second-order scenario.
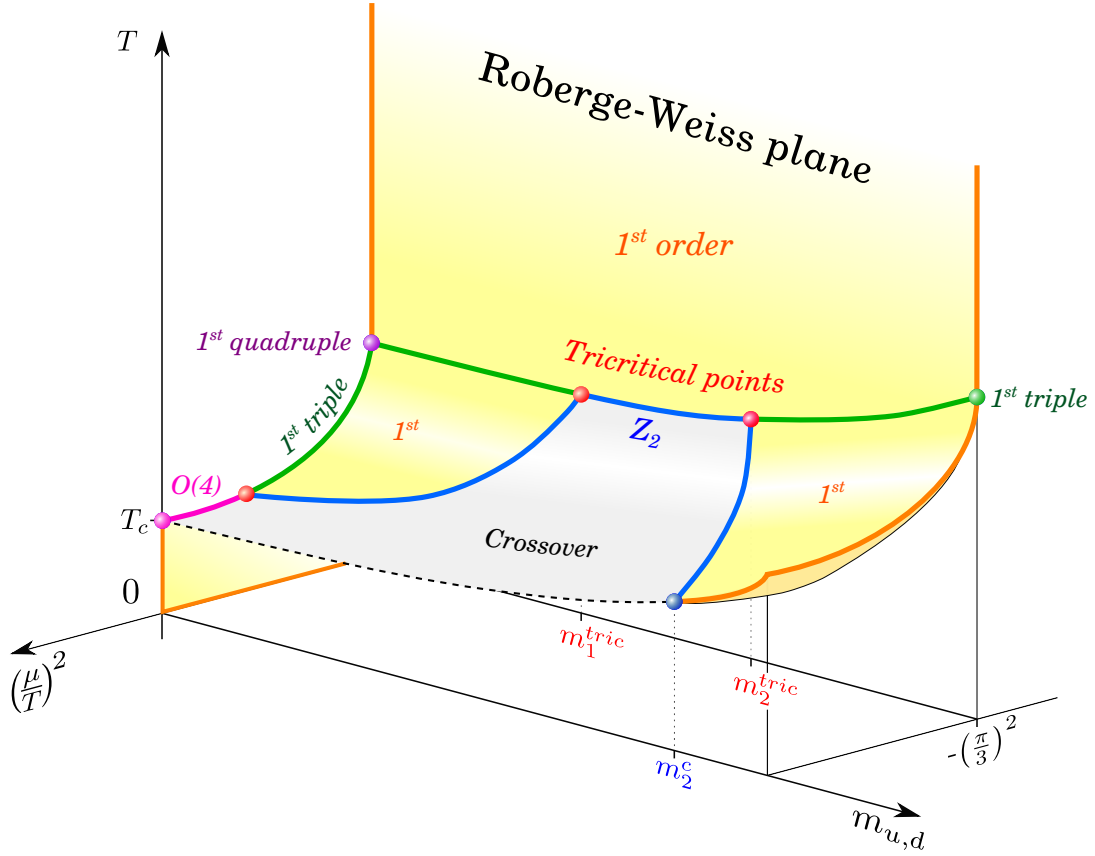
(a) $N_f = 2$ QCD phase diagram in the $T - \mu - m_{u,d}$ space.
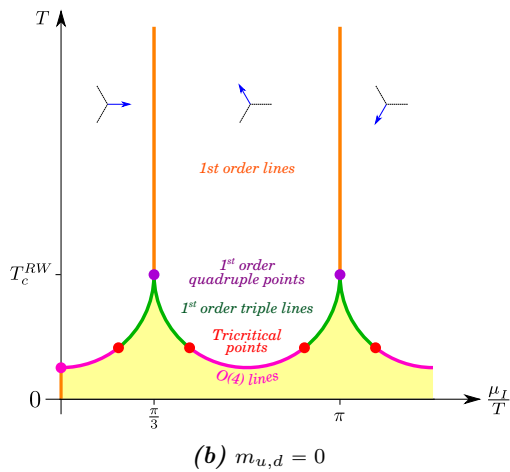
(b) $m_{u,d} = 0$

Figure 2.11: How would the QCD phase diagram at purely imaginary chemical potential change in the $N_f = 2$ case, assuming the second-order scenario for the massless limit. Observe the absence of the critical point $m_{u,d} = m_1^c$. Sectioning (a) at constant $m_{u,d}$, it is possible to produce a similar plot to Figure 2.9. Doing so, Figures 2.9(c) to 2.9(h) remain the same, while Figures 2.9(a) and 2.9(b) have to be replaced by Figure (b).

§ 2.4   The 3D Columbia plot

In the previous section, we learnt how the Columbia plot could look like and we drew its analogue at the Roberge-Weiss critical value of the purely imaginary chemical potential. These two cases are indeed two limiting cases and, in principle, it is possible to vary μ_I from 0 to $\mu_I^c = \pi\,T/3$ continuously, sketching for each value of it the order of the phase transitions in the $(m_{u,d},\,m_s)$ plane. Qualitatively, the situation at fixed $\mu_I \in (0, \mu_I^c)$ is not so different from what happens in the $\mu = 0$ plane. Nevertheless, it is interesting to discuss the differences among the possible scenarios since this will also suggest a strategy in order to understand which one of them is correct. Therefore, to complete this chapter, let us combine Figures 2.5 and 2.10 in a three dimensional plot – the so-called *3D Columbia plot* – putting the chemical potential on the vertical axis. More precisely, it is common to put the dimensionless quantity $(\mu/T)^2$ on the z-axis, so that above and below the Columbia plot we have real and purely imaginary chemical potential, respectively.

In Figures 2.12(a), 2.13(a) and 2.14 the first and two possibilities for the second order scenarios for the 3D Columbia plot are depicted. The critical lines at $\mu = 0$ span critical surfaces that get closer with increasing μ_I, ending in the Roberge-Weiss plane in tricritical lines. These surfaces separate a crossover part of space from first-order volumes that are the extensions of the chiral and deconfinement regions in the Columbia plot. The curvature of the surfaces going out from the Roberge-Weiss plane is known due to general scaling properties [67]. Actually, this is true in general for any critical line departing from a tricritical point: It has to follow a power law with known critical indices[14]. Said in other words, in the vicinity of a tricritical point, there must be *tricritical scaling*. Unfortunately, there is in general no way to predict how wide will be the tricritical scaling region and, case by case, it has to be found out empirically.

These properties can be cleverly used to get insights about the position or even the existence of a tricritical point. To give an example of this fact, let us consider the so-called *back-plane* of the 3D Columbia plot, namely the $N_f = 2$ plane. At small masses, there is a Z_2 line separating a first-order region from a crossover one. This has been highlighted in Figures 2.12(b) and 2.13(b) for possible scenarios of the Columbia plot. Clearly, the main difference is the position of the tricritical point on the $m_{u,d} = 0$ axis. If, at zero chemical potential, QCD with two massless quarks has a first-order (second-order) phase transition, this tricritical point will be above (below) the $\mu = 0$ plane. Now, independently from its location, the Z_2 line going away from the $m_{u,d} = 0$ axis has to follow a fixed functional behaviour,

$$m_{u,d}^{2/5} = C \left[\left(\frac{\mu}{T} \right)^2 - \left(\frac{\mu}{T} \right)_{\text{tric}}^2 \right], \tag{2.12}$$

where C and $(\mu/T)_{\text{tric}}^2$ are constants that have to be determined. Of course, as previously remarked, it is not known how far this relation holds and, considering that the smaller $m_{u,d}$ is the more costly is any numerical simulation, it could happen that the scaling region is not directly accessible. Nevertheless, it is possible to locate the Z_2 critical line for some values of the quark mass and check if Eq. (2.12) is fulfilled. In case it is, and if enough data belong to the scaling region, then the constants C and $(\mu/T)_{\text{tric}}^2$ can be safely estimated and the sign of the latter will tell us which scenario is realised at the lattice spacing at which the simulations have been carried out. Despite its high numerical cost, this strategy is solid and allows, in principle, to shed light on the upper-left of the Columbia plot. Recently, this method has been used both with unimproved staggered fermions [56] and with unimproved Wilson fermions [68]. All these studies found a positive value of the constant $(\mu/T)_{\text{tric}}^2$, indicating that in the two flavour massless limit the phase transition is first order. Certainly, the lattices used here are very coarse and quite big discrepancies between the two fermions formulations suggest that huge cut-off effects are still present. Therefore, no conclusion about the continuum situation can be drawn and finer lattice results are required.

---

[14]Any further information as well as a nice overview for the Reader not completely familiar with this concepts can be found, for example, in [67].
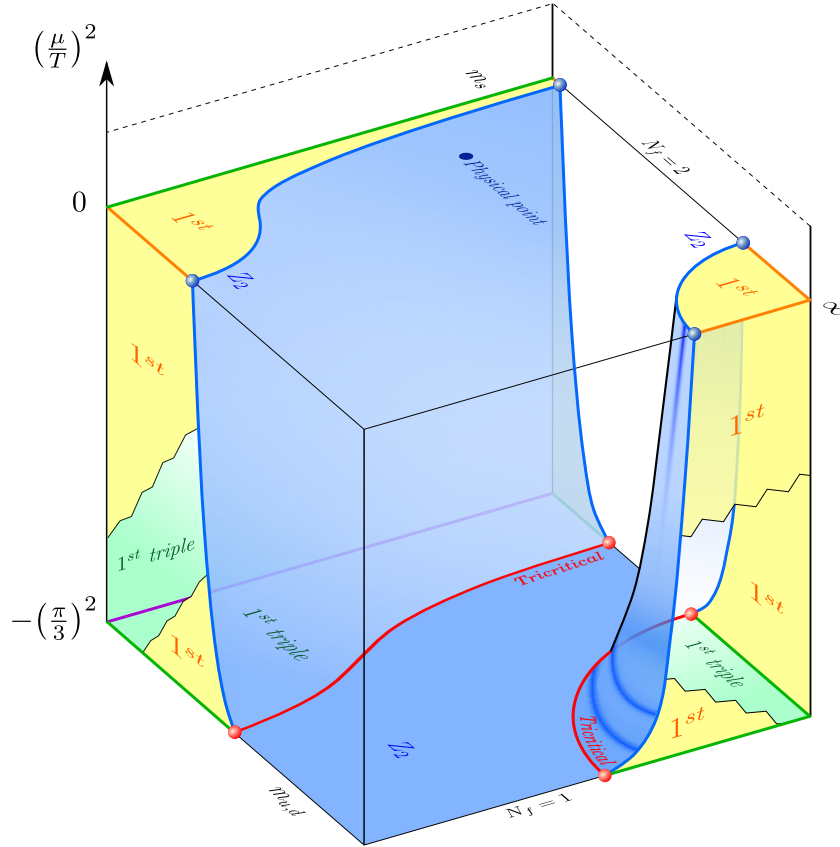
(a) *3D Columbia plot in the classic first-order scenario.*
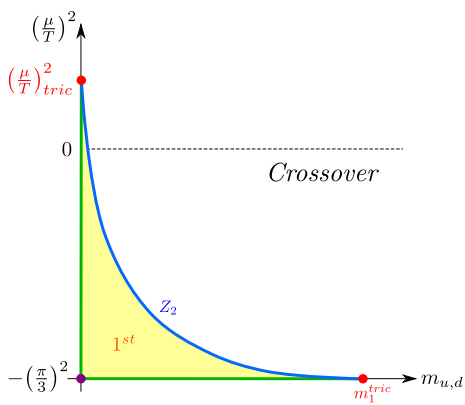
(b) *Chiral region of the $N_f = 2$ plane*

Figure 2.12: *Assuming that the left-edge of the Columbia plot is a triple line as in Figure 2.5(a) leads to the 3D Columbia plot drawn in Figure (a). The first-order regions in the $m_{u,d} = \infty$ and $m_s = 0$ planes have been interrupted to allow the Reader to look behind these surfaces. Observe that the chiral Z_2 surface at $\mu \neq 0$ does not touch the $m_{u,d} = 0$ plane. This implies a tricritical point above the Columbia plot on the $m_{u,d} = 0$, $m_s = \infty$ axis as emphasised in Figure (b). Refer to Table 2.1 for the colour conventions.*
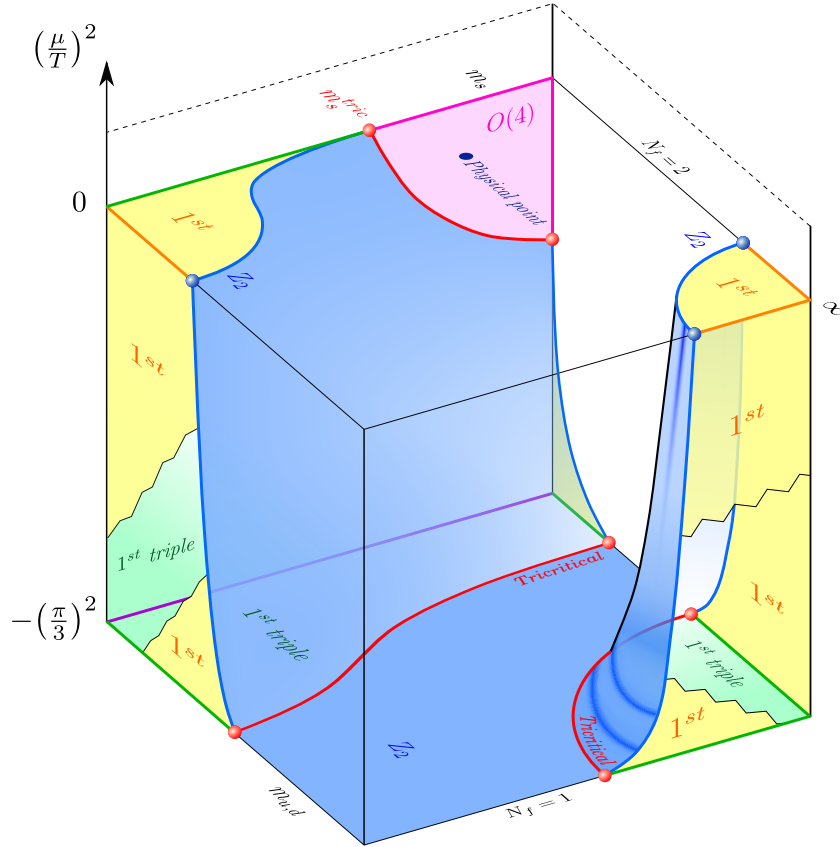
(a) *3D Columbia plot in the standard second-order scenario.*
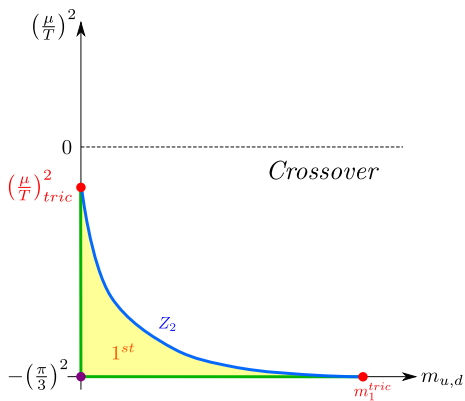
(b) *Chiral region of the $N_f = 2$ plane*

Figure 2.13: *The standard second-order scenario at $\mu = 0$ reported in Figure 2.5(b) leads to the 3D Columbia plot drawn in Figure (a). Again, the first-order regions in the $m_{u,d} = \infty$ and $m_s = 0$ planes have been interrupted to allow the Reader to look behind these surfaces. Observe that, now, the chiral Z_2 surface at $\mu \neq 0$ touches the $m_{u,d} = 0$ plane for high values of the strange quark mass. This implies the presence of a $O(4)$ region, delimited by a tricritical line, which connects the tricritical point in the Columbia plot with that in the $N_f = 2$ plane. Such a point would be located at negative $(\mu/T)^2$ as emphasised in Figure (b). Refer to Table 2.1 for the colour conventions.*

Figure 2.14: *Alternative second-order scenario for the 3D Columbia plot based on Figure 2.5(d). In this case, the chiral Z_2 surface at $\mu \neq 0$ touches the $m_{u,d} = 0$ plane for any value of the strange quark mass. Refer to Table 2.1 for the colour conventions.*

To conclude, it is worth commenting a bit more about the 3D Columbia plots depicted in Figures 2.12(a) and 2.13(a). If on one hand all the known properties have been included in these plots – like the correct bending of surfaces going out from the tricritical lines – on the other hand we had to complete the pictures in a *speculative* way. In fact, only few features between the $\mu = 0$ and the Roberge-Weiss planes have been numerically investigated and, moreover, there are zones not directly accessible in simulations, about which the most natural assumptions have been made. For example, but this is clearly an exotic possibility motivated more by pure logic than by physics intuition, the chiral Z_2 surface at $\mu \neq 0$ in Figure 2.13(a) could touch the $m_{u,d} = 0$ plane and move away from it again *only below* the Columbia plot, allowing a first-order phase transition in the two flavour massless QCD at $\mu = 0$. Said in other words, the $O(4)$ region in Figure 2.13(a) could lie entirely below the Columbia plot, implying the existence of two tricritical points on the $m_{u,d} = 0$, $m_s = \infty$ axis. This scenario, together with even more bizarre ones, is not at first considered as a concrete possibility. If, in future, numeric studies will rule out all natural alternatives, then more involved pictures shall be considered.

LQCD: Numerical aspects 3

After having described the physics background in the previous chapter and before discussing the obtained results in the next one, it is worth dedicating this chapter to give an overview of the numerical aspects of this thesis. Even though it could seem of minor importance since closer to computer science and mathematics than to physics, the computational part of LQCD is for many aspects crucial. As we will discuss in §3.2, nowadays, more and more costly problems are being tackled and this would not have been possible if part of the community had not invested resources in this direction.

The content in this chapter has been organised as follows. The first section will be devoted to work out in detail all the calculations that have to be done in order to be ready to implement the rational hybrid Monte Carlo (RHMC) algorithm [69, 70] with staggered fermions. It would have been interesting both to discuss the standard hybrid Monte Carlo (HMC) algorithm and to consider also Wilson fermions. Nevertheless, in this thesis, the main numeric task has been to implement the staggered RHMC and, thus, we decided to focus here exclusively on it. The techniques used here, together with the explanations present in the literature, should be sufficient for the Reader to implement new codes or to deal with existent ones. In §3.2 we will spend some time introducing and discussing the main aspects of $\mathtt{CL^2QCD}$, a LQCD software based on $\mathtt{OpenCL}$ that started to be developed in 2011 and which was substantially expanded for this thesis. Once explained how to produce data in (finite temperature) LQCD, we will deal with their elaboration in §3.3. In §3.4, the discussion will continue with particular attention to standard techniques used to locate phase transitions and to infer their order. Here, all the methods and the data elaboration used in our physics investigations will be introduced. We decided to keep the discussion on a rather qualitative level, often omitting theoretical explanations that would have probably made it easier to loose the thread. However, there are also in this case many textbooks the Reader can refer to and which will be cited during the chapter. To conclude, we decided to give an idea in §3.5 of how computationally costly finite temperature LQCD can be. We will explain that often many different simulations must be run concurrently and that to handle them efficiently is very important. $\mathtt{BaHaMAS}$ is a tool entirely developed in this thesis to do that and it is worth shortly presenting it.

Since valid in general and not peculiar to the RHMC algorithm, let us start discussing here few computational aspects of LQCD.

After having carried out the integration over the Grassmann variable, the partition function of QCD with N_f degenerate flavours reads

$$\mathcal{Z} = \int \mathcal{D}U \left(\det D \right)^{N_f} e^{-\mathcal{S}_g} \, , \tag{3.1}$$

where D is a generic discretisation of the Dirac operator and $\mathcal{S}_g$ is the gauge part of the action. The expectation value of a generic observable not depending on fermionic fields is then given by

$$\langle O \rangle = \frac{1}{\mathcal{Z}} \int \mathcal{D}U \, O[U] \cdot \left(\det D \right)^{N_f} e^{-\mathcal{S}_g} = \int \mathcal{D}U \, O[U] \cdot P[U] \, , \tag{3.2}$$

having defined

$$P[U] \equiv \frac{\left(\det D \right)^{N_f} e^{-\mathcal{S}_g}}{\mathcal{Z}} \, .$$

For a finite lattice, the path integrals in Eqs. (3.1) and (3.2) are integrals in a huge number of dimensions: A brute force approach in their numeric evaluation is clearly impossible. The main algorithms used since decades by now take advantage of the so-called *importance sampling*. Basically, it consists in drawing a set of configurations $\{U_i\}$ according to $P[U]$ (namely only those that are important) and in making the approximation

$$\langle O \rangle \simeq \sum_{U \in \{U_i\}} O[U] \, . \tag{3.3}$$

In order to generate the set $\{U_i\}$, a homogeneous Markov process is usually used. Roughly speaking, configurations are generated through successive updates called *Monte Carlo steps*. The prescription to make one update, producing a new configuration, is a *Monte Carlo algorithm*. The main ones – for which there exists an abundant literature about and that we will not discuss here – are the Metropolis algorithm, the heath bath algorithm, the overrelaxation algorithm, the microcanonical algorithm, the Langevin algorithm and the HMC algorithm[1]. The latter with Wilson fermions has been used in this thesis, but it was already implemented in `CL`^{2}`QCD`, while the RHMC algorithm, used as well in new physics investigations, has been added.

§ 3.1 The RHMC algorithm with staggered fermions

Due to its particular features, the staggered formulation requires the so-called rooting trick in order to simulate a generic number of flavours[2],

$$\mathcal{Z} = \int \mathcal{D}U \left(\det D \right)^{\frac{1}{4} N_f} e^{-\mathcal{S}_g} \, , \tag{3.4}$$

and

$$\langle O \rangle = \frac{1}{\mathcal{Z}} \int \mathcal{D}U \, O[U] \cdot \left(\det D \right)^{\frac{1}{4} N_f} e^{-\mathcal{S}_g} \equiv \int \mathcal{D}U \, O[U] \cdot P[U] \, . \tag{3.5}$$

In this section we will not bother about the field theoretical correctness of the rooting technique – topic addressed in appendix B – and we will focus exclusively on how to implement it. The discretisation of the Dirac matrix reads

$$D_{n,m} = \hat{M}_0 \, \delta_{n,m} + \frac{1}{2} \sum_{\mu=1}^{4} \eta_\mu(n) \left[U_\mu(n) \, \delta_{n,m-\hat{\mu}} - U_\mu^\dagger(n - \hat{\mu}) \, \delta_{n,m+\hat{\mu}} \right] \, . \tag{3.6}$$

Before deepening into the quantitative analysis of each step of the RHMC algorithm, let us give an overview, so that later it will be easier to refer to the different parts. Our goal is to build a Markov process that explores the configuration space of the system according to the probability

---

[1] A nice introduction to this topic, intended for the less experienced Reader, can be found in chapters 4 and 8 of [19] for pure gauge and dynamical fermions simulations, respectively.

[2] Strictly speaking, if $N_f \pmod 4 = 0$, the rooting trick can be avoided and an HMC algorithm can be used. Nevertheless, also if N_f is a multiple of 4, the RHMC algorithm can be still employed, on constraint that the *multiple pseudofermions* technique [71] is used. We will come back to this point at the end of the section.

distribution $P[U]$ defined in Eq. (3.5). In order to do so, it is common to introduce two auxiliary fields, the so-called *pseudofermion field* – needed to avoid a direct calculation of the determinant in Eq. (3.5) – and the *gauge momenta* – a field conjugated to the link variables that is needed to update the gauge field on every lattice site, avoiding then an ultra-local update that would lead to inevitably long simulations. It will be soon clear how these fields are technically used. Strictly speaking, one configuration of the system that need to be updated at each Monte Carlo step is composed by

- the value of the pseudofermion field (one 3-components vector per lattice site, due to the colour degree of freedom);

- the value of the gauge field (one $SU(3)$ matrix per lattice site and per direction);

- the value of the field conjugated to the link variables (one $su(3)$ matrix per lattice site and per direction).

Nevertheless, since in general the observables depend on the gauge field alone, only this is saved for later measurements and it is common to refer to it with the name *configuration*. The main ingredients of the RHMC algorithm are the Heat bath algorithm, the microcanonical algorithm (also known as *molecular dynamics*) and the Metropolis algorithm. They are combined together in order to update all the fields and one Monte Carlo step can be summarised as follows.

(*i*) At the beginning, each field is drawn randomly.

(*ii*) A candidate for a new configuration for the Markov chain is built

- updating the pseudofermion and the gauge momenta fields using a Heat bath algorithm;
- updating the gauge field using a molecular dynamics algorithm.

(*iii*) The candidate is accepted or rejected through a Metropolis acceptance test. Observe that, at each Monte Carlo update, a configuration must be saved. Therefore, if the candidate is rejected, then the previous configuration is stored again. Steps (*ii*) and (*iii*) are repeated iteratively until the desired statistics is accumulated.

§ 3.1.1   Some preliminary notions

The spatial indices of the Dirac matrix D are in general multi-indices with four components, for example $n \equiv (n_x, n_y, n_z, n_t)$. This aspect is somehow unwanted in a simulation, since it complicates all the linear algebra operations. It is, then, a common practice to "unroll" the four dimensions in one only, defining a so-called *super-index* i_s that ranges over all lattice sites,

$$i_s \equiv i_x + i_y \, N_x + i_z \, N_x \, N_y + i_t \, N_x \, N_y \, N_z \; . \tag{3.7}$$

Here, the order of the four indices i_x, i_y, i_z, i_t is arbitrary and the colour index has been ignored[3]. In this way, any field will be a N-components vector and the matrix D will be a $N \times N$ matrix – where $N \equiv N_x \, N_y \, N_z \, N_t$. Another way to introduce a super-index is to distinguish between even and odd sites, considering at first those with the same parity,

$$\begin{cases} (-1)^{i_x+i_y+i_z+i_t} = +1 & \Rightarrow \quad \text{EVEN site} \\ (-1)^{i_x+i_y+i_z+i_t} = -1 & \Rightarrow \quad \text{ODD site} \end{cases} .$$

The two possibilities are compared in a $2D$-example in Figure 3.1. Using the even-odd decomposition,

---

[3]Even if also the colour index could be included in the super index, it is easier to leave it apart, associating to each lattice site objects with a colour degree of freedom. Remember also that, in the staggered simulation, the Dirac index is not explicitly present.

EVEN-ODD SUPER-INDEX

14	6	15	7
•	•	•	•
4	12	5	13
•	•	•	•
10	2	11	3
•	•	•	•
0	8	1	9
•	•	•	•

$(0,3)$	$(1,3)$	$(2,3)$	$(3,3)$
•	•	•	•
$(0,2)$	$(1,2)$	$(2,2)$	$(3,2)$
•	•	•	•
$(0,1)$	$(1,1)$	$(2,1)$	$(3,1)$
•	•	•	•
$(0,0)$	$(1,0)$	$(2,0)$	$(3,0)$
•	•	•	•

STANDARD COORDINATES

STANDARD SUPER-INDEX

12	13	14	15
•	•	•	•
8	9	10	11
•	•	•	•
4	5	6	7
•	•	•	•
0	1	2	3
•	•	•	•
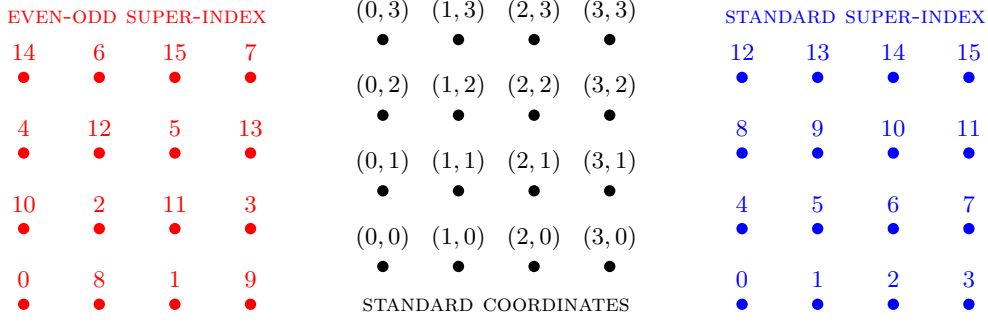
Figure 3.1: *Example of how to associate to each lattice site a super-index.*

the Dirac matrix D can be rewritten as a block matrix,

$$D = \begin{pmatrix} D_{ee} & D_{eo} \\ D_{oe} & D_{oo} \end{pmatrix} ,$$

where the e and o indices denote the parity of the connected lattice sites (for example, D_{eo} will act on fields at odd sites, returning fields at even sites). From Eq. (3.6), it follows that

$$D = \begin{pmatrix} \hat{M}_0 \, \mathbb{1} & D_{eo} \\ D_{oe} & \hat{M}_0 \, \mathbb{1} \end{pmatrix} , \tag{3.8}$$

with $D_{oe} = -D_{eo}^\dagger$ and, therefore, $D_{eo} = -D_{oe}^\dagger$. It is easy to show that

$$D^\dagger D = \begin{pmatrix} \hat{M}_0^2 - D_{eo} \, D_{oe} & \mathbb{0} \\ \mathbb{0} & \hat{M}_0^2 - D_{oe} \, D_{eo} \end{pmatrix} , \tag{3.9}$$

which means that the matrix $D^\dagger D$ does not connect lattice sites with opposite parity. Moreover, using standard linear algebra properties[4], it follows that

$$\det D = \det(\hat{M}_0 \, \mathbb{1}) \, \det\left(\hat{M}_0 \, \mathbb{1} - \frac{1}{\hat{M}_0} D_{oe} \, D_{eo} \right) = \det\left(\hat{M}_0^2 - D_{oe} \, D_{eo} \right) , \tag{3.10a}$$

$$\det D = \det(\hat{M}_0 \, \mathbb{1}) \, \det\left(\hat{M}_0 \, \mathbb{1} - \frac{1}{\hat{M}_0} D_{eo} \, D_{oe} \right) = \det\left(\hat{M}_0^2 - D_{eo} \, D_{oe} \right) . \tag{3.10b}$$

Comparing Eq. (3.9) and Eqs. (3.10), it should be clear that in the partition function $\mathcal{Z}$ of the system it is possible to use the matrix $D^\dagger D$ restricted to either even or odd sites, rather than the matrix D on the whole lattice. This apparently useless complication has, indeed, a twofold advantage. On one hand, $D^\dagger D$ is always a hermitian matrix, no matter how D looks like, and this implies that many numeric techniques limited to this class of matrices can be used. On the other, it is convenient to easily implement the update of the pseudofermion field, as it will be discussed in §3.1.2.

---

[4]In particular,

$$\det \begin{pmatrix} \mathbb{A} & \mathbb{B} \\ \mathbb{C} & \mathbb{D} \end{pmatrix} = \det(\mathbb{A}) \, \det(\mathbb{D} - \mathbb{C} \cdot \mathbb{A}^{-1} \cdot \mathbb{B}) \quad \Leftrightarrow \quad \exists \, \mathbb{A}^{-1} \quad ,$$

$$\det \begin{pmatrix} \mathbb{A} & \mathbb{B} \\ \mathbb{C} & \mathbb{D} \end{pmatrix} = \det(\mathbb{D}) \, \det(\mathbb{A} - \mathbb{B} \cdot \mathbb{D}^{-1} \cdot \mathbb{C}) \quad \Leftrightarrow \quad \exists \, \mathbb{D}^{-1} \quad .$$

A peculiar aspect of the staggered formulation is the presence of the staggered phases $\eta_\mu(n)$. According to their definition,

$$\begin{cases} \eta_1(n) = 1 \\ \eta_\mu(n) = (-1)^{\sum_{\nu<\mu} n_\nu} & \text{if } \mu \neq 1 \;, \end{cases} \qquad (3.11)$$

they are ultra-local on the lattice and they need to be evaluated site by site whenever the Dirac operator has to be used. There is a clever way to take them into account. In fact, it is possible to include them in the link variables, on constraint that the gauge part of the action is modified accordingly. Defining

$$U'_\mu(n) \;= \eta_\mu(n)\, U_\mu(n) \;,$$

we have that the plaquette changes sign,

$$\begin{aligned} \Pi'_{\mu\nu}(n) \;&=\; U'_\mu(n)\; U'_\nu(n+\hat\mu)\; U'^{\dagger}_\mu(n+\hat\nu)\; U'^{\dagger}_\nu(n) \;= \\ &=\; \eta_\mu(n)\,\eta_\nu(n+\hat\mu)\,\eta_\mu(n+\hat\nu)\,\eta_\nu(n)\,\Pi_{\mu\nu}(n) \;= \\ &=\; -\eta_\nu(n)\,\eta_\mu(n+\hat\nu)\,\eta_\mu(n+\hat\nu)\,\eta_\nu(n)\,\Pi_{\mu\nu}(n) \;=\; -\,\Pi_{\mu\nu}(n) \;, \end{aligned}$$

where a property of the staggered phases reported in Eq. (A.10b) in appendix A at page 149 was used. Thus,

$$\begin{aligned} \mathcal{S}_G \;&=\; \frac{6}{g_0^2}\, \sum_n \sum_{\mu<\nu} \left[1 - \frac{1}{3}\,\Re\Big(Tr_C\, \Pi_{\mu\nu}(n)\Big) \right] \;= \\ &=\; \frac{6}{g_0^2}\, \sum_n \sum_{\mu<\nu} \left[1 + \frac{1}{3}\,\Re\Big(Tr_C\, \Pi'_{\mu\nu}(n)\Big) \right] \equiv \mathcal{S}'_G \;. \end{aligned}$$

Said in words, it is sufficient, at the beginning of the simulation, to multiply each link by the corresponding staggered phase, to change one sign in the action and act like if $\eta_\mu(n)$ were not present. Of course, whenever an observable dependent on the gauge field has to be measured, the original link variables must be restored. This strategy, very common and described here for the sake of completeness, is sometimes not really necessary. We will discuss further this point in §3.2.2.

§ 3.1.2   The pseudofermion field and its update

The presence of the determinant of the Dirac matrix in Eq. (3.5) makes the probability distribution $P[U]$ extremely hard to be evaluated. It is therefore necessary to find a way to avoid to calculate $\det(D)$ directly. The standard solution to this problem consists in introducing a complex bosonic field ϕ, for which

$$\int \mathcal{D}\phi\, \mathcal{D}\phi^\dagger\; e^{-\phi^\dagger \cdot D \cdot \phi} \;=\; \frac{\kappa}{\det D} \;, \qquad (3.12)$$

where κ is a constant and the integral measure has the usual meaning on the lattice,

$$\mathcal{D}\phi\, \mathcal{D}\phi^\dagger \;=\; \prod_n \mathrm{d}\phi_n\, \mathrm{d}\phi_n^\dagger \;.$$

Despite the fact that it is not a Grassmann variable, people usually refer to ϕ as *pseudofermion field* (or more simply as *pseudofermion*), since it plays the role of a fermion field. It is worth remarking that the bosonic integral in Eq. (3.12) converges if D is a positive definite matrix – i.e. if all its eigenvalues have positive real parts. This is the main reason why, in general, the number of flavours is doubled using $D^\dagger D$ instead of D. In the staggered formulation, because of the structure of the

Dirac matrix, such a doubling can be avoided restricting the pseudofermion field to the even (or odd) sites, as we learnt in §3.1.1. Therefore, we have

$$\det D = \tilde{\kappa} \int \mathcal{D}\phi \, \mathcal{D}\phi^\dagger \, e^{-\left[\phi' \cdot (D'D)^{-1} \cdot \phi\right]_{\text{EVEN}}} \, ,$$

where $\tilde{\kappa}$ is another constant. Inserting this result into Eq. (3.5) leads to

$$\langle O \rangle = \frac{\tilde{\kappa}}{\mathcal{Z}} \int \mathcal{D}U \, \mathcal{D}\phi \, \mathcal{D}\phi^\dagger \, O[U] \cdot e^{-\mathcal{S}_g - \left[\phi' \cdot (D'D)^{-\frac{1}{4}N_f} \cdot \phi\right]_{\text{EVEN}}} \, . \tag{3.13}$$

Observe that the constant $\tilde{\kappa}$ is implicitly present also in $\mathcal{Z}$, where the determinant can also be rewritten using a pseudofermion field. Therefore, from now on, we will ignore this kind of constants, since, in the end, they are irrelevant in the evaluation of physical observables. Eq. (3.13) is our starting point to discuss the first step of the RHMC update, the Heat bath on the pseudofermion field. In order to draw the field ϕ according to the probability distribution

$$e^{-\left[\phi' \cdot (D'D)^{-\frac{1}{4}N_f} \cdot \phi\right]_{\text{EVEN}}} \, ,$$

we will use a smart trick. Defining

$$R \equiv \left(D^\dagger D\right)^{-\frac{1}{8}N_f} \cdot \phi \, ,$$

we have

$$e^{-\left[\phi' \cdot (D'D)^{-\frac{1}{4}N_f} \cdot \phi\right]_{\text{EVEN}}} = e^{-[R' \cdot R]_{\text{EVEN}}} = e^{-\sum_{\text{EVEN}} |R_i|^2} \, ,$$

from which it is clear how to proceed. The field R is drawn according to a Gaussian distribution and, then, the field ϕ is obtained as

$$\phi = \left(D^\dagger D\right)^{\frac{1}{8}N_f} \cdot R \, . \tag{3.14}$$

The attentive Reader will be wondering in which sense all the previous equations make sense, since in them a rational power of a matrix appears. We need to clarify this point before continuing the description of the other parts of the RHMC algorithm. This will also clear up the way in which such an operation is carried out in practice.

§ 3.1.3 The rational approximation

Let us start recalling a general property. Given a matrix A that can be put in a diagonal form D_A – and this is always the case if A is hermitian – a function f applied to it is, by definition, a matrix whose eigenvalues are given by the function applied to the eigenvalues of the starting matrix A. If Q is the transformation that diagonalises A, we will have

$$f(A) = f(Q \cdot D_A \cdot Q^{-1}) \equiv Q \cdot f(D_A) \cdot Q^{-1} \, , \tag{3.15}$$

with

$$D_A = \text{diag}(\lambda_1, \ldots, \lambda_N) \quad \Leftrightarrow \quad f(D_A) = \text{diag}\big[f(\lambda_1), \ldots, f(\lambda_N)\big] \, .$$

This definition already gives us a prescription to deal with Eq. (3.13), but it also implies the determination of the matrix Q and of its inverse at each Monte Carlo update, definitely something we would like to avoid. In the late Nineties, A. D. Kennedy, I. Horváth and S. Sint [69] proposed a clever way to solve this problem. Considering that there are already other sources of numeric errors in the various ingredients of the hybrid Monte Carlo algorithm, it is possible to perform an approximation of the function of the matrix needed in Eq. (3.13), without affecting the correctness

of the Markov process. They suggested, in particular, to approximate it using a rational expansion[5] of the form

$$f(A) \simeq \alpha_0 \cdot \frac{\prod_{k=1}^{n}(A + \gamma_k)}{\prod_{k=1}^{d}(A + \beta_k)} \,, \tag{3.16}$$

with the degree of the numerator equal to that of the denominator. This choice is particularly advantageous since it allows the use of efficient algorithms to obtain the result of operations like at the right hand side of Eq. (3.14). We will come back to this point at the end of the section. If $n = d \equiv N$, we can perform a partial fraction expansion in Eq. (3.16) obtaining

$$f(A) \simeq a_0 + \sum_{k=1}^{N} \frac{a_k}{A + b_k} \,, \tag{3.17}$$

where an identity matrix has been unambiguously understood. For a fixed degree N, according to the Chebyshev's theorem, there exist optimal coefficients a_k and b_k. Numerically, they can be found using the Remez algorithm. We will not discuss these aspects further, it is enough for us to know what just stated. The interested Reader can refer to §3 of [72] for more details. The approximation of the function f has to be valid in the interval $[\lambda_{\min}, \lambda_{\max}]$, being $\lambda_{\min}$ and $\lambda_{\max}$ the minimum and the maximum eigenvalues of the matrix to which the function f is applied. Plugging Eq. (3.17) into Eq. (3.15), it is easy to show that the explicit form of Q is not needed to evaluate $f(A)$,

$$f(A) = Q \cdot f(D_A) \cdot Q^{-1} = Q \cdot \left[a_0 + \sum_{k=1}^{N} \frac{a_k}{D_A + b_k} \right] \cdot Q^{-1} =$$

$$= Q \cdot \left[a_0 \cdot Q^{-1} \cdot Q + \sum_{k=1}^{N} a_k \cdot \left(Q^{-1} \cdot A \cdot Q + b_k \cdot Q^{-1} \cdot Q \right)^{-1} \right] \cdot Q^{-1} =$$

$$= Q \cdot \left[Q^{-1} \cdot a_0 \cdot Q + \sum_{k=1}^{N} a_k \cdot \left(Q^{-1} \cdot (A + b_k) \cdot Q \right)^{-1} \right] \cdot Q^{-1} =$$

$$= Q \cdot \left[Q^{-1} \cdot a_0 \cdot Q + \sum_{k=1}^{N} Q^{-1} \cdot a_k \cdot (A + b_k)^{-1} \cdot Q \right] \cdot Q^{-1} =$$

$$= Q \cdot Q^{-1} \cdot \left[a_0 + \sum_{k=1}^{N} a_k \cdot (A + b_k)^{-1} \right] \cdot Q \cdot Q^{-1} = a_0 + \sum_{k=1}^{N} \frac{a_k}{A + b_k} \,.$$

Even though comparing the left hand side and the right hand side it could seem that we obtained again Eq. (3.17), actually we proved that replacing the scalar operations of addition, multiplication, and inversion by their matrix analogues is enough to compute rational function of matrices.

Typically, the order N of the rational approximations used varies between 10 and 20 (we will comment further on how to choose this number in §3.1.6 when we will have a complete overview of the different parts of the RHMC algorithm). It should not be hard to imagine that the evaluation of the coefficients a_k and b_k at each Monte Carlo update can be particularly inefficient (especially since the Remez algorithm is not really fast). On the other hand, it seems unavoidable to have to calculate these coefficients for each configurations: The Dirac matrix depends on the gauge field and, since this changes trajectory after trajectory, also the spectrum of D will change. It seems natural that the way to go is to look for a good and fast algorithm to find the expansion coefficients. Actually this is not the case and a different approach is by far more profitable. In fact, with some algebra, it is possible to show that a_k and b_k can be evaluated *only once* at the beginning of the simulation and simply *adapted* at each Monte Carlo update. To understand how it is possible to do

---

[5]In principle, other forms for this approximation can be used. For example, instead of a rational expansion, a polynomial one can be used. Nevertheless, it has been shown that, in order to obtain similar precision, many more terms in the series have to be considered, implying, at the end, a higher numeric cost.

so, let us fix some notation. We need a rational approximation of the function $f(x) = x^\alpha$ valid in the interval $I = [\lambda_{\min}, \lambda_{\max}]$, where α is a rational, non-integer number. Clearly,

$$f(x) = x^\alpha = \left(\frac{\lambda_{\max}}{\lambda_{\max}} x\right)^\alpha = \lambda_{\max}^\alpha \left(\frac{x}{\lambda_{\max}}\right)^\alpha \equiv \lambda_{\max}^\alpha \, y^\alpha \, .$$

Supposing, now, to have calculated a rational expansion

$$y^\alpha \simeq a_0 + \sum_{k=1}^{N} \frac{a_k}{y + b_k}$$

valid for $y \in [x_{\min}, 1]$, then it follows that

$$f(x) \simeq \lambda_{\max}^\alpha \left[a_0 + \sum_{k=1}^{N} \frac{a_k}{\frac{x}{\lambda_{\max}} + b_k}\right] = \lambda_{\max}^\alpha \, a_0 + \sum_{k=1}^{N} \frac{\lambda_{\max}^{\alpha+1} a_k}{x + \lambda_{\max} b_k} \equiv a_0' + \sum_{k=1}^{N} \frac{a_k'}{y + b_k'}$$

valid for $x \in [x_{\min} \lambda_{\max}, \lambda_{\max}]$. This means that, if

$$x_{\min} \leqslant \frac{\lambda_{\min}}{\lambda_{\max}} \, , \tag{3.18}$$

we have obtained an approximation of the function $f(x) = x^\alpha$ valid in the interval I from that of the function y^α, without using the Remez algorithm. To summarise, it is enough to use the Remez algorithm only once at the beginning of the Markov process, approximating the function y^α in the interval $[x_{\min}, 1]$. A typical value for $x_{\min}$ in staggered simulations where all eigenvalues are positive is 10^{-5}. At each Monte Carlo update, the minimum and the maximum eigenvalues have to be estimated (for example with the power method) and the condition in Eq. (3.18) has to be checked. In case it is not fulfilled, a new rational expansion with a smaller $x_{\min}$ has to be evaluated. Afterwards, the coefficients a_k' and b_k' are found rescaling a_k and b_k as

$$a_0' = \lambda_{\max}^\alpha \, a_0 \qquad , \qquad a_k' = \lambda_{\max}^{\alpha+1} a_k \quad \text{for } k \geqslant 1 \qquad \text{and} \qquad b_k' = \lambda_{\max} b_k \, .$$

To conclude, let us consider again Eq. (3.14). Using a rational approximation for the function $f(x) = x^{\frac{1}{8} N_f}$, it becomes

$$\phi = \left(D^\dagger D\right)^{\frac{1}{8} N_f} \cdot R \simeq \left[a_0 + \sum_{k=1}^{N} \frac{a_k}{D^\dagger D + b_k}\right] \cdot R = a_0 \cdot R + \sum_{k=1}^{N} a_k \cdot (D^\dagger D + b_k)^{-1} \cdot R \, .$$

The first term is simply the multiplication of a vector by a scalar. The second one, instead, looks more complicated. Naïvely, it seems that the inverse of a matrix applied to a vector has to be evaluated N times. Fortunately, since the vector is the same and since the matrices differ for a shift only, there are efficient algorithms to get this calculation done at once (here, again, the importance of having a hermitian matrix). In general, to solve the equation

$$(A + \sigma_k) \cdot x = b$$

with respect to the vector x for a set of N different values of constants σ_k, it is possible to use, for instance, the so-called *multi-shift conjugate gradient* or more simply CG - M algorithm [73]. The vector b is fixed for all the value of k. A solution will be a set of vectors x, one for each shift σ_k. The numerical cost of the CG - M is comparable to that of a normal conjugate gradient algorithm (to be used in the case $\sigma_k = 0$) and it is, in first approximation, proportional to the condition number of the matrix A – namely to the ratio between the biggest and the smallest eigenvalue. Having a hermitian matrix is for sure an advantage, but this does not mean that this property is needed. Since decades, a big variety of different solvers for so many different situations has been studied and it is hard to make general statements about which is the best, because, after all, it depends on the problem. The Reader which would like to have more information about numerical recipes to solve linear systems can rely on the surely abundant literature on the topic (refer, for example, to [74, 75] to have a nice overview about iterative methods).

§ 3.1.4   The gauge momenta field and its update

We already said that the gauge field is updated using a molecular dynamics algorithm. In order to do so, a conjugate field to it is needed. This field, that has to be irrelevant in the calculation of any physical observable, belongs to the algebra $su(3)$, is usually called *gauge momenta field* and it will be denoted by $H_\mu(n)$. Its name is due to the fact that in a molecular dynamics algorithm an analogy with a classical mechanic system is done. Therefore, as the gauge field is the analogue of the position of a classical body, the new conjugated field will be the analogue of the momentum. Also a Hamiltonian $\mathcal{H}$ has to be defined and, using it, equations of motions for $U_\mu(n)$ and $H_\mu(n)$ are derived. We will carry out this calculation in next section. For the moment let us see how $\mathcal{H}$ looks like and how to make the gauge momenta update at each Monte Carlo update. The introduction of the field $H_\mu(n)$ can be thought as a smart rewriting of Eq. (3.13),

$$\langle O \rangle = \frac{\int \mathcal{D}U \, \mathcal{D}\phi \, \mathcal{D}\phi^\dagger \, \mathcal{D}H \; O[U] \cdot e^{-\mathcal{H}}}{\int \mathcal{D}U \, \mathcal{D}\phi \, \mathcal{D}\phi^\dagger \, \mathcal{D}H \cdot e^{-\mathcal{H}}} \; ,$$

where

$$\mathcal{H} \equiv \mathcal{S}_g + \left[\phi^\dagger \cdot (D^\dagger D)^{-\frac{1}{4}N_f} \cdot \phi \right]_{\text{EVEN}} + \frac{1}{2} \sum_{n,\mu} \mathrm{Tr}_c\!\left[H_\mu^2(n) \right] .$$

Note that the integral over the new field cancels between numerator and denominator. The form of the part of the Hamiltonian containing the gauge momenta field is somehow arbitrary, but it is common to add it as above, in analogy with the momentum part of the Hamiltonian of a classical system. Moreover, doing so, it is then straightforward to use a Heat bath algorithm to draw the field $H_\mu(n)$. In fact, since $H_\mu(n) \in su(3)$, we can write

$$H_\mu(n) = \sum_{A=1}^{8} H_\mu^A(n)\, \frac{\lambda^A}{2} \quad \text{with} \quad H_\mu^A(n) \in \mathbb{R} \; , \tag{3.19}$$

where λ^A are the Gell-Mann matrices. Using the fact that $\mathrm{Tr}_c(\lambda^A \lambda^B) = 2\, \delta_{A,B}$, it follows that

$$-\frac{1}{2} \sum_{n,\mu} \mathrm{Tr}_c\!\left[H_\mu^2(n) \right] = -\frac{1}{2} \sum_{n,\mu} \mathrm{Tr}_c\!\left[\sum_{A=1}^{8} \sum_{B=1}^{8} H_\mu^A(n)\, H_\mu^B(n)\, \frac{\lambda^A}{2}\, \frac{\lambda^B}{2} \right] =$$

$$= -\frac{1}{4} \sum_{\mu,n} \sum_{A=1}^{8} H_\mu^A(n)\, H_\mu^A(n) \; .$$

Therefore, to draw the gauge momenta field according to the probability distribution

$$e^{-\frac{1}{2} \sum_{n,\mu} \mathrm{Tr}_c\left(H_\mu^2(n) \right)} \; ,$$

it will be sufficient to draw the 8 real numbers $H_\mu^A(n)$ according to

$$p(x) = \frac{1}{\sqrt{4\pi}} \, e^{-\frac{1}{4}x^2}$$

and build up the field using Eq. (3.19).

§ 3.1.5   The Molecular Dynamics equations and the Metropolis test

Let us now discuss in detail the core of the RHMC algorithm and see, in particular, how to update the gauge field. The idea behind is rather simple: Using the Hamiltonian of the system,

equations of motions for $U_\mu(n)$ and $H_\mu(n)$ are derived and they are numerically integrated for a fixed amount of a fictitious time. Nevertheless, writing down the Hamilton equation in a naïve way,

$$
\begin{cases}
\dot{U}_\mu(n) = +\dfrac{\partial \mathcal{H}}{\partial H_\mu(n)} \\[2ex]
\dot{H}_\mu(n) = -\dfrac{\partial \mathcal{H}}{\partial U_\mu(n)}
\end{cases} ,
$$

leads to non trivial expressions to be evaluated, because of the derivation with respect to a matrix of a scalar function depending on matrices. To get the equation of motion for the link variables, the calculation can be simplified thinking to the correspondence between $U_\mu(n)$ and $H_\mu(n)$ at the level of the algebra coefficients. Doing so, we have that

$$
\dot{A}_\mu^B(n) = \frac{\partial \mathcal{H}}{\partial H_\mu^B(n)} = \frac{\partial}{\partial H_\mu^B(n)}\left[\sum_{m,\nu} \sum_{C=1}^{8} \frac{1}{4} H_\nu^C(m) \, H_\nu^C(m) \right] = \frac{1}{2} H_\mu^B(n) \; ,
$$

which implies

$$
\dot{U}_\mu(n) = \frac{d}{dt}\left[e^{\,\imath\, g_0\, a \sum_{B-1}^{8} A_\mu^B(n)\,\frac{\lambda^B}{2}} \right] = \sum_{B=1}^{8} \imath\, g_0\, a\, \frac{\lambda^B}{2}\left[e^{\,\imath\, g_0\, a \sum_{C-1}^{8} A_\mu^C(n)\,\frac{\lambda^C}{2}} \right] \dot{A}_\mu^B(n) =
$$

$$
= \sum_{B=1}^{8} \imath\, g_0\, a\, \frac{\lambda^B}{2}\, \dot{A}_\mu^B(n)\, U_\mu(n) = \imath\left[\sum_{B=1}^{8} \tilde{H}_\mu^B(n)\, \frac{\lambda^B}{2} \right] U_\mu(n) = \imath\, H_\mu(n) \cdot U_\mu(n) \; ,
$$

where

$$
\tilde{H}_\mu^B(n) \equiv \frac{1}{2}\, g_0\, a\, H_\mu^B(n) \; .
$$

The same technique could be, in principle, used to obtain the equation of motion for the gauge momenta field. Actually, it is common [76] to derive it considering that the Hamiltonian is conserved during the motion,

$$
\frac{\mathrm{d}\mathcal{H}}{\mathrm{d}t} = \big\{ \mathcal{H},\, \mathcal{H} \big\} + \frac{\partial \mathcal{H}}{\partial t} = 0 \; ,
$$

since $\mathcal{H}$ does not depend explicitly on time. We need then to evaluate the time derivative of the Hamiltonian, which we recall here for simplicity,

$$
\mathcal{H} = \frac{1}{2} \sum_{n,\mu} \mathrm{Tr}_c\big[H_\mu^2(n) \big] + \frac{6}{g_0^2} \sum_n \sum_{\mu<\nu} \left[1 - \frac{1}{3}\Re\Big(\mathrm{Tr}_c\, \Pi_{\mu\nu}(n) \Big) \right] + \phi^\dagger \cdot (D^\dagger D)^{-\frac{1}{4} N_f} \cdot \phi \; , \qquad (3.20)
$$

where we omitted the label EVEN on the last term, since it can be given as understood from now on. Despite the fact that we could reabsorb the staggered phases into the link variables as explained in §3.1.5, we will not do it and we will explicitly carry them around. To make the calculation easier to be followed, we will calculate the time derivative of the three terms in Eq. (3.20) separately. For the first one, we have immediately that

$$
\frac{\mathrm{d}}{\mathrm{d}t}\left[\frac{1}{2} \sum_{n,\mu} \mathrm{Tr}_c\big[H_\mu^2(n) \big] \right] = \sum_{n,\mu} \mathrm{Tr}_c\big[H_\mu(n)\, \dot{H}_\mu(n) \big] \; . \qquad (3.21)
$$

To take the time derivative of the second term in Eq. (3.20) we need, instead, some slightly more involved argument. If we wrote down all the terms in the sums over n and over $\mu < \nu$, we would obtain all the possible plaquettes on the lattice. Moreover, it is easy to show that all the terms in the time derivative of the trace of one plaquette have the same structure, namely they are the

product between the time derivative of one link and a three links path on the lattice, the so-called *staple.* More explicitly,

$$
\frac{\mathrm{d}}{\mathrm{d}t}\,\mathrm{Tr}_c\big(\Pi_{\mu\nu}(n)\,\big) = \mathrm{Tr}_c\Big[\ \dot{U}_\mu(n)\,U_\nu(n+\hat{\mu})\,U_\mu^\dagger(n+\hat{\nu})\,U_\nu^\dagger(n)\ +
$$
$$
+\ \dot{U}_\nu(n+\hat{\mu})\,U_\mu^\dagger(n+\hat{\nu})\,U_\nu^\dagger(n)\,U_\mu(n)\ +
$$
$$
+\ \dot{U}_\mu^\dagger(n+\hat{\nu})\,U_\nu^\dagger(n)\,U_\mu(n)\,U_\nu(n+\hat{\mu})\ +
$$
$$
+\ \dot{U}_\nu^\dagger(n)\,U_\mu(n)\,U_\nu(n+\hat{\mu})\,U_\mu^\dagger(n+\hat{\nu})\ \Big]\ ,
$$

where the cyclic property of the trace has been used to bring together the three not derived links. Considering as well that

$$
\frac{6}{g_0^2}\sum_n\sum_{\mu<\nu}\left[1-\frac{1}{3}\,\Re\Big(\mathrm{Tr}_c\,\Pi_{\mu\nu}(n)\Big)\right] = \frac{6}{g_0^2}\sum_n\sum_{\mu<\nu}\left[1-\frac{1}{6}\,\mathrm{Tr}_c\Big(\Pi_{\mu\nu}(n)\ +\ \Pi_{\mu\nu}^\dagger(n)\Big)\right]\ ,
$$

it should be easy to realise that, in the time derivative of the second term in Eq. (3.20), each link will be multiplied by the sum of all the possible staples, which surround it – some coming from $\dot{\Pi}_{\mu\nu}(n)$ and some from $\dot{\Pi}_{\mu\nu}^\dagger(n)$. Using the symbol $\mathfrak{s}_{\mu\nu}(n)$ to denote the staple that starts from the site $n+\hat{\mu}$ in direction $\hat{\mu}$ and ends to the site n, we can define the sum of all the staples that surround the link $U_\mu(n)$ as

$$
V_\mu(n) \equiv \sum_{\substack{\nu=\pm 1 \\ \nu\neq\mu}}^{\pm 4} \mathfrak{s}_{\mu\nu}(n)\ ,
$$

where a negative value of ν just indicates to go backward in direction $\hat{\nu}$. Eventually,

$$
\frac{6}{g_0^2}\sum_n\sum_{\mu<\nu}\frac{\mathrm{d}}{\mathrm{d}t}\left[1-\frac{1}{6}\,\mathrm{Tr}_c\Big(\Pi_{\mu\nu}(n)+\Pi_{\mu\nu}^\dagger(n)\Big)\right] = -\frac{\beta}{6}\sum_{n,\mu}\mathrm{Tr}_c\left[\dot{U}_\mu(n)\,V_\mu(n)+V_\mu^\dagger(n)\,\dot{U}_\mu^\dagger(n)\right]\ . \quad (3.22)
$$

We have now to deal with the last term in Eq. (3.20). Considering that the pseudofermion field ϕ is kept constant during the molecular dynamic part of the RHMC algorithm, the only time dependence lies in the Dirac matrix. We know from §3.1.3 that a rational approximation is needed to calculate the non integer power of the matrix $D^\dagger D$,

$$
(D^\dagger D)^{-\frac{1}{4}N_f} \simeq c_0 + \sum_{k=1}^N \frac{c_k}{D^\dagger D + p_k} = c_0 + \sum_{k=1}^N c_k\cdot\big(D^\dagger D + p_k\big)^{-1}\ .
$$

Hence,

$$
\frac{\mathrm{d}}{\mathrm{d}t}\left[\phi^\dagger\cdot(D^\dagger D)^{-\frac{1}{4}N_f}\cdot\phi\right] = \phi^\dagger\cdot\frac{\mathrm{d}}{\mathrm{d}t}\left[c_0 + \sum_{k=1}^N c_k\cdot\big(D^\dagger D + p_k\big)^{-1}\right]\cdot\phi
$$
$$
= \sum_{k=1}^N c_k\,\phi^\dagger\cdot\left[\frac{\mathrm{d}}{\mathrm{d}t}\big(D^\dagger D + p_k\big)^{-1}\right]\cdot\phi\ .
$$

Recalling that, given a matrix A that depends on a continuous parameter t,

$$
\frac{\mathrm{d}}{\mathrm{d}t}\,A^{-1}(t) = -A^{-1}(t)\cdot\left[\frac{\mathrm{d}}{\mathrm{d}t}A(t)\right]\cdot A^{-1}(t) \quad\Leftrightarrow\quad \forall\,t\,|\,\exists A^{-1}(t)\ ,
$$

we have

$$
\sum_{k=1}^N c_k\,\phi^\dagger\cdot\left[\frac{\mathrm{d}}{\mathrm{d}t}\big(D^\dagger D + p_k\big)^{-1}\right]\cdot\phi =
$$

$$= \sum_{k=1}^{N} c_k \, \phi^\dagger \cdot \left\{ - \left(D^\dagger D + p_k\right)^{-1} \cdot \left[\frac{\mathrm{d}}{\mathrm{d}t} \left(D^\dagger D + p_k\right)^{-1} \right] \cdot \left(D^\dagger D + p_k\right)^{-1} \right\} \cdot \phi =$$

$$= - \sum_{k=1}^{N} c_k \, X_k^\dagger \cdot \left[\frac{\mathrm{d}}{\mathrm{d}t} \left(D^\dagger D\right)^{-1} \right] \cdot X_k =$$

$$= - \sum_{k=1}^{N} c_k \, X_k^\dagger \cdot \sum_{n,\mu} \left[\frac{\partial D^\dagger}{\partial U_\mu(n)} \, \dot{U}_\mu(n) \, D + D^\dagger \frac{\partial D}{\partial U_\mu(n)} \, \dot{U}_\mu(n) + \right.$$

$$\left. + \frac{\partial D^\dagger}{\partial U_\mu^\dagger(n)} \, \dot{U}_\mu^\dagger(n) \, D + D^\dagger \frac{\partial D}{\partial U_\mu^\dagger(n)} \, \dot{U}_\mu^\dagger(n) \right] \cdot X_k \ ,$$

where, in the last but one step, we defined

$$X_k \equiv \left(D^\dagger D + p_k\right)^{-1} \cdot \phi \ .$$

To simplify further the expression above, we need to consider the explicit form of the matrix D and evaluate its derivative with respect to a link[6],

$$\frac{\partial D}{\partial U_\rho(k)} = \frac{\partial}{\partial U_\rho(k)} \left[\hat{M}_0 \, \delta_{n,m} + \frac{1}{2} \sum_{\mu=1}^{4} \eta_\mu(n) \left[U_\mu(n) \, \delta_{n,m-\hat{\mu}} - U_\mu^\dagger(n-\hat{\mu}) \, \delta_{n,m+\hat{\mu}} \right] \right] =$$

$$= \frac{1}{2} \sum_{\mu=1}^{4} \eta_\mu(n) \, \delta_{n,m-\hat{\mu}} \, \delta_{\mu,\rho} \, \delta_{n,k} = \frac{1}{2} \, \eta_\rho(k) \, \delta_{k+\hat{\rho},m} \, \delta_{n,k} \ . \tag{3.23}$$

Observe that, being the indices ρ and k fixed, the derivative of D with respect to $U_\rho(k)$ is the tensor product between the identity matrix in the colour space and a matrix in the coordinates space that has only zero entries except at the position $(k, k+\hat{\rho})$. Thus, it will commute with any link variable. Similarly,

$$\frac{\partial (D^\dagger)_{nm}}{\partial U_\rho^\dagger(k)} = \frac{1}{2} \, \eta_\rho(k) \, \delta_{m,k+\hat{\rho}} \, \delta_{k,n} \ ,$$

which compared with Eq. (3.23) implies

$$\left(\frac{\partial D_{nm}}{\partial U_\rho(k)} \right)^\dagger = \frac{\partial (D^\dagger)_{nm}}{\partial U_\rho^\dagger(k)} \ .$$

Summarising, we have that

$$\left[\frac{\partial D}{\partial U_\rho(k)}, \ \dot{U}_\mu(n) \right] = 0 \qquad\qquad \left(\frac{\partial D}{\partial U_\rho(k)} \right)^\dagger = \left(\frac{\partial D^\dagger}{\partial U_\rho^\dagger(k)} \right) \tag{3.24a}$$

and, with similar arguments, it is possible to prove that

$$\left[\frac{\partial D^\dagger}{\partial U_\rho(k)}, \ \dot{U}_\mu(n) \right] = 0 \qquad\qquad \left(\frac{\partial D^\dagger}{\partial U_\rho(k)} \right)^\dagger = \left(\frac{\partial D}{\partial U_\rho^\dagger(k)} \right) \quad . \tag{3.24b}$$

Putting everything together, it follows that

$$- \sum_{k=1}^{N} c_k \, X_k^\dagger \cdot \left[\frac{\mathrm{d}}{\mathrm{d}t} \left(D^\dagger D\right)^{-1} \right] \cdot X_k =$$

---

[6]Here, the derivation with respect to a matrix is not hard, since the function we are considering is linear in the link variable.

$$= -\sum_{k=1}^{N} c_k \, X_k^\dagger \cdot \sum_{n,\mu} \left[\frac{\partial D^\dagger}{\partial U_\mu(n)} \, \dot{U}_\mu(n) \, D + D^\dagger \, \frac{\partial D}{\partial U_\mu(n)} \, \dot{U}_\mu(n) \, + \text{h.c.} \right] \cdot X_k \, ,$$

where with *h.c.* we indicated the *hermitian conjugated* of the previous terms in the square bracket. It is possible to make a further simplification, writing explicitly all the indices that so far have been understood. Let us do it in detail for the first term in the square bracket and report only the result for the other. Neglecting for a moment the sums over k, n, μ, the coefficient $-c_k$ and the index k on X, we have

$$X^\dagger \cdot \left[\frac{\partial D^\dagger}{\partial U_\mu(n)} \, \dot{U}_\mu(n) \, D \right] \cdot X = \sum_{\substack{a_1,a_2,a_3 \\ n_1,n_2,n_3}} X^\dagger_{a_1 \atop n_1} \left[\frac{\partial D^\dagger}{\partial U_\mu(n)} \, \dot{U}_\mu(n) \right]_{a_1 \atop n_1} {}_{,}{}_{n_2}^{a_2} \, D_{a_2 \atop n_2}{}^{a_3}_{,n_3} X_{a_3 \atop n_3} =$$

$$= \sum_{\substack{a_1,a_2,a_3 \\ n_1,n_2,n_3}} X_{a_3 \atop n_3} X^\dagger_{a_1 \atop n_1} \left[\frac{\partial D^\dagger}{\partial U_\mu(n)} \, \dot{U}_\mu(n) \right]_{a_1 \atop n_1}{}_{,}{}_{n_2}^{a_2} \, D_{a_2 \atop n_2}{}^{a_3}_{,n_3} =$$

$$= \text{Tr}\left[\left(X \otimes X^\dagger \right) \cdot \frac{\partial D^\dagger}{\partial U_\mu(n)} \, \dot{U}_\mu(n) \cdot D \right] \equiv \text{Tr}\left[P \cdot \frac{\partial D^\dagger}{\partial U_\mu(n)} \, \dot{U}_\mu(n) \cdot D \right] \, ,$$

where the trace has to be carried out on all indices. Similar steps can be done for the other terms, the second one and those included in the hermitian conjugated part. Reintroducing the index k, we can define the projector

$$P_k \equiv X_k \otimes X_k^\dagger \, ,$$

whose name emphasises the fact that $(P_k)_{n,m} \neq 0$ only if n and m are both even lattice site, since the pseudofermion field lives on even sites only. Eventually, we obtain

$$\frac{\mathrm{d}}{\mathrm{d}t}\left[\phi^\dagger \cdot (D^\dagger D)^{-\frac{1}{4}N_f} \cdot \phi \right] =$$

$$= -\sum_{k=1}^{N} c_k \sum_{n,\mu} \text{Tr}\left[P_k \cdot \frac{\partial D^\dagger}{\partial U_\mu(n)} \, \dot{U}_\mu(n) \cdot D + P_k \cdot D^\dagger \cdot \frac{\partial D}{\partial U_\mu(n)} \, \dot{U}_\mu(n) \, + \text{h.c.} \right] , \qquad (3.25)$$

where, in order to be able to write +h.c., the fact that $P_k = P_k^\dagger$ has to be used together with the cyclic property of the trace.

Gathering together the results obtained in Eqs. (3.21), (3.22) and (3.25), we can write down the time derivative of the Hamiltonian of our system,

$$\dot{\mathcal{H}} = \sum_{n,\mu} \Bigg\{ \text{Tr}_c\left[H_\mu(n) \, \dot{H}_\mu(n) \, - \frac{\beta}{6}\left(\dot{U}_\mu(n) \, V_\mu(n) \, + \, V_\mu^\dagger(n) \, \dot{U}_\mu^\dagger(n) \right) \right] +$$

$$- \sum_{k=1}^{N} c_k \, \text{Tr}_c \, \text{Tr}_s\left[P_k \cdot \frac{\partial D^\dagger}{\partial U_\mu(n)} \, \dot{U}_\mu(n) \cdot D + P_k \cdot D^\dagger \cdot \frac{\partial D}{\partial U_\mu(n)} \, \dot{U}_\mu(n) \, + \text{h.c.} \right] \Bigg\} , \quad (3.26)$$

where we explicitly wrote the traces in the colour (Tr_c) and in the coordinates (Tr_s) spaces. Inserting the equation of motion

$$\dot{U}_\mu(n) \, = \imath \, H_\mu(n) \cdot U_\mu(n) \qquad (3.27)$$

of the gauge field into Eq. (3.26) and using again the cyclic property of the trace lead to

$$\dot{\mathcal{H}} = \sum_{n,\mu} \Bigg\{ \text{Tr}_c\left[H_\mu(n) \, \dot{H}_\mu(n) \, - \imath \, \frac{\beta}{6} \, H_\mu(n) \left(U_\mu(n) \, V_\mu(n) \, - \text{h.c.} \right) \right] +$$

$$
-\sum_{k=1}^{N} \imath\, c_k\, \mathrm{Tr}_c\, \mathrm{Tr}_s\Bigg[H_\mu(n) \left(U_\mu(n) \cdot D \cdot P_k \cdot \frac{\partial D^\dagger}{\partial U_\mu(n)} + U_\mu(n) \cdot P_k \cdot D^\dagger \cdot \frac{\partial D}{\partial U_\mu(n)} - \mathrm{h.c.}\right)\Bigg]\Bigg\} =
$$

$$
= \sum_{n,\mu} \mathrm{Tr}_c \Bigg\{ H_\mu(n) \Bigg[\dot{H}_\mu(n) - \imath\, \frac{\beta}{6}\left(U_\mu(n)\, V_\mu(n) - \mathrm{h.c.}\right) +
$$

$$
- \sum_{k=1}^{N} \imath\, c_k\, \mathrm{Tr}_s\left(U_\mu(n) \cdot D \cdot P \cdot \frac{\partial D^\dagger}{\partial U_\mu(n)} + U_\mu(n) \cdot P \cdot D^\dagger \cdot \frac{\partial D}{\partial U_\mu(n)} - \mathrm{h.c.}\right)\Bigg]\Bigg\} . \quad (3.28)
$$

Before going on seeing what happens when we impose $\dot{\mathcal{H}} = 0$, let us define

$$
Q_\mu^k(n) \equiv \mathrm{Tr}_s\left(D \cdot P \cdot \frac{\partial D^\dagger}{\partial U_\mu(n)} + P \cdot D^\dagger \cdot \frac{\partial D}{\partial U_\mu(n)}\right) ,
$$

in order to deal with more compact equations. Observe that such a definition can be used in the last line of Eq. (3.28), because the link $U_\mu(n)$ can be brought out of the spatial trace (it is diagonal in the coordinate space). To have the Hamiltonian conserved in time, it is enough to require the expression in the square bracket of Eq. (3.28) to be proportional to the identity matrix in the colour space. In fact, since $H_\mu(n)$ is a field of the algebra $su(3)$, it is already traceless. Indicating with θ a constant that we will fix in a moment, we have

$$
\dot{H}_\mu(n) + \imath \left[-\frac{\beta}{6}\left(U_\mu(n)\, V_\mu(n) - \mathrm{h.c.}\right) - \sum_{k=1}^{N} c_k \left(U_\mu(n)\, Q_\mu^k(n) - \mathrm{h.c.}\right)\right] = \theta\, \mathbb{1}_c .
$$

Forcing $\imath\, \dot{H}_\mu(n)$ to be equal to the traceless part of the matrix in the square bracket, we can fix θ in order to fulfil the equation. Vice versa, it is also possible to obtain $\imath\, \dot{H}_\mu(n)$ fixing θ in order to cancel the trace of the quantity $C_\mu(n) - C_\mu^\dagger(n)$ in the square bracket. In fact, from the definition of the traceless anti-hermitian part of a colour matrix,

$$
M_{\mathrm{TA}} \equiv \frac{1}{2}\left(M - M^\dagger\right) - \frac{1}{6}\, Tr_C\left(M - M^\dagger\right) \mathbb{1}_c , \quad (3.29)
$$

it follows that

$$
C_\mu(n) - C_\mu^\dagger(n) = 2\left[C_\mu(n)\right]_{\mathrm{TA}} + \frac{1}{3}\, \mathrm{Tr}_c\left[C_\mu(n) - C_\mu^\dagger(n)\right] \mathbb{1}_c ,
$$

which imply

$$
\imath\, \dot{H}_\mu(n) = -\frac{\beta}{3}\left[U_\mu(n)\, V_\mu(n)\right]_{\mathrm{TA}} - \sum_{k=1}^{N} 2\, c_k \left[U_\mu(n)\, Q_\mu^k(n)\right]_{\mathrm{TA}} , \quad (3.30)
$$

after having set

$$
\theta = \frac{\imath}{3}\, \mathrm{Tr}_c\left(C_\mu(n) - C_\mu^\dagger(n)\right) .
$$

In Eq. (3.30), it could seem strange that we did not take the traceless anti-hermitian part only once, putting all the terms together. Actually, to do so, since inside $Q_\mu^k(n)$ there is a trace in the coordinate space, it has to be shown that $\mathrm{Tr}_s(M_{\mathrm{TA}}) = \left[\mathrm{Tr}_s(M)\right]_{\mathrm{TA}}$. It is straightforward,

$$
\mathrm{Tr}_s\left(M_{\mathrm{TA}}\right) = \frac{1}{2}\left(\mathrm{Tr}_s M - \mathrm{Tr}_s\left(M^\dagger\right)\right) - \frac{1}{6}\, \mathrm{Tr}_s\, \mathrm{Tr}_c\left(M - M^\dagger\right) \mathbb{1}_C =
$$

$$
= \frac{1}{2}\left(\mathrm{Tr}_s M - \left(\mathrm{Tr}_s M\right)^\dagger\right) - \frac{1}{6}\, \mathrm{Tr}_c\, \mathrm{Tr}_s\left(M - M^\dagger\right) \mathbb{1}_C =
$$

$$
= \frac{1}{2}\left(\mathrm{Tr}_s M - \left(\mathrm{Tr}_s M\right)^\dagger\right) - \frac{1}{6}\, \mathrm{Tr}_c\left(\mathrm{Tr}_s M - \left(\mathrm{Tr}_s M\right)^\dagger\right) \mathbb{1}_C = \left[\mathrm{Tr}_s(M)\right]_{\mathrm{TA}} .
$$

Therefore,

$$\imath \, \dot{H}_\mu(n) = \left[U_\mu(n) \left(-\frac{\beta}{3} \, V_\mu(n) \, - 2 \sum_{k=1}^{N} c_k \, Q_\mu^k(n) \right) \right]_{\mathrm{TA}} .$$ (3.31)

This is the equation of motion of the gauge momenta field and it is what we were looking for. Nevertheless, there is still another simplification which can be done in $Q_\mu^k(n)$, especially useful in a practical implementation. Writing explicitly the spatial indices, we have

$$
\begin{aligned}
Q_\mu^k(n) &= \mathrm{Tr}_s \left[D \cdot P_k \cdot \frac{\partial D^\dagger}{\partial U_\mu(n)} + P_k \cdot D^\dagger \cdot \frac{\partial D}{\partial U_\mu(n)} \right] = \\[2mm]
&= \mathrm{Tr}_s \left[(D \, X_k) \cdot X_k^\dagger \cdot \frac{\partial D^\dagger}{\partial U_\mu(n)} + X_k \cdot (D \, X_k)^\dagger \cdot \frac{\partial D}{\partial U_\mu(n)} \right] = \\[2mm]
&= \sum_{n_1, n_2} \left[(D \, X_k)_{n_1} \left(X_k^\dagger \right)_{n_2} \left(\frac{\partial D^\dagger}{\partial U_\mu(n)} \right)_{n_2, n_1} + (X_k)_{n_1} \left((D \, X_k)^\dagger \right)_{n_2} \left(\frac{\partial D}{\partial U_\mu(n)} \right)_{n_1, n_2} \right] = \\[2mm]
&= \sum_{n_1, n_2} \left\{ (D \, X_k)_{n_1} \left(X_k^\dagger \right)_{n_2} \left[-\frac{1}{2} \eta_\mu(n) \right] \delta_{n_2, n} \, \delta_{n_1, n+\hat{\mu}} + \right. \\[2mm]
&\qquad\qquad \left. + (X_k)_{n_1} \left((D \, X_k)^\dagger \right)_{n_2} \left[\frac{1}{2} \eta_\mu(n) \right] \delta_{n_2, n} \, \delta_{n_1, n+\hat{\mu}} \right\} = \\[2mm]
&= -\frac{1}{2} \eta_\mu(n) \, (D \, X_k)_{n+\hat{\mu}} \left(X_k^\dagger \right)_n + \frac{1}{2} \eta_\mu(n) \, (X_k)_{n+\hat{\mu}} \left((D \, X_k)^\dagger \right)_n ,
\end{aligned}
$$

where Eq. (3.23) has been used. Keeping in mind that the pseudofermion field is defined only on even lattice sites[7], it follows that X_k is, too. This because the matrix $D^\dagger D$ connects only sites with the same parity – as shown in Eq. (3.9) – and so does the matrix $(D^\dagger D + p_k)^{-1}$ present in the definition of X_k. In conclusion,

$$
Q_\mu^k(n) = \begin{cases}
-\frac{1}{2} \eta_\mu(n) \, (D \, X_k)_{n+\hat{\mu}} \left(X_k^\dagger \right)_n & \text{if } n \text{ is EVEN} \\[3mm]
+\frac{1}{2} \eta_\mu(n) \, (X_k)_{n+\hat{\mu}} \left((D \, X_k)^\dagger \right)_n & \text{if } n \text{ is ODD}
\end{cases} ,
$$

or, using the even-odd representation of D,

$$
Q_\mu^k(n) = \begin{cases}
-\frac{1}{2} \eta_\mu(n) \, (D_{oe} X_e^k)_{n+\hat{\mu}} \left((X_e^k)^\dagger \right)_n & \text{if } n \text{ is EVEN} \\[3mm]
+\frac{1}{2} \eta_\mu(n) \, (X_e^k)_{n+\hat{\mu}} \left((D_{oe} X_e^k)^\dagger \right)_n & \text{if } n \text{ is ODD}
\end{cases} .
$$ (3.32)

Eqs. (3.27) and (3.31) form a system of coupled, differential equations that can be numerically integrated to make the gauge and gauge momenta fields evolve. Hence, a dimensionless and fictitious time is introduced and how long the equation of motions have to be integrated is somehow arbitrary. Often the time interval is set to one and people refer to it as *Monte Carlo trajectory length*.

During the molecular dynamics part of the RHMC, a numeric error due to the fact that the equations of motion cannot be integrated analytically is unavoidable. Clearly, using better integrators – so are called the numeric algorithms that make the gauge and the gauge momenta fields evolve for a usually small amount of time – it is possible to reduce such an error. Nevertheless, this leads to a change in the Hamiltonian that could make the system drift towards unphysical

---

[7]If, at the beginning, the field ϕ is introduced only on odd sites, here the discussion has to be adapted, interchanging *even* with *odd*.

situations if not corrected[8]. It is therefore crucial to make a Metropolis test to decide whether the candidate for the new configuration is good enough or not. Basically, whenever the numeric error is too large, the Hamiltonian of the system will change a lot and this fact can be used to discard the candidate. More in detail, if the Hamiltonian $\mathcal{H}_{new}$ evaluated on the new configuration is smaller than or equal to $\mathcal{H}_{old}$ evaluated using the previous one, then the new configuration is accepted. If, instead, $\mathcal{H}_{new} > \mathcal{H}_{old}$, the new configuration will be accepted with probability

$$p = e^{\mathcal{H}_{old} - \mathcal{H}_{new}} \ .$$

The Metropolis test at the end of each Monte Carlo update makes the RHMC algorithm exact. The only cost which has to be paid is that symplectic, reversible integrators must be used. This fact is crucial for the Markov process to satisfy the detailed balance principle. We will not discuss further this point, since the topic is standard and most books on the topic discuss it. A study of symplectic integrators for hybrid Monte Carlo algorithms has been carried out in 2006 by P. de Forcrand and T. Takaishi [77]. It should be intuitive that the more precisely the equations of motion are integrated the more probable is that the new configuration is accepted. It is important to monitor the acceptance rate ω during a Monte Carlo simulation, since it will give an idea of how fast the simulation is exploring the phase space of the system. It is defined as the ratio between the number of accepted new configurations and the total number of Monte Carlo updates. To get a good estimate of any observable, ω cannot be too low and, in principle, the higher the better, because moving faster in the phase space means that the configurations are less correlated between each others (the concept of autocorrelation will be discussed in §3.3). However, to have a more precise molecular dynamics update is numerically more costly and it requires more time. Therefore, a compromise is needed and usually the integration step is tuned such that $\omega \gtrsim 75\%$.

§ 3.1.6   Some further comments

Now that the structure of the RHMC algorithms has been explained in detail, we can further discuss few aspects that could be not completely trivial, especially to the less experienced Reader.

The precision of the rational approximations

In §3.1.3 we said that, fixed an order N of the rational approximation, there exist optimal coefficients a_k and b_k that can be determined, for example, with the Remez algorithm. In general, this implies a new source of errors in the RHMC algorithm: On one hand, because of the precision with which the coefficients are determined and, on the other, because of how well the rational expansions approximate the original functions. It is important to understand how to keep the situation under control. Strictly speaking, if the maximum allowed error is forced to be smaller than the machine precision – typically $\approx 10^{-15}$ – then there would be no new numeric error due to the rational approximations. Actually, this is the case in the determination of the coefficients a_k and b_k, since this calculation has to be usually done only once at the beginning of the RHMC. To increase, instead, the precision with which the rational expansions approximate the original functions is necessary to increment N and this leads to a potentially big overhead in the simulation (the bigger is N the more equations have to be solved in the multi-shift solver and the more algebra has to be done in general). Hence, to require machine precision here as well is too conservative. Indeed, it is not needed either. Already in other parts of the RHMC, whenever we have to use the solver to invert the Dirac matrix, we accept a small numeric error. It is, then, enough to demand the precision of the rational approximations to be higher of that of the solvers.

The Reader could wonder why we spoke so far about more than one rational approximation only. In the Heat bath algorithm on the pseudofermion field and in the molecular dynamics two different

---

[8]In the past, the so-called R-algorithm [76] was used, but this was correct only in the limit of an infinitesimally small time-step δt in the integration of the equation of motions of the microcanonical update. Using it without correctly extrapolating $\delta t \to 0$ led to partially incorrect results, as shown, for example, in [57].

non-integer powers of the Dirac matrix have to be used and, then, approximated. The latter is also needed in the Metropolis test to evaluate $\mathcal{H}$. Therefore, at least two rational approximations are needed. Actually, it has been shown [78] that it is advantageous to use three. Any numeric inaccuracy in the microcanonical update only alters the acceptance rate of the Metropolis test, while any numeric error in the Heat bath and/or in the Metropolis test affects the fixed point of the Markov process and, thus, the physical correctness of the algorithm. It is possible, then, to be a bit less precise in the molecular dynamics part of the RHMC in order to be faster. This technique is already used choosing two different precisions for the inversions of the Dirac matrix. Analogously, two different precisions of the rational approximations of

$$(D^\dagger D)^{-\frac{1}{4} N_f}$$

can be used. This implies to have different orders N depending on where the rational expansion is used. Typically, $N \simeq 8$ in the molecular dynamics part and $N \simeq 18$ elsewhere.

Introducing a purely imaginary chemical potential

In §2.3 we discussed in detail what happens in QCD when a purely imaginary chemical potential is introduced. Now we would like to discuss how this can be implemented in practice, namely how the RHMC algorithm has to be modified in order to include $\mu = \imath\,\mu_I \neq 0$. It is not difficult and, in theory, the only aspect that changes is the explicit form of the Dirac matrix, since the action that has now to be considered is that in Eq. (2.5) at page 52. Said in other words, in the implementation of the Dirac operator, the time direction will have to be treated differently, including some prefactors in front of the gauge links. Moreover, some other modifications have to be done. They regard mainly the force term, namely the time derivative of the gauge momenta field.

It is possible to repeat all the calculation in §3.1.5 using the new form of D,

$$D_{n,m} = \hat{M}_0\,\delta_{n,m} + \frac{1}{2}\left\{ \sum_{\mu=1}^{3} \eta_\mu(n)\left[U_\mu(n)\,\delta_{n,m-\hat\mu} - U_\mu^\dagger(n-\hat\mu)\,\delta_{n,m+\hat\mu}\right] + \right.$$

$$\left. + \eta_4(n)\left[e^{\,\imath\hat\mu_I} U_4(n)\,\delta_{n,m-\hat4} - e^{\,-\imath\hat\mu_I} U_4^\dagger(n-\hat4)\,\delta_{n,m+\hat4}\right]\right\} , \quad (3.33)$$

but we leave this as exercise to the Reader. We will just highlight the main differences and report the result. First of all, it is worth observing that the gauge part of the action does not change, because in any plaquette containing links in the time direction both the factor $e^{\,\imath\hat\mu_I}$ and $e^{\,-\imath\hat\mu_I}$ are present and cancel each other. Therefore, calculating $\dot{\mathcal{H}}$ using Eq. (3.20), only the time derivative of the third term will change introducing a non-zero purely imaginary chemical potential. Nevertheless, it is possible to prove that Eqs. (3.24) still hold. For example, we have that

$$\frac{\partial (D)_{nm}}{\partial U_\rho(k)} = \frac{1}{2}\left[1 + \delta_{\rho,4}\left(e^{\,+\imath\hat\mu_I}-1\right)\right]\eta_\rho(k)\,\delta_{k+\hat\rho,m}\,\delta_{k,n}$$

$$\frac{\partial (D^\dagger)_{nm}}{\partial U_\rho^\dagger(k)} = \frac{1}{2}\left[1 + \delta_{\rho,4}\left(e^{\,-\imath\hat\mu_I}-1\right)\right]\eta_\rho(k)\,\delta_{k+\hat\rho,n}\,\delta_{k,m} ,$$

from which it follows that

$$\left(\frac{\partial D}{\partial U_\rho(k)}\right)^\dagger = \left(\frac{\partial D^\dagger}{\partial U_\rho^\dagger(k)}\right) .$$

These properties ensures that also Eq. (3.28) holds. Also the definition of $Q_\mu^k(n)$ stays the same, but in its evaluation there will be a prefactor that discriminates between the time and the spatial

directions. It can be shown that

$$Q_\mu^k(n) \ = \ \left[1 + \delta_{\rho,4}\left(e^{+\imath\hat{\mu}_\imath} - 1\right) \right] \cdot \left[\, Q_\mu^k(n) \, \right]_{\hat{\mu}_\imath = 0}$$

or, more explicitly, that the analogue of Eq. (3.32) is

$$Q_\mu^k(n) \ = \ \left[1 + \delta_{\rho,4}\left(e^{+\imath\hat{\mu}_\imath} - 1\right) \right] \cdot \begin{cases} -\frac{1}{2}\eta_\mu(n) \left(D_{oe} X_e^k\right)_{n+\hat{\mu}} \left(\left(X_e^k\right)^\dagger\right)_n & \text{if } n \text{ is EVEN} \\[2ex] +\frac{1}{2}\eta_\mu(n) \left(X_e^k\right)_{n+\hat{\mu}} \left(\left(D_{oe} X_e^k\right)^\dagger\right)_n & \text{if } n \text{ is ODD} \end{cases} \ .$$

The multiple pseudofermions technique

In §3.1.2 we introduced the pseudofermion field in order to rewrite the fermion determinant in a more convenient way. The Heat bath algorithm on the field ϕ is, then, just a way to get an estimate of $\det D$. The attentive Reader could be wondering if it is correct to use only one value of the pseudofermion field to evaluate the functional integral

$$(\det D)^{\frac{1}{4}N_f} \ \propto \ \int \mathcal{D}\phi \, \mathcal{D}\phi^\dagger \ e^{-\left[\phi^\cdot \cdot (D^\dagger D)^{-\frac{1}{4}N_f} \cdot \phi\right]_{\text{EVEN}}} \ .$$

Indeed it is, since it leads to a Markov process with the correct fixed point, but it is true that there could be an advantage in using different values for the field ϕ. This is the idea behind the so-called *multiple pseudofermions* technique proposed by A. D. Kennedy and Clark [71] in 2006. They suggested to rewrite the determinant as

$$(\det D)^{\frac{1}{4}N_f} \ = \ \left[(\det D)^{\frac{1}{4K}N_f} \right]^K \ \propto \ \prod_{j=1}^{K} \int \mathcal{D}\phi_j \, \mathcal{D}\phi_j^\dagger \ e^{-\left[\phi_j^\cdot \cdot (D^\dagger D)^{-\frac{1}{4K}N_f} \cdot \phi_j\right]_{\text{EVEN}}} \ . \tag{3.34}$$

Without entering the details of why it is advantageous and of when this technique should be used – which can be found in [71] together with a criterion to choose the number K of pseudofermions – let us discuss which part of the RHMC algorithm has to be modified in order to use more than a single pseudofermion field.

The first remark is that different rational approximations will have to be calculated, because the non-integer power of the fermionic determinant has changed[9]. Secondly, a Heat bath algorithm will be needed per each field ϕ_j. This is easily done drawing a field R_j according to a Gaussian distribution and reconstructing the pseudofermion field as

$$\phi_j \ = \ \left(D^\dagger D\right)^{\frac{1}{8K}N_f} \cdot R_j \qquad \forall \, j \in [1, \ldots, K] \ .$$

Lastly, it has to be understood how the molecular dynamics equations get modified. The Hamiltonian of the system becomes

$$\mathcal{H} = \frac{1}{2} \sum_{n,\mu} \text{Tr}_c\left[H_\mu^2(n)\right] + \frac{6}{g_0^2} \sum_n \sum_{\mu<\nu} \left[1 - \frac{1}{3}\Re\left(\text{Tr}_c \, \Pi_{\mu\nu}(n)\right) \right] + \sum_{j=1}^K \phi_j^\dagger \cdot (D^\dagger D)^{-\frac{1}{4K}N_f} \cdot \phi_j$$

and, therefore, the equation of motion of the gauge momenta field will change accordingly. Let us see which are the main differences in the calculation done in §3.1.5. Taking the time derivative of $\mathcal{H}$, nothing will change about the first two terms. Considering the last one, we will have to carry around the sum over the pseudofermion index j that will appear on ϕ and therefore also on X_k and P_k. In particular, we will have

$$X_{kj} \equiv \left(D^\dagger D + p_k\right)^{-1} \cdot \phi_j$$

---

[9]Observe that this fact can be used in a smart way to use an RHMC algorithm as a HMC one. In principle, if $N_f \, (\text{mod}\,4) = 0$, there is no reason to use a rational algorithm and, actually, the Remez algorithm fails for obvious reasons. But using two or more pseudofermions requires the use of a rational algorithm, no matter the value of N_f.

and

$$P_{kj} \equiv X_{kj} \otimes X_{kj}^{\dagger} \ .$$

In the end, without any conceptual difficulty, we will obtain

$$\imath \, \dot{H}_{\mu}(n) = \left[U_{\mu}(n) \left(-\frac{\beta}{3} \, V_{\mu}(n) \, - 2 \sum_{j=1}^{K} \sum_{k=1}^{N} c_k \, Q_{\mu}^{kj}(n) \right) \right]_{\mathrm{TA}} \ ,$$

where

$$Q_{\mu}^{kj}(n) \ = \ \begin{cases} -\frac{1}{2}\eta_{\mu}(n) \left(D_{oe} \, X_e^{kj} \right)_{n+\hat{\mu}} \left(\left(X_e^{kj} \right)^{\dagger} \right)_n & \text{if } n \text{ is EVEN} \\[2ex] +\frac{1}{2}\eta_{\mu}(n) \left(X_e^{kj} \right)_{n+\hat{\mu}} \left(\left(D_{oe} \, X_e^{kj} \right)^{\dagger} \right)_n & \text{if } n \text{ is ODD} \end{cases} \ .$$

In CL²QCD, the multiple pseudofermions technique has not yet been implemented, but it will be soon included.

§ 3.2   The CL²QCD software

Lattice QCD is clearly one of the closest fields of physics to computer science and needs, year after year, more and more computing power as well as smart techniques to make simulations faster and more efficient. Only one decade ago, many calculations seemed almost impossible and, instead, they have been carried out; problems that appeared unapproachable have been addressed with good results. Of course, many issues remain difficult to be tackled, but, for sure, the numeric effort in the community is big and the technology in continuous evolution. On the other hand, the algorithms that are needed most of the time are quite standard and this led some collaborations to develop public software that can be, then, used by other people. Unfortunately, a third party program may not fit with the own needs, because of some missing features or due to technical reasons, like a particular architecture requirement. This is the main reason why, nowadays, dozens of different codes are available. It could be thought that it is not an efficient way to work and that having less but more general libraries would be better. To some extent this is true, but it has to be considered that, in the end, to have the same feature implemented in different software and used in different groups can mean to have indirect checks on the physics results.

Most people in the community, use standard Central Processing Units (CPUs) in order to carry out their simulations. At the beginning, any program was executed on a single core of a single CPU, but soon it has been realised that the only way to face new problems was to parallelise the calculations. This led to the construction of bigger and bigger supercomputers (also called *clusters*) that allowed on one side to reach finer lattice spacings (simulating bigger lattice volumes) and on the other to make studies requiring huge parameters scans (e.g. finite temperature investigations). Moreover, today, a typical CPU has about ten cores and this allows easier parallelisations[10]. There are many publicly available LQCD codes: openQCD developed mainly by M. Lüscher and S. Schäfer[11], tmLQCD of C. Jansen and C. Urbach [79] and the MILC code[12].

Despite this way of programming may appear satisfactory, at the beginning of the 2000s a revolutionary idea stepped into the field: The use of General Purpose Graphics Processing Units (GPGPUs), which we will call, for simplicity, just GPUs. Computations that are generally handled by the CPU can be accelerated on the GPU . The natural task of a GPU is to update the pixels of the display of a computer and this means that a GPU is composed by many processors, each working on few pixels. This is clearly something that can and has to be done in parallel. The brilliant idea was, roughly speaking, to make a matrix entry or a lattice site play the role of a pixel. In this way, an algebra operation on a field could be done on each lattice site at the same time. The gain turned out

---

[10] In particular, this helps in the development of a parallel code that can be tested also having only one CPU.

[11] See `http://luscher.web.cern.ch/luscher/openQCD/`.

[12] See `http://www.physics.utah.edu/~detar/milc/`.

to be not only in time but also in money and, after a couple of years, programs started to perform better and run faster on `GPUs` than on `CPUs`. Soon, `GPU` supercomputers appeared and they are, by now, quite widely used. Clearly, the transition from a `CPU` code to a `GPU` one is neither immediate nor trivial. Due to technical reasons, mostly related to the fact that it is a young business, to get a program running correctly and efficiently on a graphic card is more complicated than to get it right on a normal `CPU`. Moreover, there are important differences between different `GPUs` and, usually, the code has to be optimised again (or even rewritten) to run on a different card. The main two vendors of graphic cards are `AMD` and `nVIDIA`, whose application programming interfaces are `OpenCL` and `CUDA`, respectively. Unlike `OpenCL`, `CUDA`-enabled `GPUs` are only available from `nVIDIA` and this implies that a software that makes use of `CUDA` can only run on `nVIDIA`-cards. Vice versa, programs developed in `OpenCL` are much more portable, even though their optimisation will still depend on which platform they are run.

The mainly used, publicly available code to perform LQCD calculations on `GPUs` is `QUDA` [80, 81]. It is a library entirely based on `CUDA`, that provides a very wide set of actions and auxiliary operations with which the user can easily build its own software. Nevertheless, it is limited to `nVIDIA` graphic cards. There exist clusters that are built with `AMD GPUs` and, in order to use them, a different code is needed. For example, the `LOEWE-CSC` [82] and the `L-CSC` [83] supercomputers are provided with `AMD` graphic cards and software using `QUDA` cannot be run on them. This is the main motivation that led to the decision to develop a first LQCD code entirely based on `OpenCL` and, thus, independent from the architecture[13]. So came to the light CL^2QCD [84–87]. The initial project was quite modest, though original, and the physics goal was to develop a HMC algorithm with unimproved and twisted mass Wilson fermions[14]. In 2013, it was decided to also include in CL^2QCD the unimproved staggered formulation, implementing an RHMC algorithm. Many new features had to be developed, but overall the design of the software was good enough to absorb this enlargement. One year later, at *the 32nd International Symposium on Lattice Field Theory* the code was made publicly available – it can be downloaded at

$$\boxed{\texttt{https://github.com/CL2QCD/cl2qcd}}$$

In the remaining part of this section we will discuss some aspects of CL^2QCD, trying to give a general overview of it, focusing mainly on the philosophy behind the development of the code and on some details of the implementation of the RHMC algorithm. Even if it would be interesting, we cannot discuss here in detail each feature of the software. The interested Reader can find more information in the above cited references, in the Ph.D. thesis of M. Bach [88] and reading the code itself.

§ 3.2.1   An overview of the code

Let us start this overview by stressing the fact that a code should *not* just work. Even though it could sound obvious to somebody, this statement is far from being the standard in many public codes. Of course a code should do correctly what it is supposed to do, but this is, let us say, a necessary condition for it. to be a good code, not a sufficient one. On top of that, a code should be readable, maintainable, easy to extend, easy to use, hard to break and testable – just to cite some features. These characteristics are rare to be found all together, but they are for sure something we constantly aim to in the development of CL^2QCD. And this is also the reason why several parts of the code have been rewritten in the last years. A constant effort to guarantee a high-quality product is, for sure, a pillar of CL^2QCD. There are several books that help in this direction; our favourite are [89, 90]. Some Reader could be surprised or even puzzled, since this approach seems very time-consuming. Certainly it is, but the payoff on the long term makes it worth. Coding in a

---

[13]This means that the code should work on different heterogeneous platforms and therefore there should be no limitation in running the code on different `GPUs`. Of course, this does not mean that the code will be automatically optimised on any platform.

[14]In this thesis we did not discuss the twisted mass formulations, because it has not been relevant in our work. The Reader interested in it can refer to standard LQCD books – like [18] – or to the original works [33–36].
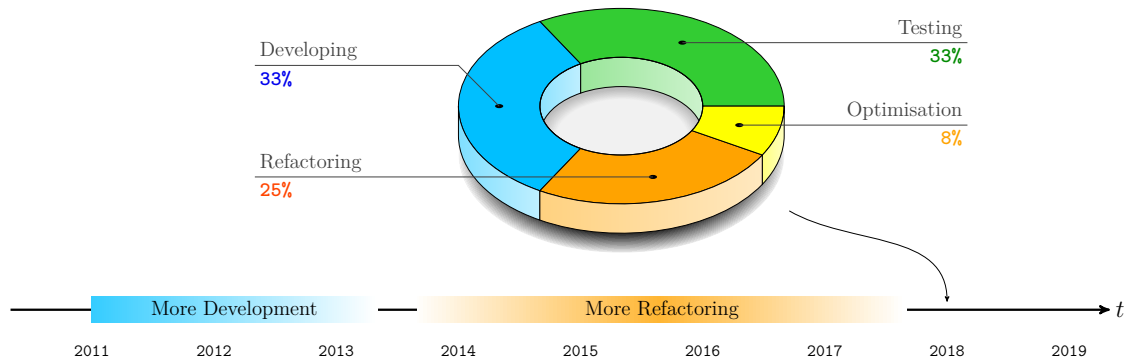
Figure 3.2: *Schematic evolution of the CL²QCD software with respect to the different area of work. The pie chart indicates how, more or less, the workload should be split in ideal conditions.*

way to ensure the qualities listed above will make the code more and more robust and it will also be harder and harder to introduce bugs. It is worth clarifying what it is meant by *readable code*. Sometimes, a program is considered not readable just because it makes use of very advanced notions of the language in which it is written. This is, definitely, nonsense. If a person does not speak a language and travels to the country where such a language is spoken, he/she cannot say that local people are not able to speak properly their language just because he/she does not understand! The fact that the reader of the code knows its programming language is an implicit prerequisite.

From what discussed so far, it should be clear that a good code should be in continuous evolution, especially if, like in the CL²QCD case, some standards were not fulfilled at the beginning. Somehow, we discovered the importance of having a high-quality program when the RHMC with staggered fermions started to be implemented. At that point, it was clear that many parts should have been refactored[15] and we undertook to improve our software. In Figure 3.2 it can be seen that a long phase of refactoring followed a period in which basically only new features were implemented. Nevertheless, even when the code shape is ideal – i.e. it fulfils given standards – some parts shall be refactored to accommodate new features. This aspect is included in the pie chart, which qualitatively depicts how the workload to implement a new algorithm should be split. The standard strategy should be to code it, to write tests to check its correctness (these two steps may be done in the reverse order), to optimise it if its performance is not satisfactory and then to refactor the code to put it in a better shape. It is important to stress that the 8% yellow slice is sometimes bigger, as it could require more work, but it is not always present. Quoting Donald E. Knuth, «*the real problem is that programmers have spent far too much time worrying about efficiency in the wrong places and at the wrong times; premature optimisation is the root of all evil (or at least most of it) in programming*».

Another central aspect to comment on is the 33% green slice, *testing*, which is, in our opinion, as important as the development slice. In CL²QCD, unit tests are implemented for every part of the code, using BOOST[16] and taking advantage of CMake[17] unit tests framework. Their are of crucial importance, mainly for two reasons. On one hand, they allow to check the correctness of the code and, on the other, the better they are written the more probable it is that they will catch any bug possibly introduced by a refactoring of the code. In this regard, they are often used as regression tests, running them immediately after any change, to be sure that everything is still fine. Again, this could be seen as an unnecessary overhead, but there is no better way to save debug time in the future than testing the code! Moreover, writing GPU code in OpenCL, it is absolutely mandatory

---

[15]So is called the process of rewriting part of the code.
[16]See http://www.boost.org/.
[17]See https://cmake.org/.

to have unit tests for each kernel[18]. To understand this point, we have to briefly discuss how a typical `OpenCL` application works. It is based on the interaction of a host, usually a `CPU`, with one or more devices, which can be `CPUs`, `GPUs` or other kind of processors. The host will handle the execution of kernels on the devices. Since, a priori, it is not known on which devices the code will be executed, this has to be compiled only at the run-time of the host, namely when it is clear on which architecture it will be run. Therefore, any kind of error in the kernels, even typos, can be discovered only running them. This is a relevant difference with respect to a standard `CPU` and it basically implies unit tests to be compulsory. It has to be also added that, sometimes, the same code on different devices does not produce the same result and, thus, unit tests should be run before any computation is started on a new architecture. Strictly speaking, unit tests should not depend on each other or, said in another way, the failure of a unit test should not make others fail. The more different parts of a software are directly interconnected the more difficult it is to fulfil this characteristic. Ideally, each part of the code should be independent from the rest and there should be interfaces between different elements, so that each can be substituted by a different implementation without having to change anything else (except, maybe, the interfaces). We have not yet achieved this point in `CL`^{2}`QCD`, but it is definitely something we are aiming to. Somehow, this is an indispensable condition to make the code easier to enlarge, simpler to test and more versatile. As last comment on how the code should be tested, let us observe that any test should not rely on any not universal characteristic. For example, in LQCD there are many operations on fields to be tested. Naïvely, it could be thought that a good test is to randomly draw the field and to use it as input for the calculation. This approach is twice wrong. First of all, it relies on the random number generator and, hence, the same test run on different architectures could have different outcome just because the drawn field is different. Secondly, which reference values are then used? A precise result cannot be predicted, unless another code is run with the same random numbers (not easy to do and neither ideal), and it is almost certain that, changing the random number generator, all the reference values will have to be modified as well. To be honest, we made this mistake in the past but, despite the fact that there are still few unit tests in `CL`^{2}`QCD` which use pseudo-random numbers, we are working on this point. In principle, the reference values for a test should be calculated analytically and, considering that most LQCD operations are local on the lattice, the fields can be chosen to be equal on all lattice sites, without loss of quality in the test. In this way, the volume dependence of the result can be evaluated and often factorised. Because it is not always trivial, we decided to implement Mathematica[19] packages with the basic operations needed to obtain any reference value for any test. Actually, we had this idea at the beginning of 2016 and, at the moment, it is completed only for the kernel tests and it is ongoing for the rest of the code.

It is now time to describe the structure of the code. Without entering too much in the details, the design of `CL`^{2}`QCD` can be illustrated as done in Figure 3.3. There are mainly four areas, which we will call *packages*: hardware, physics, meta and OpenCL kernels. Since the host code is written in `C++` and the code is clearly object oriented, from now on we will speak about *objects* or *classes* – the Reader not familiar with the language can just think to them as units that interact with each other. `CL`^{2}`QCD` has a two-levels structure: The physics and the meta packages compose the high level, while the low one consists of the hardware and the OpenCL kernels packages. Any `OpenCL` semantics is hidden in the low level of the code and, in principle, the user could build up a new application using only ingredients present at the high level, without any knowledge about `GPU` programming languages. This is, without any doubt, a valuable feature of the code. The meta package serves as connection with the user. In it all the possible simulation parameters are stored and, once set, can be used from elsewhere in the code. The meta package has also the responsibility of I/O operations like, for instance, saving a gauge configuration or the pseudo-random number generator (PRNG) state. In the physics package, all the typical ingredients of a LQCD simulation can be found: the lattice fields, the fermion matrices, the PRNG and the noise sources. These

---

[18]So is called the portion of parallel code that is executed on the `GPU`.
[19]https://www.wolfram.com/mathematica/
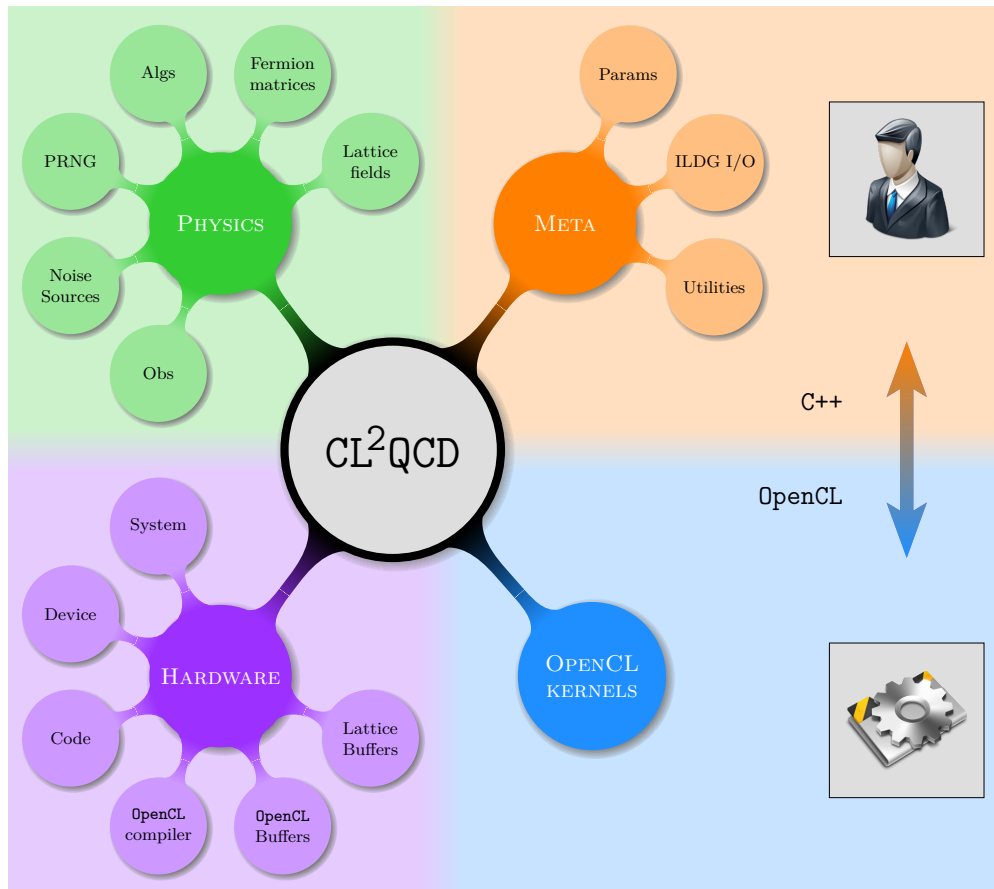
Figure 3.3: *Overview of the structure of the CL²QCD software. The physics and the meta packages represent the high-level functonality, while the hardware package, together with the OpenCL kernels, represents the low-level components. The OpenCL label next to the lower tip of the the arrow is meant to emphasise that it is required only at the low level. The C++ label, instead, only indicates that slightly more advanced feature of the language are used in the physics package (a good knowledge of C++ is needed to read the code).*

are almost exclusively wrappers of operations implemented at the low level of the code. Using them, observable measurements and various algorithms are built up. Moving down in the code, we have the hardware package that constitutes the core of the software. At the beginning of any run, the System object represents the architecture available at run-time. The latter can provide multiple computing devices (e.g. CPUs and/or GPUs), which are represented by Device objects and initialised based on run-time parameters. Each Device object handles code classes, which are instantiated the first time they are needed. During their construction, the OpenCL code contained in the OpenCL kernels package is compiled, making use of the OpenCL compiler. The OpenCL and lattice buffers are objects meant to handle correctly the memory of the devices and to manage the communications between these and the host. Even if we will not discuss the structure of the code more in detail, we reported in Figures 3.4 and 3.5 the content of each part of the physics and hardware packages in Figure 3.3. This, together with [87], should be a good guideline for the Reader who would like to have a look directly to the code.
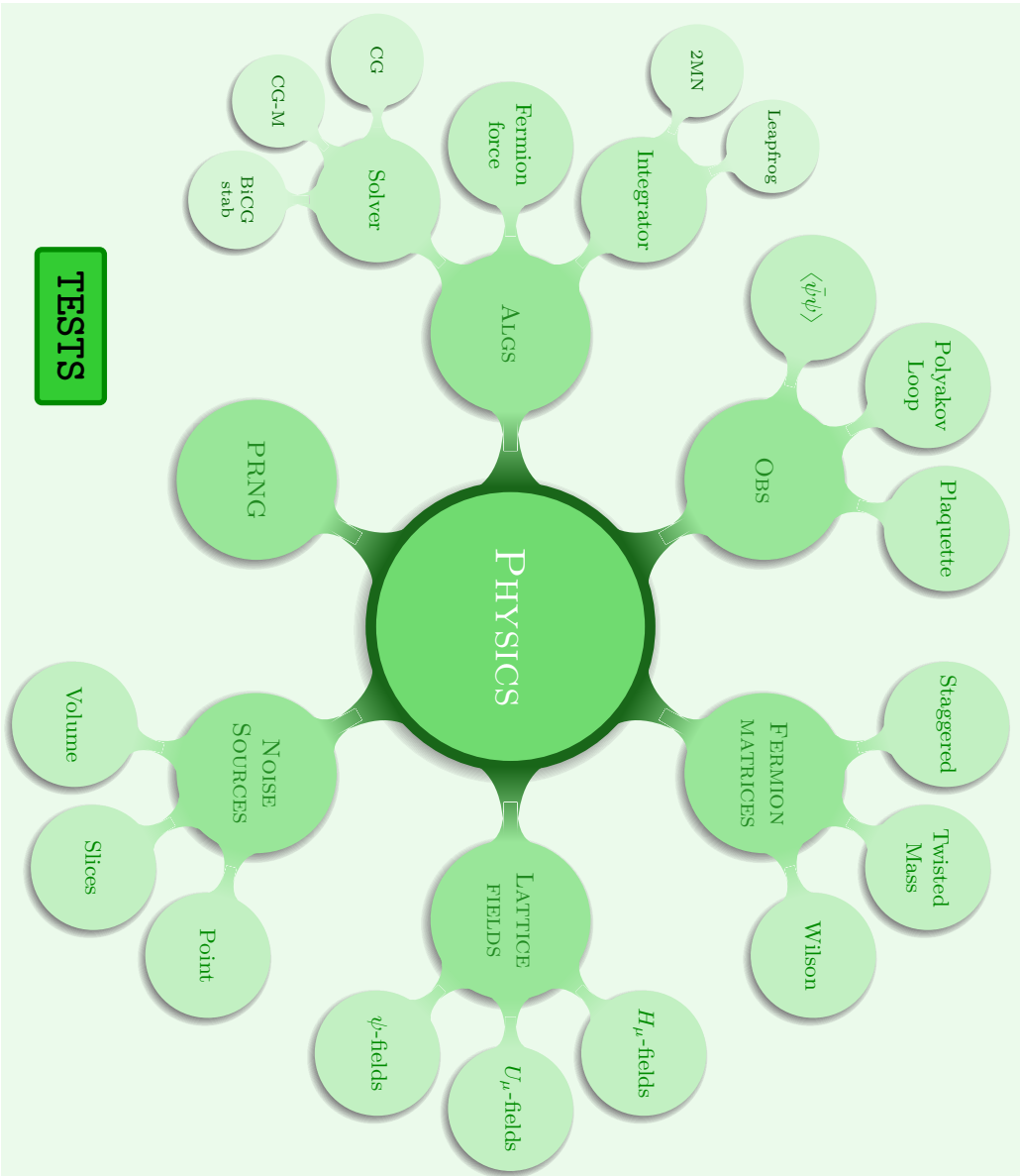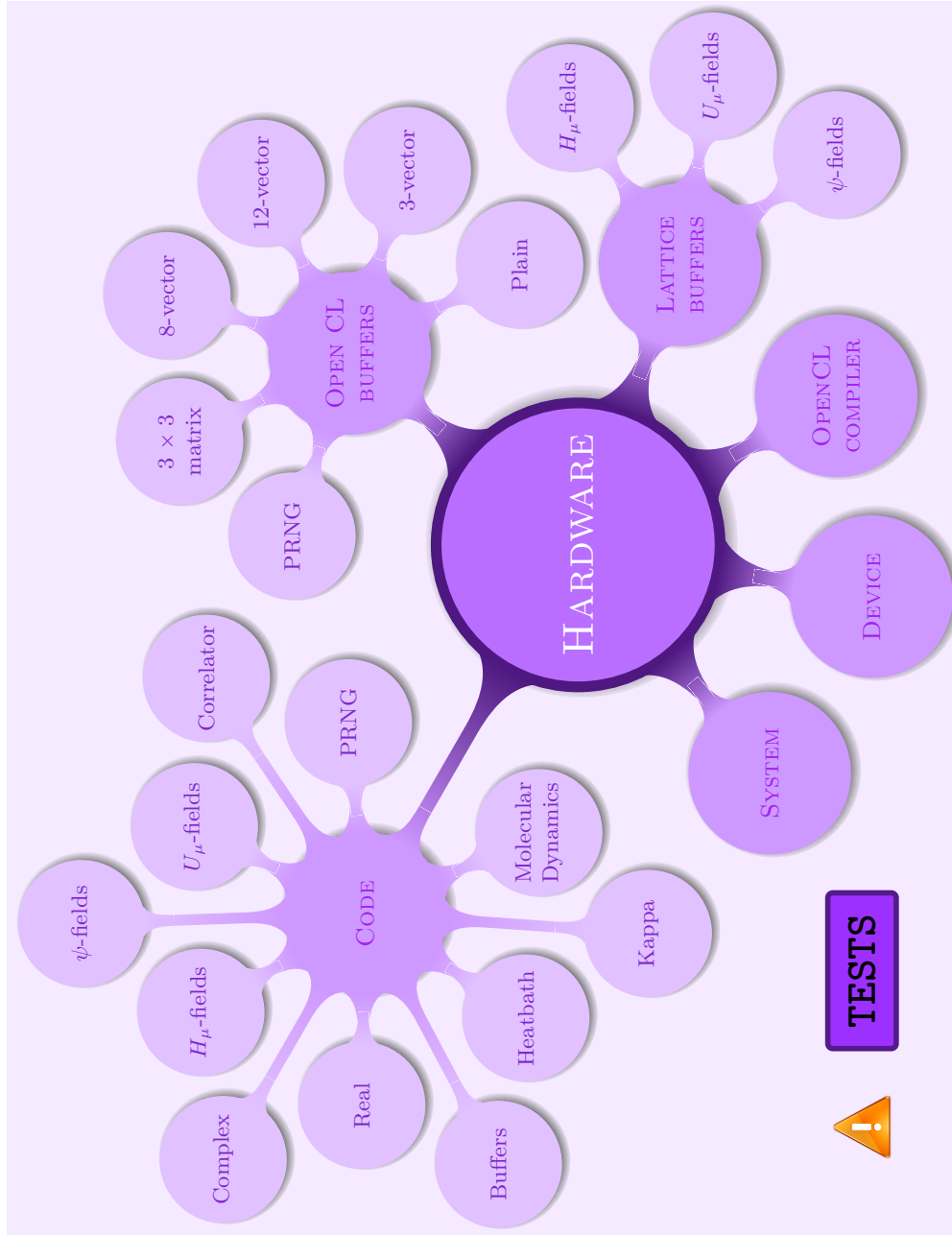
Figure 3.4: *Overview of the* `physics` *package.*

Figure 3.5: *Overview of the* hardware *package. The exclamation mark next to the tests is meant to stress the fact that testing the code modules is of utmost importance, since they are compiled by the host at run-time.*

§ 3.2.2   The RHMC implementation and some benchmarks

An important concept to keep in mind whenever an algorithm has to be accelerated on a `GPU` is that some memory communications between the host and the device are unavoidable. It is possible to define the numerical density ρ of a calculation as the ratio between the number of FLoating-point Operations Per Second (FLOPS) needed and the number of Bytes (B) that have to be communicated (read or written) from and to the device. The smaller is ρ the more an algorithm is memory-bandwidth dominated. This is the case for almost all LQCD operations. For example, in the Wilson formulation, to apply the Dirac operator to a fermion field requires to read and write 2880 B per lattice site, while *only* 1632 FLOPS per site are performed, giving a rather low numerical density, $\rho \simeq 0.57$. In the standard staggered formulation, the situation is even more bandwidth-dominated. In the $D \cdot \phi$ calculation, 570 FLOPS per each lattice site are performed and 1584 B are read or written, with a consequently smaller $\rho \simeq 0.35$. This justifies the decision not to include the staggered phases in the gauge field (as it could be done according to what explained in §3.1.1), but to calculate them whenever needed. Due to the low numerical density, a meaningful measure for the efficiency of any operation is the achieved bandwidth. After the RHMC algorithm had been implemented, we measured the performance of the Dirac operator, which is crucial for the overall speed of the code. After some optimisations, analogous to those needed in the Wilson case [88], we were able to use approximately the 80% of the maximum bandwidth of different `GPUs`, as it can be seen in Figure 3.6. It is worth remarking that, in practice, only the execution time can be measured. This quantity is, then, translated in GFLOPS or GB s^{-1} using the numbers mentioned above. The conversion factors that should be used are the theoretical ones, no matter what is done in the code[20]. Note, also, that the `CL`^{2}`QCD` software can be run on `nVIDIA` graphic cards. The lower performance on this kind of `GPUs` is only due to the fact that no optimisation was carried out here, since `AMD` was the primary development platform.

Algorithm 1 The Power Method

1: Draw randomly a vector $v^{(0)}$, set $k = 1$

2: **repeat**   ▷ Given a matrix A and a precision ε

3:       $w^{(k)} \leftarrow A \cdot v^{(k-1)}$

4:       $v^{(k)} \leftarrow w^{(k)}/\|w^{(k)}\|$ (approximate eigenvector)

5:       $k \leftarrow k + 1$

6: **until** $\|v^{(k)} - v^{(k-1)}\| < \varepsilon$

7: $\lambda_{\max} \leftarrow \left[v^{(k)}\right]^T \cdot A \cdot v^{(k)}$ (approximate eigenvalue)

The information provided so far in this chapter should be more than enough to read the RHMC code. Nevertheless, it is worth spending few more words about the methods used to estimate the maximum and the minimum eigenvalues of the $D^\dagger D$ matrix (Power Method) as well as about the multi-shift solver that was chosen. In this way, the Reader will also have a reference for any new implementation.

The Power Method is a very basic way to estimate the largest eigenvalue of a matrix (and the corresponding eigenvector). In algorithm 1, it has been sketched how it works. It converges if there is a dominant real eigenvalue[21], which is exactly our case. For our purposes, the calculation of $\lambda_{\max}$ can be carried out only once the algorithm has converged. Strictly speaking, it should be ensured that the starting vector $v^{(0)}$ has a non-zero component in the direction of the searched eigenvector,

---

[20]If, for example, some unnecessary operations are done in the implementation and they are taken into account, the code would seem to perform better just because more FLOPs are done!

[21]The convergence of the algorithm is based on the fact that $|\lambda_2/\lambda_1| < 1$, where λ_1 and λ_2 are the largest eigenvalues. For real matrices, if the largest eigenvalue is complex, there will be two complex conjugate eigenvalues such that $|\lambda_1| = |\lambda_2|$ and the algorithm does not converge.
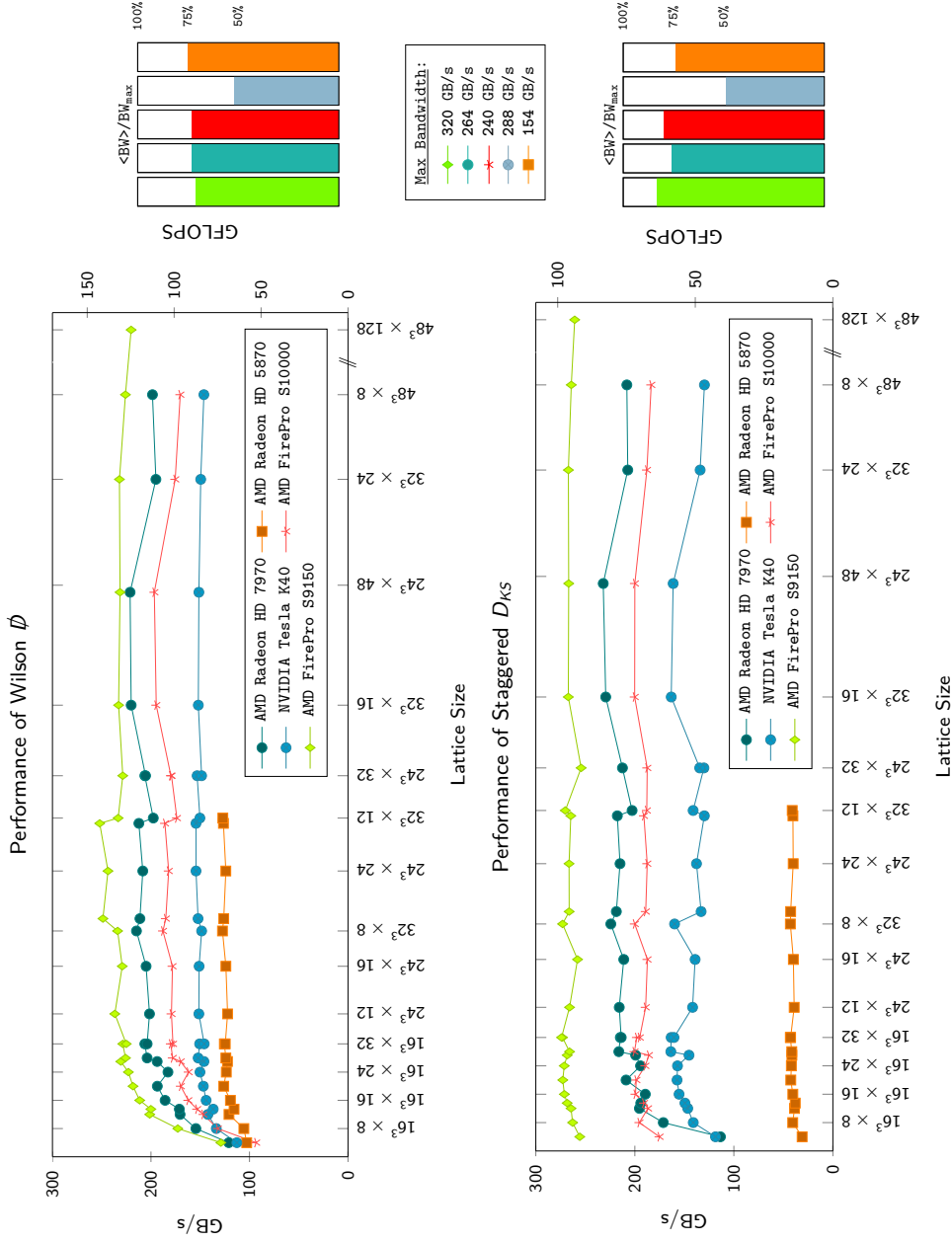
Figure 3.6: *Performance of the Dirac operator applied to a fermion field for various lattice sizes on different devices in double precision. Both with unimproved Wilson and staggered fermions approximately the 80% of the maximum bandwidth is reached on different GPUs. Note that the conversion factor from GB s⁻¹ to GFLOPS depends on the discretisation and this explains why the scale on the right axis changes, even if that on the left one is almost the same.*

otherwise the second largest eigenvalues will be, in principle, found (or the third if $v^{(0)}$ is deficient also in the direction of the second eigenvector, and so on). Actually, this is not a danger we have to worry about, since to have any component of $v^{(0)}$ equal to 0 is a very remote event. In any case, $v^{(k)}$ will have a component in the wished direction because of rounding errors sustained during the iterative procedure. Once found the maximum eigenvalue of the matrix $D^\dagger D$, to find the minimum one it is sufficient to observe that the eigenvector corresponding to the maximum eigenvalue $\mu_{\max}$ of the matrix $\lambda_{\max}\mathbb{1} - D^\dagger D$ is the one corresponding to the minimum eigenvalue $\lambda_{\min}$ of the matrix $D^\dagger D$. It is then sufficient to apply again the Power method to the matrix $\lambda_{\max}\mathbb{1} - D^\dagger D$, having then $\lambda_{\min} = \lambda_{\max} - \mu_{\max}$. More information about how to approach eigenvalue problems can be found in standard textbooks, e.g. [75].

Considering, instead, how to solve the equation

$$(A + \sigma) \cdot x = b \tag{3.35}$$

for a whole set of N values of σ, among the several possibilities [73], we decided to implement the CG - M multi-shift solver. How it works has been sketched in algorithm 2, colouring in blue the fermion fields, in red the fermion matrix and leaving in black all the scalars. Eq. (3.35) is actually a set of N equations, in which the value of σ changes. Nevertheless, no index has been put on the shift σ and exactly the letter σ has been used as index in the algorithm 2 to label quantities referring to different equations. For instance, the solution of Eq. (3.35) will be a set of fields x^σ. The parameter δ determines the precision of the inversion. There is a slight difference with respect to the standard CG algorithm: Here it can happen – and in general it happens – that the different equations converge after a different number of iterations. Continuing to update all the quantities, and in particular those referring to the already converged equations, makes $\left\lVert \zeta_{i+1}^\sigma r_{i+1} \right\rVert$ too small for some σ, causing a rounding to 0, if below the machine precision. This leads to `inf/nan` in the following iteration, since $r_{i+1} = 0$ is then put at denominator. Therefore, the `if`-clause at line 16 is extremely important. In CL²QCD, all the calculations are carried out on the device, but this does not mean that there is a kernel that solves Eq. (3.35). It would be probably inefficient to do so, because, whenever the kernels are too big and/or complicated, the `OpenCL` compiler is not really able to optimise the code. Therefore, only simple operations are done in the kernels. Because of that, the check on the convergence of the single equation has to be performed on the host, copying the residuum from the device. It turned out that doing this at each iteration causes a loss in performance and it is better to do it from time to time. Clearly, decreasing too much the frequency with which the convergence is tested will make the underflow problems that we just discussed arise.

Let us report now on some general tests we performed once the RHMC algorithm was implemented. Despite the fact that each part of the code had been tested on its own, since the algorithm implemented was quite standard, we decided to compare the output of a short run with a reference code, developed in the group of M. D'Elia. In order to keep the simulation time small, we chose the following parameters:

- $N_t \times N_s^3 = 4 \times 4^3$, $\beta = 6.0$, $\hat{M}_0 = 0.5$, $N_f = 2$;

- *cold* start condition with anti-periodic boundary conditions in time for fermions;

- *leapfrog* integrator for the molecular dynamics equations, which have been integrated using 10 steps for a total time interval $\tau = 0.1$;

- Rational Approximations calculated in the range $[10^{-5}, 1]$ (order 15, 8 and 15 for the functions $x^{+2/8}$, $x^{-2/4}$ and $x^{-2/4}$ used in the pseudofermion Heat bath, in the molecular dynamics and in the Metropolis test, respectively);

- multi-shift CG - M solver with precision $\delta^2 = 10^{-12}$ in the molecular dynamics and $\delta^2 = 10^{-23}$ elsewhere.

Algorithm 2 The CG - M solver

1: $\alpha_0 = \alpha_0^\sigma = x_0^\sigma = 0$

2: $r_0 = p_0 = p_0^\sigma = b$

3: $\beta_{-1} = \zeta_{-1}^\sigma = \zeta_0^\sigma = 1$

4: **repeat** ▷ Fixed a precision δ

5:      $\beta_i = -\dfrac{(r_i, r_i)}{(p_i,\ A \cdot p_i)}$

6:      $r_{i+1} = r_i + \beta_i\ A \cdot p_i$

7:      $\alpha_{i+1} = \dfrac{(r_{i+1}, r_{i+1})}{(r_i, r_i)}$

8:      $p_{i+1} = r_{i+1} + \alpha_{i+1}p_i$

9:      **for** $\sigma = 1, \ldots, N$ **do**

10:          **if** equation σ has not been solved yet **then**

11:          $\zeta_{i+1}^\sigma = \dfrac{\zeta_i^\sigma \zeta_{i-1}^\sigma \beta_{i-1}}{\beta_i \alpha_i (\zeta_{i-1}^\sigma - \zeta_i^\sigma) + \zeta_{i-1}^\sigma \beta_{i-1}(1 - \sigma\beta_i)}$

12:          $-\beta_i^\sigma = -\beta_i \dfrac{\zeta_{i+1}^\sigma}{\zeta_i^\sigma}$

13:          $\alpha_{i+1}^\sigma = -\alpha_{i+1} \dfrac{\zeta_{i+1}^\sigma (-\beta_i^\sigma)}{\zeta_i^\sigma \beta_i}$

14:          $p_{i+1}^\sigma = \zeta_{i+1}^\sigma r_{i+1} + \alpha_{i+1}^\sigma p_i^\sigma$

15:          $x_{i+1}^\sigma = x_i^\sigma - \beta_i^\sigma p_i^\sigma$

16:          **if** $\left\| \zeta_{i+1}^\sigma r_{i+1} \right\| < \delta$ **then**

17:              Mark equation σ as solved

18:          **end if**

19:          **end if**

20:      **end for**

21: **until** all equations have have been solved
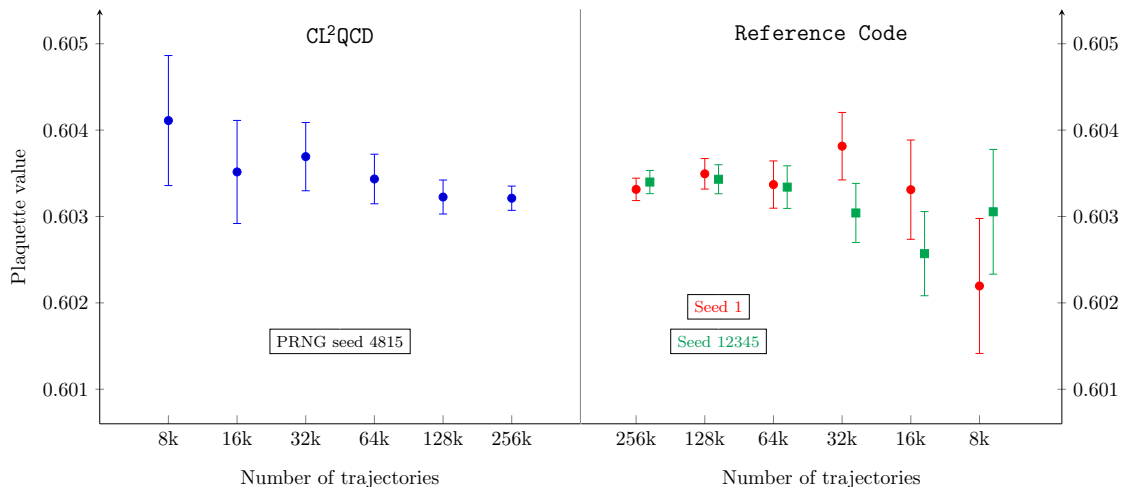
Figure 3.7: *A first overall test of the RHMC algorithm implemented in the* `CL²QCD` *software has been done measuring the plaquette on a test simulation run with a reference code, too. Even if the pseudo-random number generators used by the two software are different, we decided to run twice the reference code with two different seeds. After a sufficiently high number of trajectories, the values of the plaquettes are compatible at the level of one standard deviation.*

At each trajectory, the value of the plaquette has been measured and it has been analysed according to standard techniques, which will be discussed in §3.3. The outcome has been reported in Figure 3.7, where the agreement between the codes does not need further comments.

To conclude, a final general remark on `CL²QCD`. Given a `GPU` and an algorithm, there is a maximum lattice volume which can be simulated, because whenever the needed memory exceeds the available one the execution will fail. This explains, for example, why in Figure 3.6 there are less points for the `AMD Radeon HD 5870`, a quite old card with only $1\,\mathrm{GB}$ of memory. To simulate bigger lattices, then, a further parallelisation splitting the lattice onto different `GPUs` has to be implemented. This is everything but trivial. In `CL²QCD`, the HMC algorithm with Wilson fermions can be run on multiple `GPUs` (splitting the lattice in *only* one direction), while the other algorithms are working only on a single device[22]. This is due to the fact that, so far, we never needed such a functionality. Given that in this thesis the simulations have been run only on a single device, we will not discuss the techniques to split the lattice in several parts – all the details about how it is done in `CL²QCD` can be found in [88].

§ 3.3   The analysis of a generic observable

In this section, we will discuss some aspects of how to elaborate data produced running a Monte Carlo simulation – e.g. how, in practice, to attribute an error to Eq. (3.3) and to quantities derived from it. It would be pretentious to give here a complete and detailed overview and, to some extent, it is not really necessary since most of the topics are standard and treated in the literature. We will then focus on few topics that will be used in the rest of the thesis. This will also facilitate the introduction of some notation and general concepts used later. We encourage the Reader to refer to standard books like [91, 92] (as well as to the cited papers) to deepen into the arguments, considering the following analysis as complementary.

---

[22]Notice that only `GPUs` on the same motherboard can be used and, thus, several nodes of a supercomputer cannot be used at the moment for the same simulation.

It is well known that, in a (rational) hybrid Monte Carlo simulation, the measured observables are correlated, because each configuration in the Markov chain depends on the previous one. Therefore, in order to correctly estimate the error on the final observables, an autocorrelation time analysis is required. Indeed, given a generic observable x, the quantities $\{x_i\}$, $\{x_i^2\}$, ..., $\{x_i^n\}$ show different integrated autocorrelation times τ_{INT}. Here $\{x_i^n\}$ indicates the set of measurements for the observable x at each trajectory raised to the n-th power. Dividing the number of HMC trajectories produced by τ_{INT}, it is possible to obtain the number of *independent events* for a certain observable. Obviously, the higher this number the better. Even though there are several models which are much cheaper to be simulated (e.g. 2D Ising systems) and in which it is possible to collect thousands of independent events, in finite temperature LQCD we are still far from such a situation. Nevertheless, it is often possible to extract the desired information even without a so huge statistics. It is, thus, important to estimate τ_{INT} as precisely as possible. A detailed explanation about how to do it can be found in §4 of [91], but this requires an estimate by eye and it cannot be easily automatised. As an alternative, the method described in [93] can be used. The advantage is that it can be used as a black box, giving as input the set of data and getting τ_{INT} as output. The integrated autocorrelation time allows to estimate correctly the error on the mean value of an observable. In fact, if some data are correlated, the variance σ^2 of the mean is larger by a factor τ_{INT} than the variance $\sigma^2_{\text{uncorr.}}$ calculated on the same data considering them as uncorrelated,

$$\sigma^2 = \tau_{\text{INT}} \cdot \sigma^2_{\text{uncorr.}} \ .$$

This allows us already to state how to attribute an error to the mean value of an observable,

$$\langle O \rangle = \bar{O} \pm \frac{\sigma}{\sqrt{N}} = \bar{O} \pm \sqrt{\frac{1}{N} \, \tau_{\text{INT}} \cdot \sigma^2_{\text{uncorr.}}} \ , \tag{3.36}$$

where $\bar{O}$ is evaluated using the right hand side of Eq. (3.3),

$$\bar{O} = \frac{1}{N} \sum_{i=1}^{N} O_i \ ,$$

and N is the number of data accumulated in the Monte Carlo simulation. If just a simple measurement like $\langle O \rangle$ is needed, then Eq. (3.36) is sufficient. In general, this is not the case, though, and more complicated expressions have to be calculated. Having to estimate the value and the error of composite (or derived) observables – so are called quantities defined as functions of the mean value of one or more observables – more involved techniques are needed. Usually, these work correctly only on sets of uncorrelated data and, therefore, the autocorrelation has to be taken into account and somehow removed in a preliminary analysis. It is possible to do so using a so-called *binning* procedure. Given the initial set of N correlated data, a new set of M uncorrelated data is produced dividing the initial set in subsets of (at least) $2\,\tau_{\text{INT}}$ data and replacing each subset by the mean of the data contained in it. This technique, as easy as just described, needs nevertheless some attention. In general, N is not an even multiple of τ_{INT} and this means that the last subset of data will have less data of the others and has to be discarded[23]. To throw away the least amount of measurements, it is then important to choose the bin size as close as possible to an exact divisor of N. Using a slightly bigger bin size can be though of as having conservatively overestimated the integrated autocorrelation time. From now on, since LQCD measurements are basically always correlated, whenever we will speak about uncorrelated data, we will implicitly mean that binning has been performed on the data.

Even before analysing any data, it can be useful to look at the history of an observable in the Monte Carlo simulation or to its histogram. This is especially important when a phase transition

---

[23]It could seem a good idea to put in the new set of uncorrelated data the average of the last incomplete subset as well. Often, doing so, does not change drastically the final result, but it is simply wrong, since the weight of few data is artificially enhanced.

has to be located or just to gather information about the system. If, for example, the histogram has a clear two-peaks structure, we can probably infer that there are two distinct phases in the simulated system. We will come back to the importance of the shape of an observable distribution in §3.4. For the moment, it is enough to know that for any observable it is possible and worth looking at it. In particular, there are related quantities that often have to be calculated and for which a naïve error analysis fails. Let us then introduce some of them, in order to discuss a standard technique to correctly evaluate the error. The most relevant ones are the so-called *standardised moments*, defined as

$$B_n(O) \equiv \frac{\langle(\delta O)^n\rangle}{\langle(\delta O)^2\rangle^{\frac{n}{2}}} \qquad \text{with} \qquad \delta O \equiv O - \langle O\rangle \qquad \text{and} \qquad n \in \mathbb{N}_{>0} \ . \tag{3.37}$$

For $n = 1$ or $n = 2$, Eq. (3.37) is trivial and we have $B_1 = 0$ and $B_2 = 1$. The meaning of B_3 and B_4 will be clarified in §3.4. Here, we would like to focus on how to evaluate the error on B_n, given a set of uncorrelated data. An easy way to do it is using the jackknife method. Often, on standard textbooks, it is explained how it works in the simple case the observable O (whose error has to be estimated) is a function of the expectation value of another quantity X,

$$O = f(\langle X\rangle) \ ,$$

for instance, $O = \langle X\rangle^2 + e^{-\langle X\rangle}$. The double nested expectation value in B_n complicates a bit everything. Let us then quickly sketch, following [91], how the standard Jackknife works, generalising later the method to Eq. (3.37). Given a set $\{x_i\}$ of N *uncorrelated* data, we want to give an estimate for $f \equiv f(\langle x\rangle)$. The value and the error on f are obtained calculating at first the so-called *jackknife estimators* f_i^J (sometimes also called *partial predictions* or *pseudo-values*),

$$f_i^J = f(x_i^J) \qquad \text{with} \qquad x_i^J = \frac{1}{N-1}\sum_{k\neq i} x_k \ , \tag{3.38}$$

and using the following expressions,

$$\bar{f}^J = \frac{1}{N}\sum_{i=1}^{N} f_i^J \tag{3.39a}$$

$$\sigma^2(\bar{f}^J) = \frac{N-1}{N}\sum_{i=1}^{N}\left(f_i^J - \bar{f}^J\right)^2 \ . \tag{3.39b}$$

Observe that, in the trivial case in which $f = \langle x\rangle$, the well known unbiased estimator of mean and variance of the mean are obtained. Trying to apply Eqs. (3.39) to any standardised moment of an observable leads immediately to ask what has to play the role of the function f or what are now the jackknife estimators. Actually, dealing with composite observables like B_n, it is useful to generalise the jackknife method to the case in which the function f depends on several observables. Eq. (3.38) becomes

$$f_i^J = f\big[(x,y,z,\dots)_i^J\big] \qquad \text{with} \qquad (x,y,z,\dots)_i^J = \frac{1}{N-1}\sum_{k\neq i}(x,y,z,\dots)_k \ , \tag{3.40}$$

where the notation used is intended to emphasise that, for each observable the function f depends on, the same data is discarded in the evaluation of the jackknife estimator. Clearly, $(x,y,z,\dots)_i^J$ is a sort of vector notation and has to be considered as collective notation for x_i^J, y_i^J, z_i^J, and so on, each of which indicates the i-th pseudo-value of the corresponding observable. Eqs. (3.39) can then be used as before. Observe that, in case a binning procedure has to be carried out to take into account autocorrelation, the resulting number of bins has to be *the same* to calculate the jackknife

estimators in Eq. (3.40) – typically the biggest bin size of the observables $x, y, z, \ldots$ is used to bin them all. To clarify how Eq. (3.40) helps dealing with the standardised moments, let us consider B_4 and suppose at first that $\langle O \rangle = 0$. Under this assumption,

$$B_4 = \frac{\langle O^4 \rangle}{\langle O^2 \rangle^2} \equiv \frac{\langle x \rangle}{\langle y \rangle^2} \; .$$

It is then clear how to proceed. From the data set $\{O_i\}$, two new data sets $\{x_i\}$ and $\{y_i\}$ are created, setting $x_i = O_i^4$ and $y_i = O_i^2$ and Eq. (3.40) is applied using the function

$$f : \mathbb{R}^2 \to \mathbb{R} \qquad f(x, y) = \frac{x}{y^2} \; .$$

In the more complicated case in which we do not know anything about $\langle O \rangle$, the numerator and the denominator can be expanded,

$$B_4 = \frac{\langle O^4 \rangle - 4\langle O^3 \rangle \langle O \rangle + 6\langle O^2 \rangle \langle O \rangle^2 - 3\langle O \rangle^4}{(\langle O^2 \rangle - \langle O \rangle^2)^2} \equiv \frac{\langle x \rangle - 4\langle y \rangle \langle w \rangle + 6\langle z \rangle \langle w \rangle^2 - 3\langle w \rangle^4}{(\langle z \rangle - \langle w \rangle^2)^2}$$

Building this time four new set of quantities – $\{x_i\}$, $\{y_i\}$, $\{z_i\}$ and $\{w_i\}$ – the function to be used in Eq. (3.40) will be

$$f : \mathbb{R}^4 \to \mathbb{R} \qquad f(x, y, z, w) = \frac{x - 4\,y\,w + 6\,z\,w^2 - 3\,w^4}{(z - w^2)^2} \; .$$

The above example can be easily extended to any B_n (we preferred not to present here the most general expression, avoiding then unnecessary formal complications).

To conclude this section, we would like to sketch an alternative method to the jackknife, which can be useful in some occasions (or just most straightforward to be applied), the bootstrap method. Despite the fact it is very standard and it can be found on almost any textbook on the topic, we want to include it here since we will refer to it in §3.4.4. Suppose, again, that we want to give an estimate for $f \equiv f(\langle x \rangle)$, given a set $\{x_i\}$ of N *uncorrelated* data. A correct estimator for the value of f is

$$\bar{f} = f(\bar{x}) \qquad \text{with} \qquad \bar{x} = \frac{1}{N} \sum_{i=1}^{N} x_i \; . \tag{3.41a}$$

To evaluate the error, the initial set of data has to be resampled N_{boot} times *with repetition*. This means that, at each resampling, N data will be randomly picked up from $\{x_i\}$, allowing the same one to be drawn multiple times. Eq. (3.41a) has to be applied to each of these new data sets. In this way a set of N_{boot} estimates f_i^B of the function f is obtained and the error on $\bar{f}$ is given as

$$\Delta \bar{f} = \sqrt{\frac{1}{N_{\text{boot}}} \sum_{i=1}^{N_{\text{boot}}} \left(f_i^B - f^B \right)^2} \; , \tag{3.41b}$$

where f^B without label i is the average value of the $\{f_i^B\}$. One of the differences between the bootstrap and the jackknife methods is that the former has an external parameter to be set, N_{boot}. Typically, a thousands of resampling procedures leads to an accurate estimate of the error, but $N_{\text{boot}} \approx 100$ gives already a 10% accurancy [92]. This can be numerically advantageous, especially if the number N of data is huge, because in the jackknife the number of the pseudo-values is always equal to N and it could get expensive to calculate them, while the resampling step in the bootstrap is usually a cheap operation.

§ 3.4   Looking for a phase transition

In the previous sections of this chapter we made a quite long digression, in order to gather the knowledge and the tools needed to produce and elaborate data. It is now time to slowly come back to physics and, in particular, to discuss how, in practice, a phase transition can be located in finite temperature LQCD. Actually, we need to introduce some more details about computational techniques that are needed, but we will not do it in the most general way and we will already connect them with physically relevant examples. Doing so, it will be possible in the next chapter to completely focus on the original part of this thesis, discussing mainly the obtained results and not having to provide complementary notions, which will have been, at that time, already discussed.

§ 3.4.1   Measurement of observables during a simulation

Even if not explicitly said so far, it is well known that the first updates in a Monte Carlo simulation are needed to reach the fixed point of the Markov process. Therefore, in each run, some configurations produced at the beginning must not be considered for any final average in Eq. (3.3), because they are not sampled according to the correct probability distribution $P[U]$ in Eq. (3.2). It is common to refer to this phase of the simulation as *thermalisation phase* or simply *thermalisation*. A partial complication is due to the fact that it is not known a priori how many trajectories should be discarded. Nevertheless, it is possible to safely guess that the Markov process has reached its fixed point monitoring observables during the run. A typical technique to estimate how many thermalisation updates are necessary is to make the same simulation start twice from points in the phase space which are certainly far from the fixed point. Usually it is enough to draw randomly the gauge field for one run and to set all the links to $\mathbb{1}$ for the other run. Plotting the measured observables as function of the Monte Carlo time, their values will at some point start to fluctuate around their mean value, which by construction is different from the initial one. It is, thus, possible to estimate how long the thermalisation phase is and discard the configurations produced in it[24].

It is then clear that some observables have to be measured at each Monte Carlo update. Strictly speaking, after the thermalisation phase, because of autocorrelation, it would be advantageous to measure the needed observables, for example, only every $2\tau_{\mathrm{INT}}$, saving then some computing time. On the other hand, this is possible only by knowing in advance the value of the integrated autocorrelation time (that in general depends on the observable) and, usually, τ_{INT} is estimated a posteriori from the values of the measured quantities. Hence, the ideal strategy is to make measurements at each step *on the fly*, i.e. while the configurations are produced[25]. The relevant observables depend on the system, but it is obvious that, to locate a phase transition, the order parameter associated to it has to be measured. Studies that investigate particular features of the Columbia plot usually involve the Polyakov loop and the chiral condensate. They are exact order parameters in the infinite and zero mass limits, respectively. When the mass of the quarks is finite, both the chiral and the centre symmetries are explicitly broken and we have only approximate order parameters. Nonetheless, not too far away from the limiting case, they can still be used to investigate properties of the system. We will come back later in §3.4.2 to how to use them to locate a phase transition, for the moment let us just comment a bit more about how to measure them.

The measurement of any observable depending only on the gauge field clearly does not depend on the type of fermions used. Moreover, observables like the plaquette or the Polyakov loop are really cheap to be evaluated on `GPU` and this is the reason why, in `CL`^{2}`QCD`, they are measured by default at each Monte Carlo update. Some clarifications are needed. In Eq. (1.37) at page 20 we defined the plaquette as $\Pi_{\mu\nu}(n)$, namely as a quantity depending on the lattice site and on

---

[24]In standard applications, discarding few hundreds of trajectories would be already enough, but usually few thousands are not taken into account just to stay on the safe side.

[25]In particular cases, this strategy is numerically too costly and the needed observables will be evaluated every once in a while. The sampling frequency can be chosen even without knowing the autocorrelation time, which can be estimated later and in case taken into account in the analysis.

two directions. When practitioners refer to it, they are actually referring to a single number, which is the average of all the possible plaquette present on the lattice. Sometimes it is useful to distinguish between *spatial plaquettes*, i.e. plaquettes for which both μ and ν are spatial directions, and *temporal plaquettes*, i.e. plaquettes having two links in the temporal direction. We will adopt as well this convention. Again, people call spatial (temporal) plaquette simply the average of all spatial (temporal) plaquettes. In CL²QCD, since one gets them basically for free, all the three just mentioned plaquettes are measured on each produced configuration and they can be used, for example, to estimate the duration of the thermalisation phase. Also the Polyakov loop is measured on the fly and it is stored in the observables file distinguishing between its real part, its imaginary part and its absolute value. According to Eq. (1.68) at page 37, it should also depend on the position on the lattice, but in practice only the spatial average is considered. Naïvely, it could be asked why it is better to consider these averages rather than, for instance, the quantities at a fixed lattice site. The reason behind is that considering the average on all the lattice will give a cleaner signal of the observable during the Monte Carlo history and, to some extent, it can be thought as an indirect way to increase the statistics.

Observables that depend on the fermionic field are often less trivial to be measured and, of course, the way to calculate them changes varying the type of fermions used. The only one it will be needed for our physics studies is the chiral condensate and, then, we will just focus on it. It is worth discussing here how it can be measured in a simulation employing staggered fermions. This choice is connected to the fact that the measurement of $\langle \bar{\psi}\psi \rangle$ using Wilson fermions was already present in the CL²QCD software, while the new discretisation was added within this thesis project. Let us start considering an identity that can be easily proved,

$$(N_t\,N_s^3) \cdot \langle \bar{\psi}\psi \rangle = \frac{\partial}{\partial \hat{M}_0} \log \mathcal{Z} \, ,$$

where the prefactor arises naturally on the lattice calculating explicitly the right hand side and can be also justified using translational invariance. Using Eq. (3.4) together with the well known property of the determinant of a matrix M,

$$\det M = e^{\,\mathrm{Tr}\,(\log M)} \, ,$$

and the fact that the only mass dependence is in the Dirac matrix D, we obtain

$$(N_t\,N_s^3) \cdot \langle \bar{\psi}\psi \rangle = \frac{1}{\mathcal{Z}} \frac{\partial}{\partial \hat{M}_0} \int \mathcal{D}U \, e^{\frac{1}{4}N_f\,\mathrm{Tr}\,(\log D)} = \frac{1}{\mathcal{Z}} \int \mathcal{D}U \, \frac{\partial}{\partial \hat{M}_0} \, e^{\frac{1}{4}N_f\,\mathrm{Tr}\,(\log D)} =$$

$$= \frac{1}{\mathcal{Z}} \int \mathcal{D}U \, e^{\frac{1}{4}N_f\,\mathrm{Tr}\,\log D} \frac{\partial}{\partial \hat{M}_0}\left[\frac{N_f}{4}\,\mathrm{Tr}\,(\log D)\right] =$$

$$= \frac{1}{\mathcal{Z}} \int \mathcal{D}U \, (\det D)^{\frac{1}{4}N_f} \cdot \frac{1}{4}N_f\,\mathrm{Tr}\left(D^{-1}\frac{\partial D}{\partial \hat{M}_0}\right) = \frac{1}{4}N_f\left\langle \mathrm{Tr}\left(D^{-1}\frac{\partial}{\partial \hat{M}_0}D\right)\right\rangle_g \, .$$

Using Eq. (3.6), leads to

$$(N_t\,N_s^3) \cdot \langle \bar{\psi}\psi \rangle = \frac{1}{4}N_f\left\langle \mathrm{Tr}\left(D^{-1}\right)\right\rangle_g \, . \tag{3.42}$$

The gauge expectation value is evaluated, as for any observable, taking advantage of the importance sampling and it reduces, in practice, to an arithmetic mean. The non trivial part of Eq. (3.42) is the trace of the inverse Dirac matrix. A quite old technique to evaluate it, is to use *noise sources* to make a stochastic estimation. A noise source appears like a fermion field, but it takes particular values depending on the type of source. For example, a Gaussian volume source is a fermion field with each component at each lattice site drawn according to a normal distribution; in a Z_2 volume source, each component can be either $+1$ or -1. Apparently, Z_2 noise should be preferred [94], but in the following, the type of noise will not be relevant. Let us consider, then, L noise sources $\eta^1, \ldots, \eta^L$ such that

$$\langle \eta_i \rangle_L = 0 \qquad \text{and} \qquad \langle \eta_i^\dagger\,\eta_j \rangle_L = \delta_{i,j} \, . \tag{3.43}$$

Here, η_i and η_j are entries of the source[26] and the expectation values over L indicates an average on the noise sources ensemble, e.g.

$$\langle \eta_i\,\eta_j \rangle_L = \frac{1}{L}\sum_{l=1}^{L}\left(\eta_i^l\right)^\dagger \eta_j^l \,.$$

It follows immediately that

$$\mathrm{Tr}\left(D^{-1}\right) = \sum_{i=1}^{N}\left(D^{-1}\right)_{ii} = \sum_{i=1}^{N}\sum_{j=1}^{N}\left(D^{-1}\right)_{ij}\delta_{i,j} \simeq \sum_{i=1}^{N}\sum_{j=1}^{N}\left(D^{-1}\right)_{ij}\langle \eta_i^\dagger \eta_j \rangle_L =$$

$$= \sum_{i=1}^{N}\sum_{j=1}^{N}\frac{1}{L}\sum_{l=1}^{L}\left(\eta_i^l\right)^\dagger\left(D^{-1}\right)_{ij}\eta_j^l = \frac{1}{L}\sum_{l=1}^{L}\left(\eta^l\right)^\dagger\cdot\left(D^{-1}\right)\cdot\eta^l \,,$$

where in the last step a vector notation has been used, while the approximation symbol is due to the fact that Eqs. (3.43) can be fulfilled only in the $L \to \infty$ limit. Inserting the identity matrix $(D^\dagger)^{-1}\cdot D^\dagger$ opportunely leads to

$$\mathrm{Tr}\left(D^{-1}\right) \simeq \frac{1}{L}\sum_{l=1}^{L}\left(\eta^l\right)^\dagger\cdot\left(D^\dagger D\right)^{-1}\cdot\left(D^\dagger\,\eta^l\right)\,. \qquad (3.44)$$

There are few advantages following from Eq. (3.44). The first one is that the operator that has to be inverted is the same as that in the RHMC algorithm[27]. Moreover, using the even-odd notation, it can be shown that the matrix inversion can be carried out only on half lattice as it is always the case in the RHMC algorithm (this probably avoids the need of new code, i.e. without even-odd decomposition). Using Eqs. (3.8) and (3.9) and omitting for the moment the index l on the noise source, we have that

$$\left(D^\dagger D\right)^{-1}\cdot\left(D^\dagger\,\eta\right) = \begin{pmatrix}\left(\hat{M}_0^2 - D_{eo}\,D_{oe}\right)^{-1} & \mathbb{0} \\ \mathbb{0} & \left(\hat{M}_0^2 - D_{oe}\,D_{eo}\right)^{-1}\end{pmatrix}\cdot\begin{pmatrix}\hat{M}_0\eta_e - D_{eo}\eta_o \\ \hat{M}_0\eta_o - D_{oe}\eta_e\end{pmatrix}$$

$$= \begin{pmatrix}\left(\hat{M}_0^2 - D_{eo}\,D_{oe}\right)^{-1}\cdot\left(\hat{M}_0\,\eta_e - D_{eo}\,\eta_o\right) \\ \left(\hat{M}_0^2 - D_{oe}\,D_{eo}\right)^{-1}\cdot\left(\hat{M}_0\,\eta_o - D_{oe}\,\eta_e\right)\end{pmatrix} \equiv \begin{pmatrix}\chi_e \\ \chi_o\end{pmatrix}\,.$$

If the matrix inversion can be done on half lattice only, it means that χ_e is not independent from χ_o. Indeed,

$$D_{oe}\chi_e = D_{oe}\cdot\left(\hat{M}_0^2 - D_{eo}\,D_{oe}\right)^{-1}\cdot\left(\hat{M}_0\,\eta_e - D_{eo}\,\eta_o\right)=$$

$$= \left[\left(\hat{M}_0^2 - D_{eo}\,D_{oe}\right)\cdot\left(D_{oe}\right)^{-1}\right]^{-1}\cdot\left(\hat{M}_0\,\eta_e - D_{eo}\,\eta_o\right)=$$

$$= \left[\hat{M}_0^2\left(D_{oe}\right)^{-1} - D_{eo}\right]^{-1}\cdot\left(\hat{M}_0\,\eta_e - D_{eo}\,\eta_o\right)=$$

$$= \left[\left(D_{oe}\right)^{-1}\hat{M}_0^2 - \left(D_{oe}\right)^{-1}\cdot D_{oe}\cdot D_{eo}\right]^{-1}\cdot\left(\hat{M}_0\,\eta_e - D_{eo}\,\eta_o\right)=$$

$$= \left[\left(D_{oe}\right)^{-1}\cdot\left(\hat{M}_0^2 - D_{oe}\,D_{eo}\right)\right]^{-1}\cdot\left(\hat{M}_0\,\eta_e - D_{eo}\,\eta_o\right)=$$

---

[26] The indices i and j can be thought as multi-indices denoting the position on the lattice and the colour component of the $SU(3)$ vector lying at each lattice site.

[27] Observe that here there is no shift and, in principle, a standard solver like the CG would be sufficient. Nevertheless, the CG - M solver can be used setting the shift vector to be a scalar equals to zero and it will give the correct result. So, at first, there is no need to implement a new solver. Clearly, using a more complicated algorithm implies an overhead. Nevertheless, the need of a faster code never arose and, therefore, only the CG - M solver is implemented in CL²QCD for staggered fermions (remember the D. Knuth quotation at page 85).

$$= \left(\hat{M}_0^2 - D_{oe}\, D_{eo}\right)^{-1} \cdot D_{oe} \cdot \left(\hat{M}_0 \eta_e - D_{eo}\, \eta_o\right) =$$

$$= \left(\hat{M}_0^2 - D_{oe}\, D_{eo}\right)^{-1} \cdot \left(\hat{M}_0 D_{oe}\, \eta_e - D_{oe}\, D_{eo}\, \eta_o\right) =$$

$$= \left(\hat{M}_0^2 - D_{oe}\, D_{eo}\right)^{-1} \cdot \left[\hat{M}_0\, D_{oe}\, \eta_e + \left(\hat{M}_0^2 - \hat{M}_0^2\right) \eta_o - D_{oe}\, D_{eo}\, \eta_o\right] =$$

$$= \left(\hat{M}_0^2 - D_{oe}\, D_{eo}\right)^{-1} \cdot \left(\hat{M}_0\, D_{oe}\, \eta_e - \hat{M}_0^2 \eta_o\right) + \left(\hat{M}_0^2 - D_{oe}\, D_{eo}\right)^{-1} \cdot \left(\hat{M}_0^2 - D_{oe}\, D_{eo}\right) \cdot \eta_o =$$

$$= \hat{M}_0 \left(\hat{M}_0^2 - D_{oe}\, D_{eo}\right)^{-1} \cdot \left(D_{oe}\, \eta_e - \hat{M}_0\, \eta_o\right) + \eta_o = -\hat{M}_0\, \chi_o + \eta_o$$

Comparing the left hand side and the right hand side and reintroducing the index l on the noise source, we eventually find

$$\chi_o^l = \frac{1}{\hat{M}_0} \left(\eta_o^l - D_{oe}\, \chi_e^l\right) . \tag{3.45a}$$

Together with the even part,

$$\chi_e^l = \left(\hat{M}_0^2 - D_{eo}\, D_{oe}\right)^{-1} \cdot \left(\hat{M}_0\, \eta_e^l - D_{eo}\, \eta_o^l\right) , \tag{3.45b}$$

we can conclude that the chiral condensate, given a link configuration, can be evaluated as

$$\bar{\psi}\psi\Big|_U = \frac{N_f}{4\, N_t\, N_s^3\, L} \sum_{l=1}^{L} \left[\left(\eta_e^l\right)^\dagger \cdot \chi_e^l + \left(\eta_o^l\right)^\dagger \cdot \chi_o^l\right] , \tag{3.46}$$

and can be easily implemented making use of Eqs. (3.45). Note that the the value obtained from Eq. (3.46) is in general complex but the imaginary part of the expectation value on the gauge ensemble has to vanish. This can be a good test to check the implementation and it has been carried out in CL²QCD. Producing $1.5 \cdot 10^4$ trajectories after $5 \cdot 10^3$ of thermalisation on a 4×8^3 lattice using the RHMC algorithm (with $N_f = 2$, $\hat{M}_0 = 0.04$ and $\beta = 5.2$), we found

$$\Im\left[\langle\bar{\psi}\psi\rangle\right] = (5 \pm 6) \cdot 10^{-5} .$$

§ 3.4.2   The skewness and the kurtosis

We are now finally ready to discuss how to look, in practice, for a phase transition and how it is possible to understand its order. The first task is by far easier than the second, but there are methods which are more accurate than others. The concepts introduced in this section are completely general and then particular parameters like the temperature could be left aside and replaced by general ones with generic names. For the sake of clarity and to help the Reader to be already used to the notation in chapter 4, we will not do so and we will work using the common language of finite temperature LQCD. In §1.7 we learnt already that the temperature is varied through the gauge coupling g_0, hidden in β defined in Eq. (1.42) at page 25. Therefore, from now on, we will refer to β also as *temperature*, giving as understood the conversion in Eq. (1.53). This is a common habit in the community.

To locate a phase transition means to find the critical temperature at which it occurs. Hence, the first thing to do is to make a scan in temperature[28], namely to run a set of simulations in which the only physical parameter that changes is β. Different runs at different β values could require different parameters regarding the algorithmic aspect of the simulation. For instance, the number of integration steps done in the molecular dynamics part of a hybrid Monte Carlo may need to be adjusted to guarantee the correct value of the acceptance rate. During each simulation, the order parameter for the phase transition that is being looked for has to be measured. We will call

---

[28]We will use often this terminology. To make a scan in a given parameter α always means to run several simulations at different values of α, keeping the other physical parameters fixed.

it generically Q. Studying the Columbia plot, it will typically be $Q \equiv |L|$ or $Q \equiv \bar{\psi}\psi$ depending on the investigated mass region. The following step is to measure properties of the distribution of Q during each run, which will signal where the system undergoes a phase transition. The most important ones are the first moment m_1, the second central moment μ_2 and the third and the fourth standardised moments, B_3 and B_4 defined in Eq. (3.37).

To avoid any confusion, especially for the Reader that could be already acquainted with a particular nomenclature, it is time for a short digression to define how we will call what. In probability theory and statistics, a probability distribution can be characterised in terms of its *moments*,

$$m_n = \int_{-\infty}^{\infty} x^n f(x) \, \mathrm{d}x \ ,$$

central moments (also called *moments about the mean*),

$$\mu_n = \int_{-\infty}^{\infty} (x - m_1)^n f(x) \, \mathrm{d}x \ ,$$

or *cumulants* κ_n, which are defined in terms of the moments (here, $n \in \mathbb{N}_{\geqslant 0}$). An elegant way to get them is to take derivatives of the so-called generating functions. For a continuous probability density function $f(x)$ of a random variable X, the *moment generating function* can be written as

$$M_X(t) = \int_{-\infty}^{\infty} e^{\, t \, x} f(x) \, \mathrm{d}x \ ,$$

and, with few algebra,

$$M_X(t) = \int_{-\infty}^{\infty} \sum_{k=0}^{\infty} \frac{(t \, x)^k}{k!} f(x) \, \mathrm{d}x \ = \ \sum_{k=0}^{\infty} \frac{t^k}{k!} \int_{-\infty}^{\infty} x^k f(x) \, \mathrm{d}x \ = \ \sum_{k=0}^{\infty} \frac{t^k \, m_k}{k!} \ .$$

Therefore,

$$m_n = M_X^{(n)}(0) \ ,$$

namely the n-th moment can be obtained taking the n-th derivative of the moment generating function and evaluating it at $t = 0$. It is straightforward to show that the *central moment generating function* can be written as

$$C_X(t) = \int_{-\infty}^{\infty} e^{\, t \, (x - m_1)} f(x) \, \mathrm{d}x \ ,$$

that leads to

$$\mu_n = C_X^{(n)}(0) \ .$$

The cumulant generating function is defined as the natural logarithm of the moment generating function,

$$K_X(t) = \log M_X(t) \ ,$$

and the cumulants of a distribution are obtained via

$$\kappa_n = K_X^{(n)}(0) \ .$$

Hence, it can be shown that all these quantities are connected. Up to $n = 4$, it can be shown that

$$
\begin{aligned}
\mu_1 &= 0 & \kappa_1 &= m_1 \\
\mu_2 &= \kappa_2 & \kappa_2 &= m_2 - m_1^2 \\
\mu_3 &= \kappa_3 & \kappa_3 &= m_3 - 3 \, m_2 \, m_1 + 2 \, m_1^3 \\
\mu_4 &= \kappa_4 + 3 \, \kappa_2^2 & \kappa_4 &= m_4 - 4 \, m_3 \, m_1 - 3 \, m_2^2 + 12 \, m_2 \, m_1^2 - 6 \, m_1^4 \ .
\end{aligned}
$$

n	m_n	μ_n	B_n	κ_n	ρ_n
1	MEAN	0	0	MEAN	0
2	—	VARIANCE	1	VARIANCE	1
3	—	—	SKEWNESS	—	SKEWNESS
4	—	—	KURTOSIS	—	EXCESS KURTOSIS

Table 3.1: *Overview of particular names used to refer to raw, central or standardised moments as well as raw or standardised cumulants. Note that it is common to use the symbols μ and σ^2 to identify the mean and the variance of a distribution, respectively.*

It is worth recalling also the definition of *standardised moment*,

$$B_n \equiv \frac{\mu_n}{(\mu_2)^{\frac{n}{2}}} \ ,$$

and that of *standardised cumulant*,

$$\rho_n \equiv \frac{\kappa_n}{(\kappa_2)^{\frac{n}{2}}} \ ,$$

which can be written in this way for $n \geqslant 3$ (refer to Theorem 4.14 and Example 4.22 of [95] to understand the reason behind this restriction). So far, so good. Misleading situations arise because particular names are given to some of the quantities above or to combinations of them and because, sometimes, different people call differently the same quantity (or in the same way different things). In Table 3.1 we summarised the standard nomenclature. There is another quantity, not included in it, which was introduced by K. Binder [96] in 1981 and in honour of whom is called *Binder cumulant*,

$$U_4 \equiv 1 - \frac{\mu_4}{3\mu_2^2} \ .$$

Using the previous relations between cumulants and central moments together with the definitions of the standardised quantities, it can be shown that

$$B_4 = \rho_4 + 3 \ , \qquad \text{which implies that} \qquad U_4 = -\frac{1}{3}\rho_4 \ .$$

In the end, U_4, ρ_4 and B_4 bring the same information and this makes people sometimes less rigorous in which of these name has to be associated to which quantity. We, in the first place [97], called Binder cumulant the kurtosis. However, as soon as it is clear from the context what is being done, everything should be fine. In the rest of this thesis we will stick to the notation and nomenclature just introduced.

We can now come back to the physics and discuss what the quantities m_1, μ_2, B_3 and B_4 can tell us about a phase transition. From rapid changes in the first three, thought as a function of the temperature, it is possible to infer the critical value of β, usually denoted with β_c. In particular, the mean value of the order parameter will jump from zero (or from a small value, in case it is only approximately an order parameter) to a finite value. The second central moment will be peaked around the critical temperature, while the skewness will vanish at β_c. Intuitively, these properties can be understood thinking that far from the phase transition, the order parameter will weakly fluctuate around its mean value and its distribution will be localised around the mean. Different phases have different mean values for the order parameter and, then, when the temperature is varied across β_c, its distribution will deform and move. If it is also considered that the variance is connected to how broad is the distribution and the skewness to how asymmetric it is, it should be clear why the first shows a peak and the second crosses zero at β_c. The second statement could seem less intuitive and it is worth commenting a bit further on it. Let us imagine to vary β from $\beta \ll \beta_c$ to $\beta \gg \beta_c$. At the beginning and at the end the probability distribution of our observable is

	Crossover	first-order triple	Tricritical	3D Ising
B_4	3	1.5	2	1.604
ν	−	1/3	1/2	0.6301(4)
γ	−	1	1	1.2372(5)

Table 3.2: *Critical values of ν, γ and B_4 at a phase transition for some universality classes [98].*

probably symmetric around its mean value and, therefore, $B_3 = 0$. When the temperature gets closer to the phase transition, the shape of the distribution will change, becoming asymmetric left or asymmetric right, depending from which side β_c is approached. Therefore the skewness will be positive on one side of the phase transition and negative on the other. It follows that it has to cross zero in between and, actually, it does at β_c, when the distribution is symmetric again. If we wish to locate the phase transition as precisely as possible, given a resolution in β, the skewness is the quantity to be used, since two values around β_c are sufficient to be sure that the phase transition takes place there in between. The mean can only give us a rough estimate, while to locate the maximum of a function at least three points are needed.

The kurtosis has a minimum at the critical temperature and, then, it has the same downsides of the variance to locate β_c. Nevertheless, it is crucial to understand, once located, the type of phase transition the system undergoes. This is also possible using the peak of the susceptibility, defined as the variance of the observable multiplied by the spatial volume V of the lattice used, but we will not discuss this aspect here – the Reader can refer to §17.4 of [18], where by the way the kurtosis is called Binder cumulant. In the thermodynamic limit, i.e. when non-analytic phase transitions can exist, the kurtosis evaluated at critical couplings takes different values depending on the nature of the phase transition – as it can be seen in Table 3.2. If the volume is large enough, then, it is sufficient to evaluate the value of $B_4(\beta_c)$. Unfortunately, in practice, it is hard to understand if the requirement of large enough volume is satisfied and if, therefore, we can compare the obtained value with those of Table 3.2. This condition is met if the value of $B_4(\beta_c)$ does not change as V is increased, but it can happen that, plotting $B_4(\beta_c)$ as function of the volume V, a plateau is reached very slowly and, actually, for volumes too costly to be simulated. Said differently, if the spatial volume is finite, the kurtosis can take any value between the universal ones and its value can be inconclusive. If this is the case, another method should be used, e.g. the scaling with the volume of the peaks of the susceptibility. It is worth stressing that the value of the kurtosis brings information about the order of the phase transition only at the critical temperature, i.e. where a phase transition takes place. Far from it, the value of the kurtosis has no physical meaning, even if equal to one of its universal value. For example, when the system is not on a phase boundary, the order parameter of any phase transition will numerically fluctuate around its mean value and its distribution will be normal. If we measured the kurtosis in this case, we would find 3, but from it we cannot say that the system undergoes a crossover transition! From now on, if not differently stated, we will give as understood that the kurtosis is evaluated at β_c.

To summarise, a possible strategy to locate a phase transition is to make a scan in β and measure for each simulation the skewness B_3 of the order parameter. The critical temperature β_c is found as the β value fulfilling the condition $B_3(\beta_c) = 0$. At β_c the kurtosis of the order parameter can be evaluated and, from its value in the thermodynamic limit, the order of the phase transition can be inferred.

If our aim is to locate a phase transition and to understand its order, what explained so far

is sufficient[29]. Nevertheless, more often we are interested in studying how the order of the phase transition changes varying some typical parameter of the system. For example, natural tasks to quantitatively understand how the Columbia plot or the Roberge-Weiss Columbia plot look like are to locate the Z_2 critical point, which separates a first-order region from a crossover one, or to locate a tricritical point between a first-order triple region and a Z_2 one. To do so, it is in principle sufficient to find out the order of the phase transition varying one additional parameter. Let us give a concrete example, considering the deconfinement region of the Columbia plot on the $N_f = 2$ edge. We know from §2.2 that, said $m_q = m_q^c$ the Z_2 critical mass, the deconfinement transition is a crossover for $m_q < m_q^c$ and it is a first order for $m_q > m_q^c$. This means that the kurtosis measured at different masses will be 3 and 1 on the left and on the right of the Z_2 point, respectively. Hence, plotting B_4 as a function of the mass, a step function should be obtained and the mass value at which the change takes place coincides with m_q^c. Again, this is true only in the infinite volume limit and, as we already said, it is numerically too expensive to simulate volumes large enough to well approximate this limit and a finite size scaling analysis is, thus, needed. On finite volumes, the change in the kurtosis gets smoothed out. In principle, a $V \to \infty$ extrapolation could be done for each mass simulated, trying to reproduce the step function behaviour of the kurtosis. Nevertheless, in this case, one extrapolation only can be done, considering all the data at different masses together, as it will be discussed in §3.4.3. However, it cannot be avoided to repeat the same scan in mass and in the temperature on different volumes.

There are particular situations in which the procedures described so far to locate a phase transition and to understand its nature fail. This is the case, for example, when the position of a tricritical point in the Roberge-Weiss Columbia plot has to be found. The more complicated phase structure of the system at the critical value of the purely imaginary chemical potential described in §2.3 has to be taken into account. In particular, if μ_I is fixed to its critical value (no matter which), any value of β is critical, because of the Roberge-Weiss transition between two adjacent centre sectors. And this is true at any value of the quark masses. In this case, we are interested in finding the temperature at which the chiral or deconfinement transition takes place and we will use the symbol β_c to refer to it. This will locate the Roberge-Weiss endpoint in the (T, μ_I) plane. For a given value of the quark masses, we will need again to make a scan in β, but to measure, this time, *the kurtosis* of the order parameter for each simulation. Unfortunately, measuring the skewness is not helpful since it brings no information about β_c. In fact, it is identically zero at any temperature, due to the fact that any β is critical. But exactly because of that, we can predict that the kurtosis will be 3 for $\beta \ll \beta_c$ and 1 for $\beta \gg \beta_c$, since the Roberge-Weiss transition between the centre sectors is a crossover at low T and becomes a first-order phase transition at high T. Between these two limiting cases, the only information we have is that, depending on the nature of the Roberge-Weiss endpoint, $B_4(\beta_c)$ will be 1.5, 2 or 1.604 (these values are read out from Table 3.2). Since, then, $1 < B_4(\beta_c) < 3$, it is natural to think that the kurtosis will monotonically connects the two limit regimes. This is often the case, but values higher than 3 have been sometimes found and a simple model to explain why this is possible has been built [97]. We will describe it in detail in §4.1.3. Even if many features of the functional dependence of the kurtosis on β can be a priori predicted, a run on a single volume would allow us to find β_c only for a large enough lattice spatial volume. In fact, it can be shown that $B_4(\beta) = 2\,\Theta(\beta_c - \beta) + 1$ in the $V \to \infty$ limit (here Θ is the Heaviside step function) and this implies that β_c can be located as discontinuity point of $B_4(\beta)$. Nevertheless, ignoring for a moment the usually too high numerical cost, simulating one only large enough volume would prevent us from understanding the nature of the Roberge-Weiss endpoint at the simulated mass, because, ranging from 3 to 1, B_4 will take all the possible critical values[30] at different β. We clearly need a better idea, which is actually easy to be understood. The qualitative

---

[29]Strictly speaking, this statement is not always true. There are situations in which the described strategy fails. One example, that will be discussed later in this section, regards any investigation in the Roberge-Weiss Columbia plot.

[30]Note that, no matter how large is the simulated volume, the kurtosis will always be, in practice, a continuous function of β.

behaviour of the kurtosis that was just described is the same on *any* spatial volume. Therefore, making scans in β using different volumes allows to identify β_c as the temperature at which the kurtosis on the different volumes intersect and the order of the phase transition can be deduced by reading out the value of B_4 at β_c. Unfortunately, it is not so easy as it could sound. First of all, the kurtosis must intersect at the same β only if we are not too far from the thermodynamic limit. This is due to the general property that the critical temperature measured in a finite volume will be in general different from that in the $V \to \infty$ limit. Hence, at least three different volumes should be used and, a priori, it cannot be known if the crossing point of the kurtosis will be unique (if not at least a fourth larger volume has to be simulated). Moreover, even if the crossing point of the kurtosis on three volumes seems to be at the same β, to understand the nature of the phase transition from the raw data is really hard, because the different critical values are quite similar[31]. Again, a finite size scaling analysis is the best thing to do and once again we prefer to postpone its discussion to §3.4.3. Observe that, as the crossing of the kurtosis on different volumes gives a hint about how well such volumes approximate an infinite one, so does the crossing of the skewness in studies at a non critical value of the chemical potential. In fact, close enough to the thermodynamic limit, the skewness of the order parameter measured on different volumes should intersect at the same value of β and, there, be zero.

To conclude, it is worth shortly mentioning another technique, which is often used to get insights about the order of a phase transition. Here, only a rough estimate of the critical temperature is needed, in the sense that it is important to run simulations around and not too far from it. It is possible to show [92] that the susceptibility of the order parameter is expected to scale around β_c according to

$$\chi = N_s^{\gamma/\nu} f\big(t\, N_s^{1/\nu}\big) \,, \tag{3.47}$$

where $t \equiv (T - T_c)/T_c$ is the reduced temperature and f the universal scaling function. This means that, once the critical exponents γ and ν are fixed to the correct values using Table 3.2, $\chi/N_s^{\gamma/\nu}$ measured on different lattice sizes should collapse when plotted against $t\, N_s^{1/\nu}$. We will refer to this kind of plot as *collapse plot*. The same statement is valid for the kurtosis, with a different universal scaling function,

$$B_4 = g\big(t\, N_s^{1/\nu}\big) \,. \tag{3.48}$$

It is therefore possible to make collapse plots for different orders of the phase transition and estimate by eye which is the better one. The main drawback of this method is that sometimes all collapse plots are qualitatively the same and it is hard to rule out any possibility and even harder to decide which is probably the nature of the phase transition. This is again due to the fact that the closer the simulation is to the thermodynamic limit the better is the quality of the collapse. An example of this fact can be found in [66].

§ 3.4.3 The finite size scaling analysis of the kurtosis

To complete the information provided in §3.4.2, we need to quantitatively discuss how to keep into account the finite size effects that are present in finite temperature LQCD simulations or, said differently, how to obtain a result in the thermodynamic limit using only finite volumes, i.e. how to perform a *finite size scaling analysis*. First of all, let us clarify why we need to do so. It is well known that a phase transition is associated to a non analyticity of the partition function of the system we are studying, but as soon as the volume is finite, then $\mathcal{Z}$ becomes an analytic function and any non analytic behaviour is washed away. Clearly, close to the thermodynamic limit, traces of a real phase transition shall be observed and this is the reason why we need V as large as possible. As it can be imagined, the numerical cost of a simulation increases with the volume and, in practice, it is hard to be able to simulate in the $V \to \infty$ limit. Nevertheless, scaling properties of

---

[31]Naïvely, it could be thought that increasing the statistics and reducing the error on the raw data can solve this problem. Even if in theory this statement is correct, in practice this is not feasible as it can be seen from the already extremely high statistics accumulated in the studies presented in chapter 4.

useful quantities can be shown and used to perform finite size scaling analyses. In the following, we will focus only on the kurtosis, but the idea is much more general and it is important to stress that it is not only a numerical prescription – the Reader is encouraged to refer to standard textbooks like [92, 99] to learn more about it.

Writing explicitly all the parameters $\{\alpha_i\}$ it can depend on, the kurtosis of an observable Q reads

$$B_4(Q, \alpha_1, \ldots, \alpha_n, N_s) \equiv \frac{\langle (\delta Q)^n \rangle}{\langle (\delta Q)^2 \rangle^{\frac{n}{2}}} \qquad \text{with} \qquad \delta Q \equiv Q - \langle Q \rangle \, .$$

It can be shown that, when studying the change of the nature of a phase transition from a first order to a crossover as function of a parameter α_i, in the vicinity of the critical point α_i^c, i.e. the value of α_i at which the kurtosis would be discontinuous in the thermodynamic limit, the kurtosis is a function of *only*

$$x \equiv (\alpha_i - \alpha_i^c) N_s^{1/\nu} \, ,$$

if N_s is big enough. Keeping the other parameters α_j $(i \neq j)$ fixed and therefore omitted, it can be, then, Taylor-expanded around zero,

$$B_4(Q, \alpha_i, N_s) = B_4(\alpha_i^c, \infty) + a_1 \, x + a_2 \, x^2 + \mathcal{O}(x^3) \, .$$

In the two examples discussed in §3.4.2, we had $B_4(Q, \beta, m_q, N_s)$, once in the Columbia plot and once in the Roberge-Weiss Columbia plot. In the first case the change from a crossover to a first-order phase transition was obtained varying m_q, while in the second varying β. Therefore, assuming to have measured the kurtosis around m_q^c and β_c, the data on different volumes can be simultaneously fit using

$$B_4(Q, m_q, N_s) = B_4(m_q^c, \infty) + a_1 \, (m_q - m_q^c) \, N_s^{1/\nu} \tag{3.49a}$$

and

$$B_4(Q, \beta, N_s) = B_4(\beta_c, \infty) + a_1 \, (\beta - \beta_c) \, N_s^{1/\nu} \, , \tag{3.49b}$$

respectively. Here only the linear term of the Taylor expansion has been used, but the reliability of this assumption depends on how wide is the simulated interval around the critical point. If the simulated volumes are not too small and if the error on the kurtosis are not too large, the quality of the fit is usually good and both $B_4(\cdot, \infty)$ and ν take their universal value, from which the order of the phase transition can be deduced. A poor statistics could make the outcome of the fit inconclusive, e.g. if the error on the parameters are too large to distinguish between different phase transitions. There is an important difference between Eqs. (3.49a) and (3.49b), which is worth commenting on. In the Columbia plot we know that the point that separates the first-order region from the crossover one is a Z_2 point and therefore the values of $B_4(m_q^c, \infty)$ and ν could be fixed to their universal values or they could be deduced from the fit and checked if compatible with the correct values. In the Roberge-Weiss Columbia plot, instead, the first-order and the crossover regions in the (T, μ_I) plane are separated by the Roberge-Weiss endpoint, whose nature depends on the value of the quarks mass and is a priori unknown. How to perform this more delicate fit will be fully discussed in chapter 4.

Lastly, a side remark. From §3.4.2, it could seem that only the order parameter shows the described behaviour and it is mandatory to use it to locate the phase transition. Actually, this is not the case and it is possible to associate a critical temperature to any observable on finite volumes. This is the reason why some people prefer to call *pseudo-critical* temperature, β_{pc}, the critical temperature found on a particular finite volume. We decided not to do so, because the pseudo-critical temperatures defined using different observables will merge in the $V \to \infty$ limit, on constraint that a non-analytic phase transition exists. If in the thermodynamic limit the phase transition is an analytic crossover, they will stay separate and, maybe, the term pseudo-critical is more appropriate.

§ 3.4.4   The multiple histogram method

Often in this section we spoke about locating the zero of the skewness of an observable as well as finding the crossing point of the kurtosis. At the same time, we avoided any precise statement about *how* to do it. It could sound odd to make this kind of remark, since these are in general straightforward tasks. Nevertheless, considering the fact that a simulation for a fixed set of parameters typically lasts for weeks or even months to accumulate the needed statistics, it is clear that the resolution in β cannot be arbitrarily increased, if we want to keep the duration of the project limited. A very small $\delta\beta$ to make the scan in temperature could be used since the beginning, but this would mean running probably too many simulations with respect to the available computational resources[32] or, again, to slow down the project. Therefore, it is evident that the tasks mentioned above are all but trivial, especially if a good precision is required. Fortunately, whenever the action of the system is linear in a parameter – as it is the case in LQCD for β – it is possible to safely interpolate between measurements done at different, not too far values of such a parameter. The method to do so was introduced in 1989 by A. M. Ferrenberg and R. H. Swendsen [100] as an extension of a year earlier work of the same authors [101], in which they discussed how to extrapolate measurements in the vicinity of a simulated point. The firstly proposed technique (1988), also called *single histogram method*, is in general less suited for our purposes, because it is rare to have only one simulation point in the parameter space. The *multiple histogram method*, instead, is exactly what we need and, sometimes, people refer to it also as *Ferrenberg-Swendsen reweighting* or more simply as *reweighting*. These techniques are discussed in great detail in §8.1 and §8.2 of [92], where some technical aspects of the implementation are also examined. Therefore, it would be pointless to explain here how to reweight an observable. Nevertheless, we will discuss how to reweight a composite quantity (e.g. the skewness or the kurtosis) and how to attribute an error to the reweighted values of an observable. We encourage the Reader not familiar with the method to preliminarily read the reference given above or to think to the reweighting just as tool to interpolate data. Differently said, we will not justify most of the statements and formulae in the following.

Let us suppose that a bunch of simulations at different values $\{\beta_i\}$ of the temperature have been run and a given observable Q has been measured at each trajectory. Then, the value of Q at a new temperature β can be obtained as

$$\langle Q(\beta)\rangle = \frac{1}{\mathcal{Z}(\beta)} \sum_{i,s} \frac{Q_s(\beta_i)}{\sum_j n_j \, \mathcal{Z}^{-1}(\beta_j) \, e^{(\beta-\beta_j)\cdot E_s(\beta_i)}} \ , \tag{3.50a}$$

where the partition functions at each simulated β_j can be estimated solving iteratively the equation

$$\mathcal{Z}(\beta_j) = \sum_{i,s} \frac{1}{\sum_k n_k \, \mathcal{Z}^{-1}(\beta_k) \, e^{(\beta_j-\beta_k)\cdot E_s(\beta_i)}} \ , \tag{3.50b}$$

from which it follows that

$$\mathcal{Z}(\beta) = \sum_{i,s} \frac{1}{\sum_k n_k \, \mathcal{Z}^{-1}(\beta_k) \, e^{(\beta-\beta_k)\cdot E_s(\beta_i)}} \ . \tag{3.50c}$$

Here, the indices i, j and k identify the simulation, n is the total number of trajectories of a given run, the index s identifies a particular configuration and $E_s(\beta_i)$ is the *conjugated quantity* to β calculated on the s-th configuration of the i-th simulation. By conjugated quantity to a parameter, it is meant the part of the action that is multiplied by such a parameter (that is why the action must be linear in the parameter in which the reweighting has to be done). In our case E coincides

---

[32]Typically, on the supercomputer that are used in LQCD, there are limitations on the maximum number of simulations that can be simultaneously run. Being able to run more than 50 simulations at the same time is already a very lucky case.

with the gauge part of the action divided by β. Observe that the values of the observable Q are needed at each trajectory for each simulation, in order to obtain the ensemble average at the new value of β. Actually also the distribution of Q at the new temperature could be obtained but it is not possible – and it would be paradoxical if it was – to obtain a new Monte Carlo history at the new β. Hence, the error on $Q(\beta)$ cannot be estimated in the standard way as described in §3.3.

Using the jackknife method

The idea to apply the jackknife in the multiple histogram method is to obtain $Q_i^J(\beta)$ reweighting the data many times, leaving out at each reweighting one entry from *all* the simulation data sets. The label J stands for jackknife and i indicates that the i-th measurement in each simulation has been ignored. Q_i^J plays the role of x_i^J in Eq. (3.38) and, once obtained them, the jackknife estimators can be evaluated and it is possible to attribute an error to $\langle Q(\beta) \rangle$ using Eq. (3.39b). It is worth remembering that the data must be uncorrelated, in order for the jackknife to give a correct result. Clearly, from what said follows that the uncorrelated statistics accumulated in each run has to be the same, condition hardly met in practice. In fact, the only realistic way to fulfil this requirement is to perform a proper binning of the data, choosing a different bin size per data set. Of course, to remove the autocorrelation, each bin size has to be chosen respecting a lower bound, which typically differs from simulation to simulation. Unless τ_{INT} does not vary too much among different runs, this implies that, for some data sets, a too large bin size is used, reducing artificially the number of independent events in principle available.

Using the bootstrap method

A better approach, is to use the bootstrap method, without binning the data before and removing the autocorrelation during the resampling procedure. As already remarked, the value of the integrated autocorrelation time depends in general on the observable and it is different at different values of β_i. Let us then suppose to have calculated the bin sizes for the observable $Q(\beta_i)$. It is, then, possible to randomly select one data per bin in each simulation and produce a set of approximately uncorrelated data per simulation. Using these as input, the multi histogram method allows us to obtain $Q^B(\beta)$, from which f^B can be evaluated. Repeating this resampling and reweighting steps N_{boot} times, Eq. (3.41b) can be used to attribute an error to $\langle Q(\beta) \rangle$.

Reweighting composite quantities and reweighting in several parameters

Given the Monte Carlo histories $\{Q_s(\beta_i)\}$ of an observable Q, it is immediate to build the histories of the n-th power of it. Reweighting them, an estimate of the n-th moment $\langle Q^n(\beta) \rangle$ of Q can be obtained. Nothing more than that is needed to reweight a composite quantity, like a standardised moment of Q. To dispel any remaining doubt, let us describe how to reweight the skewness of Q. We need to evaluate

$$B_3(\beta) = \frac{\langle Q^3(\beta) \rangle - 3 \langle Q^2(\beta) \rangle \langle Q(\beta) \rangle + 2 \langle Q(\beta) \rangle^3}{(\langle Q^2(\beta) \rangle - \langle Q(\beta) \rangle^2)^{3/2}}$$

and this is straightforward once reweighted the first three moments of Q. Both the jackknife and the bootstrap can be applied to get the error on B_3, using a function of three variables,

$$f : \mathbb{R}^3 \to \mathbb{R} \qquad f(x, y, z) = \frac{x - 3\,y\,z + 2\,z^3}{(y - z^2)^2}\;.$$

To conclude, let us generalise Eqs. (3.50) to the case in which we would like to interpolate at the same time scans done in different parameters. The requirement on the linearity of the action in all parameters has still to hold. It is convenient to use a vector notation to indicate the set of

parameters in which the reweighting is being done and the correspondent conjugated quantities. Denoting them by $\mathbf{p}$ and $\mathbf{H}$, respectively, we can write down the analogue of Eqs. (3.50),

$$\langle Q(\mathbf{p}) \rangle = \frac{1}{\mathcal{Z}(\mathbf{p})} \sum_{i,s} \frac{Q_s(\mathbf{p}_i)}{\sum_j n_j \, \mathcal{Z}^{-1}(\mathbf{p}_j) \, e^{\,(\mathbf{p}-\mathbf{p}_j)\cdot\mathbf{H}_s(\mathbf{p}_i)}} \tag{3.51a}$$

$$\mathcal{Z}(\mathbf{p}_j) = \sum_{i,s} \frac{1}{\sum_k n_k \, \mathcal{Z}^{-1}(\mathbf{p}_k) \, e^{\,(\mathbf{p}_j-\mathbf{p}_k)\cdot\mathbf{H}_s(\mathbf{p}_i)}} \tag{3.51b}$$

$$\mathcal{Z}(\mathbf{p}) = \sum_{i,s} \frac{1}{\sum_k n_k \, \mathcal{Z}^{-1}(\mathbf{p}_k) \, e^{\,(\mathbf{p}-\mathbf{p}_k)\cdot\mathbf{H}_s(\mathbf{p}_i)}} \;. \tag{3.51c}$$

In the exponential function at the denominator there is now a scalar product between vectors and the meaning of the indices is the same as in Eqs. (3.50) and therefore the indices i, j and k on the vector $\mathbf{p}$ have nothing to do with the components of such a vector (as well as s on $\mathbf{H}$).

§ 3.5   The `BaHaMAS` tool

To conclude this chapter, we would like to briefly introduce a valuable tool that has been developed in the last years and which can be really helpful in finite temperature LQCD. In §3.4 we explained that a typical study of the QCD phase diagram requires a large number of simulations. Just to give an idea of how costly it can be, let us consider all the parameters that have to be varied to obtain a continuum extrapolated result of a particular feature, like to understand the order of the phase transition in the $N_f = 2$ massless limit at $\mu = 0$, using a purely imaginary chemical potential [56]. Using a bash inspired code, we can write something like

```
for Nt in ...; do           # ~3 values
  for mu in ...; do         # ~6 values
    for mass in ...; do     # ~6 values
      for Ns in ...; do     # ~3 values >= 3*Nt
        for T in ...; do    # ~5 values
          echo "Run the (R)HMC for >50k trajectories"
          # ...
        done
      done     # Consider that the typical time of a
    done       # simulation varies from weeks to months
  done
done
```

where the loop structure does not really hold in practice, because the scans in the inner loops depend in general on the parameters fixed in the outer ones. For example, to locate the phase transition at two different values of the mass, different scans in temperature will be needed. The numbers indicated in the comments in red are only a rough estimate and they can be different in practice. Considering that the simulations in the three inner loops can be carried out almost in parallel (assuming to have enough computing resources), it is plausible to say that such a project lasts for years and it can easily extend up to a decade if we consider that bigger lattices are more costly to be simulated. To that, it has to be added the unavoidable delays that arise in practice from technical problems on the clusters or simply from maintenance shutdowns. It is, then, of utmost importance to keep the simulations running and to monitor them in an effective way. Each supercomputer has a job scheduler which automatically controls the execution of programs. Therefore, the typical way to run a simulation on a cluster is to write a job-script and submit it. In this way a *job* is queued and the job scheduler will handle it. Obviously, in the job-script there are the commands to run the LQCD simulation, which in turn often uses an input file. Without deepening more into details,

it is enough to know that in the job-script the value of the physical parameters for the simulation have to be specified and doing it by hand is the most error-prone way to proceed. This can work for one or two simulations, not for hundreds. Moreover, a standard LQCD software like CL^{2}QCD produces checkpoints from which a simulation can be resumed in case of any technical problem. To resume a simulation from the last or from a previous checkpoint another job-script has to be produced and submitted and some cleaning operations in the folder where the data are stored are encouraged to keep it in order. Again, doing this manually and in an efficient way is definitely not feasible and automatic tools are unquestionably needed. These are part of the reasons that led us to develop BaHaMAS, a Bash Handler to Monitor and Administrate Simulations. Since it will be probably released in the near future, it is worth giving here an overview of it[33]. On one hand it will serve as a (very generic) documentation and on the other it will give an idea of what has to be actually daily done to obtain the results that will be discussed in chapter 4.

Let us start with a disclaimer: BaHaMAS is not the most general tool. Actually it is very specific. Since simulations were run only on the LOEWE-CSC and on the L-CSC clusters whose job scheduler is slurm[34], our scripts use particular commands not available on other clusters. On top of that, we exclusively used the CL^{2}QCD software and some feature are, then, very customised. Nevertheless, some work is planned to isolate those parts that are slurm or CL^{2}QCD specific, so that any user will be able to easily adapt the tool for her/his purposes. The philosophy behind BaHaMAS is similar to that behind CL^{2}QCD discussed in §3.2. We always tried to have a high-quality, solid and tested code[35].

Being written in bash, BaHaMAS does not need to be compiled or installed, but it needs some information to be configured. This is provided via the UserSpecificVariables.sh file, which has to be created renaming (or copying) and completing the UserSpecificVariables_template.sh file, according to the comments in it. At this point the main file JobHandler.sh can be run. A good way to get started is to run it with the -h option. Any operation described in the helper so obtained makes use of some information that must be contained in the path. It is a design decision to rely on the fact that the value of some parameters (N_f, μ, m_q, N_t and N_s) is extracted from the folder names. This makes sense, because the most natural way to keep data ordered is to create a folder per parameter. The order and the prefixes to be used can be customised in the PathManagement.sh file. If the job handler is tried to be run from a directory whose path does not contain the needed information, the script will exit. The parameters that have not to be read out from the path are given either via command line options or using the betas file.

The betas file

A Monte Carlo simulation has a bunch of parameters that need to be specified and some of them have to be tuned. It would be unpractical to specify them via command line options. Hence, it makes sense to have a setup file where to store some input values for the simulations. This file is called by default betas, since it has to be used to specify the β values. For each value of β, other parameters can be specified – e.g. the pseudo-random number generator (PRNG) seed, the number of steps to integrate the molecular dynamics equations or a trajectory from which a run has to be resumed. The betas file is needed and used by the job handler and an alternative name for it can be specified via the --betasfile option. Note that lines in the betas file starting by # are completely ignored. This allows the user to always keep all the β values in it and comment or comment out some of them, maybe using the -u and -U options, respectively.

---

[33]It is almost unavoidable to use here names of file or options that could change in future. However, the features described here will not drastically change and the user will be probably able to make the needed connections.

[34]http://slurm.schedmd.com/

[35]In BaHaMAS there are not (yet) unit tests and at the moment we just decided to test any new feature by using it. We recognise that this is an aspect which can be improved.

Starting, continuing or resuming simulations

It is worth emphasising that, typically, the job handler script is run from the folder where the betas directories have to be created. It is known that, in a Markov process some configurations have to be discarded. Since a scan in β is always needed, we will need to make different run with the same identical parameters, but different temperatures. It is, then, convenient to make one or two thermalisations from an arbitrary configuration (usually hot or cold) and to make then one thermalisation per β value that have to be simulated, starting it from the partially thermalised configuration. In this way some resources can be saved. Accordingly to this strategy, a naming scheme for the betas directories has been chosen. The common format is `bx.xxxx_syyyy_suffix` where `b` and `s` are the β-prefix and the seed-prefix, respectively; `x.xxxx` and `yyyy` are the β and the seed values, respectively and the `suffix` can be

- `thermalizeFromHot` for thermalisations started from a hot configuration;

- `thermalizeFromConf` for thermalisations started from a partially thermalised configuration;

- `continueWithNewChain` for a real run.

The first time a simulation is started, the correspondent beta directory is created. Inside it, the input file for the software (in our case CL^{2}QCD) is created, while the job script is created in the `JobScripts` folder. If desired, the job is submitted.

Let us, instead, suppose that a simulation has to be continued or resumed from some point in the Monte Carlo history. In both cases the `bx.xxxx_syyyy_continueWithNewChain` folders are already existing and inside them there are the checkpoints produced during the simulation. A checkpoint is a pair of files, the configuration file and the PRNG state. In this case, for each β specified in the `betas` file, the job handler will look for the required checkpoint, adjust in case the input file, create the job script and, if desired, submit it. Observe that, if the checkpoint is not the last one, some cleaning operations are done in the correspondent beta directory. In particular a folder `Trash_yyyy-mm-dd_hhss` is created and all the checkpoints more recent that the selected one are moved therein. Also a backup of the observables file is done and put in this folder. Finally, from the observables file in the beta folder – the one where new measurements will be added – all the data referring to trajectories after the chosen checkpoint are deleted. In this way everything is kept clean and in order.

Monitoring the status of the simulations in real time

The `-l` option of the job handler is probably one of the more used. It is possible to monitor in real time the simulations, no matter if they are running, pending or just not queued. An example of how its output looks like has been reported in Table 3.3. The content of each column should be self-explanatory, but each colour has a meaning and it is worth commenting on it.

- A red entry in the `Beta` column signals that for such a simulation some observables have changed despite that in the Metropolis test the new configuration has not been accepted and the stored configuration is identical to the previous one. Usually this is connected to a hardware problem.

- A red entry in the `Traj.  Done` column indicates that the observables file has to be cleaned, because it contains repeated trajectories.

- The two acceptance rate columns can be red, dark orange, green, yellow or orange, depending on the value. If the acceptance is too low and then red or dark orange, the simulations should be stopped and continued doing more integration steps in the molecular dynamics part. Yellow and orange acceptance rates are higher than optimal, green values.

Beta	Traj. Done (Acc.)	[Last 1000]	int0-1-2-kmp	Status	Max DS	Last tr. finished	Tr: # (time last|av.)
5.4300_s4300_NC	58786 (81.67 %)	[79.60 %]	10-17	RUNNING	4.94521	25 sec. ago	63785 (notMeasured)
5.4300_s4300_fC	4000 (97.42 %)	[97.40 %]	10-29	notQueued	0.270217	------ sec. ago	4999 (notMeasured)
5.4300_s4300_fH	1000 (97.20 %)	[97.20 %]	10-32	notQueued	11.1092	------ sec. ago	999 (notMeasured)
5.4300_s5411_NC	61330 (82.65 %)	[83.10 %]	10-17	RUNNING	4.42087	47 sec. ago	66329 (notMeasured)
5.4300_s6522_NC	61357 (82.92 %)	[80.60 %]	10-17	RUNNING	4.89215	36 sec. ago	66356 (notMeasured)
5.4300_s7633_NC	60201 (82.85 %)	[80.40 %]	10-17	RUNNING	5.74873	9 sec. ago	65200 (notMeasured)
5.4330_s4330_NC	64774 (84.54 %)	[80.00 %]	10-17	RUNNING	4.24899	30 sec. ago	69773 (notMeasured)
5.4330_s4330_fC	4000 (97.67 %)	[98.30 %]	10-29	notQueued	0.262304	------ sec. ago	4999 (notMeasured)
5.4330_s5441_NC	64909 (84.82 %)	[82.60 %]	10-17	RUNNING	5.007	38 sec. ago	69908 (notMeasured)
5.4330_s6552_NC	63938 (84.37 %)	[80.50 %]	10-17	RUNNING	5.01098	16 sec. ago	68937 (notMeasured)
5.4330_s7663_NC	63625 (84.50 %)	[76.30 %]	10-17	RUNNING	4.34834	15 sec. ago	68624 (notMeasured)
5.4350_s4350_fH	1000 (97.50 %)	[97.50 %]	10-32	notQueued	4.0071	------ sec. ago	999 (notMeasured)
5.4360_s4360_NC	66709 (86.54 %)	[86.00 %]	10-17	RUNNING	3.8505	29 sec. ago	71708 (notMeasured)
5.4360_s4360_fC	4000 (97.90 %)	[97.90 %]	10-29	notQueued	0.213323	------ sec. ago	4999 (notMeasured)
5.4360_s5471_NC	67189 (85.98 %)	[79.90 %]	10-17	RUNNING	4.17417	20 sec. ago	72188 (notMeasured)
5.4360_s6582_NC	66165 (86.06 %)	[80.30 %]	10-17	RUNNING	4.67013	12 sec. ago	71164 (notMeasured)
5.4360_s7693_NC	66726 (86.13 %)	[81.10 %]	10-17	RUNNING	3.94837	9 sec. ago	71725 (notMeasured)
5.4390_s4390_NC	69317 (82.40 %)	[78.70 %]	10-16	RUNNING	6.72853	11 sec. ago	74316 (notMeasured)
5.4390_s4390_fC	4000 (98.00 %)	[97.60 %]	10-29	notQueued	0.234035	------ sec. ago	4999 (notMeasured)
5.4390_s5401_NC	69567 (82.69 %)	[79.90 %]	10-16	RUNNING	7.41427	36 sec. ago	74566 (notMeasured)
5.4390_s6512_NC	69529 (84.67 %)	[83.70 %]	10-17	RUNNING	6.50622	23 sec. ago	74528 (notMeasured)
5.4390_s7623_NC	67410 (81.57 %)	[74.60 %]	10-16	RUNNING	6.63593	31 sec. ago	72409 (notMeasured)
5.4400_s4400_fH	1000 (96.80 %)	[96.80 %]	10-32	notQueued	11.2124	------ sec. ago	999 (notMeasured)
5.4420_s4420_NC	60880 (81.50 %)	[83.60 %]	10-16	RUNNING	7.31466	25 sec. ago	65879 (notMeasured)
5.4420_s5531_NC	59443 (80.92 %)	[66.80 %]	10-16	RUNNING	7.06359	28 sec. ago	64442 (notMeasured)
5.4420_s6642_NC	59946 (81.36 %)	[91.00 %]	10-17	RUNNING	7.90988	1 sec. ago	64945 (notMeasured)
5.4420_s7753_NC	59392 (80.49 %)	[78.00 %]	10-16	RUNNING	6.51365	13 sec. ago	64391 (notMeasured)
5.4450_s4450_NC	36555 (81.35 %)	[82.60 %]	10-16	RUNNING	5.67753	32 sec. ago	41554 (notMeasured)
5.4450_s4450_fH	1000 (98.00 %)	[98.00 %]	10-32	notQueued	8.78924	------ sec. ago	999 (notMeasured)
5.4450_s5561_NC	37272 (82.83 %)	[88.40 %]	10-16	RUNNING	6.22743	12 sec. ago	42271 (notMeasured)
5.4450_s6672_NC	36562 (81.54 %)	[76.40 %]	10-16	RUNNING	4.89611	5 sec. ago	41561 (notMeasured)
5.4450_s7783_NC	34850 (81.70 %)	[85.50 %]	10-16	RUNNING	6.07066	14 sec. ago	39849 (notMeasured)

Table 3.3: *Possible output of the status -l option of the job handler script. Each colour has a precise meaning. Content of each table from left to right: β value of the simulation, number of trajectories done, average acceptance rate during the whole simulation, average acceptance rate in the last 1000 Monte Carlo updates, number of integration steps in each timescale used, status of the simulation, maximum difference of the Hamiltonians in the Metropolis test, time elapsed since the last Monte Carlo update finished, number of last trajectory, time to complete the last update and the average time per trajectory.*

```
            AUTOMATIC REPORT FROM DATABASE (status on 26.08.2016 at 08:16)


                          Simulations on  broken GPU:     1
     Simulations with too low acceptance - last 1k:     0  -    1 [  0%,  68% )
         Simulations with low acceptance - last 1k:     0  -    1 [ 68%,  70% )
     Simulations with optimal acceptance - last 1k:    28  -   52 [ 70%,  78% ]
        Simulations with high acceptance - last 1k:   401  -  373 ( 78%,  90% ]
     Simulations with too high acceptance - last 1k:   111  -  113 ( 90%, 100% ]
                          Simulations  running:  113
                          Simulations  pending:    0
                Simulations   stuck (or finished):   10
                      Simulations  running fine:  103
                      Output files  to be cleaned:    0


           Use -ds | --dataBase --show option to display set of simulations.
```

Figure 3.8: Possible output of the database report of `BaHaMAS`. The first entry of the report has the same meaning of a red entry in the `Beta` column of the status table produced using the `-l` option of the job handler.

- A red entry in the `Max DS` column signals that suspiciously large differences of Hamiltonians in the Metropolis test have been detected and it could mean that an I/O error occurred or that something broke. This check is not done for thermalisations, where big differences can occur.

- If the time since the last trajectory has been produced becomes too large, it is coloured in red in the `Last tr.  finished` column. The corresponding simulation is either finished or probably stuck.

The simulations database and its report

The database functionality is one of the strong points of `BaHaMAS`. Since it is more than an option, we decided to make it as a sub-program (with own options as well) of the job handler, without at the same time having to execute a different script. Running the job handler `--helpDatabase` option, an overview can be obtained. Moreover, each option passed to the job handler after `-d` is intended to be for the database functionality.

Using the database, information about all the existing simulations in a project can be displayed and/or arbitrarily filtered. It is somehow an extension of the `-l` option (and internally it is implemented in terms of it). In order to use it, the database has to be created or updated. This can be done with a constant frequency or at a fixed time, once per day[36]. The most useful functionality of the database is that it can elaborate its information producing a report, which immediately gives an overview of the project signalling possible existing problems. In the present version of `BaHaMAS`, it could look like reported in Figure 3.8. How to read it does not need to be explained further. To understand which simulations are problematic cannot be easier!

---

[36]Updating it quite often in a screen session (or analog) allows to have an immediate status of a folder. This can be obtained giving to the job handler the `-dl` options.

# The nature of the Roberge-Weiss transition in two-flavours QCD

4

«*Patience and diligence, like faith, remove mountains.*»

— **William Penn** —

One central issue that has been studied for years by now and that is not yet quantitatively understood in finite temperature LQCD is the Columbia plot. In §2.2 we gave a quite broad introduction to the topic, discussing why and which scenarios are still in principle possible. We learnt that, approaching the continuum limit, some features could drastically change and this makes any prediction hard to be done. The ultimate goal would be to map out the position of the Z_2 lines in physical units and for $a \to 0$. This would also clarify the at the moment puzzling question about the chiral first order region in the $N_f = 2$ and $N_f = 3$ chiral limits. Are they still present in the continuum limit or are they only lattice artefacts that disappear once a is sent to zero? The answer to this question remains nowadays a mystery and this is mainly due to the extremely high numeric cost of a brute force approach. Though strictly speaking possible, to take the chiral limit in the Columbia plot is definitely beyond our present capabilities, since it should be done after having performed the continuum limit. This led people in the recent years to look for alternative approaches to clarify the situation and the main indirect strategy takes advantage of the use of a purely imaginary chemical potential. As discussed in §2.3, at $\mu = \imath\mu_I$, there is no sign problem and standard numerical techniques can be used to study the phase diagram of the theory in the $(m_{u,d}, m_s, \mu^2)$ space. This results in different scenarios of the 3D Columbia plot, whose differences reflect the unknown features at $\mu = 0$. In §2.4, it was described how to find the order of the chiral transition at zero chemical potential using simulations at $\mu = \imath\mu_I$ for $N_f = 2$ QCD[1]. This has been recently successfully done both with unimproved staggered fermions [56] and with unimproved Wilson fermions [68] on a very coarse lattice – $N_t = 4$ which resulted into $a \simeq 0.3$ fm. Even though both studies concluded that on such coarse lattice the chiral phase transition at zero chemical potential is a first-order phase transition, the Z_2 boundary of the chiral first-order region has been found to be very different. In particular, using the pion mass measured at $m_{u,d}^{Z_2}$ to compare the position of the second-order end point, it has been found $m_\pi^{Z_2} \simeq 560$ MeV and $m_\pi^{Z_2} \simeq 60$ MeV with Wilson and staggered fermions, respectively. This huge difference clearly suggests that the lattice used is too coarse and cut-off effects are still dominant. A similar discrepancy has also been found in the Roberge-Weiss Columbia plot, regarding the position of the chiral tricritical point, which is used as starting point to map out the Z_2 line in the 3D Columbia plot back-plane. Here, using again the pion mass measured at $m_{u,d}^{\mathrm{tric.}}$ the comparison, it was found $m_\pi^{\mathrm{tric.}} = 913(9)$ MeV and $m_\pi^{\mathrm{tric.}} \simeq 400$ MeV with Wilson [97] and staggered [66] fermions, respectively[2]. The natural following step is to repeat similar measurements on a finer lattice. Naïvely, it could be thought that the

---

[1]There would be no conceptual difference in applying the same method in the $N_f = 3$ case.

[2]Observe that the pion mass at the tricritical point in the Wilson case was originally measured in [102] but with a less accurate method than in [97].
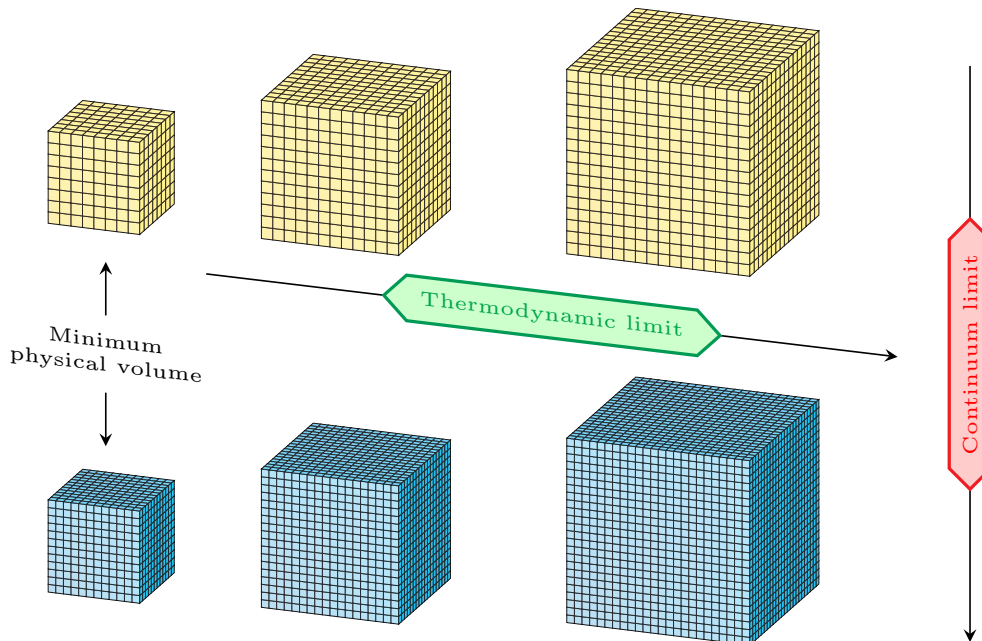
Figure 4.1: *Schematic representation of why taking the continuum limit is more and more costly. The temporal direction (lattice spacing) is understood to be larger (smaller) on the blue lattices than on the yellow ones. Observe how the number of lattice sites in the spatial direction has to be increased in order to keep the physical volume fixed and to remain in good approximation in the thermodynamic limit.*

lattice spacing has to be considerably reduced in order to get close enough to the continuum limit and to avoid, then, to obtain a result still dominated by cut-off effects. Even though theoretically correct, this would probably not be a wise decision. To simulate on a finer lattice, the temporal extension has to be increased and this has some consequences. The main one has been depicted in Figure 4.1 using 3D lattices. It is known that the bigger is the spatial volume in a simulation the more negligible are the finite size effects. This is due to the fact that, in physical units, there is a volume that can be approximately considered infinite. Fixed a lattice spacing, i.e. fixed the temporal extension of the lattice, this will result in a certain number of lattice sites in any spatial direction. When N_t is increased, and consequently a is reduced, the value of N_s to still simulate the approximately infinite lattice volume will also increase. Said in different words, finer lattices are more and more costly to be simulated! Moreover, we know that smaller quark masses will need to be simulated as a decreases, because of the shift of the chiral (tri)critical points due to reduced cut-off effects. In conclusion, it is better to choose to work on $N_t = 6$ lattices, as continuation of previous investigations. This will also lead to a better understanding about what is numerically needed (e.g. resources, optimisations) to repeat similar studies on even finer lattices in future. The core of this thesis has been to locate the tricritical points in the Roberge-Weiss Columbia plot for $N_f = 2$ QCD with unimproved both Wilson [97] and staggered [103] fermions on $N_t = 6$ lattices. For the sake of completeness, but also because it gives a lower bound for the deconfinement Z_2 point at $\mu = 0$, the deconfinement tricritical point was found, too. This chapter will be dedicated to the description of these investigations, trying to explain in detail the strategy followed, but considering understood the notions learnt so far. Hence, we will not explicitly refer to chapters 2 and 3 too often. In particular, the §3.4 is, to some extent, introductory and we encourage the less experienced Reader to refer to it for a better understanding of what presented in the following.

Actually, before presenting our original results, we decided to report on the outcome of an investigation that we did to ensure the correctness of RHMC algorithm with staggered fermions

added to the `CL²QCD` software and used later. Even if it is not about new physics, it is worth discussing it, because it will give a first concrete example of what it has been introduced in the previous chapter. Moreover, the techniques used are not peculiar of this study and they could be used in other projects.

Testing the correctness of the RHMC code in `CL²QCD`

Despite the fact that every part of the `CL²QCD` software is separately tested, before starting using the freshly implemented RHMC algorithm for any new physics study, we decided to reproduce a quite old result, in order to ensure the correctness of the code. In particular, we decided to locate the chiral Z_2 point in the Columbia plot with three degenerate flavours on a very coarse lattice with $N_t = 4$. This was done in 2007 by P. de Forcrand and O. Philipsen [57], who found, after a finite size scaling analysis, $m_q^c = 0.0263(3)$.

We repeated exactly the same investigation, proceeding as already qualitatively described in §3.4. The simulations were run on the `LOEWE-CSC` supercomputer, using one `GPU` per temperature value. Keeping in mind that our intention was only to reproduce the known result and not to perform a high precision measurement, we chose the parameters of our simulations not in the completely standard way, trying to save some computation time whenever possible. More in detail, we did an asymmetric scan in m_q around m_q^c, simulating at larger (and then cheaper) values of m_q, and we used slightly lower statistics than in [57], as it can be seen from the table in Figure 4.2. For each mass value, we made a temperature scan in order to locate the phase transition. The critical β has been found as zero of the skewness of the chiral condensate. At β_c, we evaluated the kurtosis $B_4(\bar{\psi}\psi)$ and, in this way, a point was added in the (B_4, m_q) plane. Repeating everything on three different spatial volumes ($N_s = 8, 12, 16$) we collected enough data to perform the final finite size scaling analysis. They have been reported in Figure 4.2. According to Eq. (3.49a), which we reported here for simplicity,

$$B_4(\bar{\psi}\psi, m_q, N_s) = B_4(m_q^c, \infty) + a_1 (m_q - m_q^c) N_s^{1/\nu} \,,$$

the value of the critical mass can be extracted from a fit. In this case, as done in [57], we fixed $B_4(m_q^c, \infty)$ to its universal 3D Ising value and extracted the values of a_1, m_q^c and ν from the fit. Due to the choice of the mass range and to the not ideally high statistics, the χ^2 per degree of freedom of the fit is somewhat small and, thus, the errors on the parameters a_1 and ν are still large. However, the value of the critical mass – $m_q^c = 0.0258(8)$ – is precisely enough determined to declare that the previous result has been successfully reproduced. From this point on, also the staggered part of the `CL²QCD` software has been officially considered ready to be used for new physics studies.

Lastly, it is worth remarking that this was the first time that the staggered code was massively run at physically relevant values of the parameters. This allowed us also to identify some bottlenecks and, to some extent, to speed up the code, especially working on some optimisations of the CG - M solver.

§ 4.1   On $N_t = 6$ lattices with Wilson fermions

Using Wilson fermions, it is common to use the hopping parameter κ instead of the bare quark mass $m_{u,d}$. Since they are related via

$$\kappa = \frac{1}{2(a\, m_{u,d} + 4)} \,,$$

it is common to refer to κ as *mass*, considering understood this relation. We will adopt as well this habit, keeping in mind that, then, the heavy mass region will be identified by small values of κ, while larger κ values will refer to the light mass region.

m_q	# trajectories per N_s		
0.025	170k	165k	250k
0.030	235k	160k	180k
0.035	240k	140k	180k
0.040	200k	210k	200k
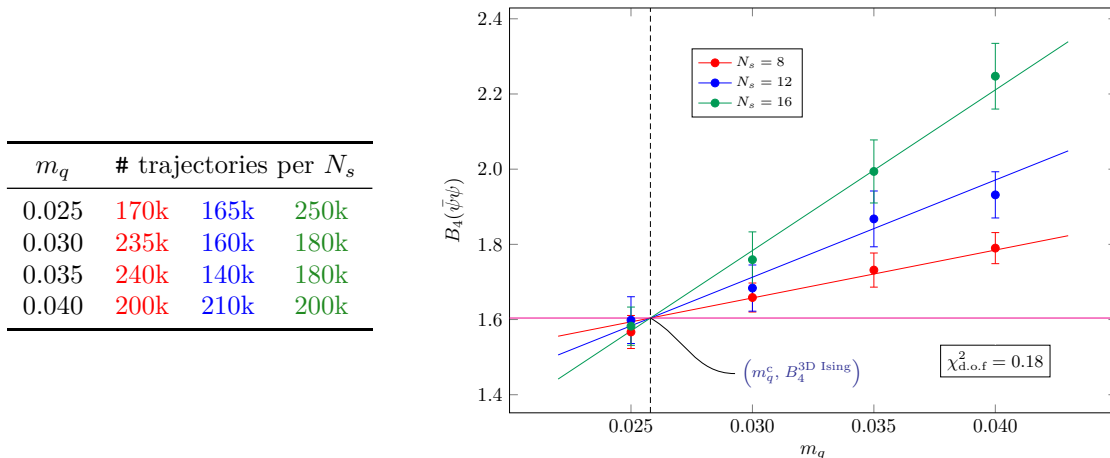
Figure 4.2: Overview of the statistics accumulated in the RHMC algorithm correctness check together with the conclusive fit of the kurtosis at different masses and different lattice spatial extent. Different colours in the table correspond to different N_s as indicated in the legend of the plot. On top of the data, the result of the multi-branch fit to Eq. (3.49a) has been drawn. The numerical values of the obtained parameters are $a_1 = 0.34(27)$, $\nu = 0.56(10)$ and $m_q^c = 0.0258(8)$. The dashed vertical line at $m_q = m_q^c$ and the horizontal magenta one at the universal 3D Ising value of the kurtosis are meant to emphasise the crossing point of the data.

Working with two degenerate flavours in the Roberge-Weiss Columbia plot means to move on the upper edge of Figure 2.10 at page 58. Our strategy to locate the two tricritical values of κ is completely analogue to that used on $N_t = 4$ lattices [102] and it was already partially sketched in §3.4. To summarise it, a scan in mass is needed; then, for each simulated value of κ, the kurtosis around the critical coupling β_c is measured and the value of ν fitting the data according to Eq. (3.49b),

$$B_4(Q, \beta, N_s) = B_4(\beta_c, \infty) + a_1 \left(\beta - \beta_c\right) N_s^{1/\nu} \ ,$$

is extracted. The changes in ν as κ is varied allow to locate the tricritical points. Here, Q should be an order parameter and we know that, as discussed in §2.3, the shifted phase $\phi = \varphi - \mu_I/T$ of the Polyakov loop is a suitable one to distinguish between the low T disordered phase and the high T ordered phase with two-state coexistence. Nevertheless, for the particular values $\mu_I/T = \pi \pm 2\pi k$, $k \in \mathbb{Z}$, the imaginary part of the Polyakov loop L_{Im} can be also used as order parameter[3]. This is the reason why we fixed $\mu_I/T = \pi$ in all our simulations (remember the symmetries of the partition function at purely imaginary chemical potential).

More in detail, the critical behaviour of the system was studied for 9 values of the bare quark mass between $\kappa = 0.1$ and $\kappa = 0.165$. For each value of κ, we simulated at the fixed temporal lattice extent $N_\tau = 6$ that implies the value $a\mu_I = \pi/6$ for the imaginary chemical potential. Three or four different spatial lattice sizes per κ have been used, always with $N_\sigma \geqslant 16$ (except for $\kappa = 0.1625$ where also $N_\sigma = 12$ was used). This gives a minimal aspect ratio of almost 3. For every lattice size, 6 up to 30 values of β around the critical value have been simulated. 40 up to 500 thousands of standard HMC [104] trajectories of unit length per β have been collected after at least 5 thousands trajectories of thermalization. An overview of the accumulated statistics can be found in Table 4.1. The observables of interest (i.e. plaquette, L_{Re} and L_{Im}) were measured for every trajectory after the thermalization. For $\kappa > 0.16$ we also measured the chiral condensate $\bar\psi\psi$ at each trajectory for qualitative cross-checks in the analysis. In each run the acceptance rate was tuned to $\omega \simeq 75\%$. For $\kappa \geqslant 0.16$, i.e. for the smallest masses, the Hasenbusch trick [105] in the integration of the

---

[3]In all this chapter, we will refer to the spatial averaged Polyakov loop simply as Polyakov loop.

N_t	κ	β range	Total statistics per spatial lattice size N_s (# of simulated β values | # of chains)								
			16	18	20	24	30	32	12	36	40
	0.1000	5.8460 - 5.9020	6.11M (24 | 2)		4.36M (16 | 2)	4.30M (16 | 2)	-			-	
	0.1100	5.8400 - 5.8660	-		3.81M (26 | 4)	1.49M (14 | 4)	4.05M (18 | 4)			1.92M (13 | 4)	
	0.1200	5.8180 - 5.8450	5.28M (10 | 4)		3.89M (9 | 4)	3.23M (9 | 4)	2.19M (8 | 4)			-	
	0.1300	5.7760 - 5.7980	-		3.94M (25 | 4)	3.76M (23 | 4)	3.56M (16 | 4)			-	
6	0.1550	5.5210 - 5.5420	1.40M (30 | 1)		1.04M (23 | 1)	1.12M (24 | 1)	0.76M (9 | 4)			-	
	0.1575	5.4750 - 5.4930		0.59M (7 | 4)	-	0.92M (7 | 4)	1.40M (7 | 4)			-	
	0.1600	5.4330 - 5.4430		0.52M (6 | 4)	-	0.86M (6 | 4)	1.12M (6 | 4)			-	
	0.1625	5.3800 - 5.3930		0.92M (12 | 4)	-	1.12M (8 | 4)	-		1.38M (7 | 4)		
	0.1650	5.3260 - 5.3370	1.99M (16 | 4)		1.09M (11 | 4)	1.71M (12 | 4)	-			-	
8	0.1300	5.9400 - 5.9800		3.69M (9 | 4)	-	5.40M (9 | 4)	2.00M (5 | 4)				1.00M (5 | 4)

Table 4.1: *Overview of the statistics accumulated in all the simulations. Since the resolution in β is not the same at different κ, the number of simulated β has been reported per each range. The accumulated statistics per β has not always been the same. Therefore the number of trajectories here is about all the trajectories produced per given N_s. Using the number of chains provided above, it can be easily estimated how long was on average each chain, even though we always accumulated higher statistics close to the critical temperature.*

Molecular Dynamics equations has been used to reduce the integrator instability, which is triggered by isolated small modes of the fermion kernel [106]. In the data analysis, the Ferrenberg-Swendsen reweighting [100] was used sometimes simply to smooth out our data, sometimes to add some new β-points. Because of the particularly delicate fitting procedure required to extract the critical exponent ν from Eq. (3.49b), we almost always produced 4 different Markov chains for each value of the coupling in order to better understand if the collected statistics was enough. We will come back to this point in a moment.

For scale-setting purposes, $T = 0$ simulations at or close to certain critical parameters have been performed: 200 up to 1600 independent configurations on 32×16^3 lattices have been produced. The scale itself is then set by the w_0 parameter using the publicly available code described in [107]. This method is based on the Wilson-flow and is very efficient and fast. In addition, the pion mass m_π was determined using these configurations.

All our numerical simulation have been performed using the CL²QCD software, which has been presented in §3.2 and which is optimised to run efficiently on GPUs. In particular, the LOEWE-CSC cluster at Goethe-University in Frankfurt and the L-CSC supercomputer at GSI in Darmstadt have been used.

§ 4.1.1 The analysis of the data

In a Monte Carlo simulation, it is not easy to decide whether the accumulated statistics is high enough. Clearly, the higher it is the better and the smaller will be the errors on the measured quantities. We know that measuring the integrated autocorrelation τ_{INT} of a given observable allows to determine the number of independent events collected. In our simulations, we collected, on average, not less than 30 independent events per HMC run for $B_4(L_{\mathrm{Im}})$. Of course, this is more a necessary than a sufficient condition to be sure to have a high enough statistics. Another way to judge on this point is to run several HMC simulations until the value of the considered observable is statistically the same on the different Markov chains. In our case, we almost always repeated the simulation four times for the same physical setup, starting each run with a different seed of the pseudo-random number generator – in Table 4.1 we reported in detail the number of *chains* (so is called each of the repeated run) produced per β depending on the volume. When the four values of the kurtosis $B_4(L_{\mathrm{Im}})$ were compatible within three standard deviations, we stopped increasing the statistics (rarely some spike beyond 3σ occurred and it was accepted if far from the critical
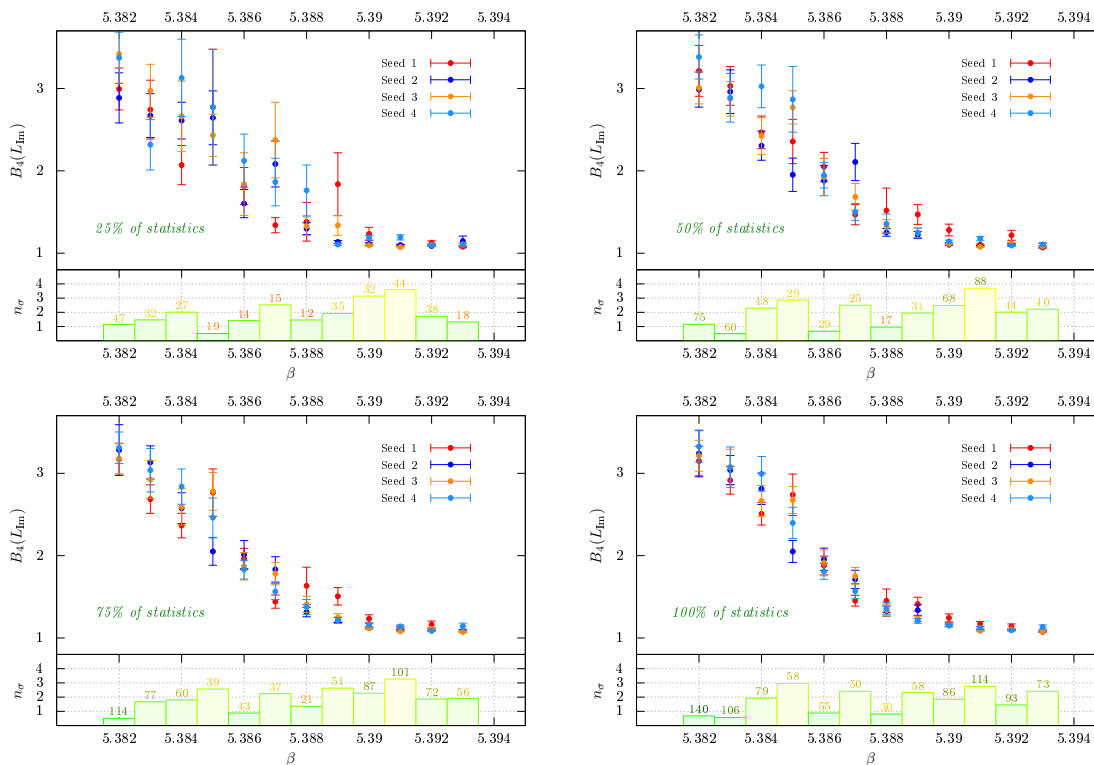
Figure 4.3: *Successive analysis of the kurtosis measurements at $\kappa = 0.1625$ on $N_s = 18$. The histogram below each plot is a guideline to judge on the statistics. n_σ at each β is the number of standard deviations at which the two most different chains are compatible. The number above each bar is the average number of independent events collected at that β. The colours have been chosen in order to reflect the goodness of the statistics, from green (statistics high enough) to red (statistics to be increased). Both n_σ and the number of independent events have to be monitored to decide when to stop increasing statistics.*

temperature). It is important to remark that the two criteria just mentioned must be combined. In fact, it could happen – and actually it happens quite often – that after few thousands trajectories one has the 4 values of $B_4(L_{\mathrm{Im}})$ compatible within 3σ (because of large errors), but the number of independent events is still too low. On the other hand, once reached a quite high amount of independent events, the four values of $B_4(L_{\mathrm{Im}})$ are often still not close together. In Figure 4.3 we show an example at $\kappa = 0.1625$ on $N_s = 18$. Note that the improvement of the signal as the statistics is enlarged is clearly visible also by eye. Finally, each chain being long enough, we merged them for the finite size scaling analysis.

As previously mentioned, we extracted the critical exponent ν performing a finite size scaling analysis, fitting the kurtosis of the imaginary part of the Polyakov loop according to Eq. (3.49b). Since it is necessary to fit at the same time data coming from different spatial lattice sizes, a multi-range fit was performed (alternatively, it is possible to fit the function $B_4(\beta, N_s)$ regarded as a function of two variables; we checked that this approach brings to the same result, as expected). The main issue here is to understand in which interval to perform the fit. In principle, one could manually change the interval where to fit the data until a good fit is found. But what does *good* mean? Supposing to have few B_4-points around β_{c} for each spatial volume, it is already hard to be sure to have found the best possible fit by hand (the number of ways in which the data can be fitted is large). Therefore, we decided to automatise this procedure, producing all possible fits (this means to choose β_{min} and β_{max} in all possible ways for each lattice size). Of course this just means

to rephrase our question: Which is now the best fit out of the thousands produced? There are few theoretical considerations that help in our filtering procedure.

- First of all, it is clear from Eq. (3.49b) that we should fit our data around β_c. We then excluded, for each volume, all the combinations for which the condition

$$\beta_c \in \left[\beta_{\min}, \beta_{\max}\right] \tag{4.1}$$

was not fulfilled. Of course, β_c is the critical temperature in the thermodynamic limit and it is known only a posteriori, after having performed the fit.

- Another information to be considered is that the scaling interval of the kurtosis around the critical β is unique in the variable $x \equiv (\beta - \beta_c) N_s^{1/\nu}$. Namely, values of the kurtosis from different volumes should collapse on the same curve in this interval when plotted against x. This also means that for larger N_s the scaling region in β around β_c is smaller and it enlarges reducing the spatial lattice extent. Therefore, indicating with $I_1, \ldots, I_n$ the intervals in β where the data coming from $N_{s1} < \ldots < N_{sn}$ were fitted, the condition

$$I_1 \supseteq \cdots \supseteq I_n \tag{4.2}$$

has to hold.

- In the definition of the scaling variable x, both β_c and ν are unknown and we cannot directly make use of this expression to deduce the interval where to fit our data. Nevertheless, we can use this information to cross-check whether the data extracted from a fit are good or not. After having fitted the data in the intervals

$$I_1 \equiv \left[\beta_1^{\min}, \beta_1^{\max}\right] \qquad \ldots \qquad I_n \equiv \left[\beta_n^{\min}, \beta_n^{\max}\right],$$

both β_c and ν are estimated. We can then map the intervals $I_1, \ldots, I_n$ into intervals

$$\tilde{I}_1 \equiv \left[x_1^{\min}, x_1^{\max}\right] \qquad \ldots \qquad \tilde{I}_n \equiv \left[x_n^{\min}, x_n^{\max}\right].$$

Theoretically, it should be $\tilde{I}_1 = \ldots = \tilde{I}_n$. In practice, due to the finite resolution in β, it should be $\tilde{I}_1 \approx \ldots \approx \tilde{I}_n$. In general, considering two intervals $A = [a_1, a_2]$ and $B = [b_1, b_2]$, it is possible to define an *overlap percentage* as

$$\Omega \equiv \begin{cases} 0 & \text{if } a_2 < b_1 \vee b_2 < a_1 \\ 100 \cdot \left(1 - \dfrac{|b_1 - a_1| + |b_2 - a_2|}{a_2 - a_1 + b_2 - b_1}\right) & \text{otherwise} \end{cases} . \tag{4.3}$$

For each fit done, we calculated such a percentage considering all the possible pairs of spatial lattice extent and we found the minimum overlap. Then, as further filtering condition we decided to require

$$\Omega \geqslant 80\% . \tag{4.4}$$

- Considering again the scaling interval of the kurtosis, the only information we know about it is that it is around the critical temperature. How far it extends from $x_c = 0$ cannot be estimated in general a priori. However, there is no reason to believe that it is not symmetric in x with respect to x_c. It should namely be

$$I_{\text{scaling}} = \left[-\bar{x}, \bar{x}\right],$$

with $\bar{x}$ unknown. Given, in general, an interval $J = [-a, b]$ with a and b non-negative and $a + b$ fixed, it is possible to define a *symmetry percentage* as

$$\Xi \equiv 100 \cdot \left(1 - \left|\frac{2a}{a + b} - 1\right|\right) = 100 \cdot \left(1 - \left|\frac{2b}{a + b} - 1\right|\right) . \qquad (4.5)$$

Clearly, $\Xi = 0\%$ (maximally asymmetric interval) for $a = 0$ or $b = 0$ and $\Xi = 100\%$ (maximally symmetric interval) for $a = b$. Again, we calculated Ξ per each interval involved in the fit and we found the minimum. Even if we did not fix a minimum value for this parameter, usually it was used to pick up the final result among the last bunch of selected fits.

- Finally, another useful parameter to judge the quality of the fit is the reduced chi-square, $\chi^2_{\text{d.o.f.}}$. Fits for which $\chi^2_{\text{d.o.f.}} \ll 1$ or $\chi^2_{\text{d.o.f.}} \gg 1$ have been discarded. The question that rises naively at this point is: Why not to consider as best fit that with the closest $\chi^2_{\text{d.o.f.}}$ to 1? Even though this could sound reasonable, it does not imply that Eq. (4.1), Eq. (4.2) and Eq. (4.4) are then automatically fulfilled. Moreover, producing all the possible fits, it happens that two fits differs only for one or two data points. In such a situations the $\chi^2_{\text{d.o.f.}}$ are very similar and it is better to rely on one of the conditions above to pick up one of the results.

Let us now quickly summarise the various filtering steps we followed to extract the critical exponent ν:

✓ fits not fulfilling conditions in Eqs. (4.1) and (4.2) are excluded;

✓ fits with $1 - \delta \leqslant \chi^2 \leqslant 1 + \delta$ are selected (typically $\delta \approx 0.2$);

✓ only fits fulfilling condition in Eq. (4.4) are considered;

✓ the fit with the highest minimum symmetry percentage Ξ is selected as best fit.

Before going on discussing the found results, let us spend some words about the preparation of the data for the fit. Due to the high numeric cost of the simulations, it is important to limit the number of β to simulate. Actually, given enough statistics, if the distributions of $\mathcal{S}_g(\beta_1)/\beta_1$ and $\mathcal{S}_g(\beta_2)/\beta_2$ have a good overlap, then it is possible to avoid any new simulation at $\beta_1 < \beta_{new} < \beta_2$, using the multiple histogram method to obtain the observables of interest at β_{new} (we discussed this technique in §3.4.4). This is for sure an important tool that helps to save time and computational resources, but it must be in any case carefully used. First of all, we never reweighted our data to new β outside the simulated β-interval, just because there is no quantitative control on the safety of this procedure. Then, it is a priori not clear how many new β-points to insert between simulated points. If the goal is to produce a collapse plot or to find where a certain observable takes a particular value, then the number of reweighted points is not important and can be increased as much as desired. Nevertheless, our aim was to perform a fit and it is obvious that increasing the number of reweighted points can arbitrarily reduce the value of the $\chi^2_{\text{d.o.f.}}$ of the fit. For this reason, we almost always reweighted our data without adding new points, but only extracted the observables at the simulated β. Roughly speaking, this means to distribute the physical information of each run to the neighbour points. Sometimes, indeed, it was necessary to add some new points, especially in the first-order regions where the the kurtosis is steeper and the curvature of $b_4(L_{\text{Im}})$ close to β_c is larger. Therefore, in order to linearly approximate the data, a higher resolution in β was needed. The final list of selected fits is given in Table 4.2.

§ 4.1.2   Discussion of the results

To get a first impression about the nature of the phase transition, we produced collapse plots of the susceptibilities at each value of κ according to Eq. (3.47),

$$\chi = N_s^{\gamma/\nu} f\left(t\, N_s^{1/\nu}\right) ,$$
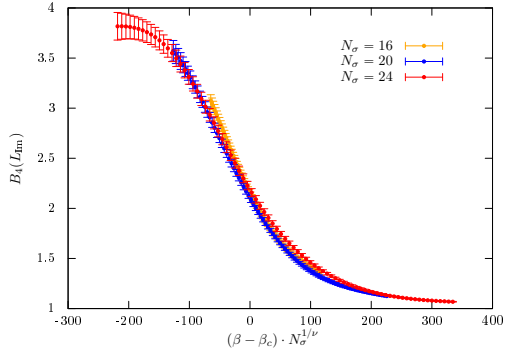
(a) $\kappa = 0.1$, first-order triple coefficients.
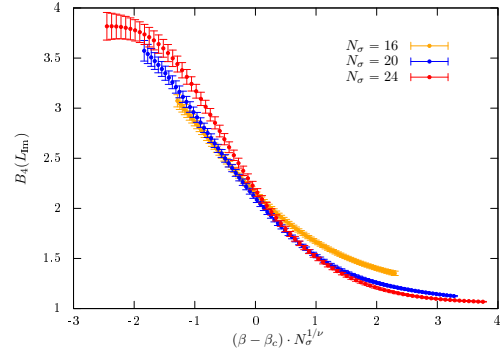
(b) $\kappa = 0.1$, second-order coefficients.
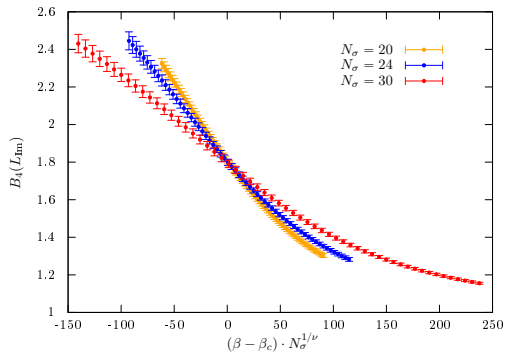
(c) $\kappa = 0.13$, first-order triple coefficients.
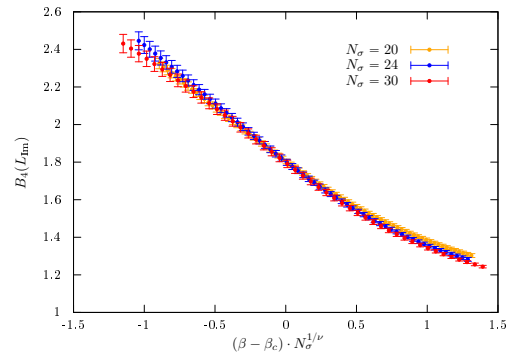
(d) $\kappa = 0.13$, second-order coefficients.
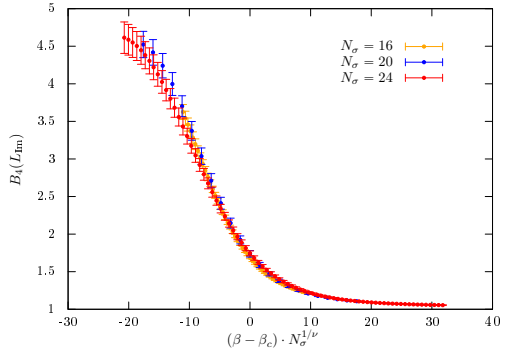
(e) $\kappa = 0.165$, first-order triple coefficients.
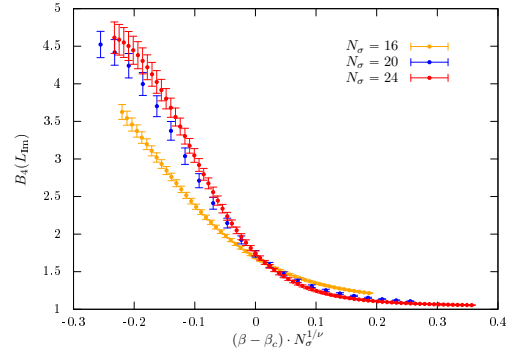
(f) $\kappa = 0.165$, second-order coefficients.

Figure 4.4: Example of collapse plots of the kurtosis of the imaginary part of the Polyakov loop.

κ	N_s	β_c	ν	$B_4(\beta_c, \infty)$	a_1	$\chi^2_{\text{d.o.f.}}$	Q(%)	$\Omega_{\min}$	$\Xi_{\min}$
0.1000	16 20 24	5.86980(29)	0.43(3)	2.141(26)	−0.09(4)	1.034	41.51	86.70	6.67
0.1100	20 24 30 36	5.85670(10)	0.478(25)	1.766(11)	−0.14(5)	0.999	46.26	83.06	20.00
0.1200	16 20 24 30	5.82870(10)	0.56(3)	1.872(8)	−0.31(10)	1.005	45.61	87.18	86.00
0.1300	20 24 30	5.78670(20)	0.67(5)	1.818(18)	−0.72(28)	0.980	45.82	84.12	82.50
0.1300	16 24 32	5.95872(26)	0.470(10)	2.048(8)	−0.050(10)	0.984	49.50	80.02	72.67
0.1550	16 20 24 30	5.52840(10)	0.59(5)	1.804(14)	−0.8(3)	1.048	40.03	81.44	40.00
0.1575	18 24 30	5.48330(10)	0.648(29)	1.990(20)	−1.4(3)	0.995	47.08	88.49	92.50
0.1600	18 24 30	5.43670(10)	0.60(4)	1.781(20)	−1.5(5)	1.017	43.04	87.14	52.00
0.1625	12 18 24	5.38620(9)	0.471(15)	1.906(5)	−0.72(13)	1.004	45.52	81.61	100.00
0.1650	16 20 24	5.33477(3)	0.350(20)	1.680(7)	−0.15(7)	1.007	45.40	91.40	65.00

Table 4.2: *Overview of the selected fits to extract the final value of ν (the grey background line refers to $N_t = 8$). The fits have been performed according to Eq. (3.49b), considering the linear term only. The N_s column contains the spatial lattice extents that have been included in the fits. $\Omega_{\min}$ and $\Xi_{\min}$ are respectively the minimum overlap percentage and the minimum symmetry percentage of Eq. (4.3) and Eq. (4.5).*

where the absolute value $|L|$ of the Polyakov loop was used as observable. Because of the different numerical values of the ratios γ/ν for a first and a second order phase transition – reported in Table 3.2 at page 104 – the collapse plots usually help to exclude one scenario. However, especially for low N_s, the collapse plots of the susceptibilities are often inconclusive and we complement them with collapse plots of the kurtosis of the imaginary part of the Polyakov loop according to Eq. (3.48). In Figure 4.4, we show examples at $\kappa = 0.1, \kappa = 0.13$ and $\kappa = 0.165$ with first-order exponents in the left column and second-order exponents in the right column. In each case, the quality of the collapse clearly prefers one set of critical exponents. This indicates that $\kappa = 0.1$ and $\kappa = 0.165$ are in the first-order region, while $\kappa = 0.13$ is in the second-order region. Note how the kurtosis takes values larger than 3 for the first-order κ, while it does not for the intermediate ones. We will come back to this particular feature in §4.1.3, where a simple model to explain it will be constructed.

The collapse plot technique is useful as an orientation, but it is only self-consistent and we also wish to actually calculate the critical exponents. Thus we fit the kurtosis data following the procedure explained in §4.1.1. Figure 4.5(a) shows the values of ν extracted from the fits, plotted as function of κ. As expected, ν changes from first-order triple to second-order values and back again. This behaviour approaches a step function in the thermodynamic limit but remains smoothed out when the lattice volume is finite. In particular, this means that ν can in principle take any value between the universal ones in the crossing region, while far away from the tricritical masses, it is compatible with $1/3$ (first-order triple) for small and large κ, and with $0.6301(4)$ (second order) for intermediate κ. From the fit, the value of the kurtosis at the critical coupling in the infinite volume limit, $B_4(\beta_c, \infty)$, can be extracted as well. In agreement with previous studies both with staggered fermions [64] and with Wilson fermions [102], this value is slightly higher than the universal one, due to finite volume corrections. It is worth commenting a bit more on this point, because it could be misleading. Correctly, the Reader could argue that the finite size scaling analysis performed doing the fit of the kurtosis should take into account any finite size effect and give the universal value of $B_4(\beta_c, \infty)$. Said differently, if $B_4(\beta_c, \infty)$ is the universal value in the infinite volume limit, how can it suffer from finite size corrections? In principle, it should not. When we claimed that the kurtosis is a function of $x \equiv (\beta - \beta_c) N_s^{1/\nu}$ *only*, we assumed to be close enough to the thermodynamic limit. In general, B_4 depends on a series of variables which are irrelevant as $N_s \to \infty$. In other words, if the spatial lattice volume is not large enough, it could be advantageous to take into account further corrections in the fit form. We encourage the Reader to refer to [108], to get more information about how to do so. In any case, the critical exponent ν suffers much less from this problem and is well suited to understand the nature of the phase transition. Using it, we estimate the two tricritical
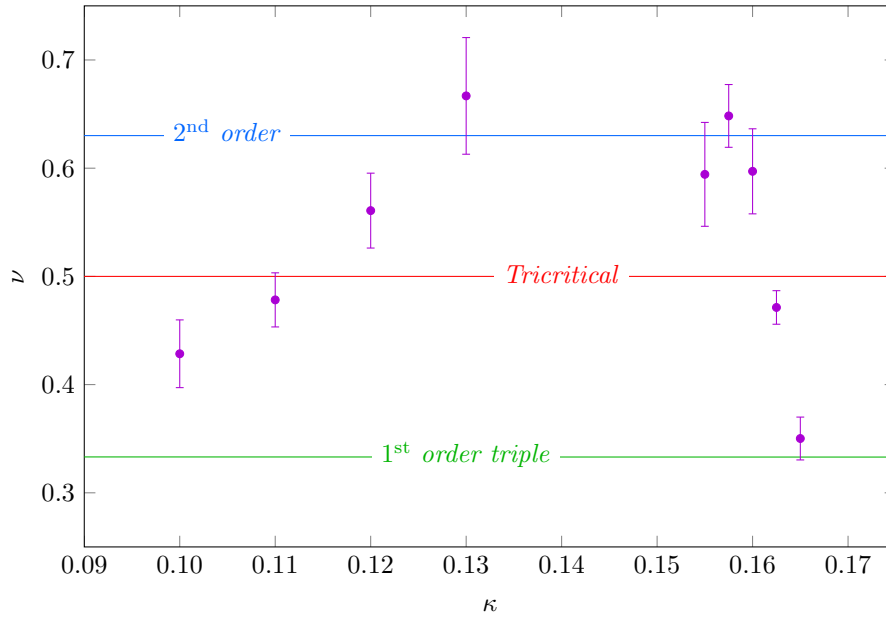
(a) *Critical exponent as function of κ.*
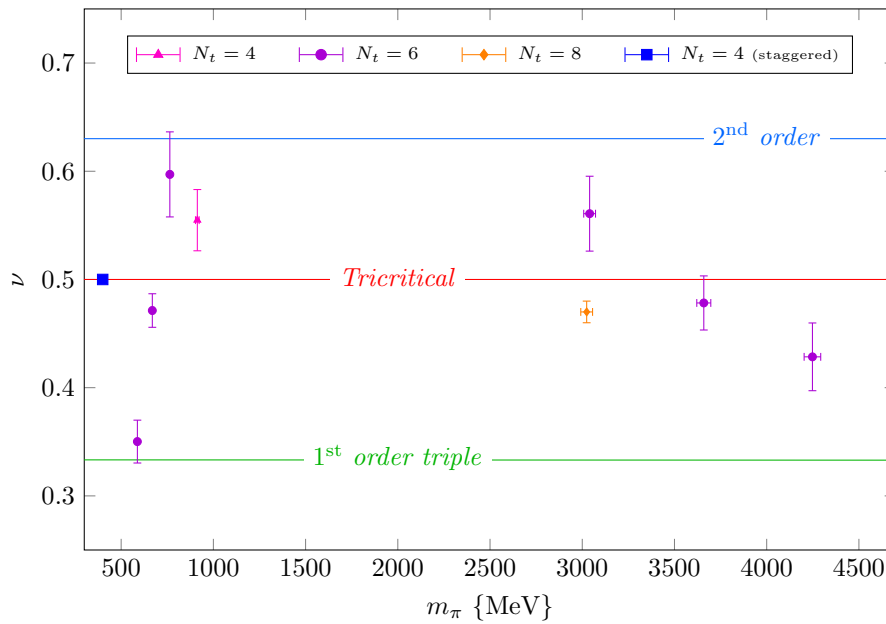
(b) *Results in terms of m_π.*

Figure 4.5: *Critical exponent ν as function of κ and of the pion mass m_π. The horizontal coloured lines indicate the critical values of ν for some universality classes. In (b), the values of ν at κ_{light}^{tric} from [66, 102] have been included as well.*

κ	β	# confs	w_0/a	$a\,m_\pi$	$a\{\mathrm{fm}\}$	$m_\pi\;\{\mathrm{MeV}\}$	N_t	$T\;\{\mathrm{MeV}\}$
0.0910	5.6655	1600	0.9161(6)	3.0107(2)	0.192(2)	3101(32)		258(3)
0.1000	5.6539	1600	0.9017(12)	2.7285(2)	0.195(2)	2766(29)	4	253(3)
0.1100	5.6341	1600	0.8789(10)	2.4250(3)	0.200(2)	2396(25)		247(3)
0.1575	5.3550	400	0.7104(3)	1.1426(17)	0.247(3)	913(9)		200(2)
0.1000	5.8698	1600	1.4650(20)	2.5793(6)	0.120(1)	4248(44)		275(3)
0.1100	5.8567	1600	1.4594(18)	2.2302(2)	0.120(1)	3659(38)		273(3)
0.1200	5.8287	1200	1.4333(20)	1.8862(4)	0.122(1)	3040(31)	6	269(3)
0.1600	5.4367	200	1.1248(14)	0.6045(15)	0.156(2)	764(8)		211(2)
0.1625	5.3862	200	1.0700(17)	0.5559(23)	0.164(2)	669(8)		201(2)
0.1650	5.3347	200	1.0082(13)	0.5184(27)	0.174(2)	588(7)		189(2)
0.1300	5.9590	1600	1.9357(44)	1.3896(2)	0.091(1)	3024(32)	8	272(3)

Table 4.3: *Results of the scale setting. $T = 0$ simulations have been performed on 32×16^3 lattices. The number of independent configurations used is reported in the third column. w_0/a has been determined and converted to physical scales using the publicly available code described in [107]. For the pion mass determination, eight point sources per configuration have been used. The table also contains the lattice spacing, the pion mass and the temperature of the corresponding finite temperature ensemble in physical units.*

values of κ as

$$\kappa_{\mathrm{heavy}}^{\mathrm{tric}} = 0.110(10) \quad \text{and} \quad \kappa_{\mathrm{light}}^{\mathrm{tric}} = 0.1625(25)\,. \tag{4.6}$$

As expected, comparing to the results from $N_t = 4$ [102], both tricritical (bare) masses move to smaller values on the finer lattice. To convert these findings into universal and physical units, we set the scale at or close to the respective β_{c} for the relevant κ. The results for the lattice spacing a, the critical temperature T_{c} and m_π are summarised in Table 4.3. Since the scale setting method using w_0 is much more precise than using the ρ mass as in [102], we evaluated again the $T = 0$ simulations from the latter study and include them here for completeness. In addition, we performed $T = 0$ simulations for the $N_t = 4$ $\kappa_{\mathrm{heavy}}^{\mathrm{tric}}$ values. The lattices coarsen going to lower masses, since g_0 decreases. All lattices considered are coarse, $0.12\,\mathrm{fm} \lesssim a \lesssim 0.18\,\mathrm{fm}$. However, compared to the $N_t = 4$ simulations, where $a \gtrsim 0.19\,\mathrm{fm}$, a clear decrease in a is achieved, as expected. Note that $m_\pi \cdot L > 6$ for all our parameter sets, so that finite size effects are likely negligible.

The measurement of the pion mass with unimproved Wilson fermions is one of the most straightforward tasks in hadron spectroscopy on the lattice. Due to this fact, we will not describe how it has been done in detail, especially because it is explained on most of the standard textbooks on the topic. For instance, a nice introduction can be found in §6 of [19], where also numeric aspects are discussed. Nevertheless we can sketch the main idea. Once identified the *hadron interpolator* O such that its corresponding Hilbert space operator $\hat{O}$ annihilates the particle state we want to analyse, it possible to write

$$\langle O(n_t)\,\bar{O}(0)\rangle = \sum_k \langle 0|\,\hat{O}\,|k\rangle \langle k|\,\hat{O}^\dagger\,|0\rangle\, e^{-n_t\,a\,E_k} = A\,e^{-n_t\,a\,E_H}\left[1 + \mathcal{O}\!\left(e^{-n_t\,a\,\Delta E}\right)\right]\,.$$

Here A is a constant, E_H is the energy of the lowest state $\langle H|$ with $\langle 0|\,\hat{O}\,|H\rangle \neq 0$, and ΔE is the energy difference to the first excited state. If n_t is big enough, any excited state can be neglected and an exponential fit allows to determine the energy of the hadron we are interested in, which coincides with its mass at zero momentum.

Our estimates of the tricritical points in physical units for the given lattice spacing then read

$$m_\pi^{\mathrm{tricr.\ heavy}} = 3659_{-619}^{+589}\,\mathrm{MeV}\,,$$

$$m_\pi^{\text{tricr. light}} = 669^{+95}_{-81} \, \text{MeV} \ .$$

Note that the heavy masses in lattice units are much larger than one[4]. Hence the continuum mass estimates still suffer from large cut-off effects. Thus, the quoted number for $m_\pi^{\text{tricr. heavy}}$ still contains a large systematic error and a quantitative evaluation of its shift from coarser lattices is impossible. On the other hand, the shift in the lower tricritical mass is from $m_\pi \approx 910 \, \text{MeV}$ to $m_\pi \approx 670 \, \text{MeV}$, or around 35%. By contrast, the critical temperature T_c does not seem to depend much on N_t and stays roughly constant at around $200 \, \text{MeV}$.

Our shifts in the tricritical pion masses are of similar magnitude as those in the $N_f = 3$ critical pion masses at $\mu = 0$ with Wilson Clover fermions [109]. Comparing our results to [66], one sees that our lighter tricritical mass on $N_t = 6$ is still higher than the staggered estimate from $N_t = 4$, which is roughly $400 \, \text{MeV}$. Altogether this shows that $N_t \leqslant 6$ is still far from the region where linear cut-off effects dominate in the standard Wilson action and suggests that drastically larger N_t are required for both discretisations. This is expected from studies of the equation of state, where different discretisations start to agree at $N_t \gtrsim 12$ only – refer to [110] for a recent overview.

As a first step towards larger N_t, we also performed simulations at $N_t = 8$ and $\kappa = 0.13$, with $N_s \in \{16, 24, 32, 40\}$, corresponding to aspect ratios of $2 - 5$, as already reported in Table 4.1. The computational costs increase dramatically with N_t and the statistics gathered for the $N_s = 40$ simulations is not as high as for the previous simulations. However, ν can be determined in a solid fashion using the data for the other three spatial volumes, giving a value of $\nu = 0.470(10)$. The lattice spacing a is now reduced from around $0.12 \, \text{fm}$ to around $0.09 \, \text{fm}$. In physical units, this new point is located at $m_\pi = 3024(32)$. Given the same caveats discussed for $N_t = 6$, this again suggests a large shift for the heavy tricritical mass. Note that T_c stays again constant when going from $N_t = 6$ to $N_t = 8$. Our findings are summarised in Figure 4.5(b), that compares the tricritical regions for the different N_t. Also included is the $N_t = 4$ value from the staggered study [66]. The figure makes apparent that much larger N_t are required in order to go to the continuum.

§ 4.1.3   The kurtosis bump

By now, it should be clear that the kurtosis of the order parameter at fixed mass in the Roberge-Weiss Columbia plot is expected to change from 3 at low T to 1 at high T. It is also known that $B_4(\beta) = 2 \, \Theta(\beta_c - \beta) + 1$ in the thermodynamic limit, where Θ is the Heaviside step function. Because of this and considering that on finite volumes any discontinuity is smoothed out, the kurtosis could be naively expected to be a monotonic function of β. Nevertheless, it turned out that B_4 takes values higher than 3 at $\beta \lesssim \beta_c$ for small and large values of κ, i.e. in the first-order triple regions. In Figure 4.6(a) the data for $\kappa = 0.165$ are shown. As it can be clearly seen, the data, coming from values around 3, rise significantly to values larger than 3, forming a sort of *bump*, before declining again when β_c is approached and finally take on values close to 1. Note how the bump gets higher and narrower on larger volumes. Moreover, the β-region where B_4 changes from 3 to 1 shrinks as N_s is increased, as expected in a first-order transition. This distorts the finite size analysis compared to the naïve expectations, and in particular leads to significantly higher values of the Binder cumulant at the intersection than expected in the thermodynamic limit [64, 102, 111]. Thus, a profound understanding is desired.

The described behaviour can be explained by modelling the distributions at work in a situation with three phases. Let us consider the distribution of the imaginary part of the Polyakov loop on a finite volume for sufficiently high statistics; it will be a normal distribution for $\beta \ll \beta_c$ and it will be the sum of two normal distributions with mean values $\pm|L_{\text{Im}}|$ for $\beta \gg \beta_c$. This is clearly visible in Figure 4.7(a), where histograms of L_{Im} are depicted. Between these two regimes, as β is increased, the L_{Im} distribution can be thought of as the sum of three Gaussian distributions, whose weights

---

[4]A pion mass in lattice units larger than one means to have $a \, m_\pi > 1$, which implies $m_\pi > a^{-1}$. But a^{-1} coincides with the cutoff of our theory, due to the regularisation onto the lattice. Therefore, this is a clear signal that the pion mass measurement should not be regarded as a meaningful result.
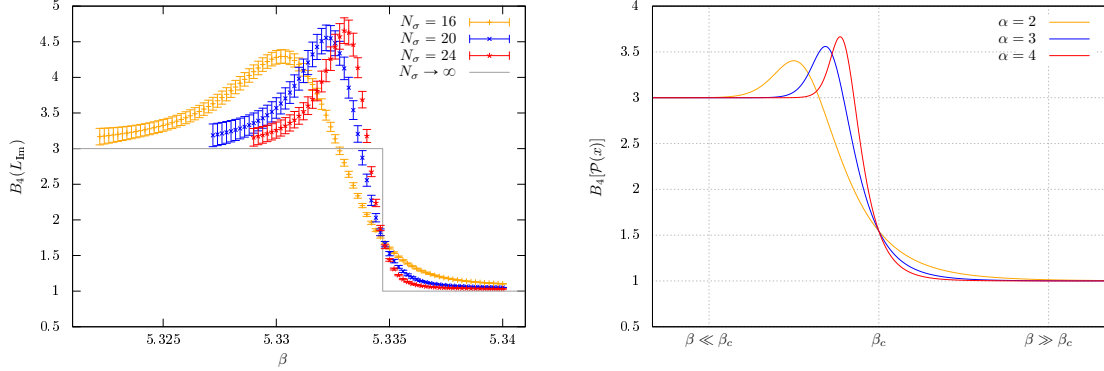
(a) *Kurtosis reweighted data for $\kappa = 0.165$.*

(b) *Kurtosis as function of β in our model.*

Figure 4.6: *Comparison between the measured kurtosis of the imaginary part of the Polyakov loop and its analytic form in our model. Three different lattice spatial extents and three different values of the parameter α have been used. The grey line in the left plot is the expected behaviour of $B_4(\beta)$ in the thermodynamic limit.*

depend on the temperature. We thus consider a probability distribution

$$\mathcal{P}(x) \equiv w_o\, \mathcal{N}(-d, \sigma) + w_i\, \mathcal{N}(0, \sigma) + w_o\, \mathcal{N}(d, \sigma) \, , \tag{4.7}$$

where

$$\mathcal{N}(\mu, \sigma) \equiv \frac{1}{\sigma\sqrt{2\pi}}\, e^{-\frac{(x-\mu)^2}{2\sigma^2}}$$

is a Gaussian distribution with mean μ and variance σ^2, d is a real non negative number, while w_o and w_i are the weights of the outer and inner distributions, respectively. Of course, $2w_o + w_i = 1$. Since our aim is only to *qualitatively* reproduce our data and not to be as general as possible, we assumed the three distributions having the same variance. The symmetry of the outer distributions with respect to zero and the fact that their weight is the same are, instead, implied by the symmetries of the physical system. It is clear that d has to be a function of β as well as w_o and w_i. In particular, for $\beta \ll \beta_\mathrm{c}$ it has to be $w_o \approx 0$ (and $d \approx 0$), while $w_i \approx 0$ and $d \gg \sigma$ (i.e. the outer Gaussian distributions are well separated) for $\beta \gg \beta_c$. Knowing the analytic expression of the distribution, the value of the kurtosis for an even function can be explicitly calculated through

$$B_4\big[\mathcal{P}(x)\big] = \frac{\int_{-\infty}^{+\infty} x^4\, \mathcal{P}(x)\ \mathrm{d}x}{\left[\int_{-\infty}^{+\infty} x^2\, \mathcal{P}(x)\ \mathrm{d}x\right]^2}$$

and we will have

$$B_4\big[\mathcal{P}_{\beta \ll \beta_c}(x)\big] = 3 \, , \tag{4.8a}$$

while

$$B_4\big[\mathcal{P}_{\beta \gg \beta_c}(x)\big] = 3 - \frac{2d^4}{(d^2 + \sigma^2)^2} \approx 1 \, . \tag{4.8b}$$

Before trying to further connect our parameters d, w_o and w_i to β, let us just study how the kurtosis of our distribution changes as they are varied. At the end of the section, we will comment further on how the quantities in our simple model are related to the physical ones.

It is possible to think to the two cases in Eqs. (4.8) as the two limits $d \to 0$ and $d \to \infty$, on condition that the weights of the distributions modify accordingly. One nice way to realise this is
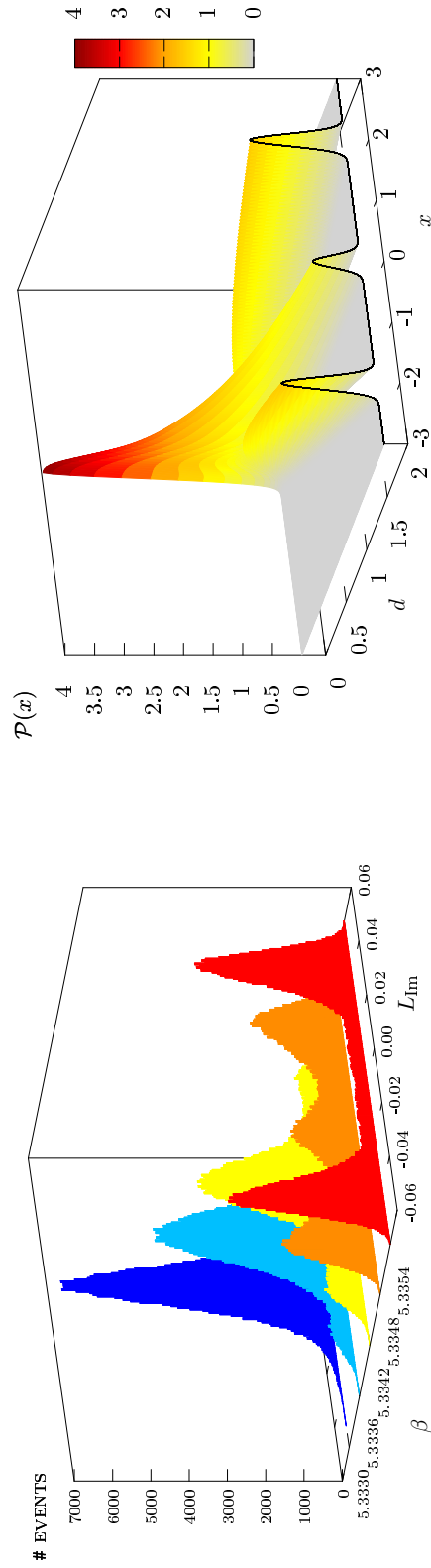
(a) Symmetrised histograms of L_{Im} for $\kappa = 0.165$ and $N_s = 24$ at various values of β around β_c.

(b) Modelled probability distribution of Eq. (4.7), plotted as function of d and x for fixed $\sigma = 0.1$ and $\alpha = 1$.

Figure 4.7: *Comparison between histograms of the imaginary part of the Polyakov loop and the corresponding probability distribution in the model. Note how d is related to β. For low (high) temperatures, only one (two) Gaussian distribution(s) is (are) present. Moreover, in (a) at β = 5.3348 (i.e. slightly after the transition), a clear three-peak structure is visible, as expected for a triple point. All these features are captured in the model.*

to assume that both w_o and w_i are functions of d. In particular, the following conditions have to be fulfilled,

$$\lim_{d \to 0} w_i(d) = 1 \qquad \text{and} \qquad \lim_{d \to 0} w_o(d) = 0 \; ;$$

$$\lim_{d \to \infty} w_i(d) = 0 \qquad \text{and} \qquad \lim_{d \to \infty} w_o(d) = \frac{1}{2} \; .$$

Now, in order to properly choose the weights to reproduce the bump of Figure 4.6(a), we have first to understand which kind of distribution has a kurtosis larger than 3. Leaving the weights of the three normal distributions completely general, it can be shown that

$$B_4\big[\mathcal{P}(x)\big] = 3 + \frac{2\,w_o\,d^4\,(w_i - 4\,w_o)}{(2\,w_o\,d^2 + \sigma^2)^2}$$

Hence, when the weight of the central distribution is more than 4 times larger than the weight of the outer distributions, the kurtosis takes values larger than 3. It is then sufficient to choose the functions $w_o(d)$ and $w_i(d)$ to respect the limits above and in a way such that

$$w_i(d) > 4\,w_o(d) \tag{4.9}$$

for some values of d. A simple choice to respect the required asymptotic behaviour is

$$w_i(d) = \frac{\frac{1}{\alpha d + 1}}{\frac{1}{\alpha d + 1} + 2\left(1 - \frac{1}{\frac{d}{\alpha} + 1}\right)} = \frac{\alpha + d}{\alpha + 3d + 2\alpha d^2} \; , \tag{4.10a}$$

$$w_o(d) = \frac{1 - \frac{1}{\frac{d}{\alpha} + 1}}{\frac{1}{\alpha d + 1} + 2\left(1 - \frac{1}{\frac{d}{\alpha} + 1}\right)} = \frac{d\,(1 + \alpha d)}{\alpha + 3d + 2\alpha d^2} \; , \tag{4.10b}$$

where $\alpha > 0$ is a parameter to calibrate how fast the weights $w_i(d)$ and $w_o(d)$ change from 1 to 0 and from 0 to 1/2, respectively. More precisely, the larger α the quicker the inner/outer Gaussian distribution(s) disappears/appear. In Figure 4.7(b) it is shown how the distribution $\mathcal{P}(x)$ changes increasing the parameter d for $\sigma = 0.1$ and $\alpha = 1$. One clearly sees that for small d there is almost only the inner Gaussian. For higher d, the middle normal distribution gradually disappears. Thus d plays the role of temperature or β, and α that of the volume.

The region where the kurtosis is larger than 3 can be found by inserting Eqs. (4.10) in Eq. (4.9). Then, it follows that

$$B_4 > 3 \quad \Leftrightarrow \quad 0 < d < \frac{-3 + \sqrt{9 + 16\alpha^2}}{8\alpha} \; ; \tag{4.11}$$

actually, using the chosen weights in Eq. (4.7), we get

$$B_4\big[\mathcal{P}(x)\big] = 3 - \frac{2\,d^5\,(1 + \alpha d)\,(4\alpha d^2 + 3d - \alpha)}{[2\,d^3\,(1 + \alpha d) + \sigma^2\,(\alpha + 3d + 2\alpha d^2)]^2} \; ,$$

which confirms what is expected in Eq. (4.11). In Figure 4.8 the kurtosis of the distribution $\mathcal{P}(x)$ is plotted as function of α and d, keeping the standard deviation σ fixed. This picture qualitatively describes our data, as can be seen comparing it to Figure 4.6(a). In particular, the height/width of the bump increases/shrinks as the parameter α is increased.

Lastly, we give some remarks about the connection between d and the temperature. As already observed, it has certainly to be that $d = d(\beta)$. This function should reproduce the fact that the kurtosis stays on the value 3 for $\beta \ll \beta_c$, it should let the bump occur for $\beta \lesssim \beta_c$ and it should make B_4 take the correct value for $\beta = \beta_c$. Since we know that the kurtosis is 3 for $d \to 0$, then the first aspect can be reproduced choosing a function of β that is almost zero for $\beta \ll \beta_c$. The other
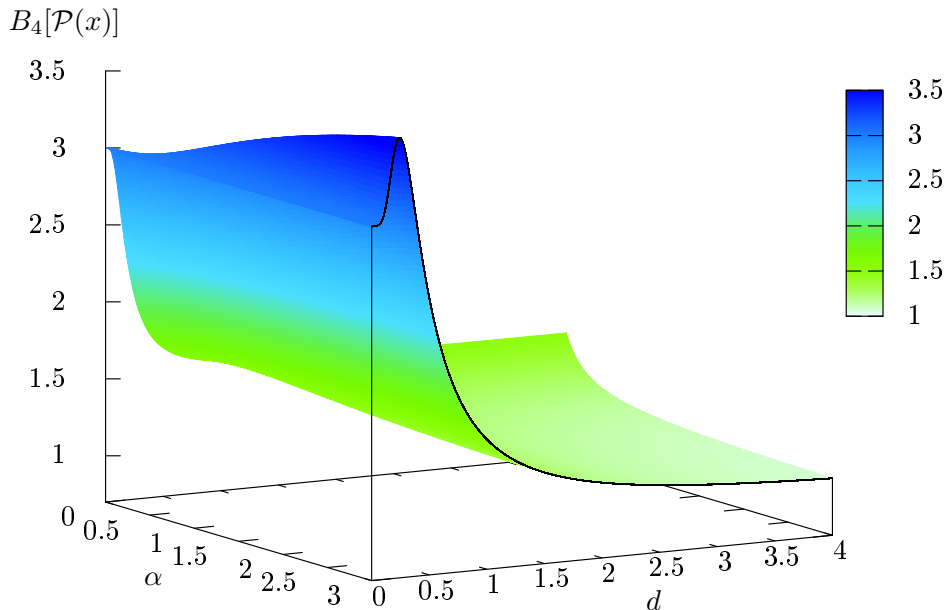
Figure 4.8: *Kurtosis of the distribution in Eq. (4.7) for $\sigma = 0.1$ with the weights of Eqs. (4.10).*

two properties, instead, could be obtained observing that the bump in Figure 4.8 occurs before $d = 1$ and that for $d = 1$ the dependence of $B_4[\mathcal{P}(x)]$ on α drops out,

$$B_4[\mathcal{P}(x)]_{d=1} = 3 - \frac{6}{(2 + 3\sigma^2)^2} \ . \tag{4.12}$$

Then one could choose the function $d(\beta)$ such that $d(\beta_c) = 1$ and choose σ in order to have the desired value of the kurtosis at the critical temperature. For the case of interest, i.e. when the Roberge-Weiss endpoint is a triple point and $B_4 = 1.5$, one should choose in our simple model $\sigma = 0$, which is clearly not allowed on finite volumes. Nevertheless, the standard deviation is known to go to 0 in the thermodynamic limit, when the kurtosis takes the universal value. We will come back to this aspect later. For the moment, if we just decide to reproduce our data, we have to set B_4 to the measured value, that is usually higher than the theoretical one (as observed in [64, 102]). For example, in Figures 4.6 to 4.8 we fixed $\sigma = 0.1$ that would mean $B_4(\beta_c) \simeq 1.544$ only slightly larger than $3/2$. Instead, the value $B_4(\beta_c) = 1.68$ extracted from our data at $\kappa = 0.165$ would lead to $\sigma \simeq 0.21$, still not so large. Another property that the function $d(\beta)$ should reproduce is the fact that for larger N_s the transition happens faster. We already noticed that α reproduces this feature in our model. Hence it makes sense to assume $\alpha \propto N_s$ and to let d depend also on α. As function of β, $d(\alpha, \beta)$ has to change more drastically around β_c for increasing values of α. One possibility which also fulfils the requirements for $\beta \to 0$ and for $\beta = \beta_c$ is

$$d(\alpha, \beta) = \frac{e^{\alpha\beta} - 1}{e^{\alpha\beta_c} - 1} \ .$$

Inserting this choice in the expression of $B_4[\mathcal{P}(x)]$, it is possible to plot the kurtosis as function of β for fixed $\sigma = 0.1$ and for some values of α (that plays the role of N_s). This has been done in Figure 4.6(b). The similarity to Figure 4.6(a) is evident. In particular, in both figures the bump shrinks and its height grows as the volume is increased. Naturally, it is also possible to take the

thermodynamic limit, that means let $\alpha \to \infty$. To do that it is sufficient to notice that

$$\lim_{\alpha \to \infty} \alpha^m \big[d(\alpha, \beta)\big]^n = \lim_{\alpha \to \infty} \alpha^m e^{n\alpha(\beta - \beta_c)} = \begin{cases} 0 \, , \ \beta < \beta_c \\ \infty \, , \ \beta > \beta_c \end{cases}$$

for integers $n > 0$ and $m \geqslant 0$. Using this relation in the expression of the kurtosis we get

$$\lim_{\alpha \to \infty} B_4\big[\mathcal{P}(x)\big] = \begin{cases} 3 & \text{for} \quad \beta < \beta_c \\ 1 & \text{for} \quad \beta > \beta_c \end{cases} , \tag{4.13}$$

which is exactly the expected behaviour in the thermodynamic limit. At $\beta = \beta_c$ we already showed in Eq. (4.12) that the kurtosis does not depend on α and that fixing σ to some finite, small value brings it to $B_4 > 1.5$, i.e. not exactly the universal value. Nevertheless, it is sufficient to assume $\sigma \propto \alpha^{-1}$ to completely reproduce the physical situation. In particular, this means that the standard deviation goes to 0 for $\alpha \to \infty$, which implies

$$\lim_{\alpha \to \infty} B_4\big[\mathcal{P}(x)\big]_{\beta = \beta_c} = 1.5$$

(observe how the limits in Eq. (4.13) are still valid assuming σ proportional to α^{-1}). The kurtosis bump is then nothing but a finite size effect!

To conclude, we want to emphasise that our intention was not to make a predictive model, but just to describe and understand our data. Clearly, we focused on first-order transition only and there is no connection to κ, even if it would probably be not so difficult to reproduce the fact that the phase transition becomes stronger moving further into the first-order region (i.e. for κ much bigger or much smaller than the tricritical values). We did this on purpose since, in order to construct a more accurate model, one should completely resolve the bump in the simulations for different volumes and different values of κ. This would mean to devote a lot of computing power to values of β far in the crossover region, which in the end would not be relevant to extract the critical exponent ν.

§ 4.2   On $N_t = 6$ lattices with staggered fermions

At the end of §4.1.2 we observed that probably much finer lattices than those simulated are needed and that we are too far from the continuum limit, because the lighter tricritical mass found on $N_t = 6$ using Wilson fermions is still higher than the staggered estimate from $N_t = 4$. Nevertheless, from our Wilson study it is not possible to make general statements about different fermions discretisations and, therefore, it is interesting to locate the tricritical points on $N_t = 6$ lattices using, for example, staggered fermions. There are further motivations behind this choice. First of all it would be the natural starting point to continue to investigate the $N_f = 2$ chiral limit transition in the Columbia plot extrapolating from purely imaginary chemical potential simulations as done in [56]. Moreover, it is not clear how much the tricritical points move and, hence, how more costly the $N_t = 6$ simulations are with respect to the $N_t = 4$ ones. In fact, unfortunately, we have to worry about this – and this clearly explains why larger temporal extensions are not chosen straightaway – because at $\mu = 0$, using three flavours of staggered fermions, it was found [50] that the bare chiral Z_2 mass divided by the critical temperature, m_q^c/T_c, moved towards the origin by a factor of 5, passing from $N_t = 4$ to $N_t = 6$. In short, it is important to understand which range of masses are needed to be simulated on a finer lattice and from this information it can be deduced how harder can be to take the continuum limit.

Clearly, there is no conceptual difference regarding how to locate the tricritical points and, therefore, what discussed in §4.1 will be taken for granted. Having a different fermion discretisation, though, implies few technical differences, first of all the choice of the parameters. Since to understand

$m_{u,d}$	β range	Total statistics per spatial lattice size N_s (# of simulated β | $\bar{\tau}_{\mathrm{INT}}$ | $n_{\min}^{\mathrm{events}}$ per chain)			
		12 | 36	18	24	30
0.007	5.420 - 5.460	0.64M (5 | 69 | 174)	1.72M (5 | 174 | 135)	1.10M (5 | 256 | 63)	-
0.008	5.430 - 5.470	0.92M (5 | 66 | 217)	0.86M (5 | 175 | 68)	1.46M (4 | 331 | 57)	-
0.009	5.430 - 5.470	1.26M (5 | 72 | 266)	1.28M (5 | 182 | 91)	1.60M (4 | 325 | 66)	-
0.010	5.430 - 5.480	1.20M (6 | 65 | 297)	0.60M (4 | 143 | 71)	1.84M (5 | 263 | 48)	-
0.011	5.430 - 5.490	0.68M (4 | 57 | 229)	1.24M (5 | 180 | 82)	1.92M (4 | 336 | 72)	-
0.150	5.590 - 5.720	1.08M (5 | 62 | 275)	5.80M (7 | 242 | 203)	5.28M (7 | 362 | 153)	-
0.250	5.600 - 5.760	4.20M (7 | 81 | 555)	2.00M (4 | 190 | 167)	4.60M (6 | 409 | 85)	-
0.350	5.720 - 5.780	6.44M (7 | 130 | 510)	3.40M (5 | 279 | 131)	5.88M (6 | 442 | 130)	-
0.400	5.750 - 5.790	-	9.00M (5 | 305 | 214)	10.60M (6 | 574 | 116)	7.80M (5 | 917 | 95)
0.450	5.760 - 5.810	2.40M (3 | 1261 | 60)	4.72M (5 | 330 | 189)	6.76M (5 | 614 | 167)	11.00M (5 | 1005 | 95)
0.500	5.780 - 5.820	7.40M (4 | 1491 | 93)	9.40M (5 | 325 | 255)	7.00M (5 | 591 | 112)	6.20M (5 | 845 | 119)
0.550	5.760 - 5.840	6.20M (5 | 1355 | 38)	10.80M (6 | 300 | 173)	6.56M (5 | 606 | 77)	7.80M (5 | 917 | 57)
0.600	5.812 - 5.827	9.15M (4 | 1703 | 120)	-	19.80M (6 | 766 | 404)	14.00M (6 | 1207 | 94)
0.650	5.817 - 5.837	5.29M (4 | 1794 | 57)	16.40M (5 | 501 | 673)	20.40M (5 | 780 | 295)	15.40M (5 | 1301 | 192)

Table 4.4: *Overview of the statistics accumulated in all the simulations (red entries are preliminary). Since the resolution in β is not the same at different $m_{u,d}$, the number of simulated β has been reported per each range. The accumulated statistics per β varies because of the criterion adopted to stop to increase the statistics on the 4 chains. Therefore we reported here the total number of trajectories produced per given N_s. For each N_s, the number of simulated β, the average integrated autocorrelation time and the smallest number of independent events per chain of $B_4(L_{Im})$ can be found in the brackets next to the total statistics. Observe that $\bar{\tau}_{\mathrm{int}}$ and n_{min}^{events} are not connected. The former is an average among all the different chains run at one fixed spatial lattice extent, while the latter is the effective length of the shorter chain for that given N_s. The number of independent events is obtained as ratio between the number of produced trajectories and the bin size, which is roughly $2\,\tau_{\mathrm{int}}$.*

the order of the phase transition at a given value of the mass is not immediate (in terms of time and numerical resources), it would be ideal to start from the beginning to simulate at all the needed mass values. This is quite optimistic and, in general, hard to achieve. Nevertheless, previous studies [50, 66] can help in choosing how to perform the scan in m_q and further adjustments can be done during the project. The list of chosen values has been reported in Table 4.4. With staggered fermions the bare mass of the quarks is directly used and the hopping parameter κ is not present[5]. Regarding the values of β used in the temperature scans, we tried to produce data more homogeneously than in the Wilson case, in the sense that, on one hand, we *always* run 4 chains per β and, on the other, we limited the number of simulations per N_s. This is possible because the multiple histogram method can be used to interpolate. In general, it works really well on constraint that no extrapolation is done and the simulated points are not too far away from each other in β. This last requirement can be checked looking at the distributions of the conjugated quantities to the reweighting parameter: If they overlap, the reweighted data can be safely trusted. Therefore, a slightly lower resolution can be used in the scan in temperature and this helps in localising β_c more easily. Some additional reweighted points are then added for the finite size scaling analysis to extract the critical exponent ν. As it can be seen comparing Table 4.4 to Table 4.1, instead, the statistics accumulated per volume has been, on average, much higher than in the Wilson case, despite the fact that less β values have been simulated. This is due to the fact that we adopted two different precisions to decide when to stop our simulations in the light and in the heavy regions. In particular, for large (small) masses we required $B_4(L_{\mathrm{Im}})$ to be the same on all the chains within

---

[5]It is probably worth stressing that a comparison of the bare masses between Wilson and staggered simulations is not as trivial as it could be thought looking at the hopping parameter definition. Remember for example that the bare quark mass is differently renormalised in these two formulations.

(a) $m = 0.01$ ***(b)*** $m = 0.45$
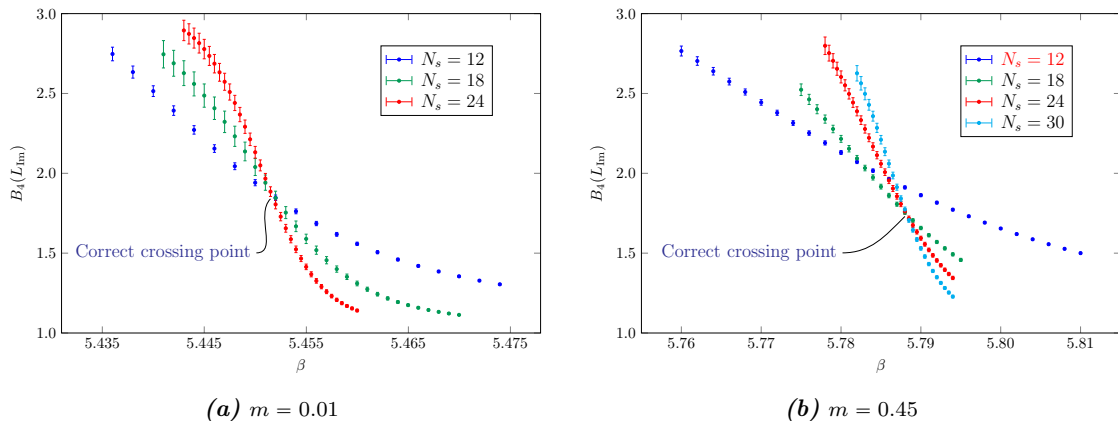
Figure 4.9: *Kurtosis of the imaginary part of the Polyakov loop as function of β at two different values of the quark mass. The plot at $m = 0.45$ is a typical example of what can happen when finite size effects are too large. Clearly, the data at $N_s = 12$ should not be included in the finite size scaling analysis.*

2 (3) standard deviations. We already observed in §4.1.1 that this condition can be met for poor statistics, because of large errors. As rough rule of thumb, we required all the 4 values of the kurtosis at a given temperature to span with their error an interval not wider than 0.5. This led to have often more than twice or three times the number of independent events collected in the study with Wilson fermions.

Another difference between the two investigations regards the spatial lattice extents used. Using staggered fermions, we decided to start using aspect ratios N_s/N_t equal to 2, 3 and 4. Only if needed, we added larger volumes. In particular, it turned out to be the case close to the tricritical masses. The fact that larger spatial volumes are needed to distinguish a weak first-order transition from a second-order one has been already encountered and discussed in the previous $N_t = 4$ study [66]. A necessary condition to consider the simulated volumes large enough is the uniqueness of the crossing point of the kurtosis as function of β on different N_s. In Figures 4.9(a) and 4.9(b), we illustrated a situation in which the smallest aspect ratio can be used and one in which it must be excluded from the finite size scaling analysis, respectively.

Before discussing the final results, let us list few more technical differences between the two studies. With staggered fermions, no method to reduce the integrator instability has been used. For the light masses, the use of the multiple pseudofermions technique explained in §3.1.6 would have been advantageous[6] but it has not been used, because not yet implemented in `CL²QCD`. The acceptance rate in the RHMC has been tuned to be $\omega \simeq 80\%$, slightly higher than in the Wilson study. The chiral condensate has been measured at each trajectory for $m \leqslant 0.011$ for qualitative cross-checks in the analysis. All the simulations have been run on the `L-CSC` supercomputer at GSI in Darmstadt.

Given the additional remarks just discussed, the values of the critical exponent ν were extracted as described in §4.1.1. Nevertheless, preparing the data for the fit, often the reweighting method was used to add new β-points and not only to smooth out the data. It is, then, important to have a criterion according to which new points are added. Clearly, a too high resolution of reweighted points would make the total number of possible fits explode and it would make the filtering procedure more complicated. Hence, we always added few reweighted points between simulated points and we increased this number only if with lower resolution it was not possible to obtain a good fit. Moreover, another important aspect should be considered in choosing the reweighting resolution.

---

[6]The optimal number of pseudofermions defined in [71] as $\frac{1}{2} \ln \kappa$, where κ is the condition number of the Dirac matrix, has been found to be 2 or even 3 at smaller masses (rounded to the previous integer).

$m_{u,d}$	N_s	# points	$\delta\beta \cdot 10^3$	β_c	ν	$B_4(\beta_c, \infty)$	a_1	$\chi^2_{\text{d.o.f.}}$	$Q(\%)$	$\Omega_{\min}$	$\Xi_{\min}$
0.007	18 24	8 9	1 0.5	5.44217(16)	0.45(4)	1.826(19)	−0.15(9)	1.084	36.71	91.06	90.57
0.008	12 18 24	7 6 6	2 1 0.5	5.44513(11)	0.472(26)	1.878(10)	−0.23(7)	0.995	45.70	94.98	85.20
0.009	12 18 24	6 8 9	2 1 0.5	5.44828(10)	0.540(25)	1.871(10)	−0.44(11)	1.001	45.51	80.52	85.60
0.010	12 18 24	6 5 8	3 2 1	5.45154(14)	0.623(26)	1.894(12)	−0.88(16)	1.005	44.65	80.74	72.80
0.011	12 18 24	6 8 11	4 2 1	5.45350(16)	0.650(27)	1.999(18)	−1.07(20)	0.994	46.71	81.53	64.29
0.150	12 18 24	6 16 10	4 1 1	5.64787(23)	0.66(4)	1.854(13)	−0.65(18)	1.007	45.43	83.79	68.40
0.250	12 18 24	8 23 11	4 1 1	5.71176(22)	0.652(26)	1.914(10)	−0.57(10)	0.990	48.67	81.19	87.43
0.350	12 18 24	5 8 10	5 2 1	5.75551(16)	0.596(18)	1.900(7)	−0.39(6)	0.997	46.08	81.96	78.00
0.400	18 24 30	5 7 10	2 1 0.5	5.77364(14)	0.59(4)	1.777(11)	−0.36(12)	0.992	46.57	85.59	72.89
0.450	24 30 36	5 10 8	2 0.5 0.5	5.78731(14)	0.56(5)	1.858(20)	−0.35(18)	1.003	45.34	91.06	52.89
0.500	24 30 36	4 7 7	2 0.5 0.5	5.80037(18)	0.60(6)	1.735(23)	−0.44(23)	0.994	45.61	83.99	58.00
0.550	24 30 36	4 12 8	2 0.5 0.5	5.81091(13)	0.51(4)	1.783(20)	−0.17(10)	0.997	46.22	82.53	90.86
0.600	24 30 36	6 8 6	1 0.5 0.5	5.82012(6)	0.457(24)	1.758(9)	−0.09(4)	0.991	46.26	90.35	70.40
0.650	24 30 36	7 8 8	1 0.5 0.5	5.82785(9)	0.481(28)	1.813(12)	−0.13(5)	0.991	46.80	81.26	94.29

Table 4.5: *Overview of the selected fits to extract the final value of ν (results on grey background are preliminary). The content is the same as in Table 4.2, except for the third and the fourth column where the number of fitted points per N_s and the reweighting resolution in β have been reported, respectively. The colours should help as guideline to distinguish the information among the different volumes. Observe how the smallest volume has systematically a smaller weight in the fit.*

The β-region in which the kurtosis is linear shrinks on larger volumes. Consequently, to choose the same resolution in β on different N_s means to consider in the fit less points coming from a larger volume and, then, finite size effects are somehow emphasised. As it can be seen in Table 4.5, the reweighting resolution in β is higher on larger N_s and therefore the information coming from the smallest volume has systematically less importance. This is even more explicit looking at how many points per N_s have been included in the fit.

Despite all the efforts to make the fit procedure to extract the critical temperature and exponent ν as solid as possible, it still relies on few arbitrary decisions like the number of reweighted points and the filtering parameters. This drawback led us to look for an alternative technique to determine the same quantities and, in general, to understand better which could be an optimal analysis of our data. It is worth discussing it now quite in detail, before presenting and discussing our results.

§ 4.2.1   A quantitative approach to the data collapse

At the end of §3.4.2 we introduced and briefly discussed the technique of the collapse plots and in Figure 4.4 we gave an example using the kurtosis as quantity. We know that the critical exponents take their universal value in the thermodynamic limit and, therefore, whenever the lattice volume is not big enough, it is hard to obtain a good collapse, even using the critical values of the correct phase transition order (listed in Table 3.2 at page 104). Finite size corrections are responsible for that and, in principle, a better collapse plot could be obtained using different (non universal) values of the exponents. Hence, in a naïve approach, the critical exponents could be varied looking for the best collapse plot. But what does exactly *best* mean? For slightly different values of the critical exponents, the collapse plots will look identical and it is in practice impossible to judge by eye which is the better one. It could be argued that this is exactly a possible way to attribute an error to our final critical exponents estimate. Only when the data start clearly not to fall on top of each other, we will have reached the upper or lower bounds for the critical exponents. Ignoring the difficulty of doing this when more than a single critical exponent has to be found, to base a data analysis on by eye judgements is rarely a very scientific method. Simply looking at the collapse plot could be sufficient to distinguish between a first and a second order phase transition, but a more rigorous method is clearly needed to determine intermediate values of the critical exponents estimating an error on them. The key idea is to construct a quantitative measure of the collapse of our data. Of course, at this point, several possibilities are available and some details in the way to proceed may depend on the particular considered quantity and on the specific physics situation. Therefore, from now on, we will focus exclusively on how to define a measure of the quality of the collapse of $B_4(L_{\mathrm{Im}})$ measured in our project. It should not be hard for the Reader to adapt the technique described here to different cases.

Considering how we judge a collapse plot by eye, it should be clear that the measure of the quality has to be connected to the distance of different points at the same value of the universal scaling variable. Therefore, fixed a value $\bar{\beta}_{\mathrm{c}}$ for the critical temperature and a value $\bar{\nu}$ for the critical exponent ν, a possible choice for the collapse quality could be

$$Q(\bar{\beta}_{\mathrm{c}}, \bar{\nu}) \equiv \frac{1}{\Delta x} \int_{x_{\min}}^{x_{\max}} \left[B_4\big(x(\bar{\beta}_c, \bar{\nu}, V_1)\big) - B_4\big(x(\bar{\beta}_c, \bar{\nu}, V_2)\big) \right]^2 \mathrm{d}x \ , \qquad (4.14)$$

where $\Delta x \equiv x_{\max} - x_{\min}$, while V_1 and V_2 are the spatial volumes of the biggest used lattices. Q is nothing but the average distance of the kurtosis measured on two different volumes. Of course, the smaller is Q the better is the collapse. Hence, it is possible to obtain an estimate for β_{c} and ν minimising Q as function of these two variables. Nevertheless, this is not a trivial task and there are some problems to be addressed. Before discussing them in detail, it is worth commenting a bit more on Eq. (4.14). By now, we know that the bigger the spatial volume of the lattice the better and this is the reason why we said that the kurtosis data obtained on the two biggest lattices should be used in the calculation of Q. Usually, though, data on three volumes are produced to be sure that not too huge finite size effects are present – as done in Figure 4.9 – and Eq. (4.14) would not

make use of the data on the smallest volume. To consider more than only two volumes at the same time, different quality definitions can be considered. A direct generalisation of Eq. (4.14) would be

$$Q(\bar{\beta}_{\mathrm{c}}, \bar{\nu}) \equiv \frac{1}{\Delta x} \int_{x_{\min}}^{x_{\max}} \frac{1}{N_V} \sum_{i=1}^{N_V} \sum_{j=1}^{N_V} \Theta(j - i) \Big[B_4\big(x(\bar{\beta}_c, \bar{\nu}, V_i)\big) - B_4\big(x(\bar{\beta}_c, \bar{\nu}, V_j))\big) \Big]^2 \mathrm{d}x \ , \qquad (4.15)$$

namely to consider the average distance between the kurtosis on different volumes (here N_V is the number of simulated volumes and the double sum with $j > i$ means that all possible pairs of volumes are considered). Another possibility, used in 1996 by Barkema and Newman [112], is to estimate the average variance of the data as

$$Q(\bar{\beta}_{\mathrm{c}}, \bar{\nu}) \equiv \frac{1}{\Delta x} \int_{x_{\min}}^{x_{\max}} \left\{ N_V \sum_{i=1}^{N_V} \Big[B_4\big(x(\bar{\beta}_c, \bar{\nu}, V_i)\big) \Big]^2 - \left[\sum_{i=1}^{N_V} B_4\big(x(\bar{\beta}_c, \bar{\nu}, V_i)\big) \right]^2 \right\} \mathrm{d}x \ , \qquad (4.16)$$

where, strictly speaking, a factor N_V^{-2} was neglected in front of the expression, since irrelevant in the critical exponent estimate.

No matter which definition for Q is chosen, it is important to be aware that the integration in the expressions above must be done numerically, since the functional form $B_4(x)$ is unknown. This, in principle, would not be a problem, if only we had the kurtosis at the same x on different volumes. Unfortunately, in lattice simulations, the kurtosis B_4 is measured at fixed values of β and the mapping between β and x depends on the unknown parameters β_{c} and ν,

$$x \equiv (\beta - \beta_{\mathrm{c}}) \cdot N_s^{1/\nu} \ .$$

Therefore, it is not possible to have simulated data which are uniform in x for any β_{c} and ν. However, to some extent, we neither need it. To perform the numeric integration (e.g. with the trapezium or the Simpson's rule), we need to know the integrand function only on a set of points. On the other hand, we know that the measured data can be interpolated in β using the multiple histogram method. Hence, it is possible to reweight in β the kurtosis in a way such that its value at the same x is available for all the volumes. After this step the calculation of Q is trivial. Actually, this implies an interpolation of the data for each pair of $\bar{\beta}_{\mathrm{c}}$ and $\bar{\nu}$ at which Q has to be evaluated and this is too costly in practice, especially if a precise determination of the final value of the critical exponent is desired. A cheaper alternative is to use the reweighting technique to obtain the kurtosis as an approximately continuous function of β, i.e. to add a huge number of points between two simulated temperatures. Doing so, the resulting kurtosis in x will be known with a very high resolution and the numeric integration to obtain Q can be performed with a probably negligible additional error[7]. Due to the particular form of the map $x(\beta)$, sometimes, especially for small values of ν, the number of interpolated points needed to have a sufficiently precise numerical integration can become very large and, therefore, the reweighting very costly. It would be nice to have a different approach.

As it can be seen in Figures 4.4 and 4.9, the kurtosis of the imaginary part of the Polyakov loop is a quite regular function of β, in the sense that no sudden variations are present. This means that a numeric interpolation of the data which does not take into account the physics – as the multiple histogram method does – will probably still find the correct value of the kurtosis. Clearly, this is true under the assumption that the resolution of the data to be interpolated is high enough. For example, the simulated data are usually too distant in temperature to be correctly interpolated without the reweighting technique. But after having applied the multiple histogram method to the data, a second interpolation can be done very cheaply. Actually, in software like Mathematica – which we used to implement the analysis we will describe in the following – it is possible to obtain an interpolated function out of a set of points and perform numeric operations

---

[7]In fact, it will happen to need B_4 at some x not present in the list of reweighted points. In this case, the value at the closest x will be used.

on it. The advantage of having a kurtosis as a "function" does not need further comments and makes the calculation of Q straightforward. Furthermore, it is possible to automatically minimise $Q(\beta_c, \nu)$ as function of two variables.

So far we did not say anything about how to estimate the statistical error on β_c and on ν. Of course, this error has to reflect the error on the reweighted points which, in turn, reflects the precision of our simulations. The error on the reweighting points is often obtained using the bootstrap method as it has been described in §3.4.4. This means that, in the reweighting procedure, N_{boot} sets of reweighted kurtosis are calculated and the bootstrap errors are extracted out of them. Now, instead of using these sets to find the errors on the kurtosis, they can be used to minimise Q, obtaining N_{boot} different estimates of β_c and of ν, which will give the desired final error. Since, typically, the number of bootstrap samples is of the order of some hundreds, it is clear that the minimisation of Q cannot take too much time[8].

Finally, let us discuss how x_{min} and x_{max} should be chosen. Clearly, in order to correctly evaluate the quality of the collapse, no extrapolation outside the simulated interval in β should be done. Thus, the biggest Δx that can be used is the common interval in x around 0 where data from *all* volumes are available. Using a too large interval of integration is, in general, not correct, since it means to assume that the data should collapse outside the critical region. On the other hand, the width of the scaling region is not known a priori and it is hard to judge whether the chosen Δx is too large. A clever solution to this problem, successfully applied in [112], consists in repeating all the analysis for decreasing Δx and, in the end, make an extrapolation of the found parameters for $\Delta x \to 0$. In this way, it is possible to avoid to understand how wide is the scaling region. Even if not said explicitly so far, since $x_c = 0$, it should be $x_{min} < 0$ and $x_{max} > 0$. For the same reasons already discussed in §4.1.1, the choice

$$|x_{min}| = |x_{max}|$$

is encouraged. Said in words, the integration interval should be symmetric around zero, since so is the scaling region.

§ 4.2.2   Discussion of the results

Using the procedures described in §4.1.1 and §4.2.1, it is possible to extract the values of the critical exponent ν in two completely independent ways. The outcome of both analysis has been reported in Tables 4.5 and 4.6 and ν has been plotted in Figure 4.10 as function of the mass $m_{u,d}$. Overall, the two techniques are in agreement and give results often compatible within one standard deviation. However, the quantitative collapse analysis seems to be systematically more precise and this could lead to an easier and better location of the tricritical points.

Unfortunately, at the time of writing, not all simulations could be considered concluded and, therefore, the following discussion shall be regarded as preliminary. Nevertheless, as in the Wilson case, the expected behaviour is already visible; a second-order region for intermediate quark masses separates two first-order triple regions. This allows to make a first conservative estimate of the position of the two tricritical points. Before doing that, it is worth making some further comments on the data in Figure 4.10. In the heavy mass region, from $m_{u,d} = 0.45$ included on, it turned out that the two smallest lattice volumes $N_s = 12$ and $N_s = 18$ cannot be included in the finite size scaling analysis and that the minimum aspect ratio to be used is $N_s/N_t = 4$. At $m_{u,d} = 0.4$ this effect started to appear, since there $N_s = 12$ resulted already too small. If on one hand it is possible to understand that a given volume is not large enough plotting $B_4(L_{Im})$ as function of β as done in Figure 4.9, on the other hand having data on three different N_s meeting at the same temperature does not ensure the absence of any finite size correction and a check of the stability of the extracted critical exponent leaving out the smaller volume is encouraged. For example, in

---

[8]In Mathematica, for example, it is possible to use the `NargMin` function, but a user implemented minimisation based on a scan in β_c and in ν is more efficient, though less precise.

$m_{u,d}$	N_s	$\beta_c^{\text{extr.}}$	$\nu^{\text{extr.}}$	$m_{u,d}$	N_s	$\beta_c^{\text{extr.}}$	$\nu^{\text{extr.}}$
0.007	18 24	5.44220(5)	0.488(20)	0.350	12 18 24	5.75559(11)	0.561(10)
0.008	12 18 24	5.44529(8)	0.514(26)	0.400	18 24 30	5.77373(7)	0.562(15)
0.009	12 18 24	5.44834(10)	0.531(19)	0.450	24 30 36	5.787187(15)	0.560(8)
0.010	12 18 24	5.45168(12)	0.544(23)	0.500	24 30 36	5.80053(4)	0.589(10)
0.011	12 18 24	5.453888(11)	0.59(3)	0.550	24 30 36	5.81096(6)	0.494(16)
0.150	12 18 24	5.64760(15)	0.657(15)	0.600	24 30 36	5.82016(5)	0.467(17)
0.250	12 18 24	5.71218(5)	0.626(19)	0.650	24 30 36	5.82777(5)	0.487(10)

Table 4.6: *Result of the quantitative collapse analysis (results on grey background are preliminary). The critical temperature β_c and the critical exponent ν have been found minimising $Q(\bar{\beta}_c, \bar{\nu})$ as defined in Eq. (4.16) for several decreasing values of Δx. $\beta_c^{extr.}$ and $\nu^{extr.}$ are the outcome of a linear extrapolation for $\Delta x \to 0$. Note that the reweighting resolution in β used to add new points between simulated ones varied between 0.004 and 0.0005 and it has been chosen in order to have around 20 values of the kurtosis to be later interpolated.*

Figure 4.9(b), it seems that $N_s = 18$ is large enough to be used, but it was not used in the end, since ν was significantly different including or excluding such a volume in the finite size scaling analysis. The fact that larger aspect ratios are needed around the heavy tricritical point has been already observed in [66]. Actually, a similar problem is sadly encountered also in the light region, for $m_{u,d} = 0.007$, where the kurtosis of the imaginary part of the Polyakov loop on $N_s = 12$ does not cross that on $N_s = 18$ and $N_s = 24$ at the same β. Since to simulate a larger volume is too costly because of the small quark mass, the finite size scaling analysis has been carried out with only two spatial volumes.

With the present state of the data, our estimate for the tricritical bare quark mass reads

$$m_{\text{light}}^{\text{tric}} = 0.008^{+0.002}_{-0.003} \quad \text{and} \quad m_{\text{heavy}}^{\text{tric}} = 0.55(10) , \tag{4.17}$$

where the lack of points in the chiral region led to the conservative choice of an asymmetric error. In the heavy region, it could be argued from Figure 4.10 that the situation is not so clear since the critical exponent obtained at $m_{u,d} = 0.65$ is really close to the tricritical value. However, looking by eye at the collapse plot of $B_4(L_{\text{Im}})$ for several values of ν, we are confident that this mass lies to the right of the tricritical point.

As done in §4.1.2, it is possible to set the scale for each mass at the critical value β_c of the coupling and to estimate the pion mass using standard spectroscopy techniques[9]. In Table 4.7 the outcome of the scale setting procedure can be found. This allows to obtain the tricritical mass estimates in physical units, even though it is not yet possible to convert their errors, since the scale was set only for the concluded simulations. Without uncertainty, then, we have $m_{\pi\,\text{light}}^{\text{tric}} = 350\,\text{MeV}$ and $m_{\pi\,\text{heavy}}^{\text{tric}} = 2.809\,\text{GeV}$. Observe that, even if the situation is slightly better than in the Wilson study, the pion mass in the heavy region does not fulfil the requirement $am_\pi < 1$ and this suggests that $m_{\text{heavy}}^{\text{tric}}$ still suffers from large cut-off effects. Therefore, any comparison of its position with that found in previous studies is premature. The Reader could wonder how big should be N_t to avoid this problem. Indeed, it is not hard to get a rough idea. In fact, assuming to desire to resolve a pion of 2.5 GeV, the coarsest lattice needed will have $a = 0.4\,\text{GeV}^{-1} = 0.08\,\text{fm}$. Assuming a critical temperature of 270 MeV, it follows $N_t = (a\,T)^{-1} = 9.3$, which suggests that temporal extents $N_t \gtrsim 10$ should be used in the deconfinement region to aim to a continuum extrapolated result in the future. A completely different situation is present in the low mass region, where this

---

[9]Strictly speaking, the measurement of the pion mass on the lattice using staggered fermions is not as straightforward as in the Wilson case. At the end of §A.4, we summarised the main ideas and provided enough references to deepen into the topic.
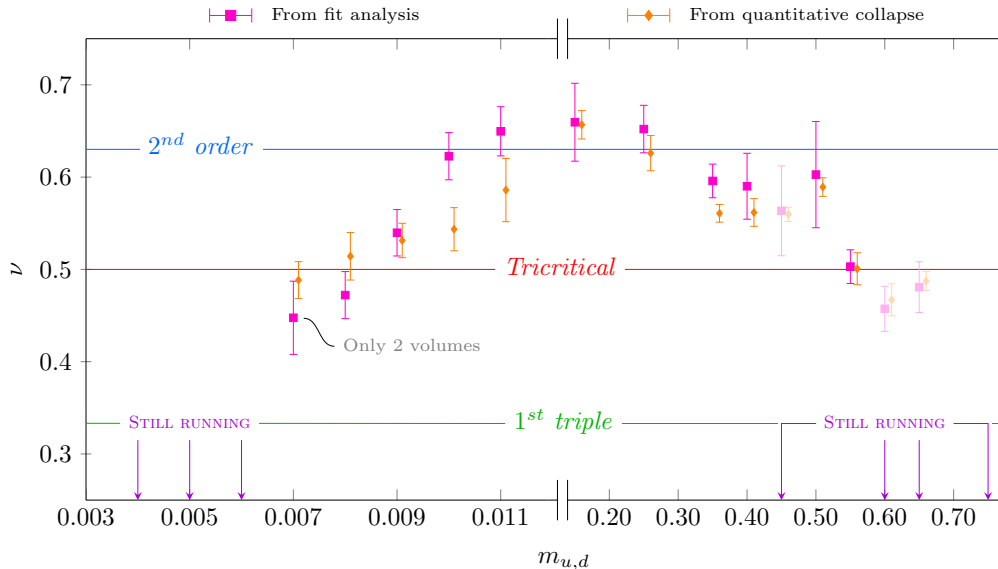
Figure 4.10: *Critical exponent ν as function of the quark mass m. The horizontal coloured lines are the critical values of ν for some universality classes. The mass axis has been broken and two different scales have been used in order to improve readability. Shaded points have to be considered preliminary. Results for mass values for which the collected statistics was too poor have been omitted.*

issue does not occur. In [66], the light tricritical pion mass was found to be $m_\pi \approx 400\,\mathrm{MeV}$ on $N_t = 4$ lattices and this implies a shift of 14% toward smaller masses when setting $N_t = 6$. Even though the lattice spacing $0.12\,\mathrm{fm} \lesssim a \lesssim 0.15\,\mathrm{fm}$ is still quite coarse, it significantly reduced with respect to $N_t = 4$, where it was roughly estimated to be $a \sim 0.3\,\mathrm{fm}$.

Using our results, it is possible to make a first comparison between what happens in the Roberge-Weiss plane with $N_f = 2$ and in the Columbia plot at $\mu = 0$ with $N_f = 3$, always in the chiral region. Clearly, this statement should be taken with a pinch of salt, since we are comparing studies with a different number of degenerate flavours. In [50], the authors present a first comparison between $N_t = 4$ and $N_t = 6$ lattices ($\mu = 0$, $N_f = 3$), finding a large shift of the Z_2 critical mass towards smaller values. In particular, the bare quark mass (expressed in units of the temperature) must be reduced by a factor ~ 5, while the ratio $m_\pi^\mathrm{c}/T_\mathrm{c}$ changes from 1.680(4) on $N_t = 4$ to 0.954(12) on $N_t = 6$. Using the results reported in [66], it seems that in the Roberge-Weiss plane the shift in the chiral region towards smaller masses is milder. With $N_f = 2$ and $\mu_I = \mu_I^\mathrm{RW}$, the bare quark mass, always expressed in units of the temperature, has been reduced by a factor ~ 4, while $m_\pi^\mathrm{tric}/T_\mathrm{c}$ is[10] 2.43 on $N_t = 4$ and 1.59 on $N_t = 6$. Observe that the ratios $m_\pi^\mathrm{tric}/T_\mathrm{c}$ are larger than $m_\pi^\mathrm{c}/T_\mathrm{c}$, reflecting the fact that the tricritical points in the Roberge-Weiss plane are located at heavier masses than the correspondent critical points in the Columbia plot.

Another interesting comparison can be done between the outcome of the same investigation using different fermion discretisations. Leaving the heavy region aside and focusing only on the position of the light tricritical point, it is clear that the staggered result is less affected by cut-off effects than the Wilson one. In fact, from $N_t = 4$ to $N_t = 6$, $m_{\pi,W}^\mathrm{tric}$ moves toward smaller masses by 35% while the shift of $m_{\pi,S}^\mathrm{tric}$ is of only 14% (here, W and S stand for *Wilson* and *staggered*, respectively). This is not not surprising, since we know that staggered fermions are automatically $\mathcal{O}(a^2)$-improved, while Wilson fermions are not. Of course, it is early to judge whether the obtained

---

[10]Here, again, no errors have been reported, because, on one hand, both the lattice spacing and the tricritical light pion mass are quoted without uncertainty in [66] and, on the other, we lack some data in our study.

$m_{u,d}$	β	w_0/a	$a\,m_\pi$	$a\,\{\mathrm{fm}\}$	$m_\pi\,\{\mathrm{MeV}\}$	$T\,\{\mathrm{MeV}\}$
0.0070	5.4422	1.1690(12)	0.2504(27)	0.1501(16)	329(5)	219.1(2.3)
0.0080	5.4451	1.1734(9)	0.2651(18)	0.1496(16)	350(4)	219.9(2.3)
0.0090	5.4483	1.1799(8)	0.2802(18)	0.1487(16)	372(5)	221.1(2.3)
0.0100	5.4515	1.1820(8)	0.2963(18)	0.1485(16)	394(5)	221.5(2.3)
0.0110	5.4535	1.1830(9)	0.3066(16)	0.1483(16)	408(5)	221.7(2.3)
0.1500	5.6479	1.3447(11)	0.9758(3)	0.1305(14)	1475(16)	252.0(2.7)
0.2500	5.7118	1.3821(11)	1.2198(3)	0.1270(13)	1896(20)	259.0(2.7)
0.3500	5.7555	1.4118(15)	1.4136(3)	0.1243(13)	2244(24)	264.6(2.8)
0.4000	5.7736	1.4236(10)	1.4995(3)	0.1233(13)	2400(25)	266.8(2.8)
0.5000	5.8004	1.4422(11)	1.6544(3)	0.1217(13)	2683(28)	270.3(2.8)
0.5500	5.8108	1.4477(13)	1.7259(3)	0.1212(13)	2809(30)	271.3(2.9)

Table 4.7: *Results of the scale setting. $T = 0$ simulations have been performed on 32×16^3 lattices always collecting 800 independent configurations. w_0/a has been determined and converted to physical scales using the publicly available code described in [107]. For the pion mass determination, eight point sources per configuration have been used. The table also contains the lattice spacing, the pion mass and the temperature of the corresponding finite temperature ensemble in physical units.*
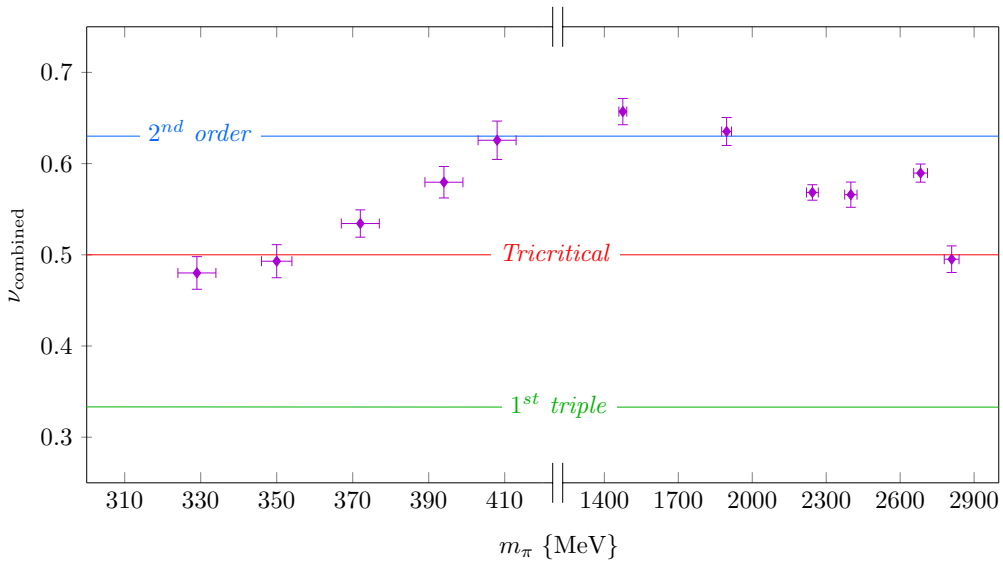
Figure 4.11: *Critical exponent ν as function of the pion mass m_π. This plot is similar to that in Figure 4.10, but the values of the critical exponent are obtained according to Eqs. (4.18) using the values in Tables 4.5 and 4.6 as input. Observe that the pion mass corresponding to a bare mass $m_{u,d} \in \{0.45, 0.60, 0.65\}$ have not been measured, yet.*

values of m_π^{tric} can be included in a future continuum extrapolation and investigations on even finer lattices will clarify this point.

To conclude, we would like to remark that, having obtained the value of the critical exponent with two different and completely independent methods, it is possible to make a final estimate for ν, combining the values reported in Tables 4.5 and 4.6 using the maximum likelihood method. Assuming a normal distribution of the values of ν around its true value, we will have

$$\nu_{\mathrm{B}} = \frac{w_{\mathrm{F}}\,\nu_{\mathrm{F}} + w_{\mathrm{C}}\,\nu_{\mathrm{C}}}{w_{\mathrm{F}} + w_{\mathrm{C}}} \pm \frac{1}{\sqrt{w_{\mathrm{F}} + w_{\mathrm{C}}}} \qquad (4.18\mathrm{a})$$

as combined estimate for it. Here, we have defined

$$w_{\mathrm{F}} = \frac{1}{\sigma_{\mathrm{F}}^2} \qquad \text{and} \qquad w_{\mathrm{C}} = \frac{1}{\sigma_{\mathrm{C}}^2} \qquad (4.18\mathrm{b})$$

and the labels B, F and C indicate our best estimate of ν, its value coming from the fit analysis and from the quantitative collapse procedure, respectively. In Figure 4.11, the values of ν_{B} have been plotted as function of the measured pion masses. Clearly, some points are missing because the pion mass should be measured in a zero temperature simulation at the critical value of the coupling and the final infinite volume estimate of it is not available, yet.

Summary, conclusions and perspectives

> «It is better to recognise that we are in darkness
> than to pretend that we can see the light.»
>
> — **Hedley Bull** —

The study of the QCD phase diagram from the theoretical point of view has been for years one of the most challenging subject of research in modern particle physics, especially because, nowadays, a universal method to investigate its structure for any value of the relevant parameters is not known. Because of the sign problem, LQCD properly works only at zero baryonic density, but indirect insights about the phase structure of strong interacting matter at finite, though small, density can be nevertheless obtained from $\mu_B = 0$ simulations.

The main goal of this thesis has been to enlarge the knowledge of the QCD phase diagram at purely imaginary chemical potential, namely using one of the possible techniques to get information about what happens at $\mu_B > 0$. This has required a fruitful and exciting interplay between theoretical physics and computer science. The starting point has been the regularisation of QCD on the lattice in chapter 1. We only focused on the unimproved Wilson and Kogut-Susskind fermion discretisations, which were used in our study. Since the details of the staggering procedure are quite involved and give rise to very technical calculations, we skipped them in first place, postponing a complete analysis to appendix A. Also an overview of the theoretical caveats underlying to the rooted staggered fermions has been given in appendix B, where a personal point of view on the issue has been presented. After having introduced how gauge invariance is realised on the lattice and what it means to take the continuum limit, we discussed the role of temperature, density and the centre symmetry in LQCD.

Chapter 2 has been devoted to a broad, original and as complete as possible analysis of the state of the art about the QCD phase diagram. The Columbia plot as well as its extension at purely imaginary chemical potential have been introduced. Here, also less probable but still logically possible scenarios have been discussed, showing how the Roberge-Weiss symmetry could help in tackling still unresolved problems.

At this point, we moved slightly away from physics towards computer science, dedicating chapter 3 to the numerical aspects of this thesis. Finite temperature LQCD simulations are extremely costly and having an efficient software is often the only way to approach several issues. Since 2011, the `OpenCL`-based software $\mathtt{CL^2QCD}$ has been developed and optimised to run on `AMD GPUs`. The initial goal was quite specific and, thanks to C. Pinke's and M. Bach's work, only simulations with two flavours of Wilson fermions using a HMC algorithm were possible. The staggered discretisation as well as an RHMC algorithm were not implemented and they were added in the first part of this project, extending substantially the range of possible applications of the software. Not only new features of the code were added, but also its quality was constantly improved. In June 2014, $\mathtt{CL^2QCD}$ was released at the 32nd International Symposium on Lattice Field Theory and two years after it was presented at DESY in Zeuthen.

The need of having an optimal way to handle the hundreds of simulations that usually are

run concurrently on supercomputers led to the development of `BaHaMAS`, which will be probably released next to `CL`^{2}`QCD` in the near future.

In order to facilitate a deep understanding of the techniques used in our project, a generic possible strategy to locate a phase transition in finite temperature LQCD simulations has been also included in chapter 3, combining theoretical explanations to references to newly developed software.

Chapter 4 includes the physical outcome of our work. Even though the final goal of any LQCD study should be to obtain a continuum extrapolated result, the amount of time needed to do so when investigating any feature of the QCD phase diagram exceeds by far the duration of this project. Nowadays, despite they have been studied for more than a decade by now, only few aspects of the 3D Columbia plot are known for vanishing lattice spacing and these results have not yet been cross-checked using, for example, different fermion discretisations. Our aim has been to locate the tricritical points present in the Roberge-Weiss plane of the 3D Columbia plot with two degenerate flavours of both Wilson and staggered fermions, using a finer lattice than that of previous investigations. Repeating the same study with different discretisations allowed a comparison of the different cut-off effects still present as well as a better understanding of the needed computational resources to achieve in future a continuum extrapolation. Our meticulous way of proceeding led also to the development of accurate analysis techniques, which will certainly help forthcoming work.

Even though we already discussed in detail our findings, it is worth repeating here the main conclusions we can draw from our work. On one hand, it is unfortunately clear that, in the deconfinement region, cut-off effects still dominate and that the used lattices are still too coarse for any conclusive physical statement. Here, a rough estimate suggests that lattices with $N_t \geqslant 10$ should be used in order to be able to take in the end the continuum limit. Therefore, a huge numerical effort is necessary and the fact that larger masses are faster to be simulated is completely balanced by the large lattice volumes that are required to perform a finite size scaling analysis. On the other hand, in the chiral region, the situation is after all less dramatic. Even if cut-off effects are never negligible, the obtained results on $N_t = 6$ lattices with staggered fermions can be probably included in a future continuum extrapolation. With Wilson fermions, instead, the sizeable shift of the chiral tricritical point suggests that finer lattices are needed. This somehow confirmed our expectations. Staggered fermions are automatically $\mathcal{O}(a^2)$ improved, while Wilson fermions are not. Thus, it is plausible that, at similar values of the lattice spacing, cut-off effects in the former formulation are less severe that in the latter. Nevertheless, it has to be stressed that staggered simulations make use of the fourth-rooting trick, whose correctness has neither been proven nor disproven. This enhances the importance of a crosscheck of any result using a different discretisation, even though only continuum extrapolated quantities should be compared.

Although the main goal of our study was to locate the tricritical points in the Roberge-Weiss plane and it has been successfully achieved, our work shall rather be regarded as a starting point for future investigations. Nevertheless, it is undoubtedly clear that the existing computational features implemented at the time of writing in `CL`^{2}`QCD` are not sufficient to continue any investigations on finer lattices in a reasonable amount of time. As soon as the temporal extent N_t is increased, also N_s needs to be enlarged with a consequent increment of the simulation duration. Moreover, at larger N_t, smaller bare quark masses must be simulated and this makes the situation even worse.

Among the several numerical expedients it can be taken advantage of, there are some which should be considered in the near future and which it is, then, worth mentioning. The need of larger volumes seems to be more relevant in the deconfinement region. The larger is the lattice to be simulated the larger is the memory required to store the fields. Considering that the size of the on-board `GPU` memory is one of the main limitations of `CL`^{2}`QCD`, it is evident how the use of several devices at the same time shall become necessary at some point. Indeed, the use of a multi-`GPU` code may be already advantageous in $N_t = 8$ studies[11]. The Wilson HMC implementation in

---

[11] A multi-`GPU` implementation could be ideally as efficient as a single device one. However, the calculation done on each `GPU` are not completely independent and, therefore, some information must be communicated between devices, usually provoking a loss of performance.

$\mathtt{CL^2QCD}$ already supports a multi-$\mathtt{GPU}$ usage, but it possible to split the lattice only in the temporal direction. This is the easiest feature to be implemented, but it is not the most suited for finite temperature LQCD studies, where the temporal lattice extent is much smaller than the spatial one. It is ongoing work to make the direction in which the lattice can be split completely arbitrary. The staggered RHMC implementation, instead, can only run on a single device and, hence, its use in the deconfinement region is mainly limited by the type of $\mathtt{GPU}$ used.

In the chiral region, instead, the main difficulty that arises on finer lattices is that smaller bare quark masses need to be simulated. In the (R)HMC algorithm the Dirac matrix is inverted several times per iteration and this inversion is slower for lighter quarks. Nevertheless, how slower this inversion becomes for decreasing masses depends on the algorithm used. For standard solvers – like the CG and the CG - M implemented in $\mathtt{CL^2QCD}$ – the critical slowing down is proportional to the inverse quark mass, but there exist more complex algorithms for which this slowing down is much milder or even almost absent. Clearly, their implementation in $\mathtt{CL^2QCD}$ has to be considered for future applications. Another problem that arises when the quark mass is reduced regards the numerical integration of the equation of motion of the fields in the molecular dynamics part of the (R)HMC algorithm, which becomes more and more instable. This means that, using the same integration step, the smaller is the mass the larger is the numeric error. Since such a large error would make the Metropolis test fail, for smaller quark masses a finer integration step in the molecular dynamics part must be used. Fortunately, there are methods to partially cure this problem, making the integrator instability being triggered at lower masses. Actually, one of these – the so-called Hasenbusch trick – was already used in our Wilson study, since it was already implemented in $\mathtt{CL^2QCD}$. An equivalent one, also known as multiple pseudofermion technique, is going to be implemented soon for staggered fermions, since it should be already advantageous at the values of the masses simulated on $N_t = 6$ lattices.

To conclude, we must admit that to have a complete understanding of the 3D Columbia plot is probably tougher than expected some years ago, but a wise interplay of physics and computer science should make it possible in next decades.

The staggered formulation A

The main ideas were given in §1.4. Here we will focus almost exclusively on technicalities with the aim of proving any result already anticipated. For simplicity, we will divide our discussion in three different parts. Firstly, we will show how to build four fermionic fields out of the sixteen single component ones living at the vertices of each lattice unit hypercube. We will then calculate the two-point function in terms of the physical fields, proving that in the continuum a theory with four Dirac particles is obtained and, to conclude, we will spend some words about the remnant chiral symmetry. This in principle would conclude this appendix. Nevertheless, we will have proven everything only in the free case (all gauge links set to $\mathbb{1}$). §A.4 will be dedicated to some general and qualitative discussion about what happens in the interacting case to the staggering procedure and about how the residual taste degree of freedom should be taken into account in hadron spectroscopy.

§ A.1 The physical fields ψ_α^f

As a warm-up, let us prove that $T(n) = \gamma_1^{n_1} \gamma_2^{n_2} \gamma_3^{n_3} \gamma_4^{n_4}$ fulfils $T^\dagger(n) \gamma_\mu T(n \pm \hat{\mu}) = \eta_\mu(n) \mathbb{1}$, implying

$$\begin{cases} \eta_1(n) = 1 \\ \eta_\mu(n) = (-1)^{\sum_{\nu < \mu} n_\nu} & \text{if } \mu \neq 1 \end{cases} . \tag{A.1}$$

The only two properties of gamma matrices we need are that

$$\{\gamma_\mu, \gamma_\nu\} = 2\delta_{\mu\nu} \qquad \text{and} \qquad \gamma_\mu^\dagger = \gamma_\mu \tag{A.2}$$

in the <u>*euclidean*</u> space. This means that $(\gamma_\mu)^2 = \mathbb{1}$ and we have the following cases

- $\mu = 1$

$$\begin{aligned} T^\dagger(n) \gamma_1 T(n \pm \hat{1}) &= \gamma_4^{n_4} \gamma_3^{n_3} \gamma_2^{n_2} \gamma_1^{n_1} \cdot \gamma_1 \cdot \gamma_1^{n_1 \pm 1} \gamma_2^{n_2} \gamma_3^{n_3} \gamma_4^{n_4} \\ &= \gamma_4^{n_4} \gamma_3^{n_3} \gamma_2^{n_2} \gamma_2^{n_2} \gamma_3^{n_3} \gamma_4^{n_4} = \mathbb{1} , \end{aligned}$$

- $\mu = 2$

$$\begin{aligned} T^\dagger(n) \gamma_2 T(n \pm \hat{2}) &= \gamma_4^{n_4} \gamma_3^{n_3} \gamma_2^{n_2} \gamma_1^{n_1} \cdot \gamma_2 \cdot \gamma_1^{n_1} \gamma_2^{n_2 \pm 1} \gamma_3^{n_3} \gamma_4^{n_4} \\ &= (-1)^{n_1} \gamma_4^{n_4} \gamma_3^{n_3} \gamma_2^{n_2} \gamma_2 \ \gamma_1^{n_1} \gamma_1^{n_1} \gamma_2^{n_2 \pm 1} \gamma_3^{n_3} \gamma_4^{n_4} \\ &= (-1)^{n_1} \gamma_4^{n_4} \gamma_3^{n_3} \gamma_2^{n_2 + 1} \gamma_2^{n_2 \pm 1} \gamma_3^{n_3} \gamma_4^{n_4} = (-1)^{n_1} \mathbb{1} , \end{aligned}$$

- $\mu = 3$

$$T^\dagger(n)\,\gamma_3\,T(n\pm\hat 3) = \gamma_4^{n_4}\,\gamma_3^{n_3}\,\gamma_2^{n_2}\,\gamma_1^{n_1}\cdot\gamma_3\cdot\gamma_1^{n_1}\,\gamma_2^{n_2}\,\gamma_3^{n_3\pm1}\,\gamma_4^{n_4}$$
$$= (-1)^{n_1+n_2}\,\gamma_4^{n_4}\,\gamma_3^{n_3}\,\gamma_3\ \ \gamma_2^{n_2}\,\gamma_1^{n_1}\,\gamma_1^{n_1}\,\gamma_2^{n_2}\,\gamma_3^{n_3\pm1}\,\gamma_4^{n_4}$$
$$= (-1)^{n_1+n_2}\,\gamma_4^{n_4}\,\gamma_3^{n_3+1}\,\gamma_3^{n_3\pm1}\,\gamma_4^{n_4} = (-1)^{n_1+n_2}\,\mathbb{1}\ ,$$

- $\mu = 4$

$$T^\dagger(n)\,\gamma_4\,T(n\pm\hat 4) = \gamma_4^{n_4}\,\gamma_3^{n_3}\,\gamma_2^{n_2}\,\gamma_1^{n_1}\cdot\gamma_4\cdot\gamma_1^{n_1}\,\gamma_2^{n_2}\,\gamma_3^{n_3}\,\gamma_4^{n_4\pm1}$$
$$= (-1)^{n_1+n_2+n_3}\,\gamma_4^{n_4}\,\gamma_4\ \ \gamma_3^{n_3}\,\gamma_2^{n_2}\,\gamma_1^{n_1}\,\gamma_1^{n_1}\,\gamma_2^{n_2}\,\gamma_3^{n_3}\,\gamma_4^{n_4\pm1}$$
$$= (-1)^{n_1+n_2+n_3}\,\gamma_4^{n_4+1}\,\gamma_4^{n_4\pm1} = (-1)^{n_1+n_2+n_3}\,\mathbb{1}\ .$$

Let us now start again from the staggered action that is here recalled,

$$\mathcal{S}_F^{(\text{stagg.})} = \frac{1}{2}\sum_{n,\mu}\eta_\mu(n)\Big[\,\bar\chi(n)\,\chi(n+\hat\mu)\,-\,\bar\chi(n)\,\chi(n-\hat\mu)\,\Big] + \hat M_0\sum_n\bar\chi(n)\,\chi(n)\ . \qquad (\text{A.3})$$

The coordinates of each site on the lattice can be rewritten as $n = 2N + \rho$ that means, in each direction, $n_\mu = 2N_\mu + \rho_\mu$. In this notation, N are the coordinates of the hypercube to which the site n belongs, while ρ is a vector whose components are either 0 or 1, so that we can select any vertex. From now on, it will be understood that vectors denoted by the Greek letter ρ (i.e. $\rho, \bar\rho, \rho'$, ...) have all components restricted to be either 0 or 1 and we will refer to them as *vectors of type ρ*. Eq. (A.3) then becomes

$$\mathcal{S}_F^{(\text{stagg.})} = \frac{1}{2}\sum_{N,\mu,\rho}\eta_\mu(\rho)\,\bar\chi(2N+\rho)\Big[\,\chi(2N+\rho+\hat\mu)\,-\,\chi(2N+\rho-\hat\mu)\,\Big]$$
$$+\ \hat M_0\sum_{N,\rho}\bar\chi(2N+\rho)\,\chi(2N+\rho)\ , \qquad (\text{A.4})$$

where we used the obvious fact that $\eta_\mu(2N+\rho) = \eta_\mu(\rho)$. Though Eq. (A.4) could look unnecessarily complicated, it will be soon clear why such a notation was introduced. Let us observe that a relabelling of the fields $\chi(n)$ is possible,

$$\chi_\rho(N) \equiv \chi(2N+\rho)\ , \qquad (\text{A.5})$$

where, again, $\rho \in \{(0,0,0,0),\ldots,(1,1,1,1)\}$, while N labels now sites of a lattice with lattice spacing $2a$. Thus, considering for example $\chi(2N+\rho+\hat\mu)$ we can infer that

- if $\rho+\hat\mu$ is a vector of type ρ, then the lattice site $2N+\rho+\hat\mu$ still belongs to the hypercube whose origin is at the site $2N$ and

$$\chi(2N+\rho+\hat\mu) \equiv \chi_{\rho+\hat\mu}(N)\ ;$$

- vice versa, if $\rho+\hat\mu$ is not a vector of type ρ, then $\rho-\hat\mu$ is such a vector and

$$\chi(2N+\rho+\hat\mu) \equiv \chi_{\rho-\hat\mu}(N+\hat\mu)\ .$$

Analogue considerations are valid for $\chi(2N+\rho-\hat\mu)$. Therefore

$$\chi(2N+\rho+\hat\mu) = \sum_{\rho'}\Big[\delta_{\rho+\hat\mu,\rho'}\,\chi_{\rho'}(N)\ + \delta_{\rho-\hat\mu,\rho'}\,\chi_{\rho'}(N+\hat\mu)\,\Big]\ , \qquad (\text{A.6a})$$

$$\chi(2N+\rho-\hat\mu) = \sum_{\rho'}\Big[\delta_{\rho-\hat\mu,\rho'}\,\chi_{\rho'}(N)\ + \delta_{\rho+\hat\mu,\rho'}\,\chi_{\rho'}(N-\hat\mu)\,\Big]\ . \qquad (\text{A.6b})$$

If now we insert Eqs. (A.6) in Eq. (A.4), recalling the expressions of the forward and backward derivatives on the lattice,

$$\hat{\partial}_\mu^F \, \chi(N) \;\equiv\; \chi(N + \hat{\mu}) \;-\; \chi(N) \tag{A.7a}$$

$$\hat{\partial}_\mu^B \, \chi(N) \;\equiv\; \chi(N) \;-\; \chi(N - \hat{\mu}) \;, \tag{A.7b}$$

we get

$$\mathcal{S}_F^{(\mathrm{stagg.})} = \frac{1}{2} \sum_{N,\mu,\rho,\rho'} \eta_\mu(\rho)\, \bar{\chi}_\rho(N) \left[\delta_{\rho+\hat{\mu},\rho'}\, \hat{\partial}_\mu^B \, \chi_{\rho'}(N) \;+\; \delta_{\rho-\hat{\mu},\rho'}\, \hat{\partial}_\mu^F \, \chi_{\rho'}(N) \right] + \hat{M}_0 \sum_{N,\rho} \bar{\chi}_\rho(N)\, \chi_\rho(N) \;.$$

It is convenient to use the symmetric derivative and the four dimensional lattice Laplace operator[1]

$$\begin{cases} \hat{\partial}_\mu^S = \dfrac{1}{2}\big(\hat{\partial}_\mu^F + \hat{\partial}_\mu^B\big) \\[2mm] \hat{\Box}_\mu = \hat{\partial}_\mu^F - \hat{\partial}_\mu^B \end{cases} \qquad \longrightarrow \qquad \begin{cases} \hat{\partial}_\mu^F = \hat{\partial}_\mu^S + \dfrac{1}{2}\,\hat{\Box}_\mu \\[2mm] \hat{\partial}_\mu^B = \hat{\partial}_\mu^S - \dfrac{1}{2}\,\hat{\Box}_\mu \end{cases} \quad ;$$

in order to get

$$\mathcal{S}_F^{(\mathrm{stagg.})} = \sum_{N,\mu,\rho,\rho'} \frac{1}{2}\, \eta_\mu(\rho)\, \bar{\chi}_\rho(N) \left[\big(\delta_{\rho+\hat{\mu},\rho'} + \delta_{\rho-\hat{\mu},\rho'}\big) \hat{\partial}_\mu^S + \frac{1}{2}\big(\delta_{\rho-\hat{\mu},\rho'} - \delta_{\rho+\hat{\mu},\rho'}\big) \hat{\Box}_\mu \right] \chi_{\rho'}(N)$$

$$+ \hat{M}_0 \sum_{N,\rho} \bar{\chi}_\rho(N)\, \chi_\rho(N) \;=$$

$$= \frac{1}{2} \sum_{N,\rho,\rho'} \bar{\chi}_\rho(N) \left[\sum_\mu \Big(\Gamma_{\rho\rho'}^\mu\, \hat{\partial}_\mu^S + \frac{1}{2}\, \Gamma_{\rho\rho'}^{5\mu}\, \hat{\Box}_\mu \Big) + 2\,\hat{M}_0\, \delta_{\rho,\rho'} \right] \chi_\rho(N) \;, \tag{A.8}$$

where the Γ-matrices

$$\Gamma_{\rho\rho'}^\mu \equiv \eta_\mu(\rho) \left[\delta_{\rho-\hat{\mu},\rho'} + \delta_{\rho+\hat{\mu},\rho'} \right] \tag{A.9a}$$

$$\Gamma_{\rho\rho'}^{5\mu} \equiv \eta_\mu(\rho) \left[\delta_{\rho-\hat{\mu},\rho'} - \delta_{\rho+\hat{\mu},\rho'} \right] . \tag{A.9b}$$

have been introduced.

Before continuing, we have to dwell on some algebraic properties of the just defined Γ-matrices. As prerequisite, let us prove that

$$\eta_\mu(\rho \pm \hat{\mu}) = \eta_\mu(\rho) \tag{A.10a}$$

$$\eta_\mu(\rho)\eta_\nu(\rho \pm \hat{\mu}) = -\eta_\nu(\rho)\eta_\mu(\rho \pm \hat{\nu}) \quad \text{with} \quad \mu \neq \nu \;, \tag{A.10b}$$

where the two $\pm$ in Eq. (A.10b) are independent:

- $\eta_\mu(\rho \pm \hat{\mu}) = (-1)^{\sum_{\nu<\mu}(\rho\pm\hat{\mu})_\nu} = (-1)^{\sum_{\nu<\mu}\rho_\nu} = \eta_\mu(\rho)$;

- $\eta_\mu(\rho)\eta_\nu(\rho \pm \hat{\mu}) = (-1)^{\sum_{\sigma<\mu}\rho_\sigma} \cdot (-1)^{\sum_{\sigma<\nu}(\rho\pm\hat{\mu})_\sigma} =$

$$= \begin{cases} (-1)^{\sum_{\sigma<\mu}\rho_\sigma} \cdot (-1)^{\sum_{\sigma<\nu}\rho_\sigma} \cdot (-1) = -\eta_\nu(\rho)\,\eta_\mu(\rho \pm \hat{\nu}) & \text{if} \quad \mu < \nu \\[2mm] (-1)^{\sum_{\sigma<\mu}\rho_\sigma} \cdot (-1)^{\sum_{\sigma<\nu}\rho_\sigma} = -\eta_\nu(\rho)\,\eta_\mu(\rho \pm \hat{\nu}) & \text{if} \quad \nu < \mu \end{cases} \;.$$

---

[1]The Laplace operator has been introduced in §1.3 and contains a sum over the μ index. Here we use the symbol $\hat{\Box}_\mu$ to refer to one term of the sum contained in $\hat{\Box}$.

We are thus ready to calculate the anti-commutators of the Γ-matrices and hence to show that they satisfy the same algebra as the matrices $\gamma_\mu \otimes \mathbb{1}_{4\times4}$ and $\gamma_5 \otimes \gamma_\mu^\star \gamma_5$. Namely,

$$\begin{aligned}
&\{\gamma_\mu \otimes \mathbb{1}_{4\times4}, \gamma_\nu \otimes \mathbb{1}_{4\times4}\} = +2\delta_{\mu,\nu}\,\mathbb{1}_{16\times16} && \{\Gamma^\mu, \Gamma^\nu\} = +2\delta_{\mu,\nu}\,\mathbb{1}_{16\times16} \\
&\{\gamma_\mu \otimes \mathbb{1}_{4\times4}, \gamma_5 \otimes \gamma_\nu^\star \gamma_5\} = 0 && \{\Gamma^\mu, \Gamma^{5\nu}\} = 0 \\
&\{\gamma_5 \otimes \gamma_\mu^\star \gamma_5, \gamma_5 \otimes \gamma_\nu^\star \gamma_5\} = -2\delta_{\mu,\nu}\,\mathbb{1}_{16\times16} && \{\Gamma^{5\mu}, \Gamma^{5\nu}\} = -2\delta_{\mu,\nu}\,\mathbb{1}_{16\times16}\quad.
\end{aligned} \tag{A.11}$$

The three properties in the left column are straightforward to be proven. It is sufficient to use the fact that

$$(A \otimes B) \cdot (C \otimes D) = (A \cdot C) \otimes (B \cdot D) \tag{A.12}$$

together with Eq. (A.2). On the other hand, the remaining three anti-commutators are not nearly easy to be proven. As example, let us show how the first can be evaluated.

$$\begin{aligned}
\{\Gamma^\mu, \Gamma^\nu\}_{\rho_1\rho_2} &= \sum_{\bar\rho} \left(\Gamma^\mu_{\rho_1\bar\rho} \Gamma^\nu_{\bar\rho\rho_2} + \Gamma^\nu_{\rho_1\bar\rho} \Gamma^\mu_{\bar\rho\rho_2} \right) = \\
&= \sum_{\bar\rho} \Big[\eta_\mu(\rho_1) \left(\delta_{\rho_1+\hat\mu,\bar\rho} + \delta_{\rho_1-\hat\mu,\bar\rho} \right) \eta_\nu(\bar\rho) \left(\delta_{\bar\rho+\hat\nu,\rho_2} + \delta_{\bar\rho-\hat\nu,\rho_2} \right) + \\
&\qquad + \eta_\nu(\rho_1) \left(\delta_{\rho_1+\hat\nu,\bar\rho} + \delta_{\rho_1-\hat\nu,\bar\rho} \right) \eta_\mu(\bar\rho) \left(\delta_{\bar\rho+\hat\mu,\rho_2} + \delta_{\bar\rho-\hat\mu,\rho_2} \right) \Big] = \\
&= \delta_{\rho_1+\hat\mu,\,\rho_2-\hat\nu} \left[\eta_\mu(\rho_1)\,\eta_\nu(\rho_1+\hat\mu) + \eta_\nu(\rho_1)\,\eta_\mu(\rho_1+\hat\nu) \right] + \\
&\quad + \delta_{\rho_1-\hat\mu,\,\rho_2+\hat\nu} \left[\eta_\mu(\rho_1)\,\eta_\nu(\rho_1-\hat\mu) + \eta_\nu(\rho_1)\,\eta_\mu(\rho_1-\hat\nu) \right] + \\
&\quad + \delta_{\rho_1+\hat\mu,\,\rho_2+\hat\nu} \left[\eta_\mu(\rho_1)\,\eta_\nu(\rho_1+\hat\mu) + \eta_\nu(\rho_1)\,\eta_\mu(\rho_1-\hat\nu) \right] + \\
&\quad + \delta_{\rho_1-\hat\mu,\,\rho_2-\hat\nu} \left[\eta_\mu(\rho_1)\,\eta_\nu(\rho_1-\hat\mu) + \eta_\nu(\rho_1)\,\eta_\mu(\rho_1+\hat\nu) \right].
\end{aligned} \tag{A.13}$$

At this point, if $\mu \neq \nu$ then Eq. (A.10b) make the four square brackets vanish. On the contrary, if $\mu = \nu$ we can use Eq. (A.10a) to simplify the square brackets and obtain

$$\{\Gamma^\mu, \Gamma^\mu\}_{\rho_1\rho_2} = 2 \left(\delta_{\rho_1+\hat\mu,\,\rho_2-\hat\mu} + \delta_{\rho_1-\hat\mu,\,\rho_2+\hat\mu} + \delta_{\rho_1+\hat\mu,\,\rho_2+\hat\mu} + \delta_{\rho_1-\hat\mu,\,\rho_2-\hat\mu} \right). \tag{A.14}$$

We are almost done. Since the difference of two vectors of type ρ cannot have any component equal to 2, the first two deltas in Eq. (A.14) are zero. Furthermore, only one of the two remaining terms can be different from zero. To see this, it is better to go back to the first step of Eq. (A.13). If $\rho_1 + \hat\mu$ is a vector of type ρ, then $\rho_1 - \hat\mu$ cannot be such a vector and then only one of the two terms in the first (and third) round brackets can be different from zero. Finally,

$$\{\Gamma^\mu, \Gamma^\nu\}_{\rho_1\rho_2} = 2\,\delta_{\mu,\nu}\,\delta_{\rho_1,\rho_2}\,.$$

We have then found two even dimensional representations of the same Clifford algebra. The fact that the dimension is even tells us that there must be a unitary transformation connecting them. But there is more! If we consider the matrix $\gamma^\mu \otimes \mathbb{1}_{4\times4}$ and we think the two matrices as acting in Dirac and in taste[2] spaces respectively, then $(\gamma^\mu \otimes \mathbb{1}_{4\times4})\partial_\mu$ is nothing but the matrix version of the kinetic term of the action of a system of four degenerate Dirac particles. Therefore, we conclude that the physical fields ψ_α^f and $\bar\psi_\alpha^f$ are connected to the staggered fields χ_ρ and $\bar\chi_\rho$ by the same transformation that connects $\gamma^\mu \otimes \mathbb{1}_{4\times4}$ and $\gamma^5 \otimes \gamma^\mu \gamma^5$ to Γ^μ and $\Gamma^{5\mu}$. It would be possible to look for this transformation exactly in this way, but we will rather *properly guess* it and check whether

---

[2]For simplicity, the Reader can think about the taste space formally as a flavour space. We will discuss in §A.4 the reason why indeed this identification is not correct.

it works. Actually it is not really a guess. In fact, because of the way the staggered fields have been introduced,

$$
\begin{cases}
\hat{\psi}(n) = T(n)\ \chi(n) \\[4pt]
\hat{\bar{\psi}}(n) = \bar{\chi}(n)\ T^\dagger(n)
\end{cases} ,
$$

and due to the presence of the phases $\eta_\mu(\rho)$ in Eq. (A.9), it makes sense to assume

$$
\begin{cases}
\hat{\psi}_{\alpha\beta}(N) = \mathcal{N}_0 \sum_{\rho'} U_{\alpha\beta,\rho'}\ \chi_{\rho'}(N) \\[8pt]
\hat{\bar{\psi}}_{\alpha\beta}(N) = \mathcal{N}_0 \sum_{\rho'} \bar{\chi}_{\rho'}(N)\, (U^\dagger)_{\rho',\alpha\beta} ,
\end{cases}
\tag{A.15a}
$$

where

$$
U_{\alpha\beta,\rho} = \frac{1}{2}(T_\rho)_{\alpha\beta} \quad \text{with} \quad T_\rho \equiv \gamma_1^{\rho_1}\gamma_2^{\rho_2}\gamma_3^{\rho_3}\gamma_4^{\rho_4} .
\tag{A.15b}
$$

It is worth spending some words about the indices structure of Eqs. (A.15). As we know, there are sixteen different vectors $\rho = (\rho_1, \rho_2, \rho_3, \rho_4)$, while α and β range from 1 to 4. Therefore U is a 16×16 matrix whose rows are identified by a double index[3]. Since we would like to use Eq. (A.15a) in Eq. (A.8), we have to invert such a transformation. It is straightforward once proven that U is a unitary matrix. Since the trace of the product of whatever number of *distinct* γ-matrices vanishes, it is trivial to show that[4]

$$
\mathrm{Tr}(T_\rho^\dagger T_{\rho'}) = 4\delta_{\rho,\rho'} .
$$

Then we have

$$
\mathrm{Tr}(T_\rho^\dagger T_{\rho'}) = \mathrm{Tr}(T_{\rho'}^T T_\rho^\ast) = \mathrm{Tr}(T_\rho^\ast T_{\rho'}^T) = \sum_{\alpha,\beta}(T_\rho^\ast)_{\alpha,\beta}\, (T_{\rho'}^T)_{\beta,\alpha} = \sum_{\alpha,\beta}(T_\rho^\ast)_{\alpha,\beta}\, \left((T_{\rho'}^T)^T\right)_{\alpha,\beta}
$$

$$
= 4\sum_{\alpha,\beta}\frac{1}{2}(T_\rho^\ast)_{\alpha,\beta}\,\frac{1}{2}(T_{\rho'})_{\alpha,\beta} = 4\sum_{\alpha,\beta}(U^\dagger)_{\rho,\alpha\beta}\, U_{\alpha\beta,\rho'} = 4\,(U^\dagger U)_{\rho,\rho'} = 4\delta_{\rho,\rho'} ,
\tag{A.18}
$$

where in the first two steps we used the cyclic property of the trace and that $\mathrm{Tr}(A) = \mathrm{Tr}(A^T)$, while in the last line we took into account that $(U^\dagger)_{\rho,\alpha\beta} = (U^\ast)_{\alpha\beta,\rho} = \frac{1}{2}(T_\rho^\ast)_{\alpha\beta}$. It is then clear that $UU^\dagger = U^\dagger U = \mathbb{1}_{16\times16}$. Inverting Eq. (A.15a) we finally get

$$
\begin{cases}
\chi_\rho(N) = \dfrac{1}{\mathcal{N}_0} \sum_{\alpha,\beta} (U^\dagger)_{\rho,\alpha\beta}\, \hat{\psi}_{\alpha\beta}(N) \\[10pt]
\bar{\chi}_\rho(N) = \dfrac{1}{\mathcal{N}_0} \sum_{\alpha,\beta} \hat{\bar{\psi}}_{\alpha\beta}(N)\, U_{\alpha\beta,\rho}
\end{cases} ,
$$

that, inserted into the staggered action in Eq. (A.8), leads to

$$
\mathcal{S}_F^{(\text{stagg.})} = \frac{1}{2}\sum_{N,\rho,\rho'} \bar{\chi}_\rho(N)\left[\sum_\mu\left(\Gamma_{\rho\rho'}^\mu\, \hat{\partial}_\mu^S + \frac{1}{2}\Gamma_{\rho\rho'}^{5\mu}\, \hat{\Box}_\mu\right) + 2\,\hat{M}_0\,\delta_{\rho,\rho'}\right]\chi_\rho(N)
$$

---

[3] Just to have an idea, given a representation of the euclidean γ-matrices, it is possible to write explicitly the U matrix. It is sufficient to calculate the 4×4 matrix T_ρ (for each ρ) and right the result as *column* in U.

[4] For $\rho \neq \rho'$ the matrix T_ρ can be the product of one, two, three or four γ-matrices, since $\gamma_\mu^2 = \mathbb{1}$. The trace of any product of an odd number of γ-matrices is identically zero. While

$$
\mathrm{Tr}(\gamma_\mu\gamma_\nu) = 4\delta_{\mu,\nu}
\tag{A.16}
$$

$$
\mathrm{Tr}(\gamma_\mu\gamma_\nu\gamma_\rho\gamma_\sigma) = 4(\delta_{\mu,\nu}\delta_{\rho,\sigma} - \delta_{\mu,\rho}\delta_{\nu,\sigma} + \delta_{\mu,\sigma}\delta_{\nu,\rho})
\tag{A.17}
$$

and both vanishes for distinct indices. For $\rho = \rho'$ it is $T_\rho = \mathbb{1}$.

$$= \frac{1}{2} \sum_{\substack{N,\rho,\rho' \\ \alpha,\beta,\alpha',\beta'}} \frac{1}{\mathcal{N}_0} \bar{\hat{\psi}}_{\alpha\beta}(N) \, U_{\alpha\beta,\rho} \, \cdot \, \left[K_{\rho,\rho'} \right] \, \cdot \, \frac{1}{\mathcal{N}_0} (U^\dagger)_{\rho',\alpha'\beta'} \, \hat{\psi}_{\alpha'\beta'}(N) \; =$$

$$= \frac{1}{2\,\mathcal{N}_0^2} \sum_{\substack{N,\alpha,\beta \\ \alpha',\beta'}} \bar{\hat{\psi}}_{\alpha\beta}(N) \left[\sum_\mu \left(\Lambda^\mu_{\alpha\beta,\alpha'\beta'} \, \hat{\partial}^S_\mu + \frac{1}{2} \, \Lambda^{5\mu}_{\alpha\beta,\alpha'\beta'} \, \hat{\Box}_\mu \right) + 2\hat{M}_0 \, \Upsilon_{\alpha\beta,\alpha'\beta'} \right] \hat{\psi}_{\alpha'\beta'}(N) \; ,$$

where we defined

$$\Upsilon_{\alpha\beta,\alpha'\beta'} \equiv \sum_{\rho,\rho'} U_{\alpha\beta,\rho} \, \delta_{\rho,\rho'} \, (U^\dagger)_{\rho',\alpha'\beta'} \; , \tag{A.19a}$$

$$\Lambda^\mu_{\alpha\beta,\alpha'\beta'} \equiv \sum_{\rho,\rho'} U_{\alpha\beta,\rho} \, \Gamma^\mu_{\rho,\rho'} \, (U^\dagger)_{\rho',\alpha'\beta'} \; , \tag{A.19b}$$

$$\Lambda^{5\mu}_{\alpha\beta,\alpha'\beta'} \equiv \sum_{\rho,\rho'} U_{\alpha\beta,\rho} \, \Gamma^{5\mu}_{\rho,\rho'} \, (U^\dagger)_{\rho',\alpha'\beta'} \; . \tag{A.19c}$$

It is now again time for an algebraic pause. We need a better expression for the above matrices, in order to give a physical interpretation of the fields ψ. This time we will not make the whole calculation in detail, since it is nothing more than products and sums of matrices. We will rather report the results together with their meaning. Obviously, we expect to obtain the matrices involved in the anti commutators of the left column of Eq. (A.11), otherwise our guess in Eq. (A.15a) is wrong. Let us start from Eq. (A.19a):

$$\Upsilon_{\alpha\beta,\alpha'\beta'} = \sum_{\rho,\rho'} U_{\alpha\beta,\rho} \, \delta_{\rho,\rho'} \, (U^\dagger)_{\rho',\alpha'\beta'} = \sum_\rho U_{\alpha\beta,\rho} \, (U^\dagger)_{\rho,\alpha'\beta'} = \mathbb{1}_{16 \times 16} \; ,$$

where we used the result obtained in Eq. (A.18). If we think how double indices behave in the direct products[5], it is quite simple to conclude that

$$\Upsilon_{\alpha\beta,\alpha'\beta'} = \delta_{\alpha,\alpha'} \delta_{\beta,\beta'} \; .$$

Going on considering Eqs. (A.19b) and (A.19c), the easiest way to get the correct result is, probably, to proceed by brute force and to evaluate the matrix product $U \cdot \Gamma^{\mu/5\mu} \cdot U^\dagger$ after having written the matrices U, Γ^μ and $\Gamma^{5\mu}$ explicitly. It is much quicker to do that in your favourite programming language than to prove it analytically[6]. Just to give an example of what this calculation produces and in order to somehow justify the following general result, let us see the case for $\mu = 2$ (every element is a 4×4 matrix):

$$\Lambda^2_{\alpha\beta,\alpha'\beta'} = \begin{pmatrix} \mathbb{0} & \mathbb{0} & \mathbb{0} & -\mathbb{1} \\ \mathbb{0} & \mathbb{0} & \mathbb{1} & \mathbb{0} \\ \mathbb{0} & \mathbb{1} & \mathbb{0} & \mathbb{0} \\ -\mathbb{1} & \mathbb{0} & \mathbb{0} & \mathbb{0} \end{pmatrix} \; ,$$

---

[5] For example:

$$\mathbf{A} \otimes \mathbf{B} = \begin{bmatrix} a_{11}\mathbf{B} & \cdots & a_{1n}\mathbf{B} \\ \vdots & \ddots & \vdots \\ a_{m1}\mathbf{B} & \cdots & a_{mn}\mathbf{B} \end{bmatrix} \; ,$$

namely, using indices, $(\mathbf{A} \otimes \mathbf{B})_{\alpha\gamma,\beta\delta} = A_{\alpha,\beta} \, B_{\gamma,\delta}$.

[6] Recall that Eqs. (A.19) are independent of the representation of γ-matrices, then the Reader can use his/her favourite. For example, we can choose:

$$\gamma_i = \begin{pmatrix} 0 & -\imath\,\sigma_i \\ \imath\,\sigma_i & 0 \end{pmatrix} \qquad \gamma_4 = \begin{pmatrix} \mathbb{1} & 0 \\ 0 & -\mathbb{1} \end{pmatrix} \qquad \gamma_5 \equiv \gamma_1\gamma_2\gamma_3\gamma_4 = \begin{pmatrix} 0 & -\mathbb{1} \\ -\mathbb{1} & 0 \end{pmatrix} \; , \tag{A.20}$$

where σ_i are the three Pauli matrices.

$$\Lambda^{52}_{\alpha\beta,\alpha'\beta'} = -\begin{pmatrix} \mathbb{0} & \mathbb{0} & \gamma_2^{\star}\gamma_5 & \mathbb{0} \\ \mathbb{0} & \mathbb{0} & \mathbb{0} & \gamma_2^{\star}\gamma_5 \\ \gamma_2^{\star}\gamma_5 & \mathbb{0} & \mathbb{0} & \mathbb{0} \\ \mathbb{0} & \gamma_2^{\star}\gamma_5 & \mathbb{0} & \mathbb{0} \end{pmatrix} \; .$$

Without reporting the other cases, it is possible to read the following impressive result from the two expressions above:

$$\Lambda^{\mu}_{\alpha\beta,\alpha'\beta'} = (\gamma_\mu)_{\alpha\alpha'} \, \delta_{\beta,\beta'}$$
$$\Lambda^{5\mu}_{\alpha\beta,\alpha'\beta'} = (\gamma_5)_{\alpha\alpha'} \, (\gamma_\mu^{\star}\gamma_5)_{\beta\beta'} \; ,$$

that plugged in the staggered action lead to

$$\mathcal{S}_F^{(\text{stagg.})} = \frac{1}{2\mathcal{N}_0^2} \sum_{\substack{N,\alpha,\beta \\ \alpha',\beta'}} \bar{\hat{\psi}}_{\alpha\beta}(N) \; \cdot K_{\alpha\beta,\alpha'\beta'} \cdot \hat{\psi}_{\alpha'\beta'}(N) \; , \tag{A.22a}$$

where

$$K_{\alpha\beta,\alpha'\beta'} = \sum_\mu \left[(\gamma_\mu)_{\alpha\alpha'} \, \delta_{\beta,\beta'} \, \hat{\partial}_\mu^S + \frac{1}{2}(\gamma_5)_{\alpha\alpha'} \, (\gamma_\mu^{\star}\gamma_5)_{\beta\beta'} \hat{\square}_\mu \right] + 2 \, \hat{M}_0 \, \delta_{\alpha,\alpha'} \, \delta_{\beta,\beta'} \tag{A.22b}$$

To conclude, we still need the normalisation factor $\mathcal{N}_0$. We will deduce it showing that Eq. (A.22a) has the correct naïve continuum limit. Let us start recalling that the term containing the operator $\hat{\square}_\mu$ vanishes in the limit $a \to 0$. If we ignore this term and we compare Eq. (A.22a) with the action of four degenerate fermions on the lattice,

$$\mathcal{S}_F^{(\text{stagg.})} = \sum_f \sum_N \bar{\hat{\psi}}^f(N) \, (\gamma_\mu\hat{\partial}_\mu + \hat{M}_0) \, \hat{\psi}^f(N) \; ,$$

we can assert that α *and β should be identified with the Dirac and taste quark-degrees of freedom respectively.* This fact is further corroborated if we reintroduce the physical units and let the lattice spacing $b \equiv 2a$ go to zero. Setting

$$\psi_{\alpha\beta} = b^{-3/2} \, \hat{\psi}_{\alpha\beta} \quad , \quad \partial_\mu^S = b^{-1} \, \hat{\partial}_\mu^S \quad , \quad \square_\mu = b^{-2} \hat{\square}_\mu \quad , \quad M = 2b^{-1} \, \hat{M}_0 \quad ,$$

we have

$$2\mathcal{N}_0^2 \cdot \mathcal{S}_F^{(\text{stagg.})} = \sum_{N,\mu} b^4 \, \bar{\psi}(Nb) \left[(\gamma_\mu \otimes \mathbb{1}) \, \partial_\mu^S + \frac{1}{2} b \, (\gamma_5 \otimes \gamma_\mu^{\star}\gamma_5) \square_\mu \right] \psi(Nb) +$$
$$+ \sum_N b^4 \, \bar{\psi}(Nb) \left[M_0(\mathbb{1} \otimes \mathbb{1}) \right] \psi(Nb) \; . \tag{A.23}$$

Eventually, taking the continuum limit with $\mathcal{N}_0 = 1/\sqrt{2}$, we obtain

$$\lim_{b \to 0} \mathcal{S}_F^{(\text{stagg.})} = \sum_{f,f',\alpha,\alpha'} \int \mathrm{d}^4x \; \bar{\psi}_\alpha^f(x) \left[(\gamma_\mu)_{\alpha\alpha'} \, \delta_{f,f'} \, \partial_\mu^S + M_0 \, \delta_{\alpha,\alpha'} \, \delta_{f,f'} \right] \psi_{\alpha'}^{f'}(x)$$

where we changed the field $\psi_{\alpha\beta}$ to ψ_α^f, using f as taste index.

§ A.2   The two-point function in the staggered formulation

It is now time to convince ourselves that in the staggered formulation there are no terms in the propagator without an analogue in the continuum[7]. It would be really a shame if, after all

---

[7]Even though there are somehow other unphysical consequences due to the remnant taste degree of freedom, the naïve continuum limit of the propagator formally exists.

the previous work, we had to throw away our theory because of lattice artefacts. Let us see that this is not the case. First of all, it is important to remark that there is no conceptual difference in proving the absence of lattice artefacts with the χ and $\bar{\chi}$ fields rather than with the ψ and $\bar{\psi}$ fields: The latter are linear combinations of the former. However, for completeness, we will calculate the two-point function with both fields. Actually, we will not deduce the correlation function between ψ fields from that of χ fields, because it is easier to directly calculate it via

$$\langle \eta_i \bar{\eta}_j \rangle = \frac{\int \mathcal{D}\bar{\eta} \, \mathcal{D}\eta \, \eta_i \bar{\eta}_j \, e^{-\sum_{i,j-1}^{N} \bar{\eta}_i A_{ij} \eta_j}}{\int \mathcal{D}\bar{\eta} \, \mathcal{D}\eta \, e^{-\sum_{i,j-1}^{N} \bar{\eta}_i A_{ij} \eta_j}} = A_{ij}^{-1} \tag{A.24}$$

where η and $\bar{\eta}$ are here general Grassmann variables. Let us begin working with the staggered fields χ. The analogue of Eq. (A.24) is

$$\langle \, \chi_\rho(N) \; \bar{\chi}_\rho(N') \, \rangle = \frac{\int \mathcal{D}\bar{\chi} \, \mathcal{D}\chi \, \chi_\rho(N) \, \bar{\chi}_{\rho'}(N') \, e^{-\mathcal{S}_F^{(\text{stagg.})}}}{\int \mathcal{D}\bar{\chi} \, \mathcal{D}\chi \, e^{-\mathcal{S}_F^{(\text{stagg.})}}} = K_{\rho,\rho'}^{-1}(N, N') \, ,$$

where

$$K_{\rho,\rho'}(N, N') = \frac{1}{2} \sum_\mu \eta_\mu(\rho) \Big[\delta_{\rho+\hat{\mu},\rho'} \, \hat{\partial}_\mu^B + \delta_{\rho-\hat{\mu},\rho'} \, \hat{\partial}_\mu^F \Big] + \hat{M}_0 \delta_{\rho,\rho'} \, \delta_{N,N'} =$$

$$= \frac{1}{2} \sum_\mu \eta_\mu(\rho) \Big[\delta_{\rho+\hat{\mu},\rho'} \, (\delta_{N,N'} - \delta_{N',N-\hat{\mu}}) +$$

$$+ \, \delta_{\rho-\hat{\mu},\rho'} \, (\delta_{N',N+\hat{\mu}} - \delta_{N,N'}) \Big] + \hat{M}_0 \delta_{\rho,\rho'} \, \delta_{N,N'} \, .$$

It is convenient to switch to momentum space and use the Fourier transform of K. Starting from its definition, we have

$$\tilde{K}_{\rho,\rho'}(\hat{p}) = \sum_{N-N'} K_{\rho,\rho'}(N, N') \, e^{-\imath \hat{p} \cdot (N-N')} =$$

$$= \frac{1}{2} \sum_\mu \eta_\mu(\rho) \Big[\delta_{\rho+\hat{\mu},\rho'} \, (1 - e^{-\imath \hat{p}_\mu}) + \delta_{\rho-\hat{\mu},\rho'} \, (e^{\imath \hat{p}_\mu} - 1) \Big] + \hat{M}_0 \, \delta_{\rho,\rho'} =$$

$$= \imath \sum_\mu \eta_\mu(\rho) \sin\left(\frac{\hat{p}_\mu}{2}\right) \Big[\delta_{\rho+\hat{\mu},\rho'} \, e^{-\imath \frac{\hat{p}_\mu}{2}} + \delta_{\rho-\hat{\mu},\rho'} \, e^{+\imath \frac{\hat{p}_\mu}{2}} \Big] + \hat{M}_0 \, \delta_{\rho,\rho'} =$$

$$= \sum_\mu \imath \, \Gamma_{\rho\rho'}^\mu(\hat{p}) \, \sin\left(\frac{\hat{p}_\mu}{2}\right) + \hat{M}_0 \, \delta_{\rho,\rho'} \, ,$$

where we introduced

$$\Gamma_{\rho\rho'}^\mu(\hat{p}) \equiv \Gamma_{\rho\rho'}^\mu \, e^{\imath \hat{p} \cdot \frac{\rho-\rho'}{2}} \, .$$

But, since from $\{\Gamma^\mu, \Gamma^\nu\} = 2\delta_{\mu,\nu} \, \mathbb{1}_{16 \times 16}$ it follows that $\{\Gamma^\mu(\hat{p}), \Gamma^\nu(\hat{p})\} = 2\delta_{\mu,\nu} \, \mathbb{1}_{16 \times 16}$, we can assert that

$$\tilde{K}_{\rho\rho'}^{-1}(\hat{p}) = \frac{-\imath \sum_\mu \Gamma_{\rho\rho'}^\mu(\hat{p}) \sin\left(\frac{\hat{p}_\mu}{2}\right) + \hat{M}_0 \, \delta_{\rho,\rho'}}{\sum_\mu \sin^2\left(\frac{\hat{p}_\mu}{2}\right) + \hat{M}_0^2} \, .$$

The correctness of the result above can be checked backwards:

$$\left[\imath \sum_\mu \Gamma^\mu(\hat{p}) \sin\left(\frac{\hat{p}_\mu}{2}\right) + \hat{M}_0 \right] \cdot \left[-\imath \sum_\nu \Gamma^\nu(\hat{p}) \sin\left(\frac{\hat{p}_\nu}{2}\right) + \hat{M}_0 \right] =$$

$$= \sum_{\mu,\nu} \Gamma^\mu(\hat{p}) \Gamma^\nu(\hat{p}) \sin\left(\frac{\hat{p}_\mu}{2}\right) \sin\left(\frac{\hat{p}_\nu}{2}\right) + \hat{M}_0{}^2 =$$

$$= \sum_{\mu,\nu} \left(\frac{1}{2}\{\Gamma^\mu(\hat{p}), \Gamma^\nu(\hat{p})\} + \frac{1}{2}\cancel{[\Gamma^\mu(\hat{p}), \Gamma^\nu(\hat{p})]} \right) \sin\left(\frac{\hat{p}_\mu}{2}\right) \sin\left(\frac{\hat{p}_\nu}{2}\right) + \hat{M}_0{}^2 = \sum_\mu \sin^2\left(\frac{\hat{p}_\mu}{2}\right) + \hat{M}_0{}^2 \ .$$

We finally obtain

$$\langle\, \chi_\rho(N) \ \bar{\chi}_{\rho'}(N') \,\rangle = \int_{-\pi}^\pi \frac{\mathrm{d}^4\hat{p}}{(2\pi)^4} \ \frac{-\imath \sum_\mu \Gamma^\mu_{\rho\rho'}(\hat{p}) \sin\left(\frac{\hat{p}_\mu}{2}\right) + \hat{M}_0\, \delta_{\rho,\rho'}}{\sum_\mu \sin^2\left(\frac{\hat{p}_\mu}{2}\right) + \hat{M}_0{}^2} \ \cdot e^{\,\imath\, \hat{p}\cdot(N-N')} \qquad . \qquad \text{(A.25)}$$

Leaving any further calculation to the Reader, it is clear from Eq. (A.25) the absence of any contributions from the boundaries of the Brillouin zone (notice the crucial factor $1/2$ in the argument of the sine).

We are now interested in proving that the actual contribution to the physical propagator of $\hat{p} = (0,0,0,0)$ is the correct one. Rather than evaluating

$$\langle\, \hat{\psi}^f_\alpha(N) \ \bar{\hat{\psi}}^{f'}_{\alpha'}(N') \,\rangle = \frac{1}{2} \sum_{\rho,\rho'} U_{\alpha f,\rho} \langle\, \chi_\rho(N) \ \bar{\chi}_{\rho'}(N') \,\rangle\, (U^\dagger)_{\rho',\alpha' f'} \ ,$$

we will invert the operator appearing in the staggered action written in term of the physical fields. Once again, let us switch to momentum space via

$$\psi(Nb) \ = \int_{-\frac{\pi}{b}}^{\frac{\pi}{b}} \frac{\mathrm{d}^4 p}{(2\pi)^4} \ \tilde{\psi}(p)\, e^{\,\imath\, p\cdot Nb} \qquad \text{and} \qquad \bar{\psi}(Nb) \ = \int_{-\frac{\pi}{b}}^{\frac{\pi}{b}} \frac{\mathrm{d}^4 p}{(2\pi)^4} \ \tilde{\bar{\psi}}(p)\, e^{-\imath\, p\cdot Nb} \ .$$

Plugging these two expressions in Eq. (A.23) (with $\mathcal{N}_0$ fixed to the correct value $1/\sqrt{2}$), we get

$$\mathcal{S}_F^{(\text{stagg.})} = \sum_{N,\mu} b^4 \int_{-\frac{\pi}{b}}^{\frac{\pi}{b}} \frac{\mathrm{d}^4 p\, \mathrm{d}^4 p'}{(2\pi)^8} \ \tilde{\bar{\psi}}(p)\, e^{-\imath\, p\cdot Nb} \left[(\gamma_\mu \otimes \mathbb{1})\, \partial_\mu^S + \frac{1}{2}\, b\, (\gamma_5 \otimes \gamma_\mu^\star \gamma_5) \Box_\mu \right] \tilde{\psi}(p')\, e^{\,\imath\, p'\cdot Nb} +$$

$$+ \sum_N b^4 \int_{-\frac{\pi}{b}}^{\frac{\pi}{b}} \frac{\mathrm{d}^4 p\, \mathrm{d}^4 p'}{(2\pi)^8} \ \tilde{\bar{\psi}}(p)\, e^{-\imath\, p\cdot Nb} \left[M_0\, (\mathbb{1} \otimes \mathbb{1}) \right] \tilde{\psi}(p')\, e^{\,\imath\, p'\cdot Nb} \ .$$

It is now easy to make the operators ∂_μ^S and $\Box_\mu$ act on $e^{\,\imath\, p'\cdot Nb}$ (on the lattice). Then, we can perform the sum over N using

$$\sum_N b^4 e^{\,\imath\,(p-p')\cdot Nb} = (2\pi)^4\, \delta_P^{(4)}(p-p')$$

and the integration over p' using the $\delta_P^{(4)}(p-p')$. The final result reads

$$\mathcal{S}_F^{(\text{stagg.})} = \int_{-\frac{\pi}{b}}^{\frac{\pi}{b}} \frac{\mathrm{d}^4 p}{(2\pi)^4} \ \tilde{\bar{\psi}}(p) \ \cdot \mathcal{J}(p) \cdot \tilde{\psi}(p) \ .$$

where

$$\mathcal{J}(p) \equiv \imath \sum_\mu \left[(\gamma_\mu \otimes \mathbb{1})\frac{1}{b}\sin(p_\mu b) + \frac{\imath}{b}\big(1 - \cos(p_\mu b)\big)(\gamma_5 \otimes \gamma_\mu^\star \gamma_5) \right] + M_0\,(\mathbb{1} \otimes \mathbb{1})$$

The physical propagator will be obtained by inverting the operator $\mathcal{J}(p)$. The key is to calculate the square of the sum in the expression above:

$$\sum_\mu \left[(\gamma_\mu \otimes \mathbb{1})\frac{1}{b}\sin(p_\mu b) + \frac{\imath}{b}\big(1 - \cos(p_\mu b)\big)(\gamma_5 \otimes \gamma_\mu^\star \gamma_5) \right] \cdot \sum_\nu \left[(\gamma_\nu \otimes \mathbb{1})\frac{1}{b}\sin(p_\nu b) + \frac{\imath}{b}\big(1 - \cos(p_\nu b)\big)(\gamma_5 \otimes \gamma_\nu^\star \gamma_5) \right] =$$

$$
= \sum_{\mu,\nu} \Bigg[(\gamma_\mu \otimes \mathbb{1})(\gamma_\nu \otimes \mathbb{1}) \frac{1}{b^2} \sin(p_\mu b)\sin(p_\nu b) - (\gamma_5 \otimes \gamma_\mu^\star \gamma_5)(\gamma_5 \otimes \gamma_\nu^\star \gamma_5) \frac{1}{b^2} \big(1 - \cos(p_\mu b)\big)\big(1 - \cos(p_\nu b)\big) +
$$

$$
+ (\gamma_\mu \otimes \mathbb{1})(\gamma_5 \otimes \gamma_\nu^\star \gamma_5) \frac{\imath}{b^2} \sin(p_\mu b)\big(1 - \cos(p_\nu b)\big) + (\gamma_5 \otimes \gamma_\mu^\star \gamma_5)(\gamma_\nu \otimes \mathbb{1}) \frac{\imath}{b^2} \sin(p_\nu b)\big(1 - \cos(p_\mu b)\big) \Bigg] =
$$

$$
= \sum_{\mu,\nu} \Bigg[(\gamma_\mu \gamma_\nu \otimes \mathbb{1}) \frac{1}{b^2} \sin(p_\mu b)\sin(p_\nu b) + (\mathbb{1} \otimes \gamma_\mu^\star \gamma_\nu^\star) \frac{1}{b^2} \big(1 - \cos(p_\mu b)\big)\big(1 - \cos(p_\nu b)\big) +
$$

$$
+ \Big[(\gamma_\mu \otimes \mathbb{1})(\gamma_5 \otimes \gamma_\nu^\star \gamma_5) + (\gamma_5 \otimes \gamma_\nu^\star \gamma_5)(\gamma_\mu \otimes \mathbb{1}) \Big] \frac{\imath}{b^2} \sin(p_\mu b)\big(1 - \cos(p_\nu b)\big) \Bigg] =
$$

$$
= \sum_{\mu,\nu} \Bigg[\Big(\{\gamma_\mu, \gamma_\nu\} \otimes \mathbb{1}\Big) \frac{1}{2b^2} \sin(p_\mu b)\sin(p_\nu b) + \Big(\mathbb{1} \otimes \{\gamma_\mu^\star, \gamma_\nu^\star\}\Big) \frac{1}{2b^2} \big(1 - \cos(p_\mu b)\big)\big(1 - \cos(p_\nu b)\big) +
$$

$$
+ \Big[\cancel{(\gamma_\mu \gamma_5 \otimes \gamma_\mu^\star \gamma_5)} + \cancel{(\gamma_5 \gamma_\mu \otimes \gamma_\nu^\star \gamma_5)} \Big] \frac{\imath}{b^2} \sin(p_\mu b)\big(1 - \cos(p_\nu b)\big) \Bigg] =
$$

$$
= \sum_{\mu} \Bigg[\frac{1}{b^2} \Big(\sin^2(p_\mu b) + \big(1 - \cos(p_\mu b)\big)^2\Big)(\mathbb{1} \otimes \mathbb{1}) \Bigg] = \sum_{\mu} \frac{4}{b^2} \sin^2\Big(\frac{p_\mu b}{2}\Big) \, .
$$

Thus, since $A^2 + B^2 = (A - \imath B)(A + \imath B)$ because $[A, B] = 0$, we conclude that

$$
\mathcal{J}^{-1}(p) = \frac{\sum_\mu \Big[-\imath(\gamma_\mu \otimes \mathbb{1})\frac{1}{b} \sin(p_\mu b) + \frac{2}{b}(\gamma_5 \otimes \gamma_\mu^\star \gamma_5)\sin^2\Big(\frac{p_\mu b}{2}\Big) \Big] + M_0 \cdot (\mathbb{1} \otimes \mathbb{1})}{\sum_\mu \frac{4}{b^2}\sin^2\Big(\frac{p_\mu b}{2}\Big) + M_0^2} \, ,
$$

where there are no contributions from the edges of the Brillouin zone thanks to the $1/2$ factor in the denominator and which implies

$$
\lim_{b \to 0} \mathcal{J}^{-1}(p) = \frac{-\imath \sum_\mu (\gamma_\mu \otimes \mathbb{1}) \cdot p_\mu + M_0 \cdot (\mathbb{1} \otimes \mathbb{1})}{p^2 + M_0^2} \, ,
$$

namely the propagator of a continuum system composed of four degenerate fermionic particles:

$$
\langle \hat{\psi}_\alpha^f(N) \hat{\bar{\psi}}_\beta^{f'}(N') \rangle = \int_{-\infty}^{+\infty} \frac{\mathrm{d}^4 p}{(2\pi)^4} \mathcal{J}_{\alpha\beta}^{-1}(p)\, \delta_{f,f'} \cdot e^{\imath\, p \cdot (N - N')b} \, ,
$$

with

$$
\mathcal{J}_{\alpha\beta}^{-1}(p) = \frac{-\imath\, (\slashed{p})_{\alpha\beta} + M_0\, \delta_{\alpha,\beta}}{p^2 + M_0^2} \, .
$$

§ A.3   The remnant $U(1) \times U(1)$ symmetry

Exactly as it happens for the Wilson fermions, the symmetry $U(4) \times U(4)$ (existing in the continuum for $M_0 = 0$) is *explicitly* broken by the term proportional to $\Box_\mu$ in Eq. (A.23). Nevertheless, even though in the Wilson formulation the axial symmetry (that involving γ_5 in the Dirac space) is completely lost, with staggered fermions a non trivial part of it survives. Its generator is $\gamma_5 \otimes \gamma_5$. Under the action of this subgroup, the physical fields transform as follows

$$
\psi(Nb) \;\rightarrow\; \psi'(Nb) \;=\; e^{\imath\,\theta(\gamma_5 \otimes \gamma_5)}\, \psi(Nb) \tag{A.26a}
$$

$$
\bar{\psi}(Nb) \;\rightarrow\; \bar{\psi}'(Nb) \;=\; \bar{\psi}(Nb)\, e^{\imath\,\theta(\gamma_5 \otimes \gamma_5)} \, , \tag{A.26b}
$$

where θ is a real parameter, not depending on N. We want now to prove that

$$
\mathcal{S}_F^{(\mathrm{stagg.})} = \sum_N b^4\, \bar{\psi}(Nb) \sum_\mu \Big[(\gamma_\mu \otimes \mathbb{1})\, \partial_\mu^S + \frac{b}{2}(\gamma_5 \otimes \gamma_\mu^\star \gamma_5)\Box_\mu \Big] \psi(Nb)
$$

is invariant under Eqs. (A.26).

Using the fact that

$$e^{\imath \theta (\gamma_5 \otimes \gamma_5)} = \sum_{j=0}^{\infty} \left[\frac{(\imath\theta)^{2j}}{(2j)!} (\gamma_5 \otimes \gamma_5)^{2j} + \frac{(\imath\theta)^{2j+1}}{(2j+1)!} (\gamma_5 \otimes \gamma_5)^{2j+1} \right] =$$

$$= \sum_{j=0}^{\infty} \left[\frac{(\imath\theta)^{2j}}{(2j)!} (\mathbb{1} \otimes \mathbb{1}) + \frac{(\imath\theta)^{2j+1}}{(2j+1)!} (\gamma_5 \otimes \gamma_5) \right] = \cos\theta \, (\mathbb{1} \otimes \mathbb{1}) + \imath \sin\theta \, (\gamma_5 \otimes \gamma_5) \, ,$$

we can prove that

$$e^{\imath \theta (\gamma_5 \otimes \gamma_5)} (\gamma_\mu \otimes \mathbb{1}) - (\gamma_\mu \otimes \mathbb{1}) \, e^{-\imath \theta (\gamma_5 \otimes \gamma_5)} = 0 \tag{A.27a}$$

and

$$e^{\imath \theta (\gamma_5 \otimes \gamma_5)} (\gamma_5 \otimes \gamma_\mu^* \gamma_5) - (\gamma_5 \otimes \gamma_\mu^* \gamma_5) \, e^{-\imath \theta (\gamma_5 \otimes \gamma_5)} = 0 \, . \tag{A.27b}$$

It is quite simple:

- $e^{\imath \theta (\gamma_5 \otimes \gamma_5)} (\gamma_\mu \otimes \mathbb{1}) - (\gamma_\mu \otimes \mathbb{1}) \, e^{-\imath \theta (\gamma_5 \otimes \gamma_5)} =$

  $$= \left[\cos\theta \, \mathbb{1}_{16 \times 16} + \imath \sin\theta \, (\gamma_5 \otimes \gamma_5) \right] (\gamma_\mu \otimes \mathbb{1}) - (\gamma_\mu \otimes \mathbb{1}) \left[\cos\theta \, \mathbb{1}_{16 \times 16} - \imath \sin\theta \, (\gamma_5 \otimes \gamma_5) \right] =$$

  $$= \imath \sin\theta \left[(\gamma_5 \otimes \gamma_5)(\gamma_\mu \otimes \mathbb{1}) + (\gamma_\mu \otimes \mathbb{1})(\gamma_5 \otimes \gamma_5) \right] = \imath \sin\theta \, \{\gamma_5, \gamma_\mu\} \otimes \gamma_5 = 0 \, ;$$

- $e^{\imath \theta (\gamma_5 \otimes \gamma_5)} (\gamma_5 \otimes \gamma_\mu^* \gamma_5) - (\gamma_5 \otimes \gamma_\mu^* \gamma_5) \, e^{-\imath \theta (\gamma_5 \otimes \gamma_5)} =$

  $$= \imath \sin\theta \left[(\gamma_5 \otimes \gamma_5)(\gamma_5 \otimes \gamma_\mu^* \gamma_5) + (\gamma_5 \otimes \gamma_\mu^* \gamma_5)(\gamma_5 \otimes \gamma_5) \right] =$$

  $$= \imath \sin\theta \, (-1)^\mu \left[\mathbb{1} \otimes \gamma_5 \gamma_\mu \gamma_5 + \mathbb{1} \otimes \gamma_\mu \right] = \imath \sin\theta \, (-1)^\mu \, \mathbb{1} \otimes (\gamma_\mu - \gamma_\mu) = 0 \, .$$

Eventually, plugging Eqs. (A.26) in $\mathcal{S}_F^{(\text{stagg.})}$ and using Eq. (A.27), we get

$$\mathcal{S}_F^{\prime (\text{stagg.})} = \sum_N b^4 \, \bar\psi(Nb) \, e^{\imath \theta (\gamma_5 \otimes \gamma_5)} \sum_\mu \left[(\gamma_\mu \otimes \mathbb{1}) \, \partial_\mu^S + \frac{b}{2} (\gamma_5 \otimes \gamma_\mu^* \gamma_5) \Box_\mu \right] e^{\imath \theta (\gamma_5 \otimes \gamma_5)} \, \psi(Nb) \; =$$

$$= \sum_N b^4 \, \bar\psi(Nb) \sum_\mu \left[(\gamma_\mu \otimes \mathbb{1}) \, \partial_\mu^S + \frac{b}{2} (\gamma_5 \otimes \gamma_\mu^* \gamma_5) \Box_\mu \right] e^{-\imath \theta (\gamma_5 \otimes \gamma_5)} \, e^{\imath \theta (\gamma_5 \otimes \gamma_5)} \, \psi(Nb) \; =$$

$$= \mathcal{S}_F^{(\text{stagg.})} \, .$$

To conclude, let us derive how the remnant chiral symmetry generator acts on the staggered fields χ and $\bar\chi$. This turns to be particularly important in simulations where, as already mentioned, the one-component fields are used. Recalling that Eqs. (A.15) connects Γ-matrices to the more common *spin* $\otimes$ *taste* representation, we have

$$\left(U^\dagger \cdot (\gamma_5 \otimes \gamma_5) \cdot U \right)_{\rho\rho'} = \sum_{\substack{\alpha,\alpha' \\ f,f'}} (U^\dagger)_{\rho,\alpha f} \, (\gamma_5)_{\alpha\alpha'} \, (\gamma_5)_{ff'} \, U_{\alpha' f', \rho'} =$$

$$= \frac{1}{4} \sum_{\substack{\alpha,\alpha' \\ f,f'}} \left[\gamma_1^{\rho_1} \gamma_2^{\rho_2} \gamma_3^{\rho_3} \gamma_4^{\rho_4} \right]_{\alpha f}^* (\gamma_5 \otimes \gamma_5)_{\alpha f, \alpha' f'} \left[\gamma_1^{\rho_1'} \gamma_2^{\rho_2'} \gamma_3^{\rho_3'} \gamma_4^{\rho_4'} \right]_{\alpha' f'} =$$

$$= (-1)^{\rho_1 + \rho_2 + \rho_3 + \rho_4} \, \delta_{\rho,\rho',} \equiv \Gamma_{\rho\rho'}^{55} \, ,$$

where we used the techniques previously learnt. Now, if we want to have a more convenient expression, we can just recall that $n = 2N + \rho$ which leads to

$$(-1)^{\rho_1 + \rho_2 + \rho_3 + \rho_4} = (-1)^{n_1 + n_2 + n_3 + n_4} \; ;$$

therefore we can conclude that

$$\Gamma^{55}(n) = (-1)^{n_1 + n_2 + n_3 + n_4} \; \mathbb{1}_{16 \times 16} \; .$$

This means that the matrix $\Gamma^{55}(n)$ is local on the original lattice with lattice spacing a and then it does not mix degrees of freedom at different lattice sites.

§ A.4   The interacting theory and the taste symmetry

In Eq. (A.23), we used a tensor matrix notation emphasising in each term the *spin $\otimes$ taste* structure. It is evident that the only term not trivial in the taste space is irrelevant in the continuum and, then, it is easy to convince ourselves that for vanishing lattice spacing the taste degrees of freedom are not mixed or, said differently, that the taste symmetry is not broken. So far we postponed any comment about the taste degree of freedom and we used the *spin $\otimes$ taste* factorisation ignoring its meaning and implications. To some extent, it represents the remaining doublers in the theory. One flavour of staggered fermions correspond to a four-taste system. The main implications regard the hadron spectroscopy that we roughly sketch at the end of the section. Before, it is worth commenting further on our previous comment on the fact that taste symmetry is exact in the continuum. From Eq. (A.23) this seems an indisputable statement, but such an equation has been obtained in the free case. How can we be sure that no relevant, taste symmetry breaking terms arise in the staggering procedure carried out in the interacting case? Simply we cannot. There is no a priori argument and, in presence of non unitary gauge fields, the spin-taste structure of the action after having reconstructed the four-component Dirac fields is much more complicated. In fact, even though to impose gauge invariance in the one-component hypercube basis is straightforward and it has been done in §1.5, to do so in the spin-taste basis gauge links have to be included in the basis transformation. Moreover, this means that all the calculations done in §A.1 – and in principle also those in §A.2 and §A.3 – have to be repeated taking into account the colour degree of freedom, the dependence on which is not trivial anymore. Eq. (A.15a) will contain products of gauge links on the edges of the hypercube with origin at the lattice site N. Inverting this transformation and inserting it in Eq. (A.8) it is possible to obtain a gauge invariant version of the action in the spin-taste basis. Unfortunately, this calculation is awful and it would not add a lot to what we just said. Therefore we will not report here any expression, but only the partially explicit result of what happens reintroducing the physical dimensions of the fields and expanding each term for small lattice spacing,

$$\mathcal{S}_F^{(\text{stagg.})} = \sum_N b^4 \, \bar{\psi}(Nb) \left[\sum_\mu (\gamma_\mu \otimes \mathbb{1}) \, \partial_\mu^S + M_0 (\mathbb{1} \otimes \mathbb{1}) \right] \psi(Nb) \, + b^5 \, \mathcal{S}_{\text{tb},1} + \mathcal{O}(b^6) \; . \qquad \text{(A.28)}$$

Here, we wrote explicitly the terms which are trivial in the taste space and gathered in $\mathcal{S}_{\text{tb},1}$ the taste symmetry breaking expressions. More in detail, $\mathcal{S}_{\text{tb},1}$ contains five fermion bilinear terms in

$$(\gamma_5 \otimes \gamma_\mu \gamma_5) \left(\partial_\mu^S \right)^2 \quad , \quad \left[(\gamma_\mu - \gamma_\nu) \otimes \mathbb{1} \right] F_{\mu\nu} \quad \text{and} \quad \left[\gamma_5 \, \sigma_{\mu\nu} \otimes (\gamma_\mu + \gamma_\nu) \gamma_5 \right] F_{\mu\nu} \; ,$$

properly summed over μ and ν and combined with the correct coefficients ($F_{\mu\nu}$ is the field strength tensor, while $\sigma_{\mu\nu} = \gamma_\mu \gamma_\nu$). Due to the power of b in front put in Eq. (A.28), these terms are all irrelevant for small lattice spacing and we obtain a taste symmetric theory with four degenerate tastes in the continuum. Eventually, *no relevant, taste symmetry breaking terms arise in the staggering procedure carried out in the interacting case.*

Even though in the continuum limit the taste symmetry is restored, the taste degree of freedom plays an important role in hadron spectroscopy. Actually, meson spectroscopy calculations gets really difficult with staggered fermions (compared, for instance, to Wilson fermions) and baryonic spectroscopy becomes even tougher. The main complication is due to the fact that the interpolators have to be written down in the spin-taste basis – the only space in which fermionic fields are connected to reality – but in the simulations only the one-component basis is used. Therefore a mapping of the two-point correlation functions is required. On top of that, from the theoretical point of view, due to the larger symmetry of the theory, there is a higher number of hadrons. For example, each pion comes in a taste multiplet of 16. These, at finite lattice spacing, because of taste-symmetry violations, have different masses and only in the continuum they become degenerate. Therefore, it is important to specify which kind of mass measurement is done in a particular project, since the concept of pion mass is not unique at $a \neq 0$. Sometimes people measure the root-mean-square pion mass, in order to take into account the taste-symmetry breaking. In some other cases, only one pions is considered.

We will not discuss further here this topic, but we would like to suggest some references to read about it. A preliminary general description can be found in §6.3 of [18]. The original works on staggered spectroscopy [113, 114] are really technical and it is not immediate to read them. Meson operators have been analysed in many other papers; [115] can be used as a completed reference. However, in order to map the interpolators from the spin-taste to the one-component basis, some techniques like the *reduction rule* described in §5 of [113] are needed. An example can be found in [116], where the calculation of the correlation function that leads to the estimation of the (pseudoscalar) pion mass is carried out in detail. Examples of splitting due to the taste symmetry breaking can be found in [117]. To conclude, we would encourage the Reader new to spectroscopy on the lattice to start reading about with Wilson fermions – for example referring to §6 of [19]. In this way, all complications are reduced and it is easier to focus on the main ideas. Later it should be easier to address the same problem in a different formulation.

Rooted staggered fermions

<div align="right">B</div>

> «*I like hearing myself talk. It is one of my greatest pleasures. I often have long conversations all by myself, and I am so clever that I sometimes don't understand a single word of what I am saying.*»

<div align="right">

— **Oscar Wilde** —

</div>

As fully discussed in §1.4 as well as in appendix A, the staggered discretisation of the fermionic action leads to a theory with four degenerate fermions. Even though there are few cases in which this is not a problem, usually we would like to have, in the continuum limit, a theory with not degenerate quarks, as QCD is. In the Eighties, there were many efforts – e.g. [114, 118] – to modify the staggered action in order to obtain four non-degenerate particles in the continuum, corresponding to the up, down, strange and charm quarks. Nevertheless, it turned out that this approach, though possible and theoretically valid, has severe numerical drawbacks, first of which the fact that the fermionic determinant is still real but not positive anymore. This cancels the main numerical advantage of staggered fermions and this approach has not been followed in practice.

Always in the Eighties, E. Marinari, G. Parisi and C. Rebbi proposed a new idea to approach the problem, at that time studying the Schwinger model [119]: To reduce the number of fermions, the naïve staggered fermionic determinant in the partition function is substituted by its fourth-root (this procedure was called afterwards *rooting trick*). Thirty-five years elapsed from that fateful moment and nobody was able to prove neither that this technique is correct nor that it is wrong. A big debate went on during years and the correctness of the rooting trick is still an open question. Around 2006, there was a kind of escalation in the discussion, since more and more practitioners were using this technique, without any rigorous motivation behind. This was justified by numeric results that were in better and better agreement with experimental values [120–125]. Many theorists in the community were sceptical and refused to use this fermionic formulation. The main one is probably M. Creutz, who tried to present arguments against the rooting trick, claiming in several occasions that it leads to wrong results [126–130]. In the same years, some other people in the community were trying to understand and solve the issue, being more in favour of its validity. For example, C. Bernard approached the problem perturbatively [131], while Y. Shamir used renormalisation group techniques [132]. Together with M. Golterman and S. Sharpe, they presented several arguments, which would suggest the correctness of the rooting trick in the continuum limit [133, 134]. There was also a series of tit for tat. S. Sharpe et al. rejected in [135] the arguments in [129] of M. Creutz, who replied again in [136]. Not so much time after, S. Sharpe et al. addressed M. Creutz's last criticisms refusing them in [137]. M. Creutz did not agree and argued in [138] that the chiral behaviour of staggered fermions had not been understood by the counterpart. A further reply appeared four days later [139]. At *The XXVI International Symposium on Lattice Field Theory*, in 2008, M. Golterman presented a review of the recent arguments that would make the rooting trick plausible, but these were not addressed by M. Creutz, in the proceeding of his

contribution to the same conference [130]. Nevertheless, he told the community about how he lived this *saga* in [140].

Since then, various other works arguing in favour or against the validity of the rooting trick have been presented. It is almost impossible to report all of them here, but it is worth mentioning a couple of them.

- G. C. Rossi and M. Testa presented in 2010 a nice, instructive, 0-dimensional calculation[141] in which they show how the rooting fails whenever the fermionic contribution to the partition function is not positive on all gauge configurations.

- A direct study of the η'-phenomenology in QCD should be the *experimentum crucis* for the rooting trick with staggered fermions, but it has always been inaccessible due to noise issues. Indeed, the conceptual issue is one-to-one matched in the massive Schwinger model with one flavour and this is the idea behind the work of S. Dürr, that in 2012 studied the quark-mass dependence of the η in the Schwinger model with zero, one and two flavours [142]. He concludes that simulations using rooted staggered fermions treat the contribution of the axial anomaly to the particle spectrum correctly.

As the Reader will already have imagined, the issue under debate is extremely technical and there are not so many experts in the world that master all the details. Therefore, it is not our intention to provide here a complete, quantitative overview of the topic, for which we refer to the surely abundant literature. After the short historical introduction above, we will only explain the main problem behind the rooting issue, trying to justify, to some extent, why and how the rooted staggered setup could give correct measurements in the continuum limit. A personal point of view will conclude this Appendix.

§ B.1   The loss of locality

To make the discussion easier to be followed, let us start recalling here few results obtained previously in appendix A. In the so-called single-component base, the unimproved staggered action reads

$$\mathcal{S}_F^{(\text{stagg.})} = \frac{1}{2} \sum_{n,\mu} \eta_\mu(n) \left[\bar{\chi}(n)\,\chi(n+\hat{\mu}) \,-\, \bar{\chi}(n)\,\chi(n-\hat{\mu}) \right] + \hat{M}_0 \sum_n \bar{\chi}(n)\,\chi(n) \ ; \qquad (\text{B.1})$$

after having recombined the degrees of freedom at the vertices of each unit lattice hypercube, the action is mapped into that of 4 tastes of 4-component Dirac fermions,

$$\mathcal{S}_F^{(\text{stagg.})} = \sum_N \bar{\psi}(N) \left[\sum_\mu (\gamma_\mu \otimes \mathbb{1})\,\partial_\mu^S + M_0\,(\mathbb{1} \otimes \mathbb{1}) + \sum_\mu \frac{1}{2}\,(\gamma_5 \otimes \gamma_\mu^\star \gamma_5)\,\square_\mu \right] \psi(N) \ . \qquad (\text{B.2})$$

Here the *spin $\otimes$ taste* notation is used. The fields χ live on a twice finer lattice than that on which the fields ψ are defined. It is worth remarking that the last term in Eq. (B.2) looks like the Wilson term in the Wilson formulation and we would end up with exactly 4 Wilson fermions via the substitution

$$(\gamma_5 \otimes \gamma_\mu^\star \gamma_5) \quad \rightarrow \quad (\mathbb{1} \otimes \mathbb{1}) \ .$$

This, as we know, would break completely the chiral symmetry, implying an additive renormalisation for the fermion mass. The nice feature of staggered fermions is that they preserve a $U(1)$ symmetry,

$$\psi(N) \ \rightarrow \ \psi'(N) \ = e^{\,\imath\,\theta(\gamma_5 \otimes \gamma_5)}\,\psi(N)$$
$$\bar{\psi}(N) \ \rightarrow \ \bar{\psi}'(N) \ = \ \bar{\psi}(N)\,e^{\,\imath\,\theta(\gamma_5 \otimes \gamma_5)} \ ,$$

which maintains the mass renormalisation multiplicative.

Looking closely at the action in Eq. (B.2), it should be clear that the last term is not relevant in the continuum limit and, since it is the only part non trivial in the taste space, we could naïvely expect that the action in the continuum is symmetric in the taste space, i.e. that the taste symmetry is restored for $a \to 0$. Actually, Eq. (B.2) is obtained from Eq. (B.1) through the staggering procedure in the *free case*, i.e. with all gauge links set to the identity. As commented in §A.4, in the interacting case, the reconstruction of the Dirac fields is not straightforward and new terms will appear in the action in the spin $\otimes$ taste basis. In principle, there is no guarantee that these terms are irrelevant in the continuum limit. Indeed they are and this was proved through a careful analysis more than thirty years ago [114, 118].

From the considerations above, we can assume that the staggered formulation without the rooting trick (the so-called *unrooted staggered fermions*) is uncontroversial and has a continuum limit corresponding to a theory with four degenerate fermions. This is one of the (reasonable) assumptions on the basis of any work dealing with the rooting problem. Let us now discuss why rooted staggered fermions could be problematic. In practice, what is done is to take the fourth-root of the fermionic determinant in the partition function and assume that it describes a theory with one fermion only. For example, for three non degenerate flavours (like up, down and strange), we would write

$$\mathcal{Z}_{QCD}^{\text{root}} = \int \mathcal{D}U \left\{ \det\!\big[D_{\text{stagg.}}(M_0^u)\big] \det\!\big[D_{\text{stagg.}}(M_0^d)\big] \det\!\big[D_{\text{stagg.}}(M_0^c)\big] \right\}^{\frac{1}{4}} e^{-\mathcal{S}_g} , \qquad (B.3)$$

where $D_{\text{stagg.}}$ is the staggered operator needed to rewrite Eq. (B.1) as

$$\mathcal{S}_F^{(\text{stagg.})} = \bar{\chi} \cdot D_{\text{stagg.}}(M_0) \cdot \chi .$$

Observe that, by construction, the positive root in Eq. (B.3) is taken. This could seem already suspicious, but indeed it is not. The massless staggered operator is anti-hermitian and its eigenvalues are purely imaginary. Due to the remnant $U(1)$ symmetry, they appear in pairs of complex conjugated numbers and this implies that $\det\!\big[D_{\text{stagg.}}(0)\big] \in \mathbb{R}_{\geqslant 0}$. A non-vanishing mass term shifts the spectrum by an amount M_0. So whether the determinant is positive or negative depends on the sign of the mass. Taking the positive root in Eq. (B.3), means that $\mathcal{Z}_{QCD}^{\text{root}}$ will describe the positive-mass physics, irrespective of the sign of the input bare mass.

<center>*What is the relation between $\mathcal{Z}_{QCD}^{root}$ and $\mathcal{Z}_{QCD}$?*</center>

This is in short the question that is open since decades by now. Of course, the rooting trick has been shown to work in other contexts and this is the reason why people tryied to use also with staggered fermions. Actually, if $a = 0$, we know that the staggered operator reduces to

$$\lim_{a \to 0} D_{\text{stagg.}} = \mathfrak{D}_1 \otimes \mathbb{1} ,$$

where $\mathfrak{D}_1$ is the continuum Dirac operator for one flavour. It is immediate to see that in this case the rooting is legitimate; in fact,

$$\det\!\big(\mathfrak{D}_{\text{stagg.}}\big) = \det\!\big(\mathfrak{D}_1 \otimes \mathbb{1}\big) = \big[\det(\mathfrak{D}_1)\big]^4 .$$

Taking, instead, the fourth-root at finite lattice spacing could be in general not correct because, roughly speaking, it is equivalent to exchange the order of two mathematical operations (a limit with the fourth-root),

$$\left\{ \lim_{a \to 0} \big[\det\!\big(D_{\text{stagg.}}\big)\big] \right\}^{\frac{1}{4}} \;\overset{?}{=}\; \lim_{a \to 0} \left\{ \big[\det\!\big(D_{\text{stagg.}}\big)\big]^{\frac{1}{4}} \right\} \qquad (B.4)$$

Using S. Sharpe classification given in [134] and inspired by a well-known western, there are three possibilities.

- Rooted staggered fermions are `GOOD` in the sense that they have the correct continuum limit, without any complications. This means that Eq. (B.4) holds and taking the fourth-root is a clean step.

- The rooting trick is wrong and the theory obtaining in the continuum using it is not QCD. In this case, any result obtained on the lattice could be close to the QCD value, but it would be nothing more than a coincidence. Rooted staggered fermions are `BAD`.

- Eq. (B.4) holds, but any prediction at finite lattice spacing is unphysical. This would require deep theoretical understanding of the issue, but it would be allowed to use the rooting trick. In this case rooted staggered fermions would be `UGLY`.

To understand whether the rooting trick is allowed or not, a first step is to investigate what it implies. C. Bernard, M. Golterman and Y. Shamir [133] proved in 2006 the following

Theorem.

Rooted staggered fermions cannot be described by a local theory with a single taste per flavour.

Proof: Since this is the root of most the problems related to the issue, it is important to understand it. Moreover the argument behind is quite straightforward and proceeds by contradiction. Let us then suppose that there exists a local, single-taste theory describing the rooted staggered formulation. This implies that

$$\left[\det\left(D_{\text{stagg.}}\right)\right]^{\frac{1}{4}} = \det(D_1)\, e^{-\delta \mathcal{S}_g^{\text{eff.}}}\;, \tag{B.5}$$

where D_1 is a local, single-taste operator and $\delta \mathcal{S}_g^{\text{eff.}}$ is a local, left-over, gauge action. This relation has to hold at least on the relevant configuration for the rooted theory. Eq. (B.5) implies, for the unrooted theory, that

$$\det\left(D_{\text{stagg.}}\right) = \left[\det(D_1)\right]^4 e^{-4\delta \mathcal{S}_g^{\text{eff.}}} = \det(D_1 \otimes \mathbb{1})\, e^{-4\delta \mathcal{S}_g^{\text{eff.}}}\;, \tag{B.6}$$

namely a theory with an exact $SU(4)$ taste symmetry, which is clearly impossible at $a \neq 0$. $\qquad \square$

Strictly speaking, as also remarked in [134], there could be a leak in the proof above. In fact, it could be that the set of configurations important in the unrooted theory does not overlap with the set of configurations relevant in the rooted case. This would mean that Eqs. (B.5) and (B.6) are not connected and it would be wrong to make the latter follow from the former. Indeed, this is a very unlikely scenario and S. Sharpe comments on it saying that he does not pursue this possibility, since there is a lot of evidence of the non-locality of the rooted theory on finite lattice spacing.

We know that a non-local theory is unphysical and this should be enough to decide not to use the rooting trick. Nevertheless, the staggered formulation is really attractive by the numerical point of view and the possibility to be able to use it to simulate any number of flavours can justify an effort to understand and hopefully *tame* the non-locality. In fact, it could happen that QCD and the rooted staggered theory have the same universality class or, said in other words, that all the effects due to the non-locality vanish in the continuum limit. This would guarantee the correctness of all the extrapolations in the $a \to 0$ limit. Whether this can be or not the case is hard to be established – and a more than thirty years long debate gives an idea of that – but it is already very difficult to understand and critically judge the several works that in the few decades appeared in favour or against the rooting trick. Therefore, we will not further discuss the problem here and we will move on in the next section providing a personal point of view. However, before doing that, let us mention that S. Sharpe concludes in his review on the topic [134] that rooted staggered fermions are `UGLY` and that, then, they have to be used consciously.

§ B.2   What do we learn from mathematics?

Often, when speaking about the rooted staggered formulation, people ask questions like: Why should rooted staggered fermions be used if there is not a solid theoretical foundation behind? Why not to use *only* uncontroversial formulations? Is it worth using computer time to obtain results in this maybe wrong framework? Everybody should personally answer these questions and, probably, there is no right or wrong answer. Nevertheless, it is interesting to look at this issue from a slightly alternative point of view.

The rooting trick problem can be thought as a conjecture that has neither been proved nor disproved. Thinking about it in this way, it could be natural to look back in history and see how people behaved in similar occasions. The closest field to physics in which comparable situations occurred is mathematics. Indeed, mathematics is plenty of conjectures whose truthfulness is, nowadays, still unclear. Some of them date back to the beginning last century or to even earlier times. In the last decades, lacking a rigorous proof, people started to take advantage of the more and more powerful computing resources and they verified the validity of certain statements numerically. Here below, we report on two examples.

The Collatz conjecture

It was formulated in 1937 and it is mostly known as $3n + 1$ conjecture. Given the function

$$f : \mathbb{N}_{>0} \to \mathbb{N}_{>0} \quad \text{with} \quad f(n) = \begin{cases} n/2 & \text{if } n \text{ even} \\ 3n + 1 & \text{if } n \text{ odd} \end{cases},$$

it is possible to define a sequence starting at n,

$$a_i = \begin{cases} n & \text{for } i = 0 \\ f(a_{i-1}) & \text{for } i > 0 \end{cases}.$$

The conjecture states that this sequence will eventually produce the number 1, independently from the starting point, $\exists\, k \mid a_k = 1 \; \forall n \in \mathbb{N}_{>0}$ (obviously, from a_k on, the sequence is trivial). Using almost one hundred of CPU years, this conjecture has been verified independently by different people up to $n = 2^{60} \approx 1.15 \cdot 10^{18}$, a quite impressive result [143, 144].

The Riemann hypothesis

In 1859, Bernhard Riemann proposed that *the real part of every non-trivial zero of the Riemann zeta function is 1/2*. Often, the Riemann zeta function is defined as

$$\zeta(s) \equiv \sum_{n=1}^{\infty} \frac{1}{n^s}$$

and, clearly, this series converges if and only if $\Re(s) > 1$. By analytic continuation, it is possible to extend the function above to the whole complex plane. It turns, then, out that $\zeta(s) = 0$ for integer, even values of s. These are the so called trivial zeros. For the interested Reader, for $\Re(s) > 0$, we have

$$\zeta(s) \equiv 2^{s-1} \sum_{n=1}^{\infty} \frac{(-1)^{n+1}}{n^s},$$

while values of ζ at negative s can ve obtained via the relation

$$\zeta(s) = 2^s\, \pi^{s-1}\, \sin\!\left(\frac{\pi\, s}{2}\right) \Gamma(1 - s)\, \zeta(1 - s).$$

Here, $\Gamma(s)$ is the Gamma function and it should be obvious the previous statement about the trivial zeros. In 2004, G. Xavier reported a study in which he proceeded to a numeric verification of the Riemann hypothesis, founding the first 10^{13} zeros on the line $\Re(s) = 1/2$ up to $\Im(s) \approx 10^{24}$, another impressive and really costly result [145].

Clearly, the fact that a conjecture seems to be true does *not* mean that it is true. Actually, looking back in the history of mathematics, there are examples of statements which seemed to be correct and that have been later proved to be wrong. Again, we report two examples.

The Mertens conjecture

In number theory, the Mertens function $M(n) : \mathbb{N}_{>0} \to \mathbb{N}_{>0}$ is defined as

$$M(n) \equiv \sum_{k=1}^{n} \mu(k) \, ,$$

where $\mu(k)$ is the Möbius function[1]. In 1897, Mertens suggested that $|M(n)| < \sqrt{n}$ for any value of $n > 1$. Despite the large amount of computational evidence in favour of the conjecture, Odlyzko and te Riele [146] disproved it in 1985. Their proof was an indirect one, since no explicit counterexample was found. It was only shown that

$$\lim_{n\to\infty} \sup M(n) \, n^{-1/2} \; > \; +1.06$$
$$\lim_{n\to\infty} \inf \, M(n) \, n^{-1/2} \; < \; -1.009 \, .$$

Thanks to some recent works [147, 148], it is now known that there must be a counterexample at $n = \bar{n}$ such that

$$10^{14} < \bar{n} < e^{\, 1.59 \cdot 10^{40}} \, .$$

Skewes' numbers

At the beginning of the last century, it was not clear in which relation were $\pi(x)$, the number of prime numbers smaller than x, and li(x), the logarithmic integral function. The situation was clarified in 1914 by J.E. Littlewood, which proved that the sign of the difference $\pi(x) - \text{li}(x)$ changes infinitely often. All the numeric evidence till that moment was suggesting that $\pi(x) < \text{li}(x)$. Unfortunately, Littlewood did not provide any estimate of x such that $\pi(x) < \text{li}(x)$. It took many years to determine an upper bound for x and it was shown in 1955 by S. Skewes [149] that

$$\exists \, x < e^{\, e^{\, e^{\, e^{\, 7.705}}}} \lesssim 10^{10^{10^{964}}} \mid \pi(x) > \text{li}(x) \, .$$

This upper bound has been reduced in the recent past. For example, in 2010, S. Zegowitz showed that

$$\exists \, x < e^{\, 727.951346801} \mid \pi(x) > \text{li}(x) \, .$$

Beyond the considerations above, it has also to be said that, often, mathematicians try to assume a conjecture as true and see what this implies. For instance, this has been done for more

---

[1]For the Reader not familiar with the topic, the Möbius function is defined to be $+1$ (-1) if its argument is a square-free positive integer with an even (odd) number of prime factors, 0 otherwise.

than one century for the Riemann hypothesis and there are, by now, many other results that would be implied. Coming back to out initial problem, what should we conclude from this mathematical excursus? At the moment, any kind of proof is missing and this can lead to two different but equally correct decisions. On one side, a reasonable person could think

> *"Since there is no rigorous proof about the **correctness** of rooted staggered fermions, I do not want to use them."*

but, on the other, an equally reasonable argument could be

> *"Since there is no rigorous proof about the **incorrectness** of rooted staggered fermions, I consciously try to use them; maybe this will also help to clarify the situation."*

Probably, this issue will not be settled in the near future and it should be recognised that the rooted staggered formulation is full of caveats. Nevertheless, the common scientific aim should be understanding the nature and if, *trying to do that*, the rooting trick turns out to be correct or incorrect, it will mean that an important step towards a better understanding will be accomplished.

Miscellaneous

«A grapefruit is a lemon that had a chance and took advantage of it!»

In this appendix we collected few technicalities that we decided not to include in the main part of the thesis for the sake of clarity. Basically, they are intended to help the Reader new to the topic. Even if all the following sections are related to previous discussions, we decided to recall here the used notation in order to avoid very far cross-references and make, then, the reading more pleasant.

§ C.1   The Fourier transform of a function on integers

Using $n \in \mathbb{Z}$ and $p \in \mathbb{R}$ to denote conjugate variables, we have that the Fourier transform of a function $f(n)$ is a function $\tilde{f}(p)$ defined as

$$\tilde{f}(p) \equiv \sum_{n=-\infty}^{\infty} f(n)\, e^{-\imath p n} \;. \tag{C.1a}$$

From its definition, it follows immediately that $\tilde{f}(p + 2\pi) = \tilde{f}(p)$, i.e. the function $\tilde{f}$ is periodic in p with period equals to 2π. Therefore we can limit the domain of p to the so-called (first) Brillouin zone, i.e. $p \in [-\pi, \pi)$. It can be easily shown that inverting Eq. (C.1a) leads to

$$f(n) = \int_{-\pi}^{\pi} \frac{\mathrm{d}p}{2\pi}\, \tilde{f}(p)\, e^{\imath p n} \;. \tag{C.1b}$$

In fact,

$$f(n) = \int_{-\pi}^{\pi} \frac{\mathrm{d}p}{2\pi}\, \tilde{f}(p)\, e^{\imath p n} = \int_{-\pi}^{\pi} \frac{\mathrm{d}p}{2\pi} \sum_{m=-\infty}^{\infty} f(m)\, e^{-\imath p m}\, e^{\imath p n} =$$

$$= \sum_{m=-\infty}^{\infty} f(m) \int_{-\pi}^{\pi} \frac{\mathrm{d}p}{2\pi} e^{\imath p (n-m)} = \sum_{m=-\infty}^{\infty} f(m)\, \delta_{n,m} = f(n) \;.$$

Let us generalise now the definitions given in Eqs. (C.1) to the case of functions of two integer variables. Denoting the new pair of conjugated variables with $m \in \mathbb{Z}$ and $k \in \mathbb{R}$, we have

$$\tilde{f}(p,k) \equiv \sum_{n=-\infty}^{\infty} \sum_{m=-\infty}^{\infty} f(n,m)\, e^{-\imath p n}\, e^{-\imath k m} \tag{C.2a}$$

$$f(n,m) = \int_{-\pi}^{\pi} \frac{\mathrm{d}p}{2\pi} \int_{-\pi}^{\pi} \frac{\mathrm{d}k}{2\pi}\, \tilde{f}(p,k)\, e^{\imath p n}\, e^{\imath k m} \;. \tag{C.2b}$$

Whenever a function depends only on the difference of its variables, a simplification is possible. As it could be guessed, it is possible to treat such a function as if it depended only on one variable. More explicitly, if $f(n, m) = g(n - m)$, we have

$$
\tilde{f}(p, k) \equiv \sum_{n=-\infty}^{\infty} \sum_{m=-\infty}^{\infty} f(n, m) \, e^{-\imath p \, n} \, e^{-\imath k \, m} =
$$

$$
= \sum_{n=-\infty}^{\infty} \sum_{m=-\infty}^{\infty} g(n - m) \, e^{-\imath p \, n} \, e^{-\imath k \, m} \, e^{-\imath p \, (m-m)} =
$$

$$
= \sum_{n=-\infty}^{\infty} \sum_{m=-\infty}^{\infty} g(n - m) \, e^{-\imath p \, (n-m)} \, e^{-\imath (k+p) \, m} =
$$

$$
= \sum_{l=-\infty}^{\infty} g(l) \, e^{-\imath p \, l} \sum_{l'=-\infty}^{\infty} e^{-\imath (k+p) \, l'} = 2\pi \, \delta(p + k) \sum_{l=-\infty}^{\infty} g(l) \, e^{-\imath p \, l} \equiv 2\pi \, \delta(p + k) \, \tilde{g}(p) \, ,
$$

which, inverted, leads to

$$
f(n, m) = \int_{-\pi}^{\pi} \frac{\mathrm{d}p}{2\pi} \int_{-\pi}^{\pi} \frac{\mathrm{d}k}{2\pi} \, 2\pi \, \delta(p + k) \, \tilde{g}(p) \, e^{\imath p \, n} \, e^{\imath k \, m} \, ,
$$

namely

$$
g(n - m) = \int_{-\pi}^{\pi} \frac{\mathrm{d}p}{2\pi} \, \tilde{g}(p) \, e^{\imath p \, (n-m)} \, .
$$

Therefore, up to the factor $2\pi \, \delta(p + k)$, this case is identical to that with functions of a single integer variable. The generalisation to a function $f : \mathbb{Z}^r \to \mathbb{R}^r$ is completely trivial and it can be shown that, whenever the function f depends on two variables n_i and n_j through the difference $n_i - n_j$ only, then the function $\tilde{f}$ depends trivially on one of its variables and it can be rewritten in a way such that it depends only on $r - 1$ variables.

Example: *Calculate the Fourier transform of* $f(n_1, n_2, m_1, m_2) = \delta_{n_1, m_1 + 2} \big(\delta_{n_2, m_2 + 1} + \delta_{n_2, m_2 - 1} \big)$.

$$
\tilde{f}(p_1, p_2, k_1, k_2) = \sum_{\substack{n_1, n_2 \\ m_1, m_2}} f(n_1, n_2, m_1, m_2) \, e^{-\imath \, (p_1 n_1 + p_2 n_2 + k_1 m_1 + k_2 m_2)} =
$$

$$
= (2\pi)^2 \, \delta(p_1 + k_1) \, \delta(p_2 + k_2) \sum_{l_1, l_2} \delta_{l_1, 2} \big(\delta_{l_2, +1} + \delta_{l_2, -1} \big) \, e^{-\imath \, (p_1 l_1 + p_2 l_2)} =
$$

$$
= (2\pi)^2 \, \delta(p_1 + k_1) \, \delta(p_2 + k_2) \sum_{l_2} \big(\delta_{l_2, +1} + \delta_{l_2, -1} \big) \, e^{-\imath \, (2p_1 + p_2 l_2)} =
$$

$$
= (2\pi)^2 \, \delta(p_1 + k_1) \, \delta(p_2 + k_2) \big(e^{-\imath p_2} + e^{\imath p_2} \big) \, e^{-\imath \, 2p_1} =
$$

$$
= 2 \, (2\pi)^2 \, \delta(p_1 + k_1) \, \delta(p_2 + k_2) \cos(p_2) \, e^{-\imath \, 2p_1} \qquad .
$$

§ C.2 On boundary conditions in simulations

The way to impose some particular boundary conditions (BC) in a simulation is not unique. Let us suppose that we want the fermionic field satisfy the following property:

$$
\chi(n + N_\mu \, \hat{e}_\mu) \, = e^{\imath \theta_\mu} \, \chi(n) \, , \tag{C.3a}
$$

where $n \equiv (n_x, n_y, n_z, n_t)$, N_μ is the extension of the lattice in the μ–direction and θ_μ is a global parameter[1]. All the lattice coordinates n_μ ranges in $[0, N_\mu - 1]$. Observe that Eq. (C.3a) implies

$$\chi(n - N_\mu \, \hat{e}_\mu) \, = e^{-\imath \theta_\mu} \, \chi(n) \; , \qquad\qquad \text{(C.3b)}$$

sending n into $n - N_\mu \, \hat{e}_\mu$. Here, we will focus only on the staggered formulation and, in particular, we will recall the two main possibilities to impose the BC in Eqs. (C.3). It is quite easy to apply all the following arguments to different formulations (e.g. Wilson fermions), therefore we leave any generalisation to the interested Reader[2]. Just to fix the notation, we will refer to the standard staggered action as

$$\mathcal{S} = \frac{1}{2} \sum_{n,\mu} \bar{\chi}(n) \, \eta_\mu(n) \left[\, U_\mu(n) \, \chi(n + \hat{\mu}) \, - \, U_\mu^\dagger(n - \hat{\mu}) \, \chi(n - \hat{\mu}) \, \right] + M_0 \sum_n \bar{\chi}(n) \, \chi(n) \; ,$$

where

$$\begin{cases} \eta_1(n) = 1 \\ \eta_\mu(n) = (-1)^{\sum_{\nu < \mu} n_\nu} & \text{if} \quad \mu \neq 1 \end{cases}$$

and the colour index has been omitted.

Strategy A: distributing the BC on the whole lattice

One very easy possibility to impose Eqs. (C.3) is to make a unitary abelian transformation on the fields that we want to satisfy such BC [150]. In particular, let us consider the following transformation,

$$\chi'(n) \, = e^{-\imath \sum_\mu \frac{\theta_\mu \, n_\mu}{N_\mu}} \, \chi(n) \, \equiv T(n) \, \chi(n) \; , \qquad\qquad \text{(C.4a)}$$

$$\bar{\chi}'(n) \, = e^{+\imath \sum_\mu \frac{\theta_\mu \, n_\mu}{N_\mu}} \, \bar{\chi}(n) \, \equiv T^\star(n) \, \chi(n) \; . \qquad\qquad \text{(C.4b)}$$

Note that $T(n \pm N_\mu \hat{e}_\mu) = e^{\mp \imath \theta_\mu} \, T(n)$. It is easy to show that, if the χ' field has *periodic* BC in every direction, then the χ field satisfy Eqs. (C.3). The transformation above in the standard staggered action leads to

$$\mathcal{S} = M_0 \sum_n \bar{\chi}'(n) \, \chi'(n) \, +$$

$$+ \, \frac{1}{2} \sum_{n,\mu} \bar{\chi}'(n) \, \eta_\mu(n) \left[e^{\imath \frac{\theta_\mu}{N_\mu}} \, U_\mu(n) \, \chi'(n + \hat{\mu}) \, - e^{-\imath \frac{\theta_\mu}{N_\mu}} \, U_\mu^\dagger(n - \hat{\mu}) \, \chi'(n - \hat{\mu}) \, \right] , \qquad \text{(C.5)}$$

from which it should be clear that, during a simulation, it is possible to impose the desired BC by using a fermionic field that has periodic BC, but that obeys a modified Dirac equation. In other words, it is sufficient to multiply each link by the proper phase. For future convenience, let us indicate the modified Dirac operator as

$$M_{n,m}^\theta \equiv \frac{1}{2} \sum_{\mu=1}^4 \eta_\mu(n) \left[e^{\imath \frac{\theta_\mu}{N_\mu}} \, U_\mu(n) \, \delta_{n+\hat{\mu},m} - e^{-\imath \frac{\theta_\mu}{N_\mu}} \, U_\mu^\dagger(n - \hat{\mu}) \, \delta_{n-\hat{\mu},m} \right] + M_0 \, \delta_{n,m} \; .$$

It is worth remarking that we just *rewrote* the action, and no particular symmetry of the theory has been used. It is simply easier from the programming point of view to deal with periodic fermionic fields (in every direction), because then it has not to be checked in the code whether the boundary of the lattice is being crossed[3].

---

[1]The BC on the gauge field are assumed to be periodic.

[2]Actually, the second strategy we will discuss is peculiar to the staggered formulation, since it makes explicit use of the staggered phases that are not present in any other discretisation.

[3]In principle, one could directly implement Eqs. (C.3) using some `if`–statements to check the actual position on the lattice. Nevertheless this is particularly time consuming and it is never done.

Strategy B: leaving the BC at the end of the lattice

Another possibility to impose the desired BC is to leave them at some point on the lattice. This statement could sound completely the opposite of what said above, but there is a trick to easily do that. It is common practice in simulations using the staggered fermions to include the staggered phases $\eta_\mu(n)$ in links and to forget about them during a simulation (refer to the last part of §3.1.1 to know more about this point). Before doing that, it is possible to multiply one staggered phase in each direction by a proper factor, fulfilling in this way Eqs. (C.3). Let us see now in more details how this procedure works.

First of all let us remark that, without loss of generality, we can choose to impose Eqs. (C.3) at the end of the lattice in each direction, namely

$$
\begin{aligned}
\chi(N_\mu \, \hat{e}_\mu) &= e^{\,\imath\theta_\mu} \, \chi(\underline{0}) \\
\chi(-1 \, \hat{e}_\mu) &= e^{\,-\imath\theta_\mu} \, \chi((N_\mu - 1) \, \hat{e}_\mu) \ ,
\end{aligned}
\tag{C.6}
$$

with $n = (0,0,0,0) \equiv \underline{0}$. Observe that the arguments of the χ-field in the equations above are to be read as four vectors with n_ν set to a generic n_x, n_y, n_z or n_t for $\nu \neq \mu$ and n_ν at the beginning or end of the lattice for $\nu = \mu$. So, it is possible to think that the fermionic field takes a phase *only* between the last and the first site in each direction. Now, to get some insight about the general argument, let us consider only non-periodic BC in the time direction (the generalisation to more complicated cases is trivial and it will be made later on). Let us indicate the site coordinates as $n \equiv (\vec{n}, t)$. Eqs. (C.3) become

$$
\begin{aligned}
\chi(\vec{n}, \, N_t) &= e^{\,\imath\theta_t} \, \chi(\vec{n}, \, 0) \\
\chi(\vec{n}, \, -1) &= e^{\,-\imath\theta_t} \, \chi(\vec{n}, \, N_t - 1) \ .
\end{aligned}
\tag{C.7a}
$$

for the temporal direction and

$$
\begin{aligned}
\chi(N_i \, \hat{e}_i, \, t) &= \chi(\vec{0}, \, t) \\
\chi(-1 \, \hat{e}_i, \, t) &= \chi((N_i - 1) \, \hat{e}_i, \, t) \ .
\end{aligned}
\qquad [i \text{ not summed}]
\tag{C.7b}
$$

for spatial directions. Again, the first arguments of the χ-field in Eq. (C.7b) above are to be read as vectors (n_x, n_y, n_z) with n_j at the beginning or end of the lattice for $j = i$. Defining $M_{n,m}$ such that

$$
\mathcal{S} = \sum_{n,m} \bar{\chi}(n) \, M_{n,m} \, \chi(m) \ ,
$$

it is easy to see that

$$
\chi(n) = \sum_m M_{n,m} \, \chi(m) = \frac{1}{2} \sum_\mu \eta_\mu(n) \left[U_\mu(n) \, \chi(n+\hat{\mu}) - U_\mu^\dagger(n-\hat{\mu}) \, \chi(n-\hat{\mu}) \right] + M_0 \, \chi(n) \ .
\tag{C.8}
$$

Obviously, there is an expression like Eq. (C.8) for each site of the lattice. Nevertheless, the temporal phase θ_t will appear only if $n = (\vec{n}, 0)$ and $n = (\vec{n}, N_t - 1)$; in particular, we have

$$
\begin{aligned}
&\chi(\vec{n}, \, 0) \, - (\ldots) = \\
&= \frac{1}{2} \, \eta_t(\vec{n}, \, 0) \Big[U_t(\vec{n}, \, 0) \, \chi(\vec{n}, \, 1) \, - \, U_t^\dagger(\vec{n}, \, -1) \, \chi(\vec{n}, \, -1) \Big] = \\
&= \frac{1}{2} \, \eta_t(\vec{n}, \, 0) \Big[U_t(\vec{n}, \, 0) \, \chi(\vec{n}, \, 1) \, - \, e^{\,-\imath\theta_t} \, U_t^\dagger(\vec{n}, \, N_t - 1) \, \chi(\vec{n}, \, N_t - 1) \Big] = \\
&= \frac{1}{2} \Big[\eta_t(\vec{n}, \, 0) \, U_t(\vec{n}, \, 0) \, \chi(\vec{n}, \, 1) \, - \, e^{\,-\imath\theta_t} \eta_t(\vec{n}, \, N_t - 1) \, U_t^\dagger(\vec{n}, \, N_t - 1) \, \chi(\vec{n}, \, N_t - 1) \Big] = \\
&= \frac{1}{2} \Big[\eta_t(\vec{n}, \, 0) \, U_t(\vec{n}, \, 0) \, \chi(\vec{n}, \, 1) \, - \, \big(e^{\,\imath\theta_t} \eta_t(\vec{n}, \, N_t - 1) \big)^{\!\star} U_t^\dagger(\vec{n}, \, N_t - 1) \, \chi(\vec{n}, \, N_t - 1) \Big]
\end{aligned}
$$

and

$$\chi(\vec{n}, \, N_t - 1) \, - (\ldots) =$$

$$= \frac{1}{2} \, \eta_t(\vec{n}, \, N_t - 1) \Big[U_t \, (\vec{n}, \, N_t - 1) \, \chi(\vec{n}, \, N_t) \, - \, U_t^\dagger (\vec{n}, \, N_t - 2) \, \chi(\vec{n}, \, N_t - 2) \Big] =$$

$$= \frac{1}{2} \, \eta_t(\vec{n}, \, N_t - 1) \Big[e^{\imath \theta_t} \, U_t \, (\vec{n}, \, N_t - 1) \, \chi(\vec{n}, \, 0) \, - \, U_t^\dagger (\vec{n}, \, N_t - 2) \, \chi(\vec{n}, \, N_t - 2) \Big] =$$

$$= \frac{1}{2} \Big[e^{\imath \theta_t} \eta_t(\vec{n}, N_t - 1) \, U_t \, (\vec{n}, \, N_t - 1) \, \chi(\vec{n}, \, 0) \, - \eta_t(\vec{n}, \, N_t - 2) \, U_t^\dagger (\vec{n}, \, N_t - 2) \, \chi(\vec{n}, \, N_t - 2) \Big] \, ,$$

where the $(\ldots)$ include the remaining terms (they have been moved to the left hand side just for layout reasons). In both first steps, Eq. (C.7a) were used, while in both last steps we took into account that the staggered phase $\eta_\mu(n)$ does not depend on n_μ. From the equations above, it is easy to read how to impose during a simulation the BC as in Eq. (C.6). On condition that each staggered phase appears *exactly* next to its link, it is sufficient to multiply the staggered phases $\eta_t(\vec{n}, N_t - 1)$ by $e^{\imath \theta_t}$ and to take the complex conjugate whenever they appear next to the hermitian conjugate of a link. It is then clear why staggered phases are often included in links: If this is the case, the complex conjugate is automatically taken, thanks to the †-operator. It is worth remarking that if we modify staggered phases, then we have to make the fermionic field satisfy periodic BC in every direction, because otherwise the BC phase would appear more than only once.

To impose the general condition reported in Eqs. (C.3), it will be necessary to multiply the staggered phases in direction μ by $e^{\imath \theta_\mu}$ at the end of the lattice in such a direction (and, again, make the phases appear next to their links and take the complex conjugate properly). For later convenience, we can define another modified Dirac operator as

$$\tilde{M}_{n,m} \equiv \frac{1}{2} \sum_{\mu=1}^4 \eta_\mu(n) \Big[\tilde{U}_\mu'(n) \, \delta_{n+\hat{\mu},m} - \, \tilde{U}_\mu'^\dagger(n - \hat{\mu}) \, \delta_{n-\hat{\mu},m} \Big] + M_0 \delta_{n,m} \, ,$$

where

$$\bullet \quad \tilde{U}_\mu'(n) \; = \begin{cases} U_\mu(n) & \text{if } n \neq N_\mu - 1 \\ e^{\imath \theta_\mu} \, U_\mu(n) & \text{if } n = N_\mu - 1 \end{cases} \, , \qquad\qquad \text{(C.10a)}$$

$$\bullet \quad \tilde{U}_\mu'^\dagger(n) \; = \begin{cases} U_\mu(n) & \text{if } n \neq 0 \\ e^{-\imath \theta_\mu} \, U_\mu(n) & \text{if } n = 0 \end{cases} \, . \qquad\qquad \text{(C.10b)}$$

Are the two strategies connected?

So far we explained how to implement the desired BC in an actual simulation, but we did not really justified why we are allowed to proceed in such a way. Furthermore the Reader will be probably wondering whether the two possibilities above discussed are equivalent and, in case, why. To sort out these doubts, let us go through the strategy B once again, this time in a more formal way. At the end it will be clear which is the connection between the two strategies and how they are linked.

Let us start again from the action of the theory,

$$\mathcal{S} = \frac{1}{2} \sum_{n,\mu} \bar{\chi}(n) \, \eta_\mu(n) \Big[U_\mu(n) \, \chi(n + \hat{\mu}) \, - \, U_\mu^\dagger(n - \hat{\mu}) \, \chi(n - \hat{\mu}) \Big] + M_0 \sum_n \bar{\chi}(n) \, \chi(n) \, ,$$

where the fermionic field χ satisfies the BC in Eqs. (C.3). In the strategy B, we said that, if the staggered phases are modified (and maybe also put inside the links), then the fermionic field has to satisfy periodic BC. Indeed, this statement seems a bit artificial and not so rigorous. We can then

start rewriting the fermionic fields in the action as done in strategy A, using Eqs. (C.4), and then investigate how to modify the staggered phases. The first step leads to

$$\mathcal{S} = M_0 \sum_n \bar{\chi}'(n)\, \chi'(n) + \frac{1}{2} \sum_{n,\mu} \bar{\chi}'(n)\, \eta_\mu(n) \left[e^{\imath \frac{\theta_\mu}{N_\mu}}\, U_\mu(n)\, \chi'(n+\hat{\mu}) - e^{-\imath \frac{\theta_\mu}{N_\mu}}\, U_\mu^\dagger(n-\hat{\mu})\, \chi'(n-\hat{\mu}) \right] ,$$

exactly the same as in Eq. (C.5). Then we perform another transformation, this time on links, that reads

$$U_\mu'(n) \;=\; W(n)\, U_\mu(n)\, W^{-1}(n+\hat{\mu}) \; , \tag{C.11a}$$

where

$$W(n) \;=\; e^{-\imath \sum_\mu \frac{\theta_\mu\, (n_\mu \bmod N_\mu)}{N_\mu}} \qquad \text{with} \qquad W(n \pm N_\mu \hat{e}_\mu) \;=\; W(n) \; . \tag{C.11b}$$

Putting Eq. (C.11a) into the action, we obtain

$$\mathcal{S} = \frac{1}{2} \sum_{n,\mu} \bar{\chi}'(n)\, \eta_\mu(n) \left[e^{\imath \frac{\theta_\mu}{N_\mu}}\, G^{-1}(n)\, U_\mu'(n)\, G(n+\hat{\mu})\, \chi'(n+\hat{\mu}) + \right.$$

$$\left. -e^{-\imath \frac{\theta_\mu}{N_\mu}}\, G^{-1}(n)\, U_\mu'^\dagger(n-\hat{\mu})\, G(n-\hat{\mu})\, \chi'(n-\hat{\mu}) \right] + M_0 \sum_n \bar{\chi}'(n)\, \chi(n) \; .$$

Now, with a bit of algebra, we have the following cases

$$\bullet \quad e^{+\imath \frac{\theta_\mu}{N_\mu}}\, G^{-1}(n)\, G(n+\hat{\mu}) \;=\; \begin{cases} 1 & \text{if } \; n_\mu \neq N_\mu - 1 \\ e^{+\imath \theta_\mu} & \text{if } \; n_\mu = N_\mu - 1 \end{cases}$$

$$\bullet \quad e^{-\imath \frac{\theta_\mu}{N_\mu}}\, G^{-1}(n)\, G(n-\hat{\mu}) \;=\; \begin{cases} 1 & \text{if } \; n_\mu \neq 0 \\ e^{-\imath \theta_\mu} & \text{if } \; n_\mu = 0 \end{cases}$$

that put in the action give

$$\mathcal{S} = \frac{1}{2} \sum_{n,\mu} \bar{\chi}'(n)\, \eta_\mu(n) \left[\tilde{U}_\mu'(n)\, \chi'(n+\hat{\mu}) \;-\; \tilde{U}_\mu'^\dagger(n-\hat{\mu})\, \chi'(n-\hat{\mu}) \right] + M_0 \sum_n \bar{\chi}'(n)\, \chi'(n) \; , \tag{C.12}$$

where $\tilde{U}_\mu'(n)$ and $\tilde{U}_\mu'^\dagger(n)$ are the same as those defined in Eqs. (C.10). We can now redefine the staggered phases in order to rewrite Eq. (C.12) in terms of the original links,

$$\mathcal{S} = \frac{1}{2} \sum_{n,\mu} \bar{\chi}'(n) \left[\tilde{\eta}_\mu(n)\, U_\mu(n)\, \chi'(n+\hat{\mu}) \;-\; \tilde{\eta}_\mu^\star(n-\hat{\mu})\, U_\mu^\dagger(n-\hat{\mu})\, \chi'(n-\hat{\mu}) \right] + M_0 \sum_n \bar{\chi}'(n)\, \chi'(n) \; ,$$

with

$$\tilde{\eta}_\mu(n) = \begin{cases} \eta_\mu(n) & \text{if } n \neq N_\mu - 1 \\ e^{\imath \theta_\mu} \eta_\mu(n) & \text{if } n = N_\mu - 1 \end{cases} \qquad \text{and} \qquad \tilde{\eta}_\mu(-\hat{\mu}) = \eta_\mu(N_\mu - 1) \; .$$

Hence, we obtained the same result of strategy B: To impose the BC of Eqs. (C.3), it is necessary to multiply the staggered phases in direction μ by $e^{\imath \theta_\mu}$ at the end of the lattice in such a direction and make them appear *exactly* next to their links, taking the complex conjugate properly.

We are now ready to compare the two strategies. From the previous detailed analysis it should be clear that to pass from strategy A to strategy B one has to transform the link configuration accordingly to Eq. (C.11a). To avoid any confusion, it is worth commenting on such a transformation a bit further. Naïvely, it could seem to be a gauge transformation, but strictly speaking it is not. In fact, the new links U' are not elements of the $SU(3)$ group, but they are only unitary. Nevertheless, this is not a problem and it is exactly analogous to what happens when the staggered phases are included in the parallel transports. Indeed, it would be better to speak about *rewriting* rather then

transformation. We just used a smart replacement to have a more straightforward way to implement our algorithm. In the simulations, we will deal with unitary matrices that are not special, since they keep trace of additional information, like the staggered phases and the boundary conditions, but this does not affect any physical quantity. It is just important to be aware of the connection between the different strategies in case numeric results[4] produced with different codes have to be compared.

---

[4]Here, we are not speaking about physical quantities, but rather thinking to reference values of tests of particular operations like the action of the Dirac operator on a given fermionic field.

Bibliography

[1] W. William Bryant: *Galileo*. CreateSpace Independent Publishing Platform, **2014**. Cited on page XV.

[2] Georges Aad et al: *«Observation of a new particle in the search for the Standard Model Higgs boson with the ATLAS detector at the LHC»*. In: *Phys. Lett.* **B716**: pp. 1–29, **2012**. Available via DOI or via arXiv. Cited on page XV.

[3] Serguei Chatrchyan et al: *«Observation of a new boson at a mass of 125 GeV with the CMS experiment at the LHC»*. In: *Phys. Lett.* **B716**: pp. 30–61, **2012**. Available via DOI or via arXiv. Cited on page XV.

[4] B. P. Abbott et al: *«Observation of Gravitational Waves from a Binary Black Hole Merger»*. In: *Phys. Rev. Lett.* **116**: p. 061102, **2016**. Available via DOI or via arXiv. Cited on page XV.

[5] Steven Weinberg: *«A Model of Leptons»*. In: *Phys. Rev. Lett.* **19**: pp. 1264–1266, **1967**. Available via DOI. Cited on page XV.

[6] Juan Martin Maldacena: *«The Large N limit of superconformal field theories and supergravity»*. In: *Int. J. Theor. Phys.* **38**: pp. 1113–1133, **1999**. Available via DOI or via arXiv. Cited on page XV.

[7] Gerard 't Hooft and M. J. G. Veltman: *«Regularization and Renormalization of Gauge Fields»*. In: *Nucl. Phys.* **B44**: pp. 189–213, **1972**. Available via DOI. Cited on page XVI.

[8] David J. Gross and Frank Wilczek: *«Ultraviolet Behavior of Nonabelian Gauge Theories»*. In: *Phys. Rev. Lett.* **30**: pp. 1343–1346, **1973**. Available via DOI. Cited on page XVI.

[9] D. J. Gross and Frank Wilczek: *«Asymptotically Free Gauge Theories 1»*. In: *Phys. Rev.* **D8**: pp. 3633–3652, **1973**. Available via DOI. Cited on page XVI.

[10] D. J. Gross and Frank Wilczek: *«Asymptotically Free Gauge Theories 2»*. In: *Phys. Rev.* **D9**: pp. 980–993, **1974**. Available via DOI. Cited on page XVI.

[11] H. David Politzer: *«Reliable Perturbative Results for Strong Interactions?»* In: *Phys. Rev. Lett.* **30**: pp. 1346–1349, **1973**. Available via DOI. Cited on page XVI.

[12] H. David Politzer: *«Asymptotic Freedom: An Approach to Strong Interactions»*. In: *Phys. Rept.* **14**: pp. 129–180, **1974**. Available via DOI. Cited on page XVI.

[13] F. J. Wegner: *«Duality in Generalized Ising Models and Phase Transitions Without Local Order Parameters»*. In: *J. Math. Phys.* **12**: pp. 2259–2272, **1971**. Available via DOI. Cited on page XVI.

[14] Kenneth G. Wilson: *«Confinement of Quarks»*. In: *Phys. Rev.* **D10**: pp. 2445–2459, **1974**. Available via DOI. Cited on page XVI.

[15] Szabolcs Borsanyi et al: *«Is there still any T_c mystery in lattice QCD? Results with physical masses in the continuum limit III»*. In: *JHEP* **09**: p. 073, **2010**. Available via DOI or via arXiv. Cited on pages XVII, 44.

[16] Matthias Troyer and Uwe-Jens Wiese: *«Computational complexity and fundamental limitations to fermionic quantum Monte Carlo simulations»*. In: *Phys. Rev. Lett.* **94**: p. 170201, **2005**. Available via DOI or via arXiv. Cited on page XVII.

[17] Heinz J. Rothe: *Lattice Gauge Theories: An Introduction*. World Scientific Publishing, **2005**. Cited on pages 1, 29.

[18] T. DeGrand and C. DeTar: *Lattice Methods for Quantum Chromodynamics*. World Scientific, **2006**. Cited on pages 1, 16, 29, 84, 104, 159.

[19] C. Gattringer and C. Lang: *Quantum Chromodynamics on the Lattice: An Introductory Presentation*. Lecture Notes in Physics. Springer Berlin Heidelberg, **2009**. Cited on pages 1, 29, 32, 34, 51, 66, 126, 159.

[20] István Montvay and Gernot Münster: *Quantum fields on a lattice*. Cambridge monographs on mathematical physics. Cambridge: Cambridge Univ. Press, **1994**. Cited on page 1.

[21] Michael E. Peskin and Daniel V. Schroeder: *An Introduction to Quantum Field Theory*. Perseus Book Publishing, **1995**. Cited on page 1.

[22] Stephen L. Adler: *«Axial vector vertex in spinor electrodynamics»*. In: *Phys. Rev.* **177**: pp. 2426–2438, **1969**. Available via DOI. Cited on page 11.

[23] J. S. Bell and R. Jackiw: *«A PCAC puzzle: $\pi_0 \rightarrow \gamma\gamma$ in the sigma model»*. In: *Nuovo Cim.* **A60**: pp. 47–61, **1969**. Available via DOI. Cited on page 11.

[24] Neda Sadooghi and Heinz J. Rothe: *«Continuum behavior of lattice QED, discretized with one sided lattice differences, in one loop order»*. In: *Phys. Rev.* **D55**: pp. 6749–6759, **1997**. Available via DOI or via arXiv. Cited on page 11.

[25] Holger Bech Nielsen and M. Ninomiya: *«No Go Theorem for Regularizing Chiral Fermions»*. In: *Phys. Lett.* **B105**: p. 219, **1981**. Available via DOI. Cited on page 11.

[26] John B. Kogut and Leonard Susskind: *«Hamiltonian Formulation of Wilson's Lattice Gauge Theories»*. In: *Phys. Rev.* **D11**: pp. 395–408, **1975**. Available via DOI. Cited on page 13.

[27] Leonard Susskind: *«Lattice Fermions»*. In: *Phys. Rev.* **D16**: pp. 3031–3039, **1977**. Available via DOI. Cited on page 13.

[28] Tom Banks et al: *«Strong Coupling Calculations of the Hadron Spectrum of Quantum Chromodynamics»*. In: *Phys. Rev.* **D15**: p. 1111, **1977**. Available via DOI. Cited on page 13.

[29] N. Cabibbo and E. Marinari: *«A New Method for Updating SU(N) Matrices in Computer Simulations of Gauge Theories»*. In: *Phys. Lett.* **B119**: pp. 387–390, **1982**. Available via DOI. Cited on page 25.

[30] Michael Creutz: *«On invariant integration over SU(N)»*. In: *J. Math. Phys.* **19**: p. 2043, **1978**. Available via DOI. Cited on page 26.

[31] K. Symanzik: *«Continuum Limit and Improved Action in Lattice Theories. 1. Principles and ϕ^4 Theory»*. In: *Nucl. Phys.* **B226**: p. 187, **1983**. Available via DOI. Cited on page 27.

[32] Satchidananda Naik: *«On-shell Improved Lattice Action for QCD With Susskind Fermions and Asymptotic Freedom Scale»*. In: *Nucl. Phys.* **B316**: p. 238, **1989**. Available via DOI. Cited on page 27.

[33] Roberto Frezzotti et al: *«A Local formulation of lattice QCD without unphysical fermion zero modes»*. In: *Nucl. Phys. Proc. Suppl.* **83**: pp. 941–946, **2000**. Available via DOI or via arXiv. Cited on pages 27, 84.

[34] ROBERTO FREZZOTTI et al: *«Lattice QCD with a chirally twisted mass term»*. In: *JHEP* **08**: p. 058, **2001**. Available via arXiv. Cited on pages 27, 84.

[35] ROBERTO FREZZOTTI, STEFAN SINT and PETER WEISZ: *«$\mathcal{O}(a)$ improved twisted mass lattice QCD»*. In: *JHEP* **07**: p. 048, **2001**. Available via DOI or via arXiv. Cited on pages 27, 84.

[36] R. FREZZOTTI and G. C. ROSSI: *«Chirally improving Wilson fermions 1. $\mathcal{O}(a)$ improvement»*. In: *JHEP* **08**: p. 007, **2004**. Available via DOI or via arXiv. Cited on pages 27, 84.

[37] CURTIS G. CALLAN Jr.: *«Broken scale invariance in scalar field theory»*. In: *Phys. Rev.* **D2**: pp. 1541–1547, **1970**. Available via DOI. Cited on page 28.

[38] K. SYMANZIK: *«Small distance behavior in field theory and power counting»*. In: *Commun. Math. Phys.* **18**: pp. 227–246, **1970**. Available via DOI. Cited on page 28.

[39] J.I. KAPUSTA and C. GALE: *Finite-Temperature Field Theory: Principles and Applications*. Cambridge Monographs on Mathematical Physics. Cambridge University Press, **2006**. Cited on pages 29, 30.

[40] R. SOMMER: *«A New way to set the energy scale in lattice gauge theories and its applications to the static force and α_s in SU(2) Yang-Mills theory»*. In: *Nucl. Phys.* **B411**: pp. 839–854, **1994**. Available via DOI or via arXiv. Cited on page 31.

[41] P. HASENFRATZ and F. KARSCH: *«Chemical Potential on the Lattice»*. In: *Phys. Lett.* **B125**: p. 308, **1983**. Available via DOI. Cited on pages 33, 34.

[42] KATSUMI ITOH et al: *«Genuine symmetry of staggered fermion»*. In: *Prog. Theor. Phys.* **114**: pp. 631–641, **2005**. Available via DOI or via arXiv. Cited on page 34.

[43] LARRY D. MCLERRAN and BENJAMIN SVETITSKY: *«Quark Liberation at High Temperature: A Monte Carlo Study of SU(2) Gauge Theory»*. In: *Phys. Rev.* **D24**: p. 450, **1981**. Available via DOI. Cited on pages 35, 37.

[44] KRISHNA RAJAGOPAL and FRANK WILCZEK: *«The Condensed matter physics of QCD»*. In: *At the Frontier of Particle Physics: Handbook of QCD*. Ed. by M. SHIFMAN. World Scientific, **2001**. Chap. 35. Available via arXiv. Cited on page 41.

[45] MARK G. ALFORD: *«Color superconducting quark matter»*. In: *Ann. Rev. Nucl. Part. Sci.* **51**: pp. 131–160, **2001**. Available via DOI or via arXiv. Cited on pages 41, 43, 44.

[46] MARK G. ALFORD et al: *«Color superconductivity in dense quark matter»*. In: *Rev. Mod. Phys.* **80**: pp. 1455–1515, **2008**. Available via DOI or via arXiv. Cited on page 41.

[47] MIKHAIL A. STEPHANOV: *«QCD phase diagram and the critical point»*. In: *Prog. Theor. Phys. Suppl.* **153**: pp. 139–156, **2004**. Available via DOI or via arXiv. Cited on pages 43, 47.

[48] SEAN GAVIN, ANDREAS GOCKSCH and ROBERT D. PISARSKI: *«QCD and the chiral critical point»*. In: *Phys. Rev.* **D49**: pp. 3079–3082, **1994**. Available via DOI or via arXiv. Cited on page 45.

[49] EDWIN LAERMANN and OWE PHILIPSEN: *«The Status of lattice QCD at finite temperature»*. In: *Ann. Rev. Nucl. Part. Sci.* **53**: pp. 163–198, **2003**. Available via DOI or via arXiv. Cited on page 46.

[50] PHILIPPE DE FORCRAND, SEYONG KIM and OWE PHILIPSEN: *«A QCD chiral critical point at small chemical potential: Is it there or not?»* In: *PoS* **LAT2007**: p. 178, **2007**. Available via arXiv. Cited on pages 47, 132, 133, 140.

[51] A. BAZAVOV et al: *«The chiral and deconfinement aspects of the QCD transition»*. In: *Phys. Rev.* **D85**: p. 054503, **2012**. Available via DOI or via arXiv. Cited on page 47.

[52] Y. AOKI et al: *«The Order of the quantum chromodynamics transition predicted by the standard model of particle physics»*. In: *Nature* **443**: pp. 675–678, **2006**. Available via DOI or via arXiv. Cited on pages 47, 51.

[53] ETTORE VICARI: *«Critical phenomena and renormalization-group flow of multi-parameter ϕ^4 field theories»*. In: *PoS* **LAT2007**: p. 023, **2007**. Available via arXiv. Cited on page 50.

[54] LUDMILA LEVKOVA: *«QCD at nonzero temperature and density»*. In: *PoS* **LAT2011**: p. 011, **2011**. Available via arXiv. Cited on page 50.

[55] HENG-TONG DING and PRASAD HEGDE: *«Chiral phase transition of N_f =2+1 and 3 QCD at vanishing baryon chemical potential»*. In: *PoS* **LAT2015**: p. 161, **2016**. Available via arXiv. Cited on page 50.

[56] CLAUDIO BONATI et al: *«Chiral phase transition in two-flavor QCD from an imaginary chemical potential»*. In: *Phys. Rev.* **D90**: p. 074030, **2014**. Available via DOI or via arXiv. Cited on pages 50, 54, 60, 110, 115, 132.

[57] PHILIPPE DE FORCRAND and OWE PHILIPSEN: *«The Chiral critical line of $N_f = 2 + 1$ QCD at zero and non-zero baryon density»*. In: *JHEP* **01**: p. 077, **2007**. Available via DOI or via arXiv. Cited on pages 51, 80, 117.

[58] YOSHINOBU KURAMASHI et al: *«Critical endline of the finite temperature phase transition for 2+1 flavor QCD around the SU(3)-flavor symmetric point»*. **2016**. Available via arXiv. Cited on page 51.

[59] PHILIPPE DE FORCRAND and OWE PHILIPSEN: *«The Chiral critical point of $N_f = 3$ QCD at finite density to the order $(\mu/T)^4$»*. In: *JHEP* **11**: p. 012, **2008**. Available via DOI or via arXiv. Cited on page 51.

[60] PHILIPPE DE FORCRAND and OWE PHILIPSEN: *«The curvature of the critical surface $(m_{u,d}, m_s)^c(\mu)$: A Progress report»*. In: *PoS* **LAT2008**: p. 208, **2008**. Available via arXiv. Cited on page 51.

[61] ANDRE ROBERGE and NATHAN WEISS: *«Gauge Theories With Imaginary Chemical Potential and the Phases of QCD»*. In: *Nucl. Phys.* **B275**: pp. 734–745, **1986**. Available via DOI. Cited on page 53.

[62] MASSIMO D'ELIA and MARIA-PAOLA LOMBARDO: *«Finite density QCD via imaginary chemical potential»*. In: *Phys. Rev.* **D67**: p. 014505, **2003**. Available via DOI or via arXiv. Cited on page 53.

[63] PHILIPPE DE FORCRAND and OWE PHILIPSEN: *«The QCD phase diagram for small densities from imaginary chemical potential»*. In: *Nucl. Phys.* **B642**: pp. 290–306, **2002**. Available via DOI or via arXiv. Cited on page 53.

[64] PHILIPPE DE FORCRAND and OWE PHILIPSEN: *«Constraining the QCD phase diagram by tricritical lines at imaginary chemical potential»*. In: *Phys. Rev. Lett.* **105**: p. 152001, **2010**. Available via DOI or via arXiv. Cited on pages 53, 124, 127, 131.

[65] OWE PHILIPSEN and PHILIPPE DE FORCRAND: *«Constraints for the QCD phase diagram from imaginary chemical potential»*. In: *PoS* **LAT2010**: p. 211, **2010**. Available via arXiv. Cited on page 53.

[66] CLAUDIO BONATI et al: *«The Roberge-Weiss endpoint in $N_f = 2$ QCD»*. In: *Phys. Rev.* **D83**: p. 054505, **2011**. Available via DOI or via arXiv. Cited on pages 57, 106, 115, 125, 127, 133, 134, 139, 140.

[67] IAN D. LAWRIE and STÉPHANE SARBACH: *«Theory of Tricritical Points»*. In: *Phase Transitions and Critical Phenomena*. Ed. by C. DOMB and J.L. LEBOWITZ. Vol. 9. Academic press, **2001**. Chap. 1. Cited on page 60.

[68] OWE PHILIPSEN and CHRISTOPHER PINKE: *«The $N_f = 2$ QCD chiral phase transition with Wilson fermions at zero and imaginary chemical potential»*. In: *Phys. Rev.* **D93**: p. 114507, **2016**. Available via DOI or via arXiv. Cited on pages 60, 115.

[69] A. D. KENNEDY, IVAN HORVATH and STEFAN SINT: *«A New exact method for dynamical fermion computations with nonlocal actions»*. In: *Nucl. Phys. Proc. Suppl.* **73**: pp. 834–836, **1999**. Available via DOI or via arXiv. Cited on pages 65, 70.

[70] M. A. CLARK and A. D. KENNEDY: *«Accelerating Staggered Fermion Dynamics with the Rational Hybrid Monte Carlo (RHMC) Algorithm»*. In: *Phys. Rev.* **D75**: p. 011502, **2007**. Available via DOI or via arXiv. Cited on page 65.

[71] M. A. CLARK and A. D. KENNEDY: *«Accelerating dynamical fermion computations using the rational hybrid Monte Carlo (RHMC) algorithm with multiple pseudofermion fields»*. In: *Phys. Rev. Lett.* **98**: p. 051601, **2007**. Available via DOI or via arXiv. Cited on pages 66, 82, 134.

[72] A. D. KENNEDY: *«Algorithms for dynamical fermions»*. **2006**. Available via arXiv. Cited on page 71.

[73] BEAT JEGERLEHNER: *«Krylov space solvers for shifted linear systems»*. **1996**. Available via arXiv. Cited on pages 72, 92.

[74] R. BARRETT et al: *Templates for the Solution of Linear Systems: Building Blocks for Iterative Methods, 2nd Edition*. Philadelphia, PA: SIAM, **1994**. Cited on page 72.

[75] JAMES W. DEMMEL: *Applied Numerical Linear Algebra*. Philadelphia, PA, USA: Society for Industrial and Applied Mathematics, **1997**. Cited on pages 72, 92.

[76] STEVEN A. GOTTLIEB et al: *«Hybrid Molecular Dynamics Algorithms for the Numerical Simulation of Quantum Chromodynamics»*. In: *Phys. Rev.* **D35**: pp. 2531–2542, **1987**. Available via DOI. Cited on pages 74, 80.

[77] TETSUYA TAKAISHI and PHILIPPE DE FORCRAND: *«Testing and tuning new symplectic integrators for hybrid Monte Carlo algorithm in lattice QCD»*. In: *Phys. Rev.* **E73**: p. 036706, **2006**. Available via DOI or via arXiv. Cited on page 80.

[78] M. A. CLARK: *The Rational Hybrid Monte Carlo Algorithm*. PhD thesis. University of Edinburgh, **2005**, 183 pages. Available here (visited on 01/12/2016). Cited on page 81.

[79] K. JANSEN and C. URBACH: *«tmLQCD: A Program suite to simulate Wilson Twisted mass Lattice QCD»*. In: *Comput. Phys. Commun.* **180**: pp. 2717–2738, **2009**. Available via DOI or via arXiv. Cited on page 83.

[80] M. A. CLARK et al: *«Solving Lattice QCD systems of equations using mixed precision solvers on GPUs»*. In: *Comput. Phys. Commun.* **181**: pp. 1517–1528, **2010**. Available via DOI or via arXiv. Cited on page 84.

[81] R. BABICH et al: *«Scaling Lattice QCD beyond 100 GPUs»*. In: *SC11 International Conference for High Performance Computing, Networking, Storage and Analysis Seattle, Washington, November 12-18, 2011*. **2011**. Available via arXiv or here (visited on 01/12/2016). Cited on page 84.

[82] MATTHIAS BACH et al: *«Optimized HPL for AMD GPU and multi-core CPU usage»*. In: *Computer Science - R&D* **26**: pp. 153–164, **2011**. Available via DOI. Cited on page 84.

[83] DAVID ROHR et al: *«Lattice-CSC: Optimizing and Building an Efficient Supercomputer for Lattice-QCD and to Achieve First Place in Green500»*. In: *High Performance Computing: 30th International Conference, ISC High Performance 2015, Frankfurt, Germany, July 12-16, 2015, Proceedings*. Ed. by JULIAN M. KUNKEL and THOMAS LUDWIG. Cham: Springer International Publishing, **2015**, pp. 179–196. Available via DOI. Cited on page 84.

[84] OWE PHILIPSEN et al: *«LatticeQCD using OpenCL»*. In: *PoS* **LAT2011**: p. 044, **2011**. Available via arXiv. Cited on page 84.

[85] MATTHIAS BACH et al: *«Lattice QCD based on OpenCL»*. In: *Comput. Phys. Commun.* **184**: pp. 2042–2052, **2013**. Available via DOI or via arXiv. Cited on page 84.

[86] Matthias Bach et al: *«Twisted-Mass Lattice QCD using OpenCL»*. In: *PoS* **LAT2013**: p. 032, **2014**. Available here (visited on 01/12/2016). Cited on page 84.

[87] Owe Philipsen et al: *«CL^{2}QCD - Lattice QCD based on OpenCL»*. In: *PoS* **LAT2014**: p. 038, **2014**. Available via arXiv. Cited on pages 84, 87.

[88] Matthias Bach: *Energy- and cost-efficient Lattice-QCD computations using graphics processing units*. PhD thesis. Frankfurt: J. W. Goethe Universität, **2015**, 197 pages. Available here (visited on 01/12/2016). Cited on pages 84, 90, 94.

[89] R.C. Martin: *Clean Code: A Handbook of Agile Software Craftsmanship*. Robert C. Martin series. Prentice Hall, **2009**. Cited on page 84.

[90] K. Beck: *Test-driven Development: By Example*. Kent Beck signature book. Addison-Wesley, **2003**. Cited on page 84.

[91] Bernd A. Berg: *Markov chain Monte Carlo simulations and their statistical analysis: with Web-based Fortran code*. World Scientific, **2004**. Cited on pages 94–96.

[92] M.E.J. Newman and G.T. Barkema: *Monte Carlo Methods in Statistical Physics*. Clarendon Press, **1999**. Cited on pages 94, 97, 106–108.

[93] Ulli Wolff: *«Monte Carlo errors with less errors»*. In: *Comput. Phys. Commun.* **156**: pp. 143–153, **2004**. Available via DOI or via arXiv. Cited on page 95.

[94] Shao-Jing Dong and Keh-Fei Liu: *«Stochastic estimation with Z_2 noise»*. In: *Phys. Lett.* **B328**: pp. 130–136, **1994**. Available via DOI or via arXiv. Cited on page 99.

[95] Thomas A. Severini: *Elements of Distribution Theory*. Cambridge University Press, **2005**. Cited on page 103.

[96] K. Binder: *«Finite size scaling analysis of Ising model block distribution functions»*. In: *Z. Phys.* **B43**: pp. 119–140, **1981**. Available via DOI. Cited on page 103.

[97] Christopher Czaban et al: *«Roberge-Weiss transition in $N_f = 2$ QCD with Wilson fermions and $N_\tau = 6$»*. In: *Phys. Rev.* **D93**: p. 054507, **2016**. Available via DOI or via arXiv. Cited on pages 103, 105, 115, 116.

[98] Andrea Pelissetto and Ettore Vicari: *«Critical phenomena and renormalization group theory»*. In: *Phys. Rept.* **368**: pp. 549–727, **2002**. Available via DOI or via arXiv. Cited on page 104.

[99] K. Huang: *Statistical mechanics*. Wiley, **1987**. Cited on page 107.

[100] Alan M. Ferrenberg and Robert H. Swendsen: *«Optimized Monte Carlo analysis»*. In: *Phys. Rev. Lett.* **63**: pp. 1195–1198, **1989**. Available via DOI. Cited on pages 108, 119.

[101] A. M. Ferrenberg and R. H. Swendsen: *«New Monte Carlo Technique for Studying Phase Transitions»*. In: *Phys. Rev. Lett.* **61**: pp. 2635–2638, **1988**. Available via DOI. Cited on page 108.

[102] Owe Philipsen and Christopher Pinke: *«Nature of the Roberge-Weiss transition in $N_f = 2$ QCD with Wilson fermions»*. In: *Phys. Rev.* **D89**: p. 094504, **2014**. Available via DOI or via arXiv. Cited on pages 115, 118, 124–127, 131.

[103] Owe Philipsen and Alessandro Sciarra: *«Roberge-Weiss transition in $N_f = 2$ QCD with staggered fermions and $N_\tau = 6$»*. In: *Proceedings, 34th International Symposium on Lattice Field Theory (Lattice 2016): Southampton, UK, July 24-30, 2016*. **2016**. Available via arXiv. Cited on page 116.

[104] S. Duane et al: *«Hybrid Monte Carlo»*. In: *Phys. Lett.* **B195**: pp. 216–222, **1987**. Available via DOI. Cited on page 118.

[105] Martin Hasenbusch: *«Speeding up the hybrid Monte Carlo algorithm for dynamical fermions»*. In: *Phys. Lett.* **B519**: pp. 177–182, **2001**. Available via DOI or via arXiv. Cited on page 118.

[106] BALINT JOO et al: *«Instability in the molecular dynamics step of hybrid Monte Carlo in dynamical Fermion lattice QCD simulations»*. In: *Phys. Rev.* **D62**: p. 114501, **2000**. Available via DOI or via arXiv. Cited on page 119.

[107] SZABOLCS BORSANYI et al: *«High-precision scale setting in lattice QCD»*. In: *JHEP* **09**: p. 010, **2012**. Available via DOI or via arXiv. Cited on pages 119, 126, 141.

[108] M. HASENBUSCH et al: *«Multicritical Nishimori point in the phase diagram of the ±J Ising model on a square lattice»*. In: *Phys. Rev.* **E77**: p. 051115, *May*2008. Available via DOI or via arXiv. Cited on page 124.

[109] XIAO-YONG JIN et al: *«Critical endpoint of the finite temperature phase transition for three flavor QCD»*. In: *Phys. Rev.* **D91**: p. 014508, **2015**. Available via DOI or via arXiv. Cited on page 127.

[110] OWE PHILIPSEN: *«The QCD equation of state from the lattice»*. In: *Prog. Part. Nucl. Phys.* **70**: pp. 55–107, **2013**. Available via DOI or via arXiv. Cited on page 127.

[111] ANDREI ALEXANDRU and ANYI LI: *«QCD at imaginary chemical potential with Wilson fermions»*. In: *PoS* **LAT2013**: p. 208, **2014**. Available via arXiv. Cited on page 127.

[112] M. E. J. NEWMAN and G. T. BARKEMA: *«Monte Carlo study of the random-field Ising model»*. In: *Phys. Rev.* **E53**: pp. 393–404, **1996**. Available via DOI. Cited on pages 137, 138.

[113] MAARTEN F. L. GOLTERMAN and JAN SMIT: *«Lattice Baryons With Staggered Fermions»*. In: *Nucl. Phys.* **B255**: pp. 328–340, **1985**. Available via DOI. Cited on page 159.

[114] MAARTEN F. L. GOLTERMAN: *«Staggered Mesons»*. In: *Nucl. Phys.* **B273**: pp. 663–676, **1986**. Available via DOI. Cited on pages 159, 161, 163.

[115] N. ISHIZUKA et al: *«Operator dependence of hadron masses for Kogut-Susskind quarks on the lattice»*. In: *Nucl. Phys.* **B411**: pp. 875–902, **1994**. Available via DOI. Cited on page 159.

[116] TIM BREITENFELDER: *Pion Spectroscopy in Lattice QCD with $N_f = 2$ and Staggered Fermions*. Bachelor Thesis. Frankfurt: J. W. Goethe Universität, **2016**, 41 pages. Cited on page 159.

[117] WEON-JONG LEE and STEPHEN R. SHARPE: *«Partial flavor symmetry restoration for chiral staggered fermions»*. In: *Phys. Rev.* **D60**: p. 114503, **1999**. Available via DOI or via arXiv. Cited on page 159.

[118] MAARTEN F. L. GOLTERMAN and JAN SMIT: *«Selfenergy and Flavor Interpretation of Staggered Fermions»*. In: *Nucl. Phys.* **B245**: pp. 61–88, **1984**. Available via DOI. Cited on pages 161, 163.

[119] E. MARINARI, G. PARISI and C. REBBI: *«Monte Carlo Simulation of the Massive Schwinger Model»*. In: *Nucl. Phys.* **B190**: p. 734, **1981**. Available via DOI. Cited on page 161.

[120] C. T. H. DAVIES et al: *«High precision lattice QCD confronts experiment»*. In: *Phys. Rev. Lett.* **92**: p. 022001, **2004**. Available via DOI or via arXiv. Cited on page 161.

[121] C. AUBIN et al: *«First determination of the strange and light quark masses from full lattice QCD»*. In: *Phys. Rev.* **D70**: p. 031504, **2004**. Available via DOI or via arXiv. Cited on page 161.

[122] C. AUBIN et al: *«Semileptonic decays of D mesons in three-flavor lattice QCD»*. In: *Phys. Rev. Lett.* **94**: p. 011601, **2005**. Available via DOI or via arXiv. Cited on page 161.

[123] C. AUBIN et al: *«Light pseudoscalar decay constants, quark masses, and low energy constants from three-flavor lattice QCD»*. In: *Phys. Rev.* **D70**: p. 114501, **2004**. Available via DOI or via arXiv. Cited on page 161.

[124] C. AUBIN et al: *«Charmed meson decay constants in three-flavor lattice QCD»*. In: *Phys. Rev. Lett.* **95**: p. 122002, **2005**. Available via DOI or via arXiv. Cited on page 161.

[125] Andreas S. Kronfeld: *«Predictions with Lattice QCD»*. In: *J. Phys. Conf. Ser.* **46**: pp. 147–151, **2006**. Available via DOI or via arXiv. Cited on page 161.

[126] Michael Creutz: *«Diseases with rooted staggered quarks»*. In: *PoS* **LAT2006**: p. 208, **2006**. Available via arXiv. Cited on page 161.

[127] Michael Creutz: *«Flavor extrapolations and staggered fermions»*. **2006**. Available via arXiv. Cited on page 161.

[128] Michael Creutz: *«Why rooting fails»*. In: *PoS* **LAT2007**: p. 007, **2007**. Available via arXiv. Cited on page 161.

[129] Michael Creutz: *«Chiral anomalies and rooted staggered fermions»*. In: *Phys. Lett.* **B649**: pp. 230–234, **2007**. Available via DOI or via arXiv. Cited on page 161.

[130] Michael Creutz: *«Comments on staggered fermions: Panel discussion»*. In: *PoS* **CON-FINEMENT8**: p. 016, **2008**. Available via arXiv. Cited on pages 161, 162.

[131] C. Bernard: *«Staggered chiral perturbation theory and the fourth-root trick»*. In: *Phys. Rev.* **D73**: p. 114503, **2006**. Available via DOI or via arXiv. Cited on page 161.

[132] Yigal Shamir: *«Renormalization-group analysis of the validity of staggered-fermion QCD with the fourth-root recipe»*. In: *Phys. Rev.* **D75**: p. 054503, **2007**. Available via DOI or via arXiv. Cited on page 161.

[133] Claude Bernard, Maarten Golterman and Yigal Shamir: *«Regularizing QCD with staggered fermions and the fourth root trick»*. In: *PoS* **LAT2006**: p. 205, **2006**. Available via arXiv. Cited on pages 161, 164.

[134] Stephen R. Sharpe: *«Rooted staggered fermions: Good, bad or ugly?»* In: *PoS* **LAT2006**: p. 022, **2006**. Available via arXiv. Cited on pages 161, 163, 164.

[135] Claude Bernard et al: *«Comment on 'Chiral anomalies and rooted staggered fermions'»*. In: *Phys. Lett.* **B649**: pp. 235–240, **2007**. Available via DOI or via arXiv. Cited on page 161.

[136] Michael Creutz: *«Reply to: 'Comment on: 'Chiral anomalies and rooted staggered fermions''»*. In: *Phys. Lett.* **B649**: pp. 241–242, **2007**. Available via DOI or via arXiv. Cited on page 161.

[137] Claude Bernard et al: *«'t Hooft vertices, partial quenching, and rooted staggered QCD»*. In: *Phys. Rev.* **D77**: p. 114504, **2008**. Available via DOI or via arXiv. Cited on page 161.

[138] Michael Creutz: *«Comment on "'t Hooft vertices, partial quenching, and rooted staggered QCD"»*. In: *Phys. Rev.* **D78**: p. 078501, **2008**. Available via DOI or via arXiv. Cited on page 161.

[139] Claude Bernard et al: *«Reply to: 'Comment on: "t Hooft vertices, partial quenching, and rooted staggered QCD"'»*. In: *Phys. Rev.* **D78**: p. 078502, **2008**. Available via DOI or via arXiv. Cited on page 161.

[140] Michael Creutz: *«The Saga of rooted staggered quarks»*. **2008**. Available here (visited on 01/12/2016). Cited on page 162.

[141] G. C. Rossi and M. Testa: *«A 0-dimensional counter-example to rooting?»* In: *Phys. Lett.* **B688**: pp. 248–249, **2010**. Available via DOI or via arXiv. Cited on page 162.

[142] Stephan Durr: *«Physics of η' with rooted staggered quarks»*. In: *Phys. Rev.* **D85**: p. 114503, **2012**. Available via DOI or via arXiv. Cited on page 162.

[143] Tomás Oliveira e Silva: *«Computational verification of the $3x + 1$ conjecture»*. Available here (visited on 01/12/2016). Cited on page 165.

[144] Eric Roosendaal: *«On the $3x + 1$ problem»*. Available here (visited on 01/12/2016). Cited on page 165.

[145] Gourdon Xavier: *«The 10^{13} first zeros of the Riemann zeta function, and zeros computation at very large height»*. Available here (visited on 01/12/2016). Cited on page 166.

[146]   A.M. Odlyzko and H.J.J. te Riele: *«Disproof of the Mertens conjecture»*. In: *Journal für die reine und angewandte Mathematik*, pp. 138–160, **1985**. Available via DOI. Cited on page 166.

[147]   T. Kotnik and J. van de Lune: *Further Systematic Computations on the Summatory Function of the Möbius Function*. Report MAS. Centrum voor Wiskunde en Informatica, **2003**. Cited on page 166.

[148]   Tadej Kotnik and Herman te Riele: *«The Mertens Conjecture Revisited»*. In: *Algorithmic Number Theory: 7th International Symposium, ANTS-VII, Berlin, Germany, July 23-28, 2006. Proceedings*. Ed. by Florian Hess, Sebastian Pauli and Michael Pohst. Berlin, Heidelberg: Springer Berlin Heidelberg, **2006**, pp. 156–167. Available via DOI. Cited on page 166.

[149]   S. Skewes: *«On the Difference $\pi(x) - li(x)$ (II)»*. In: *Proceedings of the London Mathematical Society* **s3-5**: pp. 48–70, **1955**. Available via DOI or here. Cited on page 166.

[150]   G. M. de Divitiis, R. Petronzio and N. Tantalo: *«On the discretization of physical momenta in lattice QCD»*. In: *Phys. Lett.* **B595**: pp. 408–413, **2004**. Available via DOI or via arXiv. Cited on page 171.

Alessandro Sciarra

Curriculum Vitae

Lessingstraße 6
61440, Oberursel
Deutschland

℘ +49 176 61890008
✉ alessandro.sciarra@yahoo.it

Education

12.2012 – 12.2016	**Ph.D. student**, *J. W. Goethe Universität*, Frankfurt am Main, Germany.
09.2010 – 11.2012	**Master student**, *Università degli studi di Genova*, Italy.
09.2007 – 09.2010	**Bachelor student**, *Università degli studi di Genova*, Italy.

Theses

Ph.D. **The QCD phase diagram at purely imaginary chemical potential from the lattice**, *Supervisor: Prof. Dr. Owe Philipsen*.

The QCD phase diagram at purely imaginary chemical potential has been studied using lattice techniques both with Wilson and staggered fermions. The CL^2QCD software, a GPU code based on OpenCL which was made public in 2014, has been ameliorated and used. An RHMC algorithm with staggered fermions has been added and optimised. Many analysis tools have been implemented, with particular attention to their maintainability. A completely new Bash library to automatically handle and monitor simulations on supercomputers has been developed.

Master **Chiral properties of lattice QCD**, *Supervisor: Prof. Dr. Massimo D'Elia*.

The chiral properties of a new lattice action have been investigated. Adding additional terms to the standard, unimproved staggered action, it is possible to modify the spectrum of the Dirac operator, so that modes with different chirality are separated. The discrete rotational lattice symmetry should be broken, though. An RHMC algorithm has been implemented to investigate this aspect numerically.

Bachelor **The specific heat of solids**, *Supervisor: Prof. Dr. Riccardo Ferrando*.

Teaching experience

J. W. Goethe Universität, Frankfurt am Main

WS16 **Introduction to programming for physicists (Fortran)**, *Prof. Dr. Eberhard Engel*.

SS15 **Advisor of Tim Breitenfelder**, *Bachelor Thesis*.
 «*Pion Spectroscopy in Lattice QCD with $N_f = 2$ and Staggered Fermions*»

WS15 **Introduction to programming for physicists (Fortran)**, *Prof. Dr. Eberhard Engel*.

WS14 **Statistical Physics**, *Prof. Dr. Owe Philipsen*.

SS14 **Introductory Quantum Mechanics**, *Prof. Dr. Owe Philipsen*.

WS13 **Introduction to programming for physicists (C)**, *Jun Prof. Dr. Marc Wagner*.

SS13 **Advanced Quantum Mechanics**, *Prof. Dr. Owe Philipsen*.

WS12 **Quantum Field Theory I**, *Jun Prof. Dr. Marc Wagner*.

Presentations

25.07.2016 **XXXIV International Symposium on Lattice Field Theory (Southampton, UK)**
 «*Roberge-Weiss transition in $N_f = 2$ QCD with staggered fermions and $N_t = 6$*»

11.07.2016 **Palaver (Goethe Universität)**
 «*The QCD phase diagram at imaginary chemical potential*»

20.06.2016 **Lattice seminar (DESY, Zeuthen)**
 «*CL^2QCD – An open source LQCD software based on OpenCL*»

03.06.2016	**Lattice seminar (Goethe Universität)**
	«The fourth rooting trick with staggered fermions: yes, no or maybe?»
16.12.2015	**C++ user meeting (FIAS, Frankfurt am Main)**
	«(Some) Good C++ practices»
03.07.2015	**Lattice seminar (Goethe Universität)**
	«The (R)HMC algorithm with staggered fermions»
06.02.2015	**Lattice seminar (Goethe Universität)**
	«Chiral properties of a new staggered action»
15.12.2014	**Palaver (Goethe Universität)**
	«Phase transitions in $N_f = 2$ lattice QCD»
24.06.2014	**XXXII International Symposium on Lattice Field Theory (New York, USA)**
	«CL^{2}QCD – Lattice QCD based on OpenCL»
30.01.2014	**Lattice seminar (Goethe Universität)**
	«The fermion doubling issue and the staggering procedure»
11.02.2013	**Palaver (Goethe Universität)**
	«Chiral properties of lattice QCD»

Publications

2016	**O. Philipsen and A. Sciarra**
	«Roberge-Weiss transition in $N_f = 2$ QCD with staggered fermions and $N_t = 6$»
	`arXiV:1610.09979`
	C. Czaban, F. Cuteri, O. Philipsen, C. Pinke and A. Sciarra
	«Roberge-Weiss transition in $N_f = 2$ QCD with Wilson fermions and $N_t = 6$»
	Phys. Rev. D**93** (2016) No.5, 054507, DOI: 10.1103/PhysRevD.93.054507, `arXiV:1512.07180`
2015	**F. Cuteri, C. Czaban, O. Philipsen, C. Pinke and A. Sciarra**
	«The nature of the Roberge-Weiss Transition in $N_f = 2$ QCD with Wilson Fermions on $N_t = 6$ lattices»
	PoS LAT**2015** 148, `arXiV:1511.03105`
2014	CL^{2}QCD first release: https://github.com/CL2QCD/cl2qcd
	M. Bach, O. Philipsen, C. Pinke and A. Sciarra
	«CL^{2}QCD – Lattice QCD based on OpenCL»
	PoS LAT**2014** 038, `arXiV:1411.5219`

Computer skills

Working knowledge
C++, OpenCL, Bash, Slurm, Gnuplot, LaTeX

Basic knowledge
Mathematica, Python, Fortran, OpenOffice

Languages

Italian	**Mother tongue**	
English	**Advanced**	
French	**Advanced**	*DELF B2*
German	**Intermediate**	*Daily life communication, reading and writing skills*